Dissertation zur Erlangung des
Doktorgrades der Fakultät für Chemie und
Pharmazie der Ludwig-Maximilians-
Universität München

Molecular Frameworks – From Morphological Control to Electronic Properties

Julian Markus Rotter

aus

München, Deutschland

2020

Diese Dissertation wurde im Sinne von § 7 der Promotionsordnung vom 28. November 2011 von Herrn Prof. Dr. Thomas Bein betreut.

Eidesstattliche Versicherung

Diese Dissertation wurde eigenständig und ohne unerlaubte Hilfe bearbeitet.

München, den 06.01.2020 _____

Julian Rotter

Dissertation eingereicht am 09.01.2020

1. Gutachter: Prof. Dr. Thomas Bein

2. Gutachter: Prof. Dr. Stefan Wuttke

Mündliche Prüfung am 06.02.2020

Meinen Eltern.

Acknowledgement

After a good four years of Ph.D. time, there are many people who have contributed in various ways to the creation of this work. I would like to thank them here.

First of all, I would like to thank my supervisor Prof. Thomas Bein. Many thanks for the exciting and challenging topic of my dissertation. It was great to be able to work on different projects with so much freedom and to be able to realize my own interests. Thank you for the many exciting discussions, the always motivating words, the support in attending international conferences and the provision of such exceptional laboratory equipment.

Many thanks also to Professor Stefan Wuttke for the excellent and exciting cooperation in our projects and also for the fact that you were willing to judge my work as a second reviewer in faraway Spain.

I would also like to thank Dana Medina in particular. It was great to work together and realize our many projects. Without you, this dissertation would undoubtedly have been a completely different one. Thanks a lot for all the uplifting words, especially when I ever lost faith in science. I fondly remember our crazy working hours and review rounds and how we sometimes got on each other's nerves, but in the end, we were always proud of our joint achievements.

I would also like to thank my collaboration partners. Many thanks to my external partners Prof. Menny Shalom, Prof. Adelheid Godt and Tobias von Zons, and Prof. Vladimir Dyakonov, Michael Auth and Andreas Sperlich, Alexander Biewald und Prof. Achim Hartschuh. Also, many thanks to all the people I was working with within the group. I would especially like to thank Andre, Erika, Maria, Roman, Simon, and Torben, with whom I was able to work on great projects. But also to the rest of the COF/MOF Subgroup a big thank you for the many discussions and the mutual support over the years. In general, it was great to work with so many talented and motivated people from the AK Bein and to learn something from all of them.

Special thanks also go to Corinna, Regina, and Tina for their great support during my time at AK Bein. Thanks to Markus, Steffen and Michi for all your efforts in electron microscopy,

Abstract

Molecular frameworks are materials that are available through bottom-up synthesis from organic or inorganic building blocks. The intrinsic properties of the materials can be systematically designed through the use of specially constructed building blocks, while physical properties, such as porosity or pore shape, can be additionally tailored through the means of reticular chemistry. This thesis is focusing on two emerging classes of molecular frameworks, namely covalent organic frameworks (COFs) and metal-organic frameworks (MOFs).

COFs are a class of highly ordered, crystalline polymers, which possess high surface areas and defined pore sizes. They are typically synthesized by covalently linking two organic building blocks through a condensation reaction. By tailoring and adjusting the organic linkers, a variety of structural, physical and chemical properties can be encoded in the resulting COFs. This allows COFs to be used as materials for many (including potential) applications, such as gas storage, chemical sensing, catalysis, charge storage, charge transport or optoelectronics. The ability to grow covalent organic frameworks as films allows for studying their properties as solid layers and enables the incorporation of these materials into a variety of functional devices. In the introduction of this thesis, a comprehensive overview of the techniques for fabricating COF films is given, along with different examples for applications.

The incorporation of sterically demanding or highly insoluble building blocks often requires the introduction of special side groups into the organic linker. In the third chapter of this thesis, the effects of incorporating ethoxy side chains into a 2D π-stacked benzodithiophene-based (BDT) COF are studied. The resulting BDT-OEt COF is a crystalline mesoporous material featuring high surface area and accessible hexagonal pores. Furthermore, a series of COFs was studied, containing both BDT and BDT-OEt building units at different ratios. The impact of the gradual incorporation of the BDT-OEt building units into the COF backbone on the crystallinity and porosity was investigated. Furthermore, molecular dynamics simulations shed light on the possible processes governing the COF assembly from molecular building blocks.

In the fourth chapter, a new concept of depositing COFs onto surfaces is studied, based on electrophoretic deposition (EPD). It is demonstrated that the EPD technique is suitable

for depositing COFs featuring two- and three-dimensional structures linked by imine or boronate ester bonds, namely, BDT-ETTA COF, COF-300, and COF-5. For the deposition, COF nanoparticle suspensions were prepared by dispersing the as-synthesized bulk materials in solvents with low dielectric constants. Subsequently, two electrodes were immersed into the COF particle suspensions, and upon inducing electric fields ranging from 100 to 900 V cm^{-1}, COFs were deposited as films on the positively charged electrode. Through EPD, within 2 min large-area films of up to 25 cm^2 were obtained on smooth or corrugated surfaces. COF films prepared by EPD feature an inherent textural porosity and tunable thickness, demonstrated from 400 nm to 24 μm. By controlling the deposition parameters such as duration, particle concentration, and applied potential, deposits of precise thickness could be produced. Furthermore, co-depositions of different COFs, as well as COF/Pt nanoparticles from mixed suspensions, were demonstrated. The film morphologies obtained by EPD were shown to be advantageous for catalysis, as demonstrated for sacrificial agent-free photoelectrochemical water reduction. Here, BDT-ETTA COF photocathodes showed a strongly increased photocurrent density compared to the respective dense and oriented films. Typical BDT-ETTA COF/Pt nanoparticle hybrid films exhibited photocurrent densities of over 100 μA cm^{-2}. The rapid and scalable deposition of COF particles as films and coatings through EPD is a versatile addition to the toolbox of COF film fabrication techniques, allowing for tailoring COF film architectures for desired functionalities.

The fifth chapter describes a study of the intrinsic electrical conductivities of two COFs and how chemical doping affects their properties. For the incorporation of COFs into optoelectronic devices, efficient charge carrier transport and intrinsic conductivity are essential. Here, we report the synthesis of WTA and WBDT, two imine-linked COFs, featuring a redox-active Wurster-type motif based on the twisted tetragonal *N,N,N',N'*-tetraphenyl-1,4-phenylenediamine node. By condensing this unit with either terephthalaldehyde (TA) or benzodithiophene dialdehyde (BDT), COFs were obtained as highly crystalline materials with large specific surface areas and a mesoporous dual-pore topology. In addition, the experimental high conduction band energies of both COFs render them suitable candidates for oxidative doping. The incorporation of a benzodithiophene linear building block into the COF allowed for high intrinsic macroscopic conductivity. Both the anisotropic and average conductivities were probed by van-der-Pauw measurements using oriented films and pressed pellets, respectively.

Furthermore, the impact of different dopants such as F$_4$TCNQ, antimony pentachloride and iodine on the conductivity of the resulting doped COFs was studied. By using the strong organic acceptor F$_4$TCNQ, long-term stable electrical conductivity as high as 3.67 S m^{-1} was achieved for the anisotropic transport in an oriented film, the highest for any doped COF to date. Interestingly, no significant differences between isotropic and anisotropic charge transport were found in films and pressed pellets. This work expands the list of possible building nodes for electrically conducting COFs from solely highly planar systems to twisted geometries. The achievement of high and stable electrical conductivity may ultimately promote the use of COFs in organic (opto-)electronics.

The sixth chapter is focused on the on-surface synthesis of metalorganic frameworks (MOFs) as thin films. Similar to COFs, MOFs are synthesized from molecular precursors but in this case, from inorganic metal salts and organic molecules. These interconnect through coordination bonds forming extended, mostly 3D frameworks, featuring high crystallinity and porosity. In this part, the synthesis of thin zirconium-based MOF films by vapor-assisted conversion (VAC) is presented. Synthesis protocols were established for the growth of UiO-66, UiO-66(NH$_2$), UiO-67, and UiO-68(NH$_2$), as well as the porous, interpenetrated Zr-organic framework, PPPP-PIZOF-1, as highly oriented thin films. Through the VAC approach, precursors in a cast solution layer on a bare gold surface reacted to form a porous continuous MOF film, oriented along the [111] crystal axis, by exposure to a solvent vapor at elevated temperature of 100 °C and 3 h reaction time. It was found that the concentration of dicarboxylic acid, the modulator, the liquid volume and the reaction time are vital parameters to be controlled for obtaining oriented MOF films. Using VAC for the MOF film growth on gold surfaces modified with thiol SAMs and on a bare silicon surface yielded oriented MOF films, rendering the VAC process robust toward chemical surface variations. Ethanol sorption experiments showed that a substantial part of the material pores is accessible. Thereby, the practical VAC method is an important addition to the toolbox of synthesis methods for thin MOF films. It is expected that the VAC approach will open new horizons in the formation of highly defined functional thin MOF films for numerous applications.

Table of Contents

Introduction

Porous materials have become an indispensable part of modern life. Zeolites, in particular, are widely used today, whether in the petrochemical industry for the separation of hydrocarbons, for the catalysis of chemical reactions or in domestic use as ion exchangers for water softening.[1–4] Besides zeolites, other highly porous materials such as aerogels, composed of silica or metal oxides, as well as porous carbons are used as adsorbers, catalysts, thermal isolation or energy storage.[5–7] The wide range of possible applications and their commercial success has also motivated research into new, nanoporous classes of materials, such as porous organic polymers, metal-polymer hybrid materials and porous liquids.[7,8] Of particular interest are materials that exhibit a high order or crystallinity, which allow for high specific areas and precisely defined pore sizes. By incorporating organic building blocks into the porous framework of such materials, particularly high specific surfaces and a wide range of physical and chemical properties can be achieved. In the following, two such material classes are presented.

1.1.   Metal-Organic Frameworks

In 1999 Yaghi and coworkers coined the term of metal-organic frameworks (MOFs).[9] MOFs are coordination polymers consisting of metal ions or metal clusters (often called secondary building units (SBU)), which are connected by coordinative bonds of organic building blocks in two or three dimensions. The resulting networks can have a variety of different topologies that affect pore sizes and specific surface areas.[10] The first MOFs were based on metal cation carboxylate coordination chemistry, in which metal oxo clusters were cross-linked three-dimensionally via two- or multi-dentate organic building blocks via carboxyl groups. Crystalline structures could be generated that had high surface areas ($> 2000 \ m^2 \ g^{-1}$) due to open and accessible micro- or mesopores. An example is the cubic MOF-5, which consists of tetrahedral Zn_4O^{6+} clusters that are octahedrally bridged by coordination with 1,4-benzodicarboxylic acid (Figure 1.1).[9]
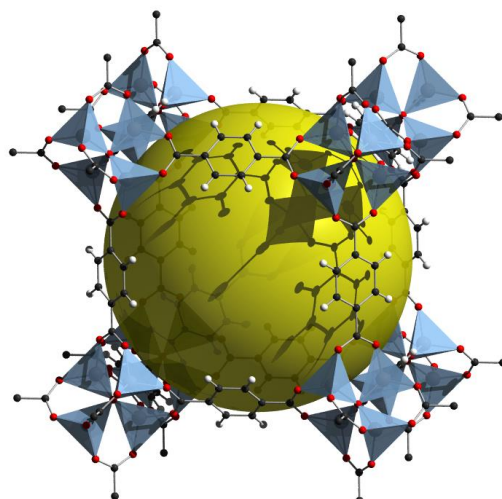
Figure 1.1: Structure of the cubic MOF-5 with the Zn_4O^{6+} metal-oxo clusters displayed as coordination tetrahedra and a yellow sphere indicating the open pore volume of the structure. Figure adapted from reference 9.

The topology of MOFs can often be systematically predicted by the so-called principle of reticular synthesis. This allows for predicting pore shape and size by taking into account the connectivity of organic linkers and metal centers.[11] A class of MOFs which is particularly well suited to describe reticular synthesis is the UiO series (University of Oslo) with UiO-66 as the prototypical representative.[12] This cubic MOF consists of an octahedral centric cage that is connected to eight corner tetrahedral cages through triangular windows. The SBUs of the MOF are zirconium-oxo-clusters of the formula $Zr_6O_4(OH)_4$, interconnected by 1,4-benzodicarboxylic acid (Figure 1.2).[13,14] Thereby, two pores, namely an octahedral one with 12.0 Å and a tetragonal one with 7.5 Å diameter are generated, which give a Langmuir surface area of 1187 m^2 g^{-1}.[12]
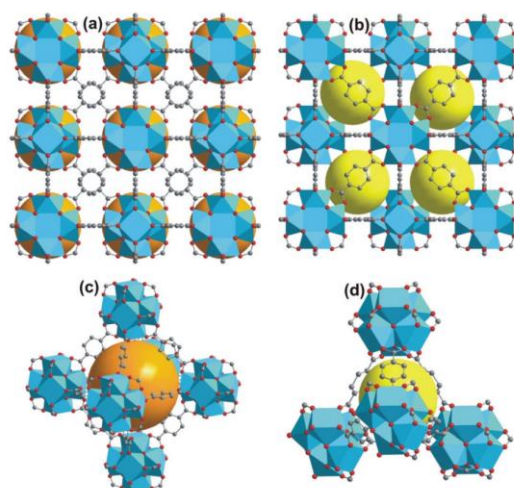
Figure 1.2: Presentation of the UiO-66 structure in ball-and-stick form. The pores formed by the octahedral and tetrahedral cages are highlighted as orange or yellow spheres, respectively. (a, b) show the spatial arrangement of multiple pores, while (c, d) show the arrangement of the octahedral and tetrahedral cages in more detail. Figure adapted from reference 14.

The isoreticular expansion of the UiO-series is done by increasing the length of the organic linker. By expanding the benzene-based UiO-66 linker to a biphenyl one, UiO-67 is obtained, with pore sizes of 12.0 Å and 16.0 Å and an increased BET surface area of about 3000 m² g⁻¹. Consequently, a further elongation to terphenyl gives UiO-68, however, this MOF is only accessible by side functionalizations of the terphenyl building block.[15] Further elongation of the organic building block still retains the coordination arrangement, but the MOF forms as a two-fold interpenetrated network, a so-called porous-interpenetrated zirconium-organic framework (PIZOF) (Figure 1.3).[16] Frameworks based on the UiO, or PIZOF structure, respectively, often show remarkable stability, which is mainly caused by the high oxygen affinity of the zirconium ions, rendering them especially suitable for applications such as catalysis or adsorption.[17]
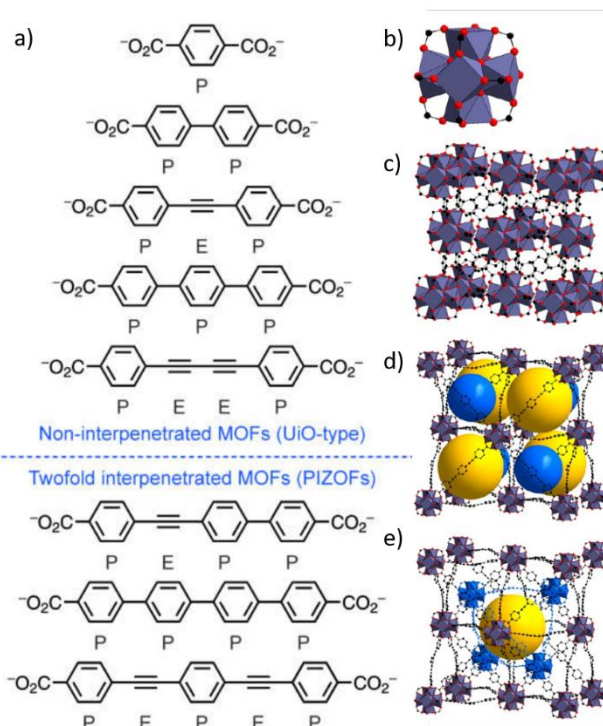
Figure 1.3: Isoreticular expansion of the UiO-series. a) different organic linkers forming the non-interpenetrated UiO-topology or the twofold interpenetrated PIZOF-topology. b) presentation of the $Zr_6O_4(OH)_4(CO_2)$ SBU (C in black, O in red, Zr in the center of the polyhedra. c) framework topology of UiO-66. d) framework topology of PEPEP-PIZOF. The yellow sphere represents empty space within the framework, while the blue sphere indicates the space-filling of the second, interpenetrating SBU. e) the full structure of PEPEP-PIZOF with the interpenetrating network marked in blue. Figure adapted from reference 16.

1.2.   Covalent Organic Frameworks (COFs)

In 2005, the fully organic equivalent of the MOF, the so-called covalent organic framework (COF), was introduced by Yaghi and coworkers.[18] COFs consist of organic building blocks (which typically contain heteroatoms), and therefore they are mainly formed from light elements such as carbon, nitrogen, hydrogen, oxygen, sulfur, and boron. The organic building blocks interconnect through covalent bonds and form, predetermined by the functionalization and geometry of the building blocks, porous 2D or 3D materials. While 3D COFs feature covalent bonds extending in all three dimensions, 2D COFs consist of 2D layers, which stack on top of each other in the third dimension by dispersive forces. By changing the connectivities and sizes of the building blocks, pore sizes, geometries and surface areas of the resulting COFs can be rationally designed .[19,20]
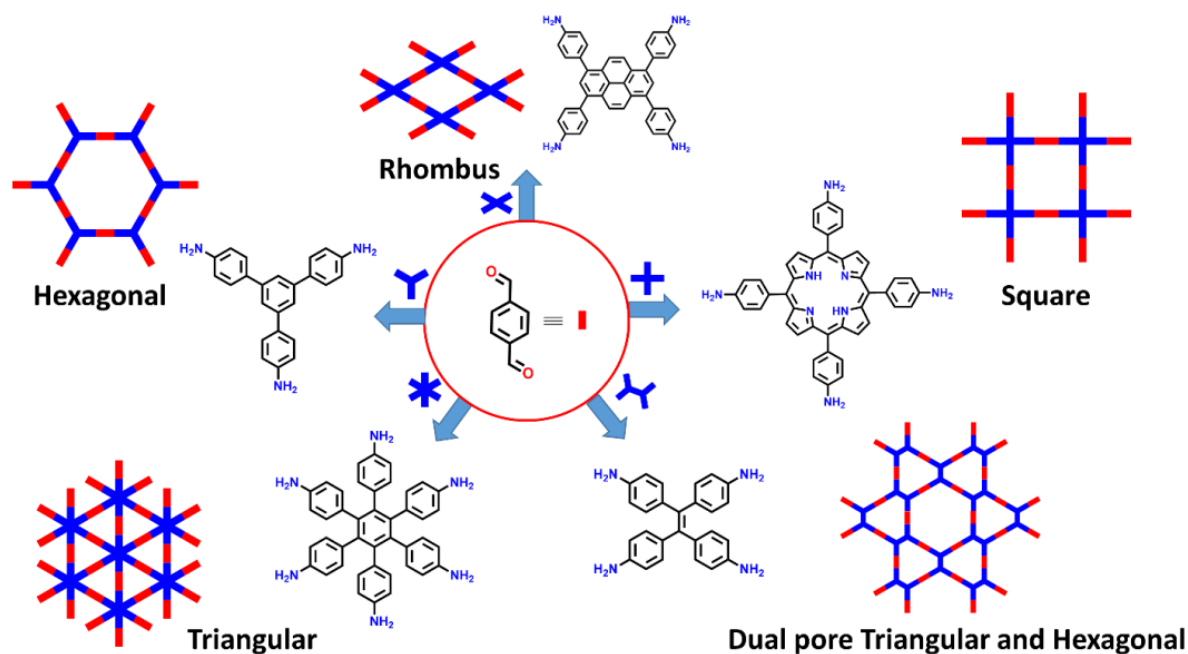
Figure 1.4: Examples of linker topologies and the resulting pore shapes for 2D COFs. Figure adapted from reference 21.

The covalent bonds between the respective building blocks are typically formed through condensation reactions and the elimination of water. Common condensation reactions used for the formation of COFs are based on the condensation of boronic-acids, forming boroxines of boronate esters,[18] Schiff-base condensations,[22] hydrazone formation,[23] imide-formation[24] or Michael addition-elimination reactions.[25] More recently, several non-condensation-based reactions were used for the synthesis of crystalline COFs, such as triazine-linkages or C-C-coupling reactions (Figure 1.5), which made highly π-conjugated systems accessible.[19,21,26,27]
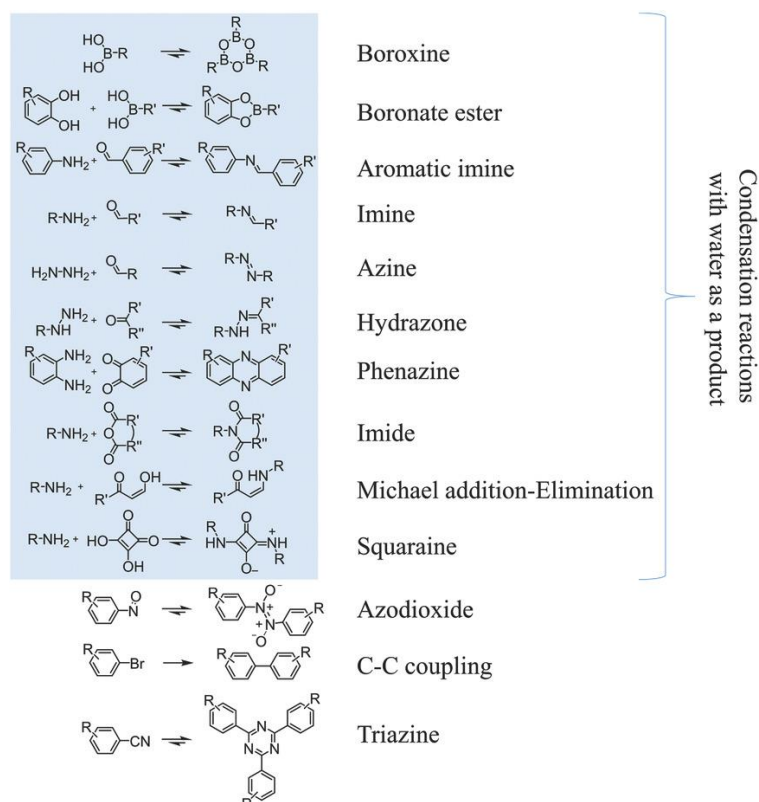
Figure 1.5: Overview of the various linkage motifs used for the synthesis of COFs. Figure adapted from reference 21.

Ideally, the condensation reactions are carried out under solvothermal, near equilibrium conditions, so that the reversible bond formations allow for error correction during framework synthesis. Establishing these reaction conditions is a major task in the synthesis of new COFs. Several parameters, such as the solvent system and polarity, temperature, and the concentration of potential catalysts, have to be adjusted to obtain highly ordered materials with few defects.[19] Typically, the solvent system plays the most crucial role in adjusting parameters for COF synthesis. It does not only influence the solubility of the building blocks but is also essential in governing the organization of the aromatic 2D layers for 2D COFs or the intercalation behavior for 3D systems.[28] Under optimal conditions, COFs are obtained as powdered materials of high crystallinity and large accessible surface areas with defined pore sizes. One of the prototypical and intensely studied COFs is COF-5, a boronic ester-based framework, in which benzene-1,4-diboronic acid (BDBA) and hexahydroxytriphenylene (HHTP) condense into hexagonal 2D sheets which stack on top of each other through dispersive forces.[18,29] The AA-type, eclipsed stacking of the 2D layers creates 1D pore channels oriented perpendicular to the

2D layers and endows the COF with high permanent porosity (BET surface area 1590 m^2 g^{-1}) and high thermal stability (> 300 °C as determined by TGA).[18,30]

By varying the organic building blocks and linkages, different properties can be incorporated into the frameworks. Therefore, COFs can be optimized for diverse applications such as gas storage and separation,[31,32] catalysis,[33–36] energy storage,[37,38] or optoelectronics.[19,39–41]

1.3.   References

(1) Funke, H. H.; Kovalchick, M. G.; Falconer, J. L.; Noble, R. D. Separation of Hydrocarbon Isomer Vapors with Silicalite Zeolite Membranes. *Ind. Eng. Chem. Res.* **1996**, *35*, 1575–1582.

(2) Ma, Y.; Tong, W.; Zhou, H.; Suib, S. L. A review of zeolite-like porous materials. *Microporous Mesoporous Mater.* **2000**, *37*, 243–252.

(3) Seike, T.; Matsuda, M.; Miyake, M. Preparation of FAU type zeolite membranes by electrophoretic deposition and their separation properties. *J. Mater. Chem.* **2002**, *12*, 366–368.

(4) Ennaert, T.; van Aelst, J.; Dijkmans, J.; Clercq, R. D.; Schutyser, W.; Dusselier, M.; Verboekend, D.; Sels, B. F. Potential and challenges of zeolite chemistry in the catalytic conversion of biomass. *Chem. Soc. Rev.* **2016**, *45*, 584–611.

(5) Lamy-Mendes, A.; Silva, R. F.; Durães, L. Advances in carbon nanostructure–silica aerogel composites: a review. *J. Mater. Chem. A* **2018**, *6*, 1340–1369.

(6) Barrios, E.; Fox, D.; Li Sip, Y. Y.; Catarata, R.; Calderon, J. E.; Azim, N.; Afrin, S.; Zhang, Z.; Zhai, L. Nanomaterials in Advanced, High-Performance Aerogel Composites: A Review. *Polymers* **2019**, *11*.

(7) Wuttke, S.; Medina, D. D.; Rotter, J. M.; Begum, S.; Stassin, T.; Ameloot, R.; Oschatz, M.; Tsotsalas, M. Bringing Porous Organic and Carbon-Based Materials toward Thin-Film Applications. *Adv. Funct. Mater.* **2018**, *28*, 1801545.

(8) Giri, N.; Pópolo, M. G. D.; Melaugh, G.; Greenaway, R. L.; Rätzke, K.; Koschine, T.; Pison, L.; Gomes, M. F. C.; Cooper, A. I.; James, S. L. Liquids with permanent porosity. *Nature* **2015**, *527*, 216–220.

(9) Li, H.; Eddaoudi, M.; O'Keeffe, M.; Yaghi, O. M. Design and synthesis of an exceptionally stable and highly porous metal-organic framework. *Nature* **1999**, *402*, 276–279.

(10) Li, M.; Li, D.; O'Keeffe, M.; Yaghi, O. M. Topological analysis of metal-organic frameworks with polytopic linkers and/or multiple building units and the minimal transitivity principle. *Chem. Rev.* **2014**, *114*, 1343–1370.

(11) Yaghi, O. M.; O'Keeffe, M.; Ockwig, N. W.; Chae, H. K.; Eddaoudi, M.; Kim, J. Reticular synthesis and the design of new materials. *Nature* **2003**, *423*, 705–714.

(12) Cavka, J. H.; Jakobsen, S.; Olsbye, U.; Guillou, N.; Lamberti, C.; Bordiga, S.; Lillerud, K. P. A new zirconium inorganic building brick forming metal organic frameworks with exceptional stability. *JACS* **2008**, *130*, 13850–13851.

(13) Hajek, J.; Caratelli, C.; Demuynck, R.; Wispelaere, K. de; Vanduyfhuys, L.; Waroquier, M.; van Speybroeck, V. On the intrinsic dynamic nature of the rigid UiO-66 metal-organic framework. *Chem. Sci.* **2018**, *9*, 2723–2732.

(14) Biswas, S.; Zhang, J.; Li, Z.; Liu, Y.-Y.; Grzywa, M.; Sun, L.; Volkmer, D.; van der Voort, P. Enhanced selectivity of CO2 over CH4 in sulphonate-, carboxylate- and iodo-functionalized UiO-66 frameworks. *Dalton Trans.* **2013**, *42*, 4730–4737.

(15) Schaate, A.; Roy, P.; Godt, A.; Lippke, J.; Waltz, F.; Wiebcke, M.; Behrens, P. Modulated Synthesis of Zr-Based Metal–Organic Frameworks: From Nano to Single Crystals. *Chem. Eur. J.* **2011**, *17*, 6643–6651.

(16) Lippke, J.; Brosent, B.; Zons, T. von; Virmani, E.; Lilienthal, S.; Preuße, T.; Hülsmann, M.; Schneider, A. M.; Wuttke, S.; Behrens, P.*; et al.* Expanding the Group of Porous Interpenetrated Zr-Organic Frameworks (PIZOFs) with Linkers of Different Lengths. *Inorg. Chem.* **2017**, *56*, 748–761.

(17) Zou, D.; Liu, D. Understanding the modifications and applications of highly stable porous frameworks via UiO-66. *Mater. Today Chem.* **2019**, *12*, 139–165.

(18) Côté, A. P.; Benin, A. I.; Ockwig, N. W.; O'Keeffe, M.; Matzger, A. J.; Yaghi, O. M. Porous, crystalline, covalent organic frameworks. *Science* **2005**, *310*, 1166–1170.

(19) Lohse, M. S.; Bein, T. Covalent Organic Frameworks: Structures, Synthesis, and Applications. *Adv. Funct. Mater.* **2018**, *355*, 1705553.

(20) Diercks, C. S.; Yaghi, O. M. The atom, the molecule, and the covalent organic framework. *Science* **2017**, *355*.

(21) Medina, D. D.; Sick, T.; Bein, T. Photoactive and Conducting Covalent Organic Frameworks. *Adv. Energy Mater.* **2017**, *7*, 1700387.

(22) Uribe-Romo, F. J.; Hunt, J. R.; Furukawa, H.; Klöck, C.; O'Keeffe, M.; Yaghi, O. M. A crystalline imine-linked 3-D porous covalent organic framework. *JACS* **2009**, *131*, 4570–4571.

(23) Uribe-Romo, F. J.; Doonan, C. J.; Furukawa, H.; Oisaki, K.; Yaghi, O. M. Crystalline covalent organic frameworks with hydrazone linkages. *JACS* **2011**, *133*, 11478–11481.

(24) Fang, Q.; Zhuang, Z.; Gu, S.; Kaspar, R. B.; Zheng, J.; Wang, J.; Qiu, S.; Yan, Y. Designed synthesis of large-pore crystalline polyimide covalent organic frameworks. *Nat Commun*, *5*, 1–8.

(25) Rao, M. R.; Fang, Y.; Feyter, S. de; Perepichka, D. F. Conjugated Covalent Organic Frameworks via Michael Addition-Elimination. *JACS* **2017**, *139*, 2421–2427.

(26) Kuhn, P.; Antonietti, M.; Thomas, A. Porous, Covalent Triazine-Based Frameworks Prepared by Ionothermal Synthesis. *Angewandte Chemie International Edition* **2008**, *47*, 3450–3453.

(27) Jin, E.; Asada, M.; Xu, Q.; Dalapati, S.; Addicoat, M. A.; Brady, M. A.; Xu, H.; Nakamura, T.; Heine, T.; Chen, Q.*; et al.* Two-dimensional sp2 carbon–conjugated covalent organic frameworks. *Science* **2017**, *357*, 673–676.

(28) Ma, X.; Scott, T. F. Approaches and challenges in the synthesis of three-dimensional covalent-organic frameworks. *Commun. Chem.*, *1*, 1–15.

(29) Evans, A. M.; Parent, L. R.; Flanders, N. C.; Bisbey, R. P.; Vitaku, E.; Kirschner, M. S.; Schaller, R. D.; Chen, L. X.; Gianneschi, N. C.; Dichtel, W. R. Seeded growth of single-crystal two-dimensional covalent organic frameworks. *Science* **2018**, *361*, 52–57.

(30) Calik, M.; Sick, T.; Dogru, M.; Döblinger, M.; Datz, S.; Budde, H.; Hartschuh, A.; Auras, F.; Bein, T. From Highly Crystalline to Outer Surface-Functionalized Covalent Organic Frameworks—A Modulation Approach. *JACS* **2016**, *138*, 1234–1239.

(31) Fan, H.; Mundstock, A.; Feldhoff, A.; Knebel, A.; Gu, J.; Meng, H.; Caro, J. Covalent Organic Framework-Covalent Organic Framework Bilayer Membranes for Highly Selective Gas Separation. *JACS* **2018**, *140*, 10094–10098.

(32) Li, Z.; Feng, X.; Zou, Y.; Zhang, Y.; Xia, H.; Liu, X.; Mu, Y. A 2D azine-linked covalent organic framework for gas storage applications. *Chemical communications (Cambridge, England)* **2014**, *50*, 13825–13828.

(33) Ding, S.-Y.; Gao, J.; Wang, Q.; Zhang, Y.; Song, W.-G.; Su, C.-Y.; Wang, W. Construction of covalent organic framework for catalysis: Pd/COF-LZU1 in Suzuki-Miyaura coupling reaction. *JACS* **2011**, *133*, 19816–19822.

(34) Aiyappa, H. B.; Thote, J.; Shinde, D. B.; Banerjee, R.; Kurungot, S. Cobalt-Modified Covalent Organic Framework as a Robust Water Oxidation Electrocatalyst. *Chem. Mater.* **2016**, *28*, 4375–4379.

(35) Lin, C.-Y.; Zhang, D.; Zhao, Z.; Xia, Z. Covalent Organic Framework Electrocatalysts for Clean Energy Conversion. *Advanced materials (Deerfield Beach, Fla.)* **2018**, *30*.

(36) Sick, T.; Hufnagel, A. G.; Kampmann, J.; Kondofersky, I.; Calik, M.; Rotter, J. M.; Evans, A.; Döblinger, M.; Herbert, S.; Peters, K.*; et al.* Oriented Films of Conjugated 2D Covalent Organic Frameworks as Photocathodes for Water Splitting. *JACS* **2018**, *140*, 2085–2092.

(37) Chandra, S.; Roy Chowdhury, D.; Addicoat, M.; Heine, T.; Paul, A.; Banerjee, R. Molecular Level Control of the Capacitance of Two-Dimensional Covalent Organic Frameworks: Role of Hydrogen Bonding in Energy Storage Materials. *Chem. Mater.* **2017**, *29*, 2074–2080.

(38) DeBlase, C. R.; Silberstein, K. E.; Truong, T.-T.; Abruña, H. D.; Dichtel, W. R. β-Ketoenamine-linked covalent organic frameworks capable of pseudocapacitive energy storage. *JACS* **2013**, *135*, 16821–16824.

(39) Calik, M.; Auras, F.; Salonen, L. M.; Bader, K.; Grill, I.; Handloser, M.; Medina, D. D.; Dogru, M.; Löbermann, F.; Trauner, D.*; et al.* Extraction of photogenerated electrons and holes from a covalent organic framework integrated heterojunction. *JACS* **2014**, *136*, 17802–17807.

(40) Medina, D. D.; Werner, V.; Auras, F.; Tautz, R.; Dogru, M.; Schuster, J.; Linke, S.; Döblinger, M.; Feldmann, J.; Knochel, P.*; et al.* Oriented thin films of a benzodithiophene covalent organic framework. *ACS Nano* **2014**, *8*, 4042–4052.

(41) Guo, J.; Xu, Y.; Jin, S.; Chen, L.; Kaji, T.; Honsho, Y.; Addicoat, M. A.; Kim, J.; Saeki, A.; Ihee, H.*; et al.* Conjugated organic framework with three-dimensionally ordered stable structure and delocalized π clouds. *Nat. Commun.*, *4*, 2736.

1.4. Thin Covalent Organic Framework Films

This chapter is based on the following publication:

1.4.1. Introduction

Covalent organic frameworks (COFs) are a class of hierarchical porous material formed by a covalent attachment of organic building units through reversible chemical reactions.[1-2] This mode of assembly allows for a self-repair mechanism thereby endows COFs with the outstanding feature of structural long-range order.[3] The synthesis of COFs is modular, and a careful selection of building units dictates their crystalline structure, the pore shape and size, and functionality.[4] For instance, combining subunits of distinct planar character results in the formation of extended two-dimensional polymer layers that undergo self-organization guided by weak interactions to form defined molecular columnar stacks yielding one-dimensional ordered channels, so called two-dimensional covalent-organic frameworks (2D COFs).[3, 5] Employing building blocks of spatial character such as a tetrahedral carbon or silicon results in the formation of three-dimensional extended networks.

Commonly, COFs are synthesized under solvothermal conditions namely through condensation reactions in a solvent of high boiling point at elevated temperatures.[3] Under these conditions, COFs are precipitated as an insoluble powder of intergrown crystallite microstructures. Therefore, COFs immobilization onto a surface involves meeting the strict synthesis requirements ensuring appropriate reaction rates permitting long-range order and permanent porosity in the process of a film growth.[6] In this context, exploring the reaction paths under which COFs are formed has a great potential to assist in developing advanced procedures for the synthesis of COF thin films. An important aspect in the deposition of 2D COF films is the orientation of the COF crystallites on the surface.[7-8] For applications requiring charge percolation and high pore accessibility a precise positioning of the COF layers parallel to the surface enabling a direct path thought

the overlapped π-system and beneficial open porous channels perpendicular to the surface.[9-11] To date, a number of methods were reported for the growth of 2D COF on a verity of surfaces. However, some of these methods were reported for COF structures obtained by specific type of covalent link type. Here, we will briefly overview the developed methods for COF films on a substrate. We will discuss the different deposition approaches with respect to the COF chemical compositions, and crystal structures and crystallites orientation on the surface and their utilization in different device platforms. In addition, we will present the preparation of free-standing COF films and their application.

1.4.2.   Solvothermal, *in-situ,* growth

In a typical solvothermal synthesis, the respective COF precursors are added to a mixture of organic solvents, producing homogeneous or heterogeneous reaction mixtures. Then, the reaction vessel is sealed and placed in a preheated oven for several days. At the end of the reaction, COF powder material precipitates. The deposition of COFs as thin films under solvothermal conditions was first reported by Dichtel and coworkers. In that report, the bulk COF synthesis conditions were used without alterations for producing COF thin films. Immersing substrates decorated with a single layer of graphene (SLG) into the different synthesis mixtures, resulted in a thin COF deposit on the SLG along with COF powder precipitation in the reaction tube (Figure 1). Using this method, several boronic ester-based COFs, such as the well-known hexagonal COF-5,[12] consisting of 2,3,6,7,10,11-hexahydroxytriphenylene (HHTP) and 1,4-benzenediboronic acid, and a tetragonal, nickel-coordinated phthalocyanine containing NiPc-COF, were deposited on different SLG supported substrates such as fused silica, SiC or copper. Grazing incidence X-ray diffraction (GIXRD) studies revealed that the COF crystallites in the film were oriented with the layers deposited parallel to the substrate (Figure 1.6). The films exhibited high uniformity namely, a large area substrate coverage and thicknesses ranging from about 220 nm down to 70 nm. Using the COF films grown on optically transparent SLG/ fused silica allowed additional access to higher resolved optical absorption and emission spectra of the COFs compared to previous diffuse reflectance measurements of bulk material.[7]
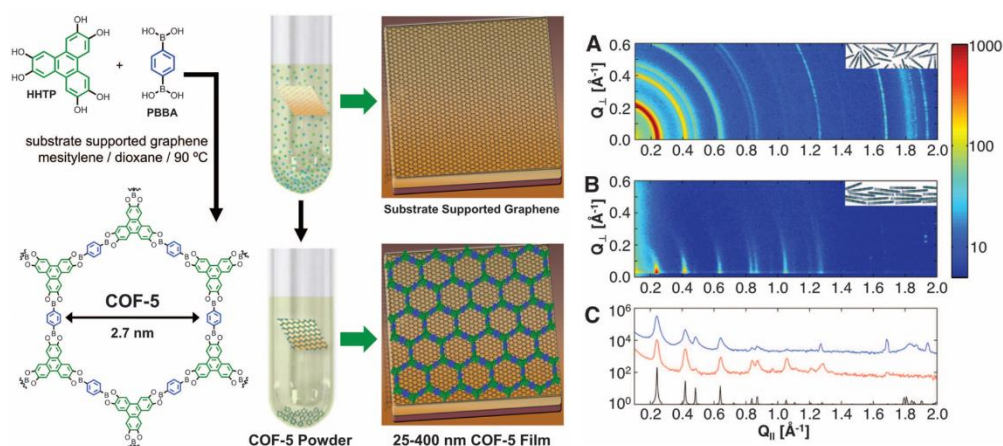
Figure 1.6. Left: Solvothermal synthesis of COF-5 thin films by submerging a substrate-supported SLG surface into the reaction. Thereby, a film on the surface, as well as powder, is obtained. Right: (A) PXRD data as obtained from COF-5 powder. (B) GIXRD data of an oriented COF-5 film grown on SLG/Cu. (C) Projections of (A) (top/blue) and (B) (middle/red) near $Q_\perp = 0$, and the simulated powder diffraction spectrum (bottom/black) for COF-5.[7]

In subsequent reports Dichtel and coworkers generalized the *in-situ* epitaxy synthesis route by transferring it to several other tetragonal and hexagonal COFs. Different zinc containing pthalocyanine (ZnPc) COFs were synthesized on SLG/SiO₂ with pore sizes ranging from 2.7 nm to 4.4 nm and the hexagonal HHTP-DPB COF, comprising 4,4'-diphenylbutadiynebis(boronic acid) (DPB), with a pore size of 4.7 nm was demonstrated.[13]

Later, Dichtel and coworkers illustrated the selective growth of COF films on lithographically patterned SLG/fused silica. Employing the general solvothermal synthesis protocol developed for oriented thin film synthesis of boronate ester COFs, namely performing the COF film synthesis in the appropriate solvent mixture dimetheylacetoimide and *o*-dichlorobenzene, film formation occurs unselectively on all exposed surfaces e.g. SLG functionalized and non-functionalized fused silica substrates. By employing a different solvent mixture for the film synthesis, namely methanol and 1,4-dioxane, a selective growth of the COF film on the SLG modified fused silica was achieved. The authors postulate that without the addition of an aromatic solvent, the large π -systems containing precursors readily adhere to the SLG from whereon film formation is promoted.[14]

Bein and coworkers demonstrated the growth of an electron-donor consisting of boronic acid-based benzodithiophene, BDT-COF, as highly oriented films on non-modified,

polycrystalline surfaces, such as gold, indium-doped tin oxide (ITO) or glass by the solvothermal *in-situ* synthesis route. Here, the pore accessibility of the COF films was assessed for the first time by krypton sorption measurements, giving a surface area of 175 cm^2 cm^{-2}. Subsequently, the porous BDT-COF films were infiltrated with acceptor molecules, such as [C70]PCBM and the successful incorporation was illustrated by a significant photoluminescence (PL) quenching. The dynamics of photo-generated hole-polarons was further studied by transient absorption spectroscopy showing an elongation of the radical cation life-times upon the incorporation of acceptor phase into the thin COF films. Additionally, insights into the film growth process were provided by halting the film synthesis at different times. Ending the synthesis prematurely revealed that film formation occurs through an island growth mode, the formed COF island continue to grow with progressing synthesis time to form a continuous film (Figure 1.7).[6]
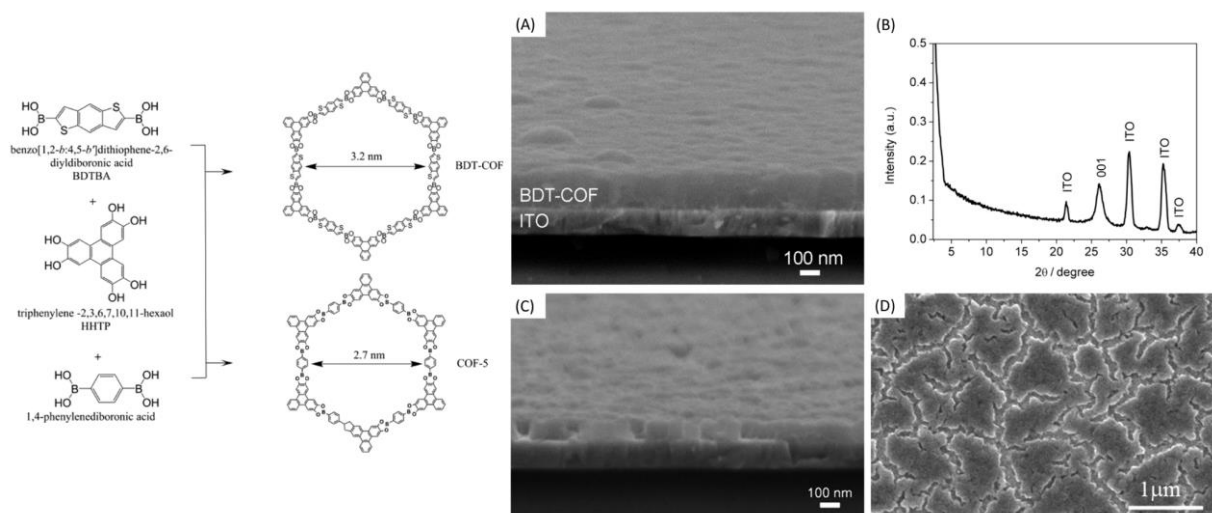
Figure 1.7. Left: Reaction scheme for the synthesis of BDT-COF and COF-5 used for the vapor-assisted conversion approach. Right: (A) SEM micrographs of BDT-COF grown on ITO. (B) X-ray diffraction pattern of BDT-COF film grown on ITO-coated glass at a low incident angle. (C) SEM micrographs of BDT-COF films synthesized at shortened reaction times in cross-section and (D) top view.[6]

In a subsequent study, highly oriented thin BDT-COF films were grown on semiconducting substrates allowing for studying the directional charge-carrier transport along the molecular columns of the π-stacked COF layers and in transverse direction. Hole-mobility for the BDT-COF columnar stacks was evaluated by constructing hole-only devices (HOD) in diode configuration where the BDT-COF film served as an active layer between hole-selective MoOx layers (Figure 1.8). I-V characteristics of the HODs revealed that the hole-

mobility along the stacked COF layers is dependent on film thickness with a two order of magnitude increase in hole-mobility towards thinner films (3×10^{-7} cm^2 V^{-1} s^{-1}). Using the well aligned COF layers parallel to the surface, in-plane electrical conductivity measurements of BDT-COF grown on glass modified with interdigitated gold electrodes showed a conductivity value of 5×10^{-7} S cm^{-1}, where the large resistance was attributed to the non-conjugated boronate ester linkage. Nevertheless, the measured in-plane conductivity value for BDT-COF thin films is three orders of magnitude higher than the value measured for BDT-COF in a pressed pellet.[15]

Bein and coworkers reported on the synthesis of boronate-ester linked thienothiophene-based TT-COF showing an efficient charge transfer to an infiltrated fullerene acceptor phase. The TT-COF films were integrated into a photovoltaic device with ITO/TT-COF:PCBM/Al architecture. A power conversion efficiency of 0.053 % and an external quantum efficiency of 3.4 % were measured for this device. Later, TP-COF consisting of linear porphyrin and HHTP building blocks forming a donor-acceptor stacks segregated by the non-conjugated boronate ester bond resulting in a COF integral heterojunction was synthesized as an oriented thin film. In the oriented film, the donor-acceptor stacks are arranged in an optimal way to transport charge carriers to the respective selective electrodes. Using a ITO/MoO$_x$/COF/ZnO/Al device layout charge carriers were extracted, and the successful design was proven by an external quantum efficiency of 30 % upon applying an external bias.[9]

Dichtel and coworkers expanded the *in-situ* COF film synthesis to the chemically stable *β*-ketoenamine linkage motif. A DAAQ-TFP COF, containing highly redox-active anthraquinone moieties and 1,3,5-triformylphloroglucinol (TFP) was grown as an oriented film on gold electrodes for charge-storage application. The oriented COF film featured a 400 % increase in capacitance compared to electrodes functionalized with bulk COF material,[16] which was attributed to the improved interfacing between the electrode and the film. A high capacitance value of 3.0 mF cm^{-1} was measured for the DAAQ-TFP COF and galvanostatic charge-discharge experiments showed the high cycling stability of the COF films in electrochemical storage applications. [17]

Multi-layered structures consisting of oriented *β*-ketoenamine linked COF thin films and conducting electrodes were fabricated by Lu and coworkers. For the multilayered structure, oriented *β*-ketoenamine linked COF film was grown on an ITO substrate subsequently the exposed COF film was coated with platinum metal *via* sputtering and an

additional COF layer was grown on the new exposed platinum layer under solvothermal conditions featuring an alternating stacked of metal/COF structure.[18]

The in-situ approach was found to be another suitable route for the synthesis of stable imine-linked COFs. Liu and coworker synthesized oriented thin imine-linked tetrathiafulvalene containing COF. The conductivity for this COF was assessed by growing oriented COF films on non-conductive glass substrates decorated with two gold electrodes. Two-point probe in-plane conductivity measurements were carried out on the oriented TTF-COF film revealing conductivity values of 1.2×10^{-6} S cm^{-1} for the pristine material which increased by two orders of magnitude, upon iodine doping, to 2.8×10^{-4} S cm^{-1}.[19]

A vertical field effect transistor using a COF consisting of pyrene and terephthalaldehyde was constructed by growing an oriented thin film on a SLG/SiO$_2$/ Si substrate. The transistor device was completed by evaporating two gold electrodes serving as the source and drain on top of the COF films (Figure 1.8). The device showed ambipolar transport and high on-current densities of over 4.1 A cm^{-2}. Since the device performance was found to be strongly linked to film thickness, thin films of 50 nm and less were used to create short channel lengths. The COF measured behaved as p-type transistor with high on-current densities for holes of 6.8 A cm^{-2} and 4.1 A cm^{-2} for electron transport.[11]
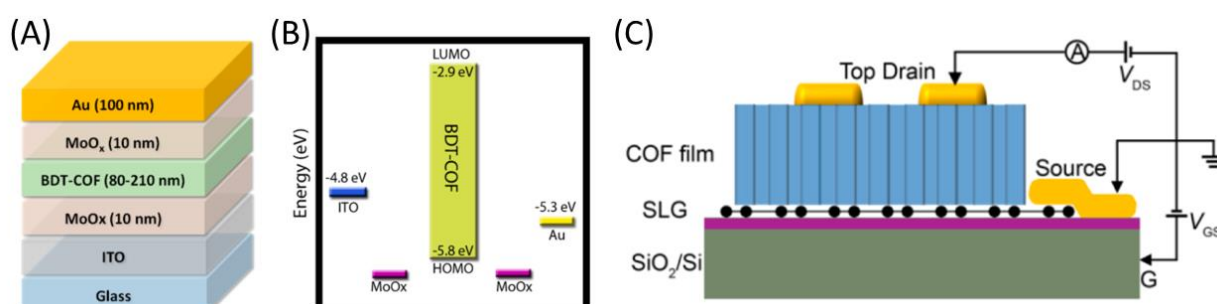
Figure 1.8. (A) Schematic representation of BDT-COF hole-only device layout and the corresponding energy diagram (B). (C) Vertical field effect transistor layout for a COF/SLG/SiO$_2$/Si device.[11, 15]

Very recently, Bein and co-workers reported the synthesis of oriented PyTII COF films containing of near-infrared (NIR) dyes isoindigo or thieno-isoindigo, and a central pyrene building block. These films were used to construct a photodetector with invertible spectral sensitivity. A device layout of ITO/MoO$_x$/COF:[C71]PCBM/PFN/Ag was chosen,

upon applying an external bias, the spectral sensitivity towards incident light could be changed from blue and red to an enhanced responsiveness in the green and NIR absorption regions.[20]

An imine-linked COF thin film, containing photoactive benzodithiophene and tetraohenylethylene building blocks, was used as a novel type of photoelectrode by Bein and coworkers. The high absorbance of visible light allowed the generation of photo-excited electrons which were used for proton reduction and hydrogen evolution in aqueous electrolytes. The COF photocathode showed high corrosion stability and steady performance over several hours of operation.[21]

In the context of electrocatalytical performance of COFs Yaghi and coworkers introduced a series of cobalt porphyrin containing COFs for the electrocatalytic reduction of CO_2 to CO. Here, the growth of the oriented frameworks directly on the substrate showed a significant advantage over bulk material, deposited on a conductive carbon fabric, attributed to the enhanced electrochemical contact between the electrodes and COFs. The reduction reactions showed high selectivity and current densities and could be performed at low overpotentials.[22-23]

Very recently Yaghi and coworkers employed a different strategy for the fabrication of a weaving COF, COF-112, using a protected building block in homogeneous conditions. The *in situ* deprotection of the BOC protecting groups by trifluoroacetic acid slowed down the imine condensation reaction and facilitate the crystallization of COF-112. Adapting this approach for the thin film synthesis, oriented films of the imine-linked LZU-1 framework, consisting of 1,3,5-triformylbenzene and 1,4-diaminobenzene, were grown from the homogeneous precursor solutions yielding uniform films of 190 nm in thickness within 2 h. Optical characterizations via ellipsometry were carried out for the first time on a COF where a high refractive index of 1.83 at 632.8 nm was found, which hints to a strong in-plane conductivity of the obtained films.[24]

A systematic study of thin imine-linked LZU-1 COF films growth by the solvothermal approach was conducted by Liu and coworkers. The formation of crystalline COF films was studied with relation to the COF precursor concentrations and duration of the film synthesis reactions. Systematic GIXRD studies showed that film formation occurs through two main steps. First, oriented material is deposited on the substrate and subsequently a disoriented phase from solution adheres on top. The non-oriented phase then reorganizes

through an interface-initialized templating effect between the formerly deposited, oriented crystallites and the non-oriented material. The reorientation step is considered by the authors as the majorly contributing mechanism of COF film growth. Time-dependent studies showed an almost linear increase in film thickness up to the first 48 h of the film synthesis and that the rate of growth is highly dependent on COF precursor concentration. High precursor concentrations lead to significantly faster reaction rates and growth of film thickness when compared to lower concentrations. Additionally, a more pronounced disoriented phase could be observed during film formation at higher concentrations, indicating a kinetically formed, metastable phase (Figure 1.9).[8]
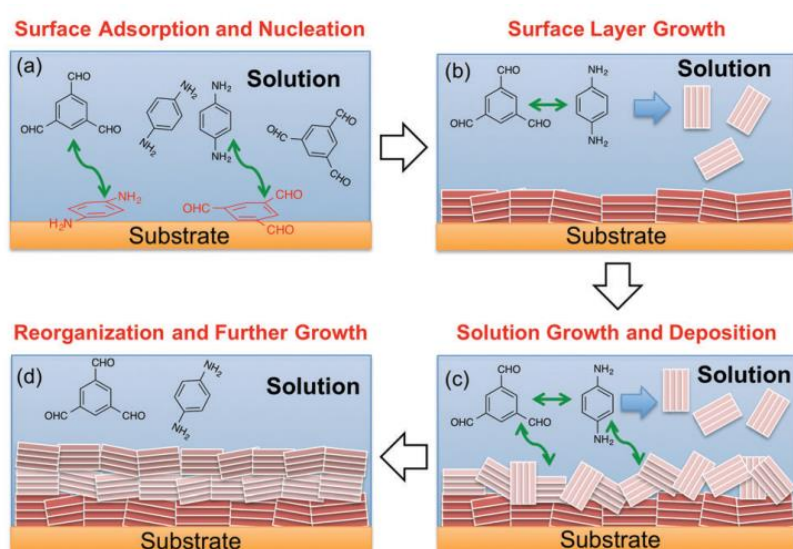
Figure 1.9. Illustration of the different film growth stages. (a) Surface adsorption of precursor molecules and nucleation. (b) Surface layer growth. (c) Solution crystallite growth and deposition on top of previous surface layers. (d) Reorientation of solution deposited crystallite layers and further growth. The green double-headed arrows indicate reactions between different species.[8]

1.4.3. Direct deposition of COF thin films

1.4.3.1. Vapor-assisted conversion

The *in-situ* thin film synthesis paves the way for the study of COF film in form of a device. However, a few aspects such as scalability, control over the film morphology, preventing undesired secondary nucleation from solution are still challenging. To address these issues, several other film synthesis methods have been developed mainly aiming at a direct deposit COF material onto a surface.

Bein and coworkers developed the vapor-assisted conversion (VAC) protocol to synthesize COF films at room temperature. In a typical VAC synthesis, the respective COF building blocks are dissolved in a mixture of polar low boiling point solvents and drop-cast onto various substrates. Then, the cast substrates are transferred into a reactor equipped with a vessel containing low vapor pressure solvents such as mesitylene and 1,4-dioxane. Upon a tight sealing of the reactor, the arising vapor atmosphere of the solvents in the reactor assist the conversion of the drop-cast precursor solutions into a crystalline COF phase within reaction times of 3 h. Through VAC, highly crystalline COF films of boronic ester and boroxine linkages were obtained with random COF crystallite orientation in the film and homogeneous growth and coverage over the whole substrate. By altering the drop-cast precursor solution volumes and concentrations in the droplet film thicknesses ranging from 300 nm to 7.5 μm were obtained. Additionally, a thickness dependent morphology of the films was found in which thin films show a dense morphology of intergrown COF crystallites suitable for device fabrication and thicker films feature an additional textural porosity between COF particles (Figure 1.10). The VAC synthesis route illustrates the direct deposition of COF building blocks on a surface and quantitative conversion into the respective crystalline frameworks.[25]
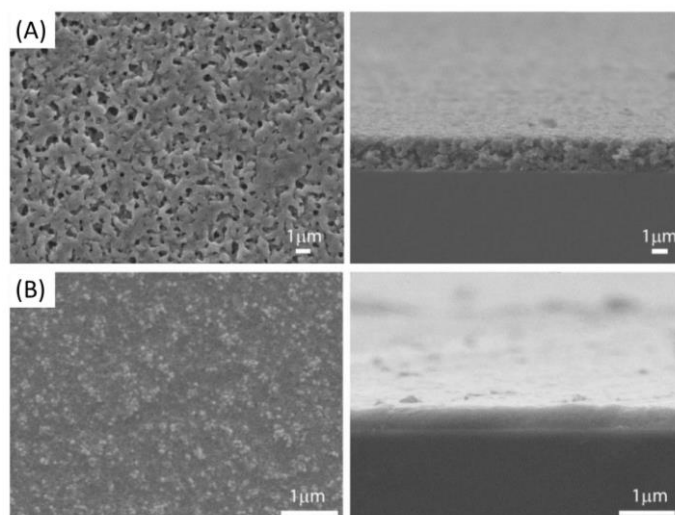
Figure 1.10: BDT-COF films prepared by vapor-assisted conversion on glass as top views (left) and cross-sections (right). (A) Films of 2 μm thickness revealing the textural porosity between intergrown particles. (B) Thin films of 300 nm showing a dense morphology.[25]

1.4.3.2. Continuous flow growth

A continuous flow growth approach was developed by Dichtel and coworkers featuring a direct film deposition on a substrate. In this report, homogeneous precursor solutions are pumped through a heated tubing for given retention times. Thereby, the precursors polymerize within the tubing, forming oligomers, and are subsequently passed over a substrate where they adhere and crystallize into COFs. Through this growth approach, several boronic ester linked frameworks were synthesized and deposited as crystalline and oriented materials within several minutes. Keeping the precursor concentrations constant through the continuous flow, linear deposition rates were achieved which allow for a better control over film thickness, this was studied by depositing the COFs directly on QCM chips and monitoring the mass increase on the chip.[26]

1.4.3.3. Free-standing COF films

Bao and coworkers synthesized COF films of an imine-linked dialkoxy benzodithiophene COF at the solution/air interface at room temperature. Altering the COF growth time yielded films of a different thickness ranging from 2 to 200 nm. The material could be transferred as free-standing films by extraction from the growth solution onto substrates. The authors discovered that by using this particular synthesis method as opposed to a more conventional solvothermal film synthesis, the roughness of the film was decreased,

however, this in turn resulted in the crystallinity and crystallite orientation being reduced. The synthesized COF film was characterized in a top-contact transistor device and showed characteristics of organic FET behavior with measured hole mobilities of 3.0 x 10^{-6} cm^2 V^{-1} s^{-1}.[27]

Banerjee and coworkers introduced a new strategy for the preparation of β-ketoenamine linked COFs as free-standing porous COF membranes. In this scalable process, a paste of molecular precursors is ground and knife-casted onto substrates and subsequently baked in an oven. Thereby, flexible, thick free-standing COF films of 200 – 700 μm were synthesized as defect- and crack-free membranes. The obtained films were used for molecular sieving applications where they exhibited high permeance for polar organic solvents.[28]

A further development to use COFs for the construction of membranes was subsequently demonstrated by Banerjee and coworkers. Here, COFs were grown as films at a liquid / liquid interface between water and an organic solvent. By dissolving one precursor in the organic phase and introducing the second one as an ammonium salt through the water phase, β-ketoenamine linked COFs could be synthesized as free-standing thin films in thicknesses ranging from 50 – 200 nm which were readily transferable to substrates and could be used as selective molecular sieves for organic solvents.[29]

Following up on the liquid / liquid interface growth, Dichtel and coworkers synthesized imine-linked COF films by using a scandium triflate catalyst in the aqueous phase and the organic linkers dissolved in an organic phase. Thereby, films thicknesses from 2.5 nm to 100 μm were fabricated, depending on the initial concentration of precursors in the organic phase.[30]

1.4.3.4. Spin-coating and drop-casting COF suspensions

In addition to the direct synthesis as substrate-supported or free-standing films, COF thin films were also fabricated through a post-synthesis direct casting of COF suspensions in organic solvent on a surface. Using this method, boronic ester based porphyrin COF films of 1.5 μm thickness were prepared as an active material on ITO and contacted to Al electrode. For these films, the number of photoinduced charge carriers was assessed via time-of-flight (TOF) measurements. The frameworks showed charge carrier generation yields in the range of 10^{-5} in respect of generated charge carriers per incident photon and TOF transient current integration measurements gave hole mobility values of 10^0 cm^2 V^{-1}

s^{-1}. Using this deposition method in combination with TOF measurements, charge carrier generation and hole mobilities were measured for a several boronic ester and imine-linked frameworks.[31-33] Furthermore, a photovoltaic device was constructed by Jiang and coworkers using COF powder combined with [C60]PCBM, which was spin-coated as a 100 nm thin film onto ITO. The evaporation of an electron selective Al layer on top of the COF@[C60]PCBM completed a solar devices featuring a power conversion efficiency of 0.9% and a large open-circuit voltage of 0.98 V.[34]

Dichtel and coworkers showed the fabrication of free-standing COF films of COF-5 with preferential crystallite orientation by solution casting of stable colloidal COF particles. The material was deposited in the form of a colloidal mixture of crystalline COF particles in an organic solvent onto a substrate. Upon solvent removal at elevated temperature, the particles aggregated, resulting in a free-standing film, which readily cleaves from the substrate. The COF crystallites in the film show a preferential orientation in which the COF layer stacking direction is perpendicular to the substrate.[35]

[1]   N. Huang, P. Wang, D. Jiang, *Nat. Rev. Mater.* 2016, 1, 16068.

[2]   D. D. Medina, T. Sick, T. Bein, *Adv. Energy Mater.* 2017, 7, 1700387.

[3]   P. J. Waller, F. Gándara, O. M. Yaghi, *Acc. Chem. Res.* 2015, 48, 3053.

[4]   C. S. Diercks, O. M. Yaghi, *Science* 2017, 355.

[5]   L. M. Salonen, D. D. Medina, E. Carbo-Argibay, M. G. Goesten, L. Mafra, N. Guldris, J. M. Rotter, D. G. Stroppa, C. Rodriguez-Abreu, *Chem. Commun.* 2016, 52, 7986.

[6]   D. D. Medina, V. Werner, F. Auras, R. Tautz, M. Dogru, J. Schuster, S. Linke, M. Döblinger, J. Feldmann, P. Knochel, T. Bein, *ACS Nano* 2014, 8, 4042.

[7]   J. W. Colson, A. R. Woll, A. Mukherjee, M. P. Levendorf, E. L. Spitler, V. B. Shields, M. G. Spencer, J. Park, W. R. Dichtel, *Science* 2011, 332, 228.

[8]   H. Wang, B. He, F. Liu, C. Stevens, M. A. Brady, S. Cai, C. Wang, T. P. Russell, T. W. Tan, Y. Liu, *J. Mater. Chem. C* 2017, 5, 5090.

[9]   M. Dogru, M. Handloser, F. Auras, T. Kunz, D. Medina, A. Hartschuh, P. Knochel, T. Bein, *Angew. Chem., Int. Ed.* 2013, 52, 2920.

[10]   M. Calik, F. Auras, L. M. Salonen, K. Bader, I. Grill, M. Handloser, D. D. Medina, M. Dogru, F. Löbermann, D. Trauner, A. Hartschuh, T. Bein, *J. Am. Chem. Soc.* 2014, 136, 17802.

[11]   B. Sun, C.-H. Zhu, Y. Liu, C. Wang, L.-J. Wan, D. Wang, *Chem. Mater.* 2017, 29, 4367.

[12]   A. P. Côté, A. I. Benin, N. W. Ockwig, M. O'Keeffe, A. J. Matzger, O. M. Yaghi, *Science* 2005, 310, 1166.

[13]   E. L. Spitler, J. W. Colson, F. J. Uribe-Romo, A. R. Woll, M. R. Giovino, A. Saldivar, W. R. Dichtel, *Angew. Chem., Int. Ed.* 2012, 51, 2623.

[14]   J. W. Colson, J. A. Mann, C. R. DeBlase, W. R. Dichtel, *J. Polym. Sci., Part A: Polym. Chem.* 2015, 53, 378.

[15]   D. D. Medina, M. L. Petrus, A. N. Jumabekov, J. T. Margraf, S. Weinberger, J. M. Rotter, T. Clark, T. Bein, *ACS Nano* 2017, 11, 2706.

[16]   C. R. DeBlase, K. E. Silberstein, T.-T. Truong, H. D. Abruña, W. R. Dichtel, *J. Am. Chem. Soc.* 2013, 135, 16821.

[17]   C. R. DeBlase, K. Hernández-Burgos, K. E. Silberstein, G. G. Rodríguez-Calero, R. P. Bisbey, H. D. Abruña, W. R. Dichtel, *ACS Nano* 2015, 9, 3178.

[18]   X. Gou, Q. Zhang, Y. Wu, Y. Zhao, X. Shi, X. Fan, L. Huang, G. Lu, *RSC Adv.* 2016, 6, 39198.

[19]   S.-L. Cai, Y.-B. Zhang, A. B. Pun, B. He, J. Yang, F. M. Toma, I. D. Sharp, O. M. Yaghi, J. Fan, S.-R. Zheng, W.-G. Zhang, Y. Liu, *Chem. Sci.* 2014, 5, 4693.

[20]   D. Bessinger, L. Ascherl, F. Auras, T. Bein, *J. Am. Chem. Soc.* 2017, 139, 12035.

[21]   T. Sick, A. G. Hufnagel, J. Kampmann, I. Kondofersky, M. Calik, J. M. Rotter, A. Evans, M. Döblinger, S. Herbert, K. Peters, D. Böhm, P. Knochel, D. D. Medina, D. Fattakhova-Rohlfing, T. Bein, *J. Am. Chem. Soc.* 2018, 140, 2085.

[22]   S. Lin, C. S. Diercks, Y.-B. Zhang, N. Kornienko, E. M. Nichols, Y. Zhao, A. R. Paris, D. Kim, P. Yang, O. M. Yaghi, C. J. Chang, *Science* 2015, 349, 1208.

[23]   C. S. Diercks, S. Lin, N. Kornienko, E. A. Kapustin, E. M. Nichols, C. Zhu, Y. Zhao, C. J. Chang, O. M. Yaghi, *J. Am. Chem. Soc.* 2018, 140, 1116.

[24]   Y. Zhao, L. Guo, F. Gándara, Y. Ma, Z. Liu, C. Zhu, H. Lyu, C. A. Trickett, E. A. Kapustin, O. Terasaki, O. M. Yaghi, *J. Am. Chem. Soc.* 2017, 139, 13166.

[25]   D. D. Medina, J. M. Rotter, Y. Hu, M. Dogru, V. Werner, F. Auras, J. T. Markiewicz, P. Knochel, T. Bein, *J. Am. Chem. Soc.* 2015, 137, 1016.

[26]   R. P. Bisbey, C. R. DeBlase, B. J. Smith, W. R. Dichtel, *J. Am. Chem. Soc.* 2016, 138, 11433.

[27]   J. I. Feldblyum, C. H. McCreery, S. C. Andrews, T. Kurosawa, E. J. G. Santos, V. Duong, L. Fang, A. L. Ayzner, Z. Bao, *Chem. Commun.* 2015, 51, 13894.

[28]   S. Kandambeth, B. P. Biswal, H. D. Chaudhari, K. C. Rout, S. Kunjattu H, S. Mitra, S. Karak, A. Das, R. Mukherjee, U. K. Kharul, R. Banerjee, *Adv. Mater.* 2017, 29, 1603945.

[29]   M. A. Khayum, S. Kandambeth, S. Mitra, S. B. Nair, A. Das, S. S. Nagane, R. Mukherjee, R. Banerjee, *Angew. Chem., Int. Ed.* 2016, 55, 15604.

[30]   M. Matsumoto, L. Valentino, G. M. Stiehl, H. B. Balch, A. R. Corcos, F. Wang, D. C. Ralph, B. J. Mariñas, W. R. Dichtel, *Chem* 2017, 4, 308.

[31]   X. Feng, L. Chen, Y. Honsho, O. Saengsawang, L. Liu, L. Wang, A. Saeki, S. Irle, S. Seki, Y. Dong, D. Jiang, *Adv. Mater.* 2012, 24, 3026.

[32]   X. Feng, L. Liu, Y. Honsho, A. Saeki, S. Seki, S. Irle, Y. Dong, A. Nagai, D. Jiang, *Angew. Chem., Int. Ed.* 2012, 51, 2618.

[33]   S. Dalapati, M. Addicoat, S. Jin, T. Sakurai, J. Gao, H. Xu, S. Irle, S. Seki, D. Jiang, *Nat. Commun.* 2015, 6, 7786.

[34]   J. Guo, Y. Xu, S. Jin, L. Chen, T. Kaji, Y. Honsho, M. A. Addicoat, J. Kim, A. Saeki, H. Ihee, S. Seki, S. Irle, M. Hiramoto, J. Gao, D. Jiang, *Nat. Commun.* 2013, 4, 2736.

[35]   B. J. Smith, L. R. Parent, A. C. Overholts, P. A. Beaucage, R. P. Bisbey, A. D. Chavez, N. Hwang, C. Park, A. M. Evans, N. C. Gianneschi, W. R. Dichtel, *ACS Cent. Sci.* 2017, 3, 58.

2. Analytical Techniques

This chapter contains the theoretical foundations of the analytical methods used to obtain the scientific results presented in this thesis.

2.1. X-Ray Diffraction

X-ray diffraction (XRD) is an important method in materials science to examine the internal structure of solids by diffraction. It is a rapid, non-destructive technique, which allows for the study of ordered structural motifs inside of materials, the composition of materials and the degree of crystallinity. Due to the high sensitivity of the method and the use of modern X-ray detectors, only small amounts of sample, often in the form of powders, are needed. By observing the interaction of incident X-ray photons with the lattices of a crystalline material, it is possible to determine atomic positions and thereby phases, lattice parameters and geometries of molecules inside a solid. X-ray photons are generated in a vacuum tube in which electrons are accelerated from a heated cathode towards an anode by applying a high electric potential between the electrodes. Upon impact of the accelerated electron onto the anode (typical materials are copper or molybdenum), these electrons can remove orbital electrons from inner shells of the atoms of the anode material. The resulting vacancies are filled up by an electron from a more energetic outer shell. The energy difference of these orbitals during the recombination process is then emitted as an X-ray photon. This results in X-rays of characteristic, material dependent wavelengths since orbital energy differences can only be of discrete values.

Further X-ray radiation is generated by the scattering of the high-velocity electrons with the strong electric field of the metal nuclei upon impact onto the anode. In this case, the emitted X-rays have a continuous spectrum with a maximum energy corresponding to the potential of the tube.

For XRD experiments, it is desirable to use X-rays of specific wavelengths only. This is achieved by using a monochromator. To resolve atomic positions, it is important that the used wavelength is shorter than the interatomic distances in the lattice.

XRD analysis is based on the scattering of X-ray radiation. The incoming photon transfers its energy to an electron of the crystalline material. Therefore, the electron of the crystalline material is excited and starts to emit radiation at the same frequency as the

incoming photon but the emission originating from the electron is spherical. This effect is called Thomson scattering. If the scattering occurs at different atoms in a system, the resulting waves can interfere constructively or destructively. Constructive interference occurs when the path length difference is an integer number of the wavelength (AB + BC = nλ) (Figure 2.1).
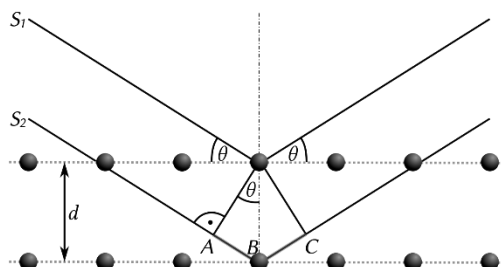

Figure 2.1: Bragg diffraction of parallel beams at two different atoms.[1]

This interference is furthermore described by the Bragg equation (1), where d is the distance between lattice planes, θ is the angle of incidence of the X-ray photons, n is an integer number and λ is the wavelength of the incident X-ray photons.

$$2\,d\,\sin\theta = n\,\lambda \tag{1}$$

The effect of constructive interference is maximized when each scattering atom on a series of planes parallel to the one with indices *hkl* at a distance *nd* is diffracting in phase. Reflection positions and intensities give characteristic diffraction patterns that allow for database-assisted crystal identification or structure determination. Furthermore, peak shape and width can be used to calculate crystalline domain sizes.

Powder XRD (PXRD) is an effective method for the analysis of microcrystalline samples. Due to the random orientation of the crystallites in the powdered samples, the diffraction spots are averaged into cones. This loss of information complicates the structure solution and modern, computer-assisted methods need to be employed for structure refinement.

X-ray diffraction was carried out in reflection mode using a Bruker D8 Discover instrument with Ni-filtered Cu K_α-radiation (1.54 Å) and a position-sensitive detector (Bruker LynxEye).

Grazing-incidence X-ray diffraction (GIXRD) is a technique used to analyze the crystallinity of very thin layers of material on a surface. Here, a very small X-ray incidence angle is used to illuminate the sample across an extended area parallel to the photon path and therefore, to maximize the potential interaction area of the film with the X-ray photons. This small angle is generally chosen to be close, but below the critical angle (in which total reflection of the X-rays occurs) of the studied material. A typical geometry for a GIXRD measurement is shown in Figure 2.2. Here, the angle of the incident beam is defined as α_I and the reflected beam as α_F. The sample plane is defined by x and y, where x is parallel to the incident X-ray beam and y is perpendicular to it. Consequently, the z-axis is defined perpendicular to the xy-plane. The corresponding scattering vectors are defined as q_x, q_y and q_z (Figure 2.2). Depending on the grid spacing, or the 2 theta ranges, GIXRD experiments differentiate between GIWAXS and GISAXS. GIWAXS experiments typically consider 2 theta ranges between 1.5° and 40°, while GISAXS experiments consider angles <1.5° (for Cu K$_\alpha$ radiation).
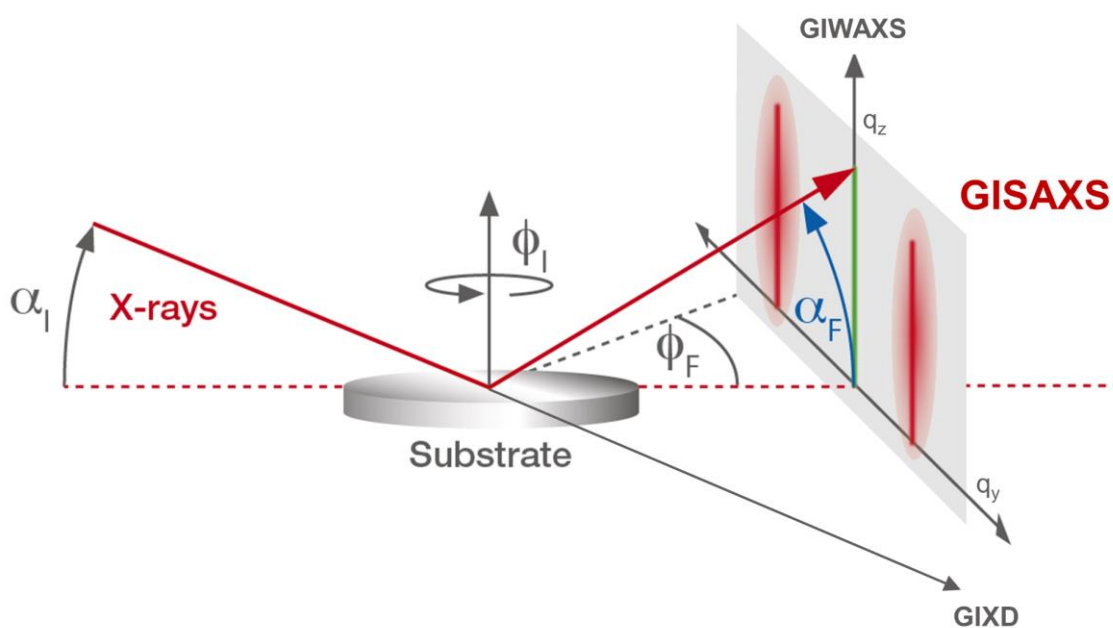

Figure 2.2: Scheme of the geometry of a GIWAXS / GIWAXS measurement.

GIXRD data is often recorded using 2D detectors. Therefore, in addition to the standard XRD data, information about the orientation of crystal lattices is obtained. By analyzing the diffuse scattering of the film, insights can be gathered into the morphology and roughness of the film.

GIXRD was carried out using an Anton-Paar SAXSPACE system equipped with a Cu K$_\alpha$ X-ray microfocus source and a beamwidth of 50 µm. A Dectris EIGER R 1M detector was used to collect 2D X-ray scattering data.

2.2.   Electron microscopy

Electron microscopy is a well-suited method for the characterization of materials featuring properties in the nanometer regime. Microscopes that use light in the visible regime are limited by diffraction to a resolution of about 200 nm. Electron microscopy uses accelerated electrons that can have 100,000 times shorter wavelengths for imaging and therefore, much smaller structures can be resolved, up to the atomic level. The electron beam for electron microscopy is generated under high vacuum (typically 10^{-7} mbar) using a field emission gun (pin-shaped tungsten filament) or a thermal emitter (heated tungsten or lanthanum hexaboride filament). Subsequently, the electrons are accelerated using high potentials and focused onto the sample by electromagnetic lens systems.

2.2.1.   Scanning electron microscopy (SEM)

SEM is a method for the characterization of morphologies of surfaces of materials with high resolution (up to about 0.6 nm). Here, the image is generated by scanning the sample line by line with an electron beam. This electron beam is generated thermoionically in a vacuum by a hot filament or, nowadays, often by a field emission gun and by applying voltages of 0.1 to 30 kV (a typical SEM design is shown in Figure 2.3).
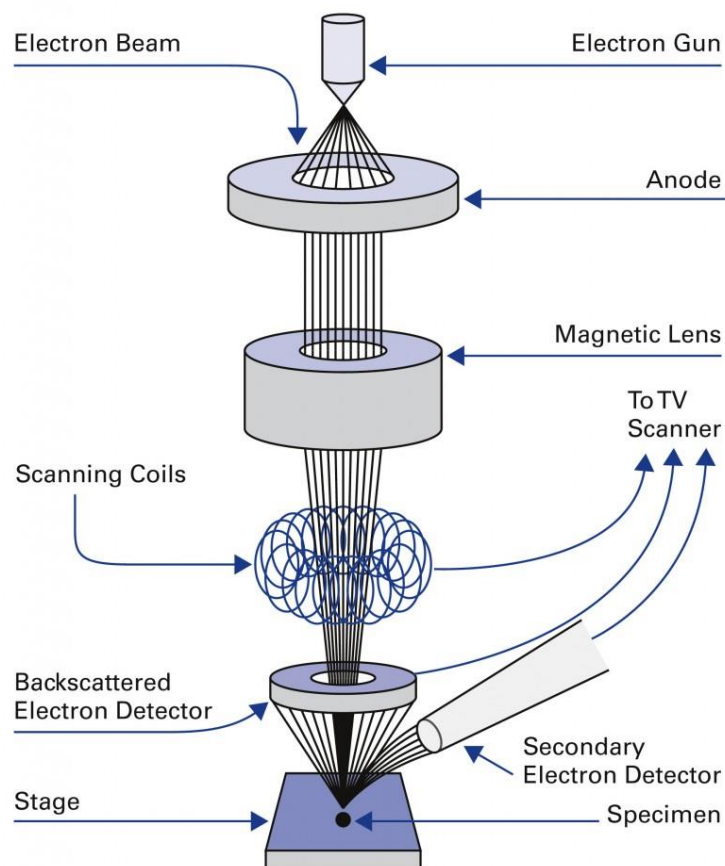
Figure 2.3: Schematic presentation of an SEM.[1]

The interactions of the focused beam with the sample are subsequently measured as secondary signals by various detectors, which allows for the analysis of the morphology, as well as the chemical composition of the sample. Depending on the acceleration voltage, the electron beam penetrates the sample volume at different depths and different secondary signals can be detected. For SEM analysis, the most important signals are secondary electrons (SE), backscattered electrons (BSE) and characteristic X-rays for energy-dispersive X-ray spectroscopy (EDX) (Figure 2.4).
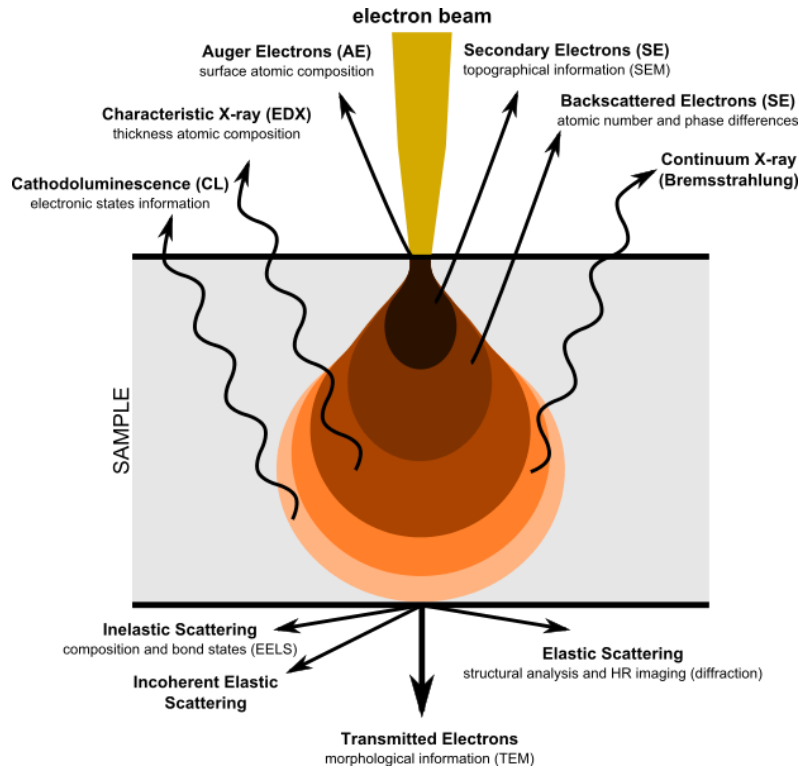
Figure 2.4: Scheme of the interaction of the incident electron beam with the sample, the interaction volume and the different resulting signals.[2]

Generally, imaging is carried out by collecting the secondary, low-energy (<50 eV) electrons with a scintillator-photomultiplier system. Because of their low energy, only electrons originating from the first layers of the surface can be collected at the detector. The resulting image can be seen as an intensity map of the detected secondary electrons, resulting in images that can often be interpreted similarly to light micrographs. Beam electrons that strike the surface perpendicularly produce similar amounts of secondary electrons, rendering flat areas similarly bright. Tilted areas appear brighter since the path for secondary electrons through the material is shortened. BSE are high energy electrons resulting from elastic scattering at the atomic nuclei. Different elements can be distinguished by the number and nature of backscatter events, thereby creating a contrast depending on the atomic number Z. This allows for studying the chemical composition and elemental distribution throughout a sample by analyzing differences in contrast. EDX is used to determine the elemental composition of a sample precisely. The incident electron beam may excite and eject an electron from the inner shell of an atom of the sample. Thereby, an electron-hole is generated, which is filled by a higher-energy outer-shell electron. The energy difference between the outer shell and the inner shell orbital is

subsequently released in the form of element-characteristic X-rays, which can be measured by an EDX detector.

SEM images were recorded using a JEOL JSM-6500F or an FEI Helios NanoLab G3 UC microscope at acceleration voltages of 1–30 kV.

2.2.2. Transmission electron microscopy

The transmission electron microscope (TEM) uses elastically scattered or transmitted electrons that penetrate the sample for imaging. Therefore, thin samples and highly accelerated electrons (60–300 kV) are needed. The TEM images can be obtained, for example, by illuminating a fluorescent screen and recording the resulting fluorescence with a digital camera. The images in the TEM are contrast maps resulting from the ratio of inelastically to elastically scattered electrons at the sample. More precisely, the contrast is generated by the number of electrons reaching the detector. This number of recorded electrons can be reduced by the objective aperture, which removes electrons depending on their scattering angles, and an energy filter, which removes electrons that lost most of their energy by sample interaction. Therefore, the detector signal is highly dependent on the density and thickness of the sample. For bright field imaging, the objective aperture is centered around the primary beam, and electrons that are scattered to high angles are removed. In darkfield mode, this low angle scattering region is excluded, and only strongly scattered electrons are recorded, which allows for an additional Z-contrast due to stronger electron-atom scattering intensity at higher atomic Z-numbers.

In high-resolution TEM, the images are generated by the elastically scattered electrons. Prior to sample interaction, the electrons are in phase. Subsequently, depending on the crystallinity and crystal orientations within the sample, the phases of the electrons interfere through Bragg diffraction. This is then translated into different intensities on the detector, creating the contrast within the image.

TEM images were recorded using an FEI Titan Themis 60 – 300 microscope at an acceleration voltage of 120 – 300 kV.

2.3.   Physisorption

Gas physisorption is a widely used technique for the characterization of porous materials. It allows for obtaining information about surface areas, pores sizes and pore volumes. The method uses chemically inert gases (adsorptives), such as nitrogen or argon, and studies the reversible interactions, such as van-der-Waals or dispersive forces, with the substrate. More specifically, physisorption is used to study the adsorption and desorption of the gases under isothermal conditions. The behavior of materials during physisorption is described with sorption isotherms, in which the adsorbed volume is plotted against the relative pressure. This relative pressure is the ratio of the equilibrium pressure p and the saturated vapor pressure p_0 of the pure adsorptive. A sorption isotherm is typically obtained from a sample that was activated under a high vacuum and at elevated temperatures to remove any guest molecules prior to the measurements. Subsequently, the sample is exposed to increased gas pressures at predefined relative pressures p/p_0 until a relative pressure close to 1 is reached. Thereby, the adsorption branch of the isotherm is obtained. Afterward, the desorption branch is determined by decreasing the relative pressure p/p_0 to predefined pressure points.

The shape of the resulting sorption isotherms is dependent on the pore sizes and shapes of the materials. Pore sizes are typically divided into three classes: micropores with <2 nm, mesopores with 2–50 nm and macropores with >50 nm. To standardize and classify sorption isotherms, IUPAC classified eight typical isotherm shapes (Figure 2.5).

Type I isotherms are generally observed for microporous materials. The small pore diameter allows only for limited adsorption where the adsorbate layer can only become a few layers thick. The attractive potential results in a complete pore condensation, the so-called micropore filling. Characteristic for this isotherm is the high uptake at low partial pressures.

Type II and III isotherms are typical for large meso-, or macroporous materials or for materials with no porosity. The reversible type II isotherm is the most typical one and represents an unrestricted monolayer-multilayer adsorption process. The arrow indicates the partial pressure region, in which monolayer coverage is complete and the multilayer adsorption starts.

A type III isotherm indicates that interactions between the adsorbate and the absorbent are weak, and adsorbate-adsorbate interactions are favored.

Type IV isotherms describe mesoporous materials. In type IV(a), a hysteresis loop occurs due to capillary condensation inside the mesopore. Type IV(b) describes an isotherm of a mesoporous material in which no capillary condensation takes place. The existence of a hysteresis loop depends on the stability of the adsorbed multilayer during adsorption and on the nucleation barrier for creating a liquid phase in the pores. This depends on the pore shape, interface energies and the temperature. A highly stable adsorbate multilayer results in a pore condensation at higher partial pressures during the adsorption, while the desorption process is a reversible liquid-vapor transition under near equilibrium conditions, which occurs at lower partial pressures. Additionally, the form of the hysteresis can give further information on pore shapes and openings.

Type V isotherms are similar to type III isotherms, but for porous materials.

Type VI isotherms are very rare and indicate a multi-step, layer-by-layer adsorption on a uniform, non-porous surface.
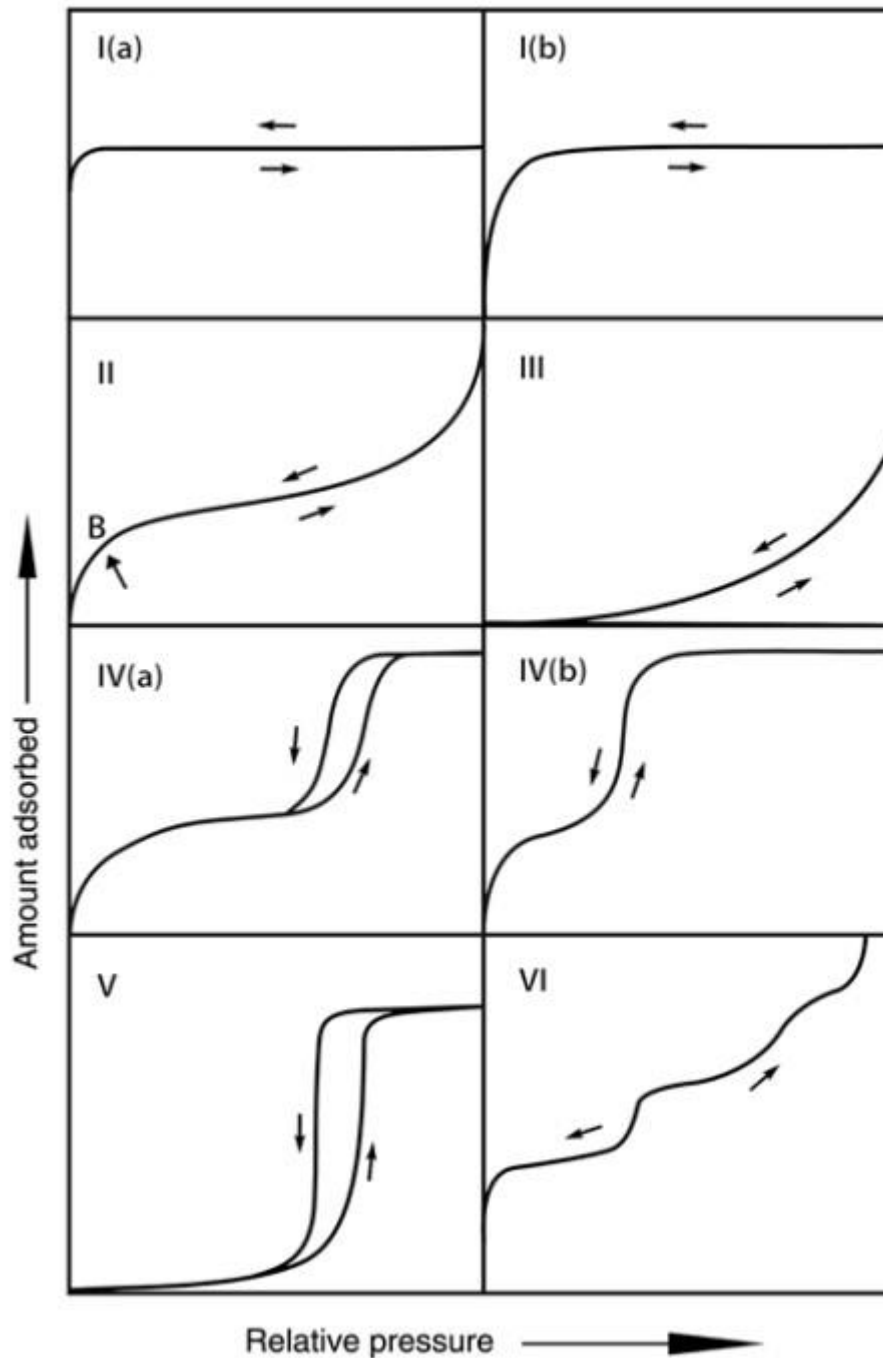
Figure 2.5: Isotherm shapes as classified by IUPAC.[3]

Surface areas are mostly calculated by the Brunauer-Emmett-Teller theory (BET), which explains the adsorption of gases onto surfaces of porous materials. Here, the capacity of the monolayer is derived by transforming the physisorption isotherm into a BET plot. Then the BET plot is used to calculate the adsorptive capacity of the monolayer, and subsequently the BET surface area is calculated from the BET capacity and the cross-sectional area of the adsorptive.

Although several adsorptives are used for physisorption, nitrogen has become the standard, mainly due to its availability and low cost. BET calculations are generally quite accurate (as long as pore sizes are not too small), but often overestimate surface areas for highly polar pore environments.[4] This is caused by the diatomic nature of the molecule, which results in a quadrupole moment and therefore an additional partial charge that can increase molecular interactions. To overcome these limitations, it is possible to use argon at liquid argon temperature for sorption, since it has no quadrupolar moment. It is furthermore possible to use argon at liquid nitrogen temperature. This leads to cooling argon 6.5 K below its bulk triple point, resulting in questionable values for the reference properties. By using a lower saturation pressure for the supercooled liquid argon (p_0 = 230 torr) it is possible to carry out surface area measurements. However, since calculation models for nitrogen are so far superior to argon, nitrogen sorption remains the more accurate method for most measurements.[5]

Pore size distributions are calculated using density functional theory (DFT) simulations. Here, the interactions of adsorptives with different pore geometries and surface polarities were simulated and based on this, various models, so-called kernels, were developed. Based on these kernels, theoretical isotherms can be modeled and fitted against the experimentally obtained one by changing pore widths. This modeling is either done with the non-local density functional theory (NLDFT), or the more recent quenched-solid density functional theory (QSDFT), as NLDFT neglects surface roughness and heterogeneity.[5]

2.4.   UV-vis-NIR spectroscopy and photoluminescence

The interaction of UV-vis-NIR electromagnetic radiation with matter can be studied by absorption spectroscopy. The absorption of radiation in this range results in electronic transitions within the material, and electrons are excited from the ground state to higher excited energy states, leaving an electron-hole. This allows for studying the energy difference between the HOMO-LUMO orbitals, or the valence band and conduction band.[6] If the electron is excited to energies higher than the lowest-energy excited state, the electron first relaxes non-radiatively, until the vibrational ground state of the excited state is reached. Subsequently, the energy difference to the ground state is released by the emission of a photon and the excited electron recombines with the electron-hole.[7]

The kinetics of this recombination process, and thereby the lifetime of the excited states, can be assessed by time-correlated single-photon counting (TCSPC). Here, the sample is excited by a short laser pulse of known duration and subsequently, the time between the end of the laser pulse and the detection of a photon is measured. Using laser pulse frequencies in the kHz or MHz range allows for statistical analysis of the lifetimes of the excited states. The collected decay data can then be fitted with an exponential function to gain information about the half-life time of the excited states and the number of different relaxation pathways.[8]

2.5.   Cyclic voltammetry (CV)

CV is an electrochemical analysis method in which the potential of an electrode is changed linearly against time, and the resulting current is recorded. The potential is scanned cyclically between two predefined vertex potentials at linear, fixed rates. The resulting current is subsequently plotted against the applied potential. CV is commonly used to probe electron transfer in redox-active systems. Upon reaching a specific potential at the working electrode, a current starts to flow, indicating the start of an electron transfer between the electrode and the redox-active substance. An oxidation will occur when the potential energy of the energetically highest electron in the substance is higher than the energy of the electrons in the working electrode. Accordingly, a reduction will occur when the potential energy of the electrons in the working electrode is higher than the energy of accessible electronic levels in the substance. Therefore, the driving force of the electron transfer is the minimization of the potential energy difference between the electrode and the substance. By referencing the potential at which this electron transfer occurs against a known redox-system, such as Ag/AgCl (used within the reference electrode), the absolute energies can be determined at which an oxidation or reduction takes place.[9]

CV measurements are conducted in a solution of a solvent and an electrolyte. Typically, an electrochemical cell for CV consists of three electrodes, namely the working electrode, the counter electrode, and the reference electrode. The current is measured between the working electrode and the counter electrode, while the potential is measured between the working electrode and the reference electrode.

References

(1) Monospektra. SEM Scheme.
https://www.monospektra.com/positioning/applications/drives-positioning-systems-electron-microscopes/ (accessed December 13, 2019).

(2) Claudionico. Electron Interaction with Matter.
https://commons.wikimedia.org/wiki/File:Electron_Interaction_with_Matter.svg (accessed December 13, 2019).

(3) Thommes, M.; Kaneko, K.; Neimark, A. V.; Olivier, J. P.; Rodriguez-Reinoso, F.; Rouquerol, J.; Sing, K. S.W. Physisorption of gases, with special reference to the evaluation of surface area and pore size distribution (IUPAC Technical Report). *Pure Appl. Chem.* **2015**, *87*, 1051–1069.

(4) Galarneau, A.; Desplantier, D.; Dutartre, R.; Di Renzo, F. Micelle-templated silicates as a test bed for methods of mesopore size evaluation. *Microporous and Mesoporous Materials* **1999**, *27*, 297–308.

(5) Lowell, S.; Shields, J. E.; Thomas, M. A.; Thommes, M. *Characterization of porous solids and powders: surface area, pore size and density*; Particle Technology Series 16; Springer: Dordrecht, 2004.

(6) Clark, B. J.; Frost, T.; Russell, M. A., Eds. *UV spectroscopy: Techniques, instrumentation, data handling*, 1. ed.; Techniques in visible and ultraviolet spectrometry 4; Chapman & Hall: London, 1993.

(7) Lakowicz, J. R. *Principles of fluorescence spectroscopy*, 3. ed.; Springer Science+Business Media LLC: Boston, MA, 2006.

(8) Phillips, D.; Drake, R. C.; O'Connor, D. V.; Christensen, R. L. Time Correlated Single-Photon Counting (Tcspc) Using Laser Excitation. *Instrumentation Science & Technology* **1985**, *14*, 267–292.

(9) Elgrishi, N.; Rountree, K. J.; McCarthy, B. D.; Rountree, E. S.; Eisenhart, T. T.; Dempsey, J. L. A Practical Beginner's Guide to Cyclic Voltammetry. *J. Chem. Educ.* **2018**, *95*, 197–206.

3. From Benzodithiophene to Diethoxy-Benzodithiophene Covalent Organic Frameworks - Structural Investigations

This chapter is based on the following publication:

3.1. Abstract

The incorporation of side groups into a covalent organic framework (COF) backbone can be of significant importance for developing new frameworks with enhanced properties. Here we present a novel π-stacked thiophene-based COF containing a benzodithiophene building unit modified with ethoxy side chains. The resulting BDT-OEt COF is a crystalline mesoporous material featuring high surface area and accessible hexagonal pores. We further synthesized a series of COFs containing both BDT and BDT-OEt building units at different ratios. The impact of the gradual incorporation of the BDT-OEt building units into the COF backbone on the crystallinity and porosity was investigated. Furthermore, molecular dynamic simulations shed light on the possible processes governing the COF assembly from molecular building blocks.

3.2.   Introduction

The self-organization of π-stacked organic layers into highly ordered three-dimensional porous structures endows covalent organic frameworks (2D COFs) with interesting properties for diverse applications, including chemical separations, catalysis and optoelectronics.[1-7] The extended organic layers constituting a 2D COF are generally obtained by the copolymerization of rigid building units having complimentary geometries through the formation of strong yet reversible covalent bonds. Boroxines and boronic esters, obtained by condensation reactions of boronic acids and diols, are commonly utilized as integral COF assembly motifs and thereby enable the growth of planar two-dimensional layers.[8] Along with the condensation reactions, stacking of the formed organic layers takes place through dispersive forces.[9] Therefore, 2D COFs connected through boronate esters feature an assembly of organic building units (or linkers) in a columnar fashion. This permits the formation of supramolecular structures having long-range order, one-dimensional channels and high surface areas.[10-15]

Tuning the structural and physical properties of a COF while maintaining its key features, namely porosity and crystallinity, can pose significant synthetic challenges. For example, incorporating building units having a large conjugated π-system into a framework can be highly desirable for enhanced light absorption properties.[11, 16] However, such attractive building units tend to exhibit poor solubility under the reaction conditions, often leading to poor crystallinity of the resulting COF.[17] To overcome solubility limitations, a modification of the building units with solubilizing agents such as alkyl side chains can be considered. In the final COF structure, the solubilizing side chains are oriented orthogonally to the COF pore walls and therefore need to be compatible with the stacking of the COF layers. In addition, these groups can play an important role in defining the electronic properties of the COF. Electron donating or electron withdrawing side groups can have a strong impact on the COF optical bandgap, and they can affect the fine balance between the Coulomb repulsion and the weak attractive London dispersion interactions holding the COF layers together.

In an early study, Lavigne and co-workers reported the synthesis of a boronate ester-linked COF-18 series where the catechol building units were modified with linear alkyl side chains ranging from methyl to propyl groups. The impact of the integrated alkyl side chains on guest molecule uptake was investigated.[18] In a later study, enhanced stability

towards humidity of the propyl modified COF structure was shown within the COF-18 series.[19] However, the overall long-range order of the COF-18 series was significantly diminished with the elongation of the side groups. Jiang and co-workers introduced an azide-modified benzo diboronic acid (BDBA) for the purpose of COF backbone post-modification.

In that report, the overall crystallinity of the modified COF-5 was maintained as the azide units having a planar configuration were extended along the plane of the COF layers.[20] Dichtel and co-workers introduced an effective crystallization route for boronate ester linked COFs starting from saturated homogenous precursor solutions.[9, 21] Applying this method, COF structures having high surface area and long-range order were obtained. This crystallization route illustrates the importance of the COF precursor's solubility under reaction conditions.

Recently, we reported the synthesis under solvothermal conditions of oriented thin films of an electron donor COF based on benzodithiophene units, BDT COF.[22] We also introduced a novel vapor-assisted conversion approach for the direct deposition of BDT COF films under mild thermal conditions.[23]

Herein, we describe the synthesis of a highly porous boronate ester linked BDT-OEt COF containing (4,8-diethoxybenzo[1,2-b:4,5-b']dithiophene-2,6-diyl)diboronic acid. The BDT core is modified with electron-donating ethoxy side chains thereby expanding the family of thiophene-based COFs.[7, 22, 24, 25] We synthesized a series of COFs consisting of BDT and BDT-OEt building unit mixtures and studied their structural properties (Scheme 3.1). The impact of the gradual layer perturbation imposed by the increased fraction of incorporated BDT-OEt building units into the COF backbone on the crystallinity and porosity was investigated. Furthermore, molecular dynamic simulations shed light on the possible processes governing the COF assembly from molecular building units.
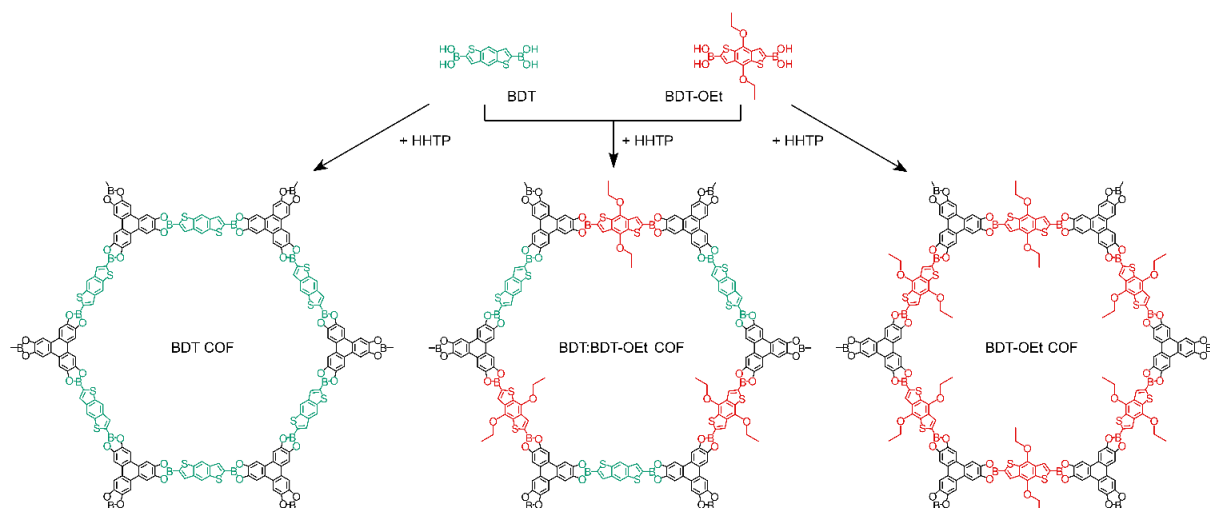
Scheme 3.1: Schematic representation of the synthesis of BDT COF (left), BDT:BDT-OEt 1:1 COF (middle), and BDT-OEt COF (right).

3.3. Results

A novel BDT-OEt COF featuring a BDT core decorated with ethoxy side chains was synthesized through the co-condensation of (4,8-diethoxybenzo[1,2-b:4,5-b']dithiophene-2,6-diyl)diboronic acid and HHTP (2,3,6,7,10,11-hexahydroxytriphenylene) under solvothermal conditions (for more details see experimental section).
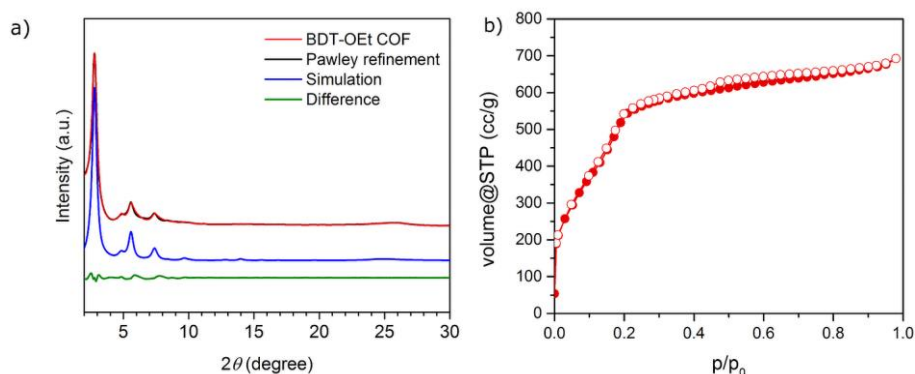

Figure 3.1: (a) XRD patterns of BDT-OEt COF: experimental (red), Pawley refinement (black), simulated pattern (blue), and difference plot (green). (b) Nitrogen sorption isotherm of BDT-OEt COF. Full symbols: adsorption, empty symbols: desorption.

Powder X-ray diffraction data of the newly synthesized BDT-OEt COF clearly indicate the formation of a crystalline framework. The diffraction pattern reveals an intensive reflection at 2.78° corresponding to the (100) plane. Additional reflections observed at

4.85°, 5.58° and 7.38°, 9.71° and ~25.7° (broad) are attributed to the (110), (200), (120), (220) and (001) planes, respectively (Figure 3.1a). The obtained *d*-values correspond to lattice parameters of a = b =3.66 nm for an ideal hexagonal BDT-OEt COF structure. Effective crystallite domain sizes of 21 nm in diameter for BDT-OEt COF were calculated using the Scherrer equation for reflection broadening. Molecular mechanics simulations for the possible COF layer arrangements were carried out using Materials Studio software and the Forcite module. Assuming a hexagonal symmetry, the BDT-OEt COF unit cell was constructed in the *P*6 space group corresponding to an ideal eclipsed AA COF layer arrangement and featuring a completely open pore system (Figure S3.1). To obtain the final unit cell parameters and the crystallite domain sizes, Pawley refinement was employed. For this purpose, the geometry optimized BDT-OEt COF unit cell was refined against the experimental powder X-ray diffraction pattern. Lattice parameters of a = b = 3.65 nm, c = 0.365 nm and crystallite sizes of 20 nm in diameter were obtained. The simulated powder diffraction pattern corrected for reflection broadening is in very good agreement with the experimentally observed pattern with regard to reflection positions and relative intensities (Figure 3.1a). Additionally, we simulated the BDT-OEt COF unit cell in the triclinic *P*1 space group where no symmetry constraints are imposed. After geometry optimization and Pawley refinement, the refined unit cell reveals an eclipsed configuration with tilted COF layers.[36] This layer configuration produced a nearly identical simulated diffraction pattern, and therefore the exact eclipsed layer arrangement cannot be determined based on the experimental diffraction pattern (see Figure S3.5). To confirm the eclipsed layer arrangement for the BDT-OEt COF, we also simulated the X-ray diffraction pattern for an alternative hexagonal unit cell with *P*6$_3$ space group corresponding to a staggered, AB layer arrangement (Figure S3.8). Based on the comparison of the simulated AA and AB patterns with the experimentally obtained pattern, we conclude that BDT-OEt crystalizes with an eclipsed layer arrangement allowing for an open pore system.

In previous reports, the side groups decorating the pore walls were considered as an amorphous contribution to the X-ray scattering data, having no preferred orientation in the pore due to their free rotation.[18, 20, 37] To investigate the preferred orientation of the ethoxy groups in the pores, several separate molecular dynamics simulations were carried out (Figure S3.10). Independent of the initial orientation of the groups, which can either face the adjacent hydrogen or sulfur atom of the BDT core or alternate between these two

cases, nearly all ethoxy-groups rotated to face the sulfur atom within less than 1 ns. The ethoxy groups retained their position, indicating that the groups can in principle rotate at room temperature, and that the sulfur-facing position is favoured in the crystal (Figure S3.10). This was confirmed by DFT calculations at the PBE+D level, which indicate that the sulfur-facing geometry is more stable by 0.2 eV (corresponding to a Boltzmann population ratio of approx. 4×10^{-4} for the hydrogen-facing geometry at room temperature). This preference can be attributed to the electrostatic attraction between the sulfur lone-pairs and the ethoxy hydrogen atoms.

Nitrogen sorption analysis of an activated BDT-OEt COF powder reveals a type IV sorption isotherm, with a distinct nitrogen uptake at relative low partial pressures, typical for a mesoporous material (Figure 3.1b). The Brunauer-Emmett-Teller (BET) surface area was calculated to be as high as 1844 m^2/g (p/p_0 = 0.05-0.13 in the adsorption branch) and the pore volume to be 1.07 cm^3/g. These values are in good agreement with the simulated Connolly surface area of 2075 m^2/g and calculated pore volume of 1.06 cm^3/g for a BDT-OEt COF with an eclipsed layer arrangement. BDT-OEt COF exhibits a narrow pore size distribution as derived from the sorption isotherm with a pore size of 2.9 nm corresponding to a defined mesoporous structure (Figure S12).

An aggregation process of COF crystallites into larger domains was discussed as a crucial non-reversible step for the formation of COF precipitates.[9] Scanning electron microscopy (SEM) micrographs of BDT-OEt COF bulk material indicate that the small BDT-OEt COF crystallites aggregate into micrometer spherical agglomerates upon COF powder precipitation (Figure S13). Transmission electron microscopy (TEM) images reveal an
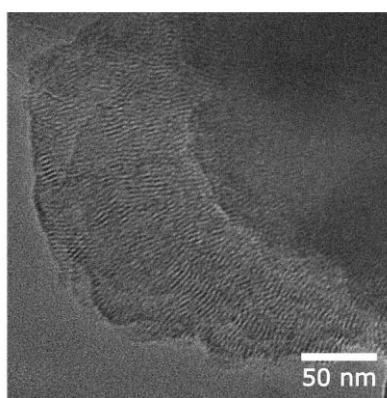

Figure 3.2: Transmission electron microscopy image of BDT-OEt COF showing polycrystalline domains and the COF channels.

intergrowth of small BDT-OEt COF crystallites into larger polycrystalline domains. In contrast to the BDT COF, less regular fairly short COF channels can be observed (Figure 3.2). These observations are in accordance with the reflection broadening observed in the X-ray analysis and suggest that the incorporation of ethoxy side chains can influence the COF growth process in both the ab-plane and the stacking direction.

Thermogravimetric analysis (TGA) of the COF powder displays a major mass loss at 400°C that is attributed to framework decomposition (Figure S3.19).

The formation of a boronate ester motif in the COF framework was confirmed by FT-IR and solid-state NMR spectroscopy. IR-bands at 1346 and 1238 cm^{-1} are attributed to the B−O and C−O vibrational modes of the ester formed (Figure S3.20). In the ^{11}B solid-state NMR spectrum of BDT-OEt COF, a strong peak at 20.9 ppm confirms the presence of a trigonal-planar boron atom of a boronate ester (Figure S3.22). In the ^{13}C solid-state NMR spectrum, the signals at 13.2 ppm and 67.7 ppm are attributed to the methyl and methylene carbon atoms in the ethoxy side chain (Figure S3.23).

Boronate ester linked COFs consisting of building unit mixtures have been introduced in a series of COF-5 structures modified with azide side chains as a platform for a gradual post synthetic modification via click chemistry.[20] Herein, we aim at investigating the structural changes imposed by ethoxy groups on a well-defined and highly crystalline COF structure such as the BDT COF. For this purpose, we synthesised a series of COFs where both building units BDT and BDT-OEt are randomly distributed within the COF backbone at different ratios. The BDT:BDT-OEt COF series was synthesised under solvothermal conditions similarly to the synthesis of BDT-OEt COF, with BDT:BDT-OEt building unit ratios of 1:0, 3:1, 1:1, 1:3 and 0:1 (for more information see experimental section).
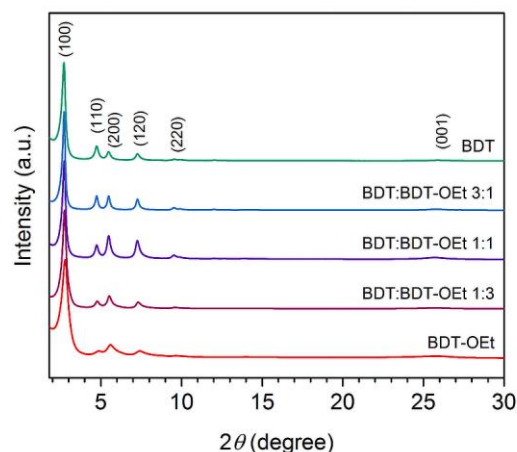
Figure 3.3: PXRD patterns of BDT COF, BDT:BDT-OEt COFs, and BDT-OEt COF.

Powder X-ray diffraction patterns of the obtained BDT:BDT-OEt COFs confirmed the formation of a series of crystalline frameworks (Figure 3.3). Upon the incorporation of ethoxy side chains into the BDT COF backbone, gradual changes in the BDT:BDT-OEt COF diffraction patterns were observed. The relative intensities of the (110) and the (200) planes change with the increased fraction of BDT-OEt building units. This is in excellent agreement with the simulated diffraction patterns of BDT and BDT-OEt COFs and further confirms the successful incorporation of BDT-OEt into the frameworks (Figure S3.9). A broadening of the X-ray reflections is evident in BDT-OEt-rich COFs. The effective crystallite domain sizes calculated for BDT:BDT-OEt 3:1 and BDT:BDT-OEt 1:3 COFs are 95 nm and 47 nm, respectively. Therefore, we attribute the reflection broadening to a regular decrease in the crystallite domain sizes with increasing the BDT-OEt building unit content. A gradual small shift of the reflections corresponding to the ab plane to higher 2 theta values with the higher integrated fraction of BDT-OEt building units is observed as well (Figure S3.21). Interestingly, the broad reflection at ~25.7°, attributed to the layer stacking, maintained its position and its relative intensity. The gradual shift to higher 2 theta values implies that the incorporation of ethoxy groups into the frameworks induced structural modifications expressed in the unit cell parameters. This can be either attributed to a gradual shrinkage of the hexagonal unit cell or to a gradual increase of layer dynamics resulting in a P1 like structure (Figure S3.4).[36]

Molecular dynamics simulations regarding the layer interactions provided further insights into the effect of the ethoxy groups on the dynamics and order of the system. A comparison of the sulfur-sulfur radial distribution functions $g_{SS}(r)$ for the ethoxy

substituted and pristine BDT COF reveals a significant increase in short-range disorder in the former COF (Figure S3.11). This is evident from the broadening and shifted position towards larger distances of the first peak in $g_{SS}(r)$ corresponding to the closest sulfur-sulfur distance between adjacent layers. The increased short-range disorder is attributed mainly to increased movement of the layers in the ab-plane, since more displaced geometries are stabilized by the interactions between the ethoxy groups. Interestingly, the average interlayer distance in the simulations increases when the ethoxy groups are present, which might be expected due to the spatial demands of the ethyl groups. However, this trend regarding the interlayer distances is not observed in the experimental pattern.
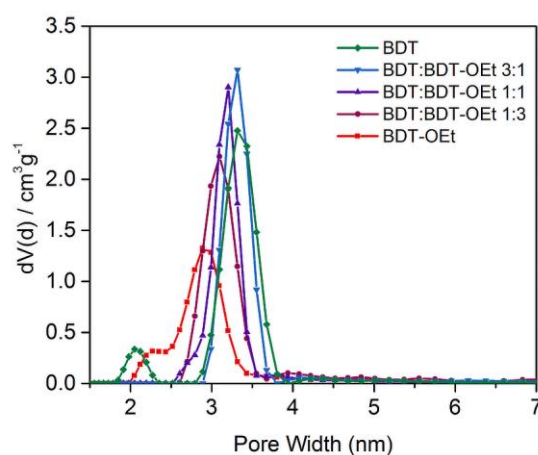
Figure 3.4: Detail of the pore size distributions of BDT COF, mixed BDT:BDT-OEt COFs and BDT-OEt COF showing the decrease of the main pore diameter upon the incorporation of ethoxy side chains into the COF structure.

The impact of the gradual incorporation of the ethoxy side chains on the pore accessibility of the frameworks was investigated by nitrogen sorption. The BDT:BDT-OEt COF series retained the typical type IV isotherms for mesoporous materials. The relative partial pressure of the slope of the nitrogen uptake is shifted to lower values as expected for the gradually increasing pore occupancy with ethoxy side chains. Pore size distribution evaluation revealed a gradual decrease of the pore size upon the incorporation of ethoxy side chains. In all the BDT:BDT-OEt COF structures only one type of pore is present, indicating a random integration of the ethoxy groups into the frameworks, as opposed to the formation of phase-separated domains. High surface areas were calculated for the BDT:BDT-OEt COF series. This clearly illustrates that the incorporation of BDT-OEt building units into the framework does not affect the accessible surface areas and pores of the BDT:BDT-OEt COF (Figure 3.4, S3.12).

The solubility of the respective building units under the reaction conditions plays an important role regarding their incorporation into the COF backbone. If a significant solubility difference would exist, their ratio in the frameworks might deviate from the initial stoichiometric mixture. To determine the final BDT:BDT-OEt ratio incorporated into the frameworks, samples of the respective BDT:BDT-OEt COF series were hydrolysed in wet DMSO-$d6$ for ^{1}H NMR spectroscopy. Integrating the proton signals of the building units showed that the observed intensities are in very good agreement with the intended stoichiometric ratios of BDT, BDT-OEt and HHTP building units for all COFs. Therefore, defects in the form of precursor deficiencies within the frameworks are not observed (Figure 3.5 and Section 9 in the SI).
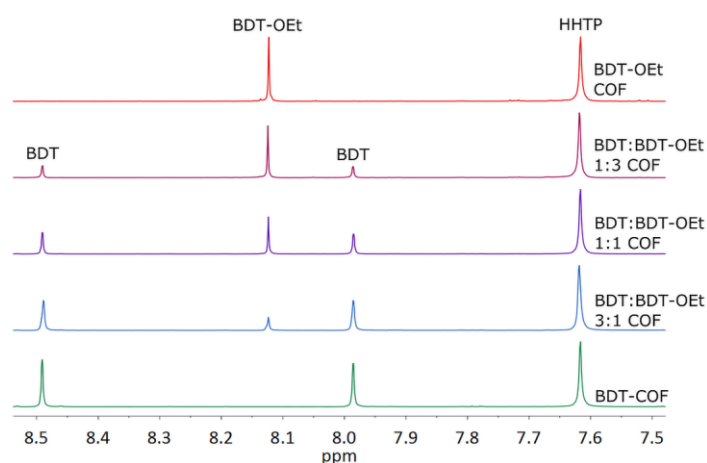
Figure 3.5: ^{1}H-NMR spectra of the hydrolyzed COFs showing the stoichiometric incorporation of BDT and BDT-OEt linkers into the respective frameworks.

SEM micrographs reveal a similar overall morphology for all investigated COFs. Small unevenly shaped particles form large aggregates, comparable with the morphology we observed for BDT-OEt COF (Figure S3.13). In TEM images, BDT-rich COFs show intergrown cauliflower morphology. Depending on the crystallite orientation, ordered channels or the typical honeycomb structure are visible. BDT-OEt-rich COFs feature smaller crystallite domain sizes and shorter COF channels (Figure S3.14). TGA traces were recorded to determine the thermal stability of the COF series. For all COFs, the major mass loss attributed to the decomposition of the framework takes place at 400°C, showing a similar thermal stability of all investigated frameworks (Figure S3.15-S3.19).

These analyses confirm that with BDT and BDT-OEt building units, COFs can be formed from freely selected ratios of the respective boronic acids. While mixing these building

units in a COF leads to structural changes in the framework, a highly porous, crystalline and thermally stable framework is generated in all cases.

3.4.   Conclusions

In conclusion, a novel ethoxy-functionalized benzodithiophene based COF, namely BDT-OEt COF, was synthesized under solvothermal conditions. BDT-OEt COF features crystallinity, mesoporosity and high surface area. A series of COFs consisting of both BDT and BDT-OEt building units in different ratios was synthesized. Highly crystalline, mesoporous frameworks were obtained for all BDT:BDT-OEt COFs. A nearly linear evolution from BDT to BDT-OEt COF was observed with regard to pore size and crystallite domain sizes upon the gradual incorporation of BDT-OEt building unit into the COF backbone. Furthermore, we show that the final building unit ratios in the framework can be predetermined prior to the COF synthesis. Therefore, the COF backbones and chemical pore environment can be finely tuned towards desired properties while an eclipsed layer arrangement is retained. Molecular dynamics simulations and DFT calculations shed light on the preferred orientation of the ethoxy groups in the pore. Furthermore, the simulations illustrate that the incorporation of ethoxy chains facilitates a subtle lateral displacement of the BDT COF layers relative to each other.

3.5.   References

1.   A. P. Côté, A. I. Benin, N. W. Ockwig, M. O'Keeffe, A. J. Matzger and O. M. Yaghi, *Science*, 2005, **310**, 1166-1170.

2.   N. Huang, X. Chen, R. Krishna and D. Jiang, *Angewandte Chemie International Edition*, 2015, **54**, 2986-2990.

3.   H. Xu, J. Gao and D. Jiang, *Nat Chem*, 2015, **7**, 905-912.

4.   S. Lin, C. S. Diercks, Y.-B. Zhang, N. Kornienko, E. M. Nichols, Y. Zhao, A. R. Paris, D. Kim, P. Yang, O. M. Yaghi and C. J. Chang, *Science*, 2015, **349**, 1208-1213.

5.   C. R. DeBlase, K. E. Silberstein, T.-T. Truong, H. D. Abruña and W. R. Dichtel, *Journal of the American Chemical Society*, 2013, **135**, 16821-16824.

6.   M. S. Lohse, T. Stassin, G. Naudin, S. Wuttke, R. Ameloot, D. De Vos, D. D. Medina and T. Bein, *Chemistry of Materials*, 2016, **28**, 626-631.

7.   M. Dogru, M. Handloser, F. Auras, T. Kunz, D. Medina, A. Hartschuh, P. Knochel and T. Bein, *Angewandte Chemie International Edition*, 2013, **52**, 2920-2924.

8.   J. W. Colson and W. R. Dichtel, *Nat Chem*, 2013, **5**, 453-465.

9.   B. J. Smith and W. R. Dichtel, *Journal of the American Chemical Society*, 2014, **136**, 8783-8789.

10.   L. Chen, K. Furukawa, J. Gao, A. Nagai, T. Nakamura, Y. Dong and D. Jiang, *Journal of the American Chemical Society*, 2014, **136**, 9806-9809.

11.   S. Jin, X. Ding, X. Feng, M. Supur, K. Furukawa, S. Takahashi, M. Addicoat, M. E. El-Khouly, T. Nakamura, S. Irle, S. Fukuzumi, A. Nagai and D. Jiang, *Angewandte Chemie International Edition*, 2013, **52**, 2017-2021.

12.   S. Jin, K. Furukawa, M. Addicoat, L. Chen, S. Takahashi, S. Irle, T. Nakamura and D. Jiang, *Chemical Science*, 2013, **4**, 4505-4511.

13.   J. Guo, Y. Xu, S. Jin, L. Chen, T. Kaji, Y. Honsho, M. A. Addicoat, J. Kim, A. Saeki, H. Ihee, S. Seki, S. Irle, M. Hiramoto, J. Gao and D. Jiang, *Nat Commun*, 2013, **4,** 2736.

14.   E. L. Spitler, J. W. Colson, F. J. Uribe-Romo, A. R. Woll, M. R. Giovino, A. Saldivar and W. R. Dichtel, *Angewandte Chemie International Edition*, 2012, **51**, 2623-2627.

15.   H. Yang, Y. Du, S. Wan, G. D. Trahan, Y. Jin and W. Zhang, *Chemical Science*, 2015, **6**, 4049-4053.

16.   M. Calik, F. Auras, L. M. Salonen, K. Bader, I. Grill, M. Handloser, D. D. Medina, M. Dogru, F. Löbermann, D. Trauner, A. Hartschuh and T. Bein, *Journal of the American Chemical Society*, 2014, **136**, 17802-17807.

17.   S. Jin, M. Supur, M. Addicoat, K. Furukawa, L. Chen, T. Nakamura, S. Fukuzumi, S. Irle and D. Jiang, *Journal of the American Chemical Society*, 2015, **137**, 7817-7827.

18.   R. W. Tilford, S. J. Mugavero, P. J. Pellechia and J. J. Lavigne, *Advanced Materials*, 2008, **20**, 2741-2746.

19.	L. M. Lanni, R. W. Tilford, M. Bharathy and J. J. Lavigne, *Journal of the American Chemical Society*, 2011, **133**, 13975-13983.

20.	A. Nagai, Z. Guo, X. Feng, S. Jin, X. Chen, X. Ding and D. Jiang, *Nat Commun*, 2011, **2**, 536.

21.	B. J. Smith, N. Hwang, A. D. Chavez, J. L. Novotney and W. R. Dichtel, *Chemical Communications*, 2015, **51**, 7532-7535.

22.	D. D. Medina, V. Werner, F. Auras, R. Tautz, M. Dogru, J. Schuster, S. Linke, M. Döblinger, J. Feldmann, P. Knochel and T. Bein, *ACS Nano*, 2014, **8**, 4042-4052.

23.	D. D. Medina, J. M. Rotter, Y. Hu, M. Dogru, V. Werner, F. Auras, J. T. Markiewicz, P. Knochel and T. Bein, *Journal of the American Chemical Society*, 2015, **137**, 1016-1019.

24.	G. H. V. Bertrand, V. K. Michaelis, T.-C. Ong, R. G. Griffin and M. Dincă, *Proceedings of the National Academy of Sciences*, 2013, **110**, 4923-4928.

25.	S. Duhović and M. Dincă, *Chemistry of Materials*, 2015, **27**, 5487-5490.

26.	D. W. Slocum and P. L. Gierer, *J. Org. Chem.*, 1976, **41**, 3668-3673.

27.	S. L. Mayo, B. D. Olafson and W. A. Goddard, *The Journal of Physical Chemistry*, 1990, **94**, 8897-8909.

28.	O. Alexiadis and V. G. Mavrantzas, *Macromolecules*, 2013, **46**, 2450-2467.

29.	A. K. Rappe and W. A. Goddard, *The Journal of Physical Chemistry*, 1991, **95**, 3358-3363.

30.	J. Clark Stewart, D. Segall Matthew, J. Pickard Chris, J. Hasnip Phil, I. J. Probert Matt, K. Refson and C. Payne Mike, *Journal*, 2005, **220**, 567.

31.	J. P. Perdew, K. Burke and M. Ernzerhof, *Physical Review Letters*, 1996, **77**, 3865-3868.

32.	S. Grimme, *Journal of Computational Chemistry*, 2006, **27**, 1787-1799.

33.	E. R. McNellis, J. Meyer and K. Reuter, *Physical Review B*, 2009, **80**, 205414.

34.	D. Vanderbilt, *Physical Review B*, 1990, **41**, 7892-7895.

35.	H. J. Monkhorst and J. D. Pack, *Physical Review B*, 1976, **13**, 5188-5192.

36.   E. L. Spitler, B. T. Koo, J. L. Novotney, J. W. Colson, F. J. Uribe-Romo, G. D. Gutierrez, P. Clancy and W. R. Dichtel, *Journal of the American Chemical Society*, 2011, **133**, 19416-19421.

37.   H. Xu, X. Chen, J. Gao, J. Lin, M. Addicoat, S. Irle and D. Jiang, *Chemical Communications*, 2014, **50**, 1292-1294.

3.6.   Supporting Information

Materials: All materials (if not otherwise noted) were purchased from Aldrich, Fluka, Acros or TCI Europe in the common purities purum and puriss. All materials were used as received without further purification. Benzo[1,2-b:4,5-b']dithiophene-4,8-dione was prepared following a literature procedure.[26]

Synthesis of 4,8-diethoxybenzo[1,2-*b*:4,5-*b*']dithiophene (1). The reaction was performed based on a literature procedure. A mixture of benzo[1,2-*b*:4,5-*b*']dithiophene-4,8-dione (1.10 g, 4.99 mmol, 1.0 equiv), zinc dust (0.981 g, 15.0 mmol, 3.0 equiv), NaOH (10 mL) and EtOH (10 mL) was stirred at 95 °C for 2h. Ethyl *p*-toluenesulfonate (3.00 g, 15.0 mmol, 3.0 equiv) was added and the resulting solution was stirred at 95 °C for additional 3 h. The reaction mixture was allowed to cool down to room temperature and was diluted with dichloromethane (DCM) (70 mL). The aqueous layer was extracted with DCM (4 × 100 mL) and the combined organic fractions were dried over Na_2SO_4. After filtration, the solvents were evaporated *in vacuo*. The crude product was purified by flash column chromatography (silica, *iso*hexane/DCM = 3:1) to afod **1** as a colorless solid (0.675 g, 49%). Mp: 96.9 – 102.6 °C. ^{1}H NMR (400 MHz, $CDCl_3$) δ/ppm = 7.46 (d, *J* = 5.5 Hz, 2H), 7.35 (d, *J* = 5.5 Hz, 2H), 4.35 (q, *J* = 7.0 Hz, 4H), 1.47 (t, *J* = 7.0 Hz, 6H). ^{13}C NMR (100 MHz, $CDCl_3$) δ/ppm = 144.3, 131.8, 130.4, 126.0, 120.3, 69.4, 16.1. IR (cm^{-1}): $\tilde{v}$ = 3100, 2980, 2873, 1892, 1515, 1477, 1436, 1372, 1347, 1199, 1106, 1085, 1029, 977, 873, 810, 752, 736, 695, 661. MS (70 eV, EI) m/z (%) = 278 (27, M[+]), 223 (11), 222 (13), 221 (100), 111 (37), 44 (31), 43 (80). HRMS for $C_{14}H_{14}O_2S_2$ (278.0435) found: 278.0428.

Synthesis of 2,6-dibromo-4,8-diethoxybenzo[1,2-b:4,5-b']dithiophene (2). In a dry argon flushed Schlenk-flask, equipped with a magnetic stirring bar and septum, 1 (1.39 g, 5.0 mmol, 1.0 equiv) was dissolved in *N,N*-dimethylformamide (25 mL) and cooled down to 0 °C. N-bromosuccinimide (1.78 g, 10.0 mmol, 2.0 equiv) was added in one portion and the resulting solution was warmed to room temperature and stirred for 4 h. The reaction mixture was diluted with water (100 mL) and extracted with Et_2O (3 × 30 mL).

The combined organic layers were washed with water (6 × 100 mL) and dried over Na_2SO_4. After filtration, the solvents were evaporated *in vacuo*. The crude product was purified by flash column chromatography (silica, *iso*hexane) to give 2 as a colorless solid (1.50 g, 69%). Mp: 158.7 - 161.9 °C. ^{1}H NMR (400 MHz, $CDCl_3$) δ/ppm = 7.41 (s, 2H), 4.26 (q, *J* = 7.0 Hz, 4H), 1.44 (t, *J* = 7.0 Hz, 6H). ^{13}C NMR (100 MHz, $CDCl_3$) δ/ppm = 142.3, 131.4,

131.1, 123.2, 115.0, 69.7, 16.0. IR (cm^{-1}): $\tilde{v}$ = 2980, 2927, 2886, 1905, 1520, 1479, 1442, 1370, 1350, 1265, 1170, 1104, 1042, 999, 935, 894, 873, 809, 689, 668. MS (70 eV, EI) m/z (%) = 434 (23, M$^+$), 409 (25), 407 (44), 405 (22), 381 (54), 380 (18), 379 (100), 378 (14), 377 (47), 300 (30), 298 (28), 191 (16), 189 (11), 109 (11), 61 (12), 45 (11), 43 (70). HRMS for $C_{14}H_{12}O_2Br_2S_2$ (433.8640) found: 433.8649.

Synthesis of 4,8-diethoxybenzo[1,2-b:4,5-b']dithiophene-2,6-diyldiboronic acid (3). In a dry argon flushed Schlenk-flask, equipped with a magnetic stirring bar and septum, 2 (434 mg, 1.00 mmol, 1.0 equiv) was dissolved in tetrahydrofuran (THF) (8 mL) and cooled down to -40 °C. n-BuLi (1.06 mL, 2.5 mmol, 2.5 equiv, 2.35 M in hexane) was added and the resulting solution was stirred for 1.5 h and cooled down to -85 °C. Then, triisopropyl borate (0.69 mL, 3.0 mmol, 3.0 equiv) was added and the reaction mixture was allowed to warm to room temperature and stirred overnight. The solution was diluted with half-concentrated aq NH$_4$Cl solution (25 mL). The alkaline solution was acidified to pH 6 (with 2.0 M HCl) and extracted with a 3:1 THF:diethyl ether mixture (3 × 150 mL). The combined organic layers were dried over Na$_2$SO$_4$. After filtration, the solvents were evaporated *in vacuo*. The crude product was suspended in isohexane (70 mL) and the mixture was stirred at room temperature for 5 h. The precipitate was filtered off and dried *in vacuo.* 3 was obtained as green solid (184 mg, 50%) and was used without further purification. Mp: 271.9 – 274.3 °C. ^{1}H NMR (400 MHz, acetone-*d6*) δ/ppm = 8.14 (s, 2H), 4.39 (q, *J* = 7.2 Hz, 4H), 1.47 (t, *J* = 7.2 Hz, 6H). ^{13}C NMR (75 MHz, acetone-*d6*) δ/ppm = 145.5, 135.1, 134.5, 130.3, 70.4, 16.8. IR (cm^{-1}): $\tilde{v}$ = 3209, 2978, 1532, 1445, 1373, 1344, 1320, 1161, 1084, 1046, 989, 959, 850, 788, 700. HRMS for $C_{14}H_{15}O_6B_2S_2$ (365.0496) found: 365.0501.

COF synthesis. A 25 mL Schott Duran glass bottle with a teflon sealed polybutylene terephthalate cap was equipped with 2,3,6,7,10,11-hexahydroxytriphenylene, HHTP (11 mg, 0.034 mmol) and a total of 0.051 mmol of BDT:BDT-OEt linkers in molar ratios of 1:0, 3:1, 1:1, 1:3, and 0:1. The reaction mixture was suspended in 1.5 mL of a 1:1 (v/v) solution of mesitylene/dioxane and heated for 72 h at 100 °C. Afterwards, the green precipitate was isolated by filtration and dried *in vacuo* for 72 h at 150 °C.

Computational details. The models were defined as periodic supercells containing ten COF layers. MD simulations were performed in the isothermal-isobaric ensemble (at 25 °C and 1 atm), using the Dreiding forcefield as implemented in Forcite Plus and a timestep of 1 fs.[27] This forcefield has been shown to provide high quality descriptions of polythiophenes

in the condensed phase.[28] The average temperature was kept constant using the Andersen thermostat during equilibration and the Nosé-Hoover-Langevin thermostat during production runs. Isotropic pressure was kept constant using the Berendsen barostat. Charges for the periodic COF network were calculated using the QEq scheme.[29] Long range electrostatic and van der Waals interactions were treated via the Ewald summation method, with a 6 Å cutoff on the repulsive contribution to the van der Waals energy. In all dynamics runs, the system was equilibrated for 0.1 ns and results were collected over 10 ns. DFT calculations were performed with CASTEP,[30] using the PBE functional and the D2 dispersion correction as implemented in the DFT-SEDC code.[31-33] We used a plane wave basis set with a 340 eV cutoff and ultrasoft pseudopotentials.[34] k-point sampling was performed with a 1x1x6 Monkhorst-Pack grid.[35]

Characterization. Fourier-transform infrared spectra were measured with a Bruker Equinox 55 equipped with a PIKE MIRacle ATR-unit at room temperature in the scan range 650-4000 cm^{-1}. Nitrogen sorption was measured with 20-25 mg sample using a Quantachrome AUTOSORB-1 station at 77.3 K after degassing the sample for at least 12 h under vacuum at 150 °C. The Brunauer–Emmett–Teller (BET) surface areas were calculated from the adsorption branch in the range of p/p_0 = 0.05-0.13. Pore sizes were calculated with a QSDFT adsorption model of N_2 on carbon (cylindrical, adsorption branch). Powder X-ray diffraction (PXRD) measurements were carried out in reflection mode on a Bruker D8 Discover diffractometer with Ni-filtered Kα-radiation (λ=1.54060 Å) and a position-sensitive detector (LynxEye). Molecular geometry optimization was performed with Accelrys MS Modeling 4.4 using the universal and Dreiding forcefield method. The final hexagonal unit cell was calculated with the geometric parameters from the optimized structure. For the Pawley refinement and simulation of the PXRD patterns the Reflex module was used (a software package implemented in MS Modeling 4.4). Scanning electron microscopy (SEM) was performed on a JEOL 6500F instrument at an acceleration voltage of 2-5 kV. The samples were coated with a thin carbon layer by carbon fiber flash evaporation at high vacuum. Transmission electron microscopy (TEM) data were obtained with a FEI Titan Themis 60-300 microscope at an acceleration voltage of 300 kV. Cross-polarized ^{11}B and ^{13}C solid-state NMR (ssNMR) measurements were performed on a Bruker Avance III-500 spectrometer in a 4 mm ZrO_2 rotor with a spinning rate of 10 kHz. Thermogravimetric analyses (TGA) were recorded on a Netzsch STA 440 C TG/DSC. The measurements proceeded at a heating rate of 10 °C/min up to 900 °C, in a

stream of synthetic air of about 25 mL/min. Hydrolyzed COF ^{1}H NMR solution spectra were recorded on a Bruker Avance III-400 MHz spectrometer. 5 mg of COF powder was dissolved in DMSO-*d6* containing 5% D_2O in every case. A relaxation delay of 8 s was employed to increase the precision of aromatic signal integration.

BDT-OEt COF simulated structures

Molecular mechanics simulations for the BDT-OEt COF unit cell were carried out using Materials Studio software 4.4 and the Forcite module. First, we constructed a bare hexagonal *P*6 space group unit cell with lattice parameters reported for the BDT-COF. Based on the functional groups and the geometry of the BDT-OEt COF precursor molecules, the repeating unit was constructed and placed in the bare hexagonal unit cell to obtain the complete unit cell. The geometry of the BDT-OEt COF layer was optimized in the unit cell using the Dreiding forcefield and the QEq correction for weak interactions. The Reflex package in the Materials Studio software allows for Pawley refinement for the simulated unit cell parameters according to the experimental PXRD. The simulated unit cell parameters were refined against the experimental PXRD. The refinement parameters R_p and R_{wp} are 3.37% and 4.95%, respectively, the final unit cell parameters are a = b = 36.56±0.04 Å, c = 3.65±0.04 Å.

Table S3.1. Refined crystal data.

Formula	$C_{78} O_{18} B_6 S_6 H_{48}$
Formula weight	1530.49 g/mol
Crystal system	Hexagonal
Space group	*P*6
Unit cell dimensions	a = b = 36.56 Å c = 3.65 Å
Cell Volume	4234.14 Å^3

Table S2. Fractional atomic coordinates.

Atom	Wyck.	x	y	z
C1	6d	0.58577	0.36594	0.44433
C2	6d	0.58777	0.32954	0.44062
C3	6d	0.49211	0.45890	0.47547
C4	6d	0.56198	0.47912	0.46663
C5	6d	0.54195	0.53395	0.48791
C6	6d	0.66044	0.40711	0.44743
C7	6d	0.62166	0.40426	0.44828
O8	6d	0.55181	0.37005	0.44579
B9	6d	0.56817	0.41435	0.45221
O10	6d	0.61299	0.43536	0.45323
C11	6d	0.54370	0.43609	0.45827
C12	6d	0.53300	0.49234	0.47430
S13	6d	0.48972	0.41092	0.45743
C14	6d	0.66425	0.37067	0.44362
C15	6d	0.62683	0.33073	0.44244
H16	6d	0.55974	0.30310	0.43696
H17	6d	0.59341	0.49907	0.46773
H18	6d	0.68480	0.43656	0.45058
O19	6d	0.58285	0.56389	0.51939
C20	6d	0.60015	0.60358	0.69692
C21	6d	0.64333	0.61313	0.83124
H22	6d	0.58033	0.60202	0.92893
H23	6d	0.60269	0.62792	0.50983
H24	6d	0.66339	0.61603	0.59942
H25	6d	0.63977	0.58737	1.00418
H26	6d	0.65821	0.64193	0.99045
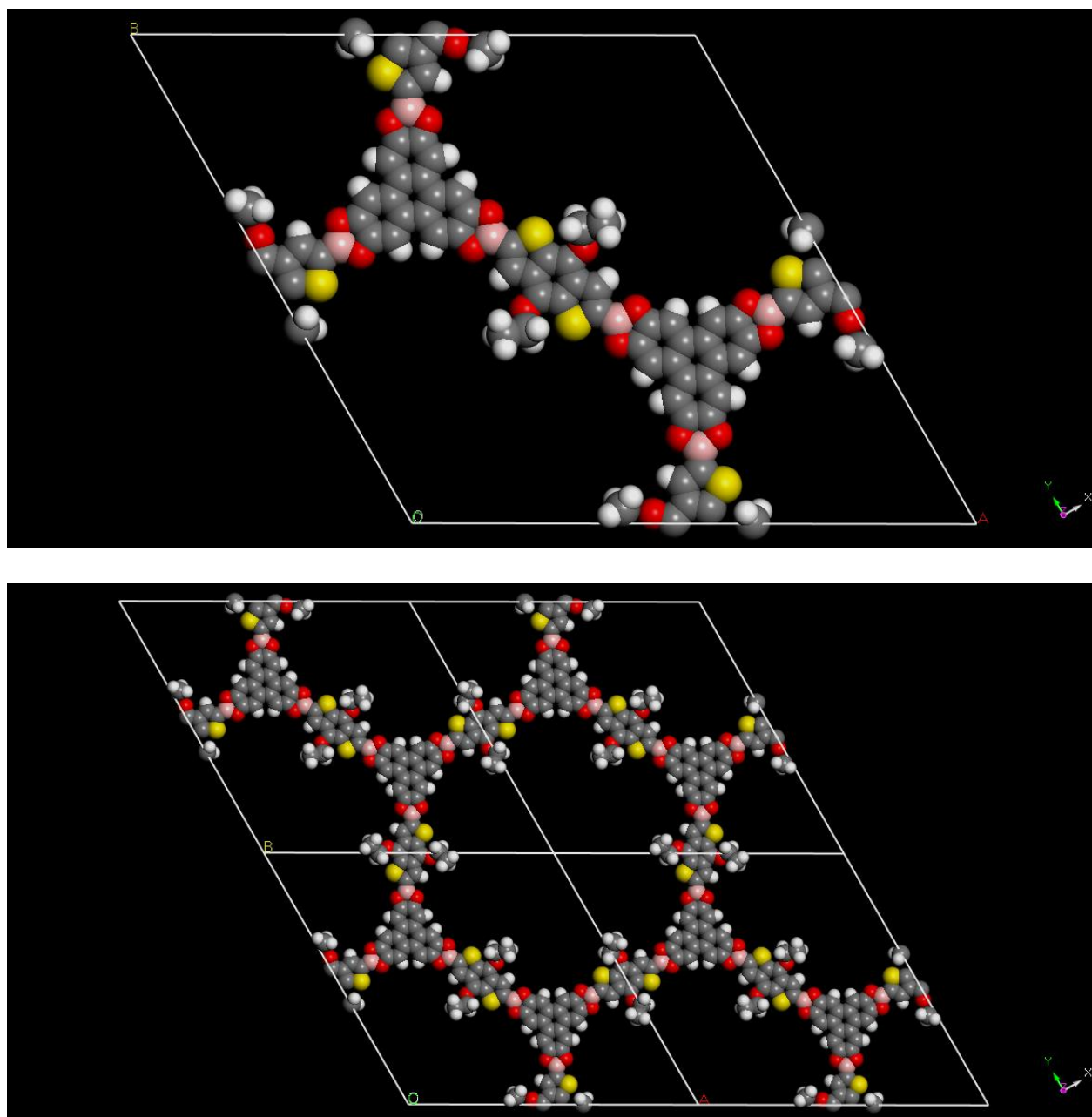
Figure S3.1. Simulation of BDT-OEt COF unit cells calculated in an eclipsed arrangement in the P6 space group. Top: top view on ab plane, bottom: four BDT-OEt COF unit cells fused to form the hexagonal pore.
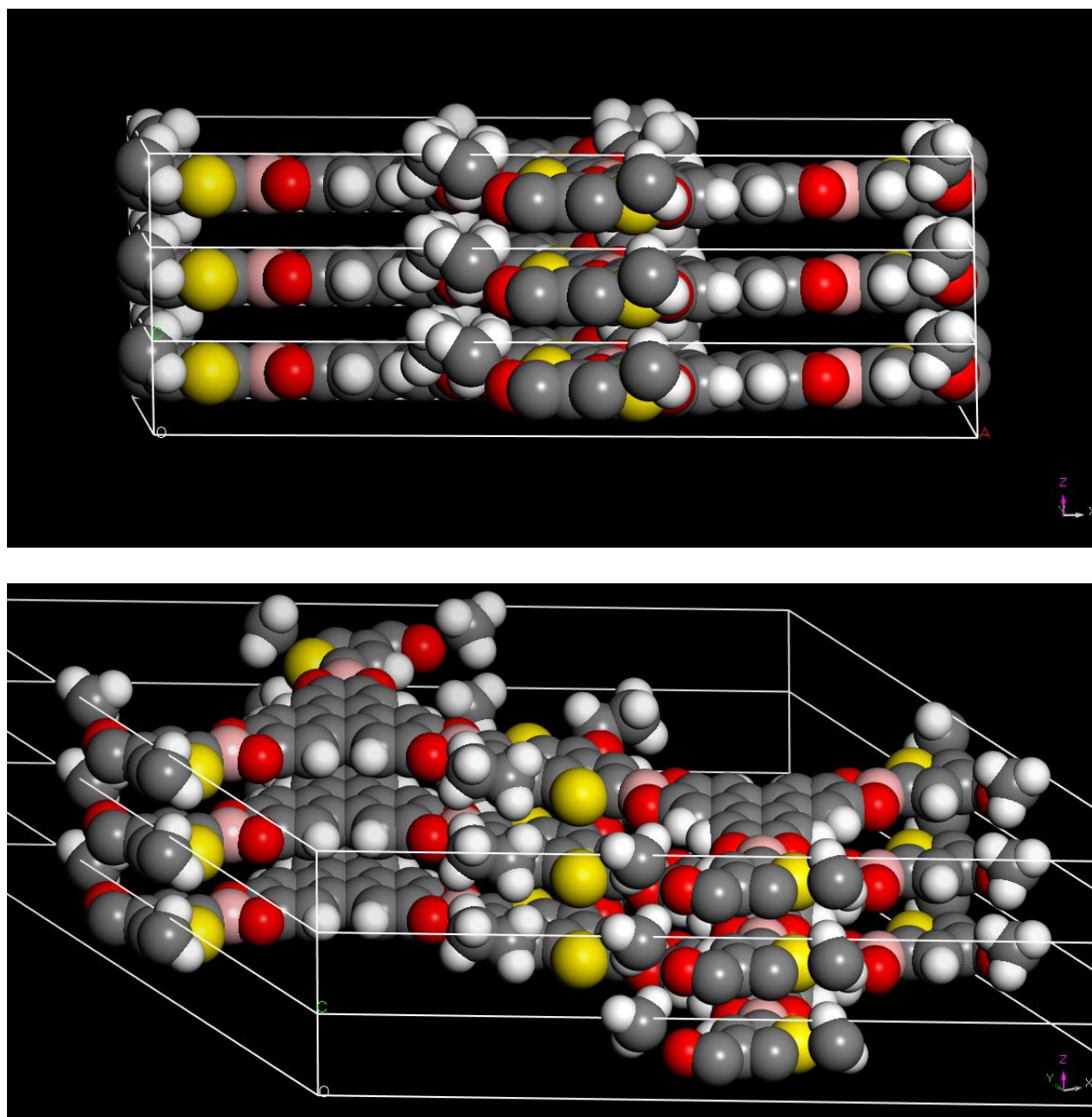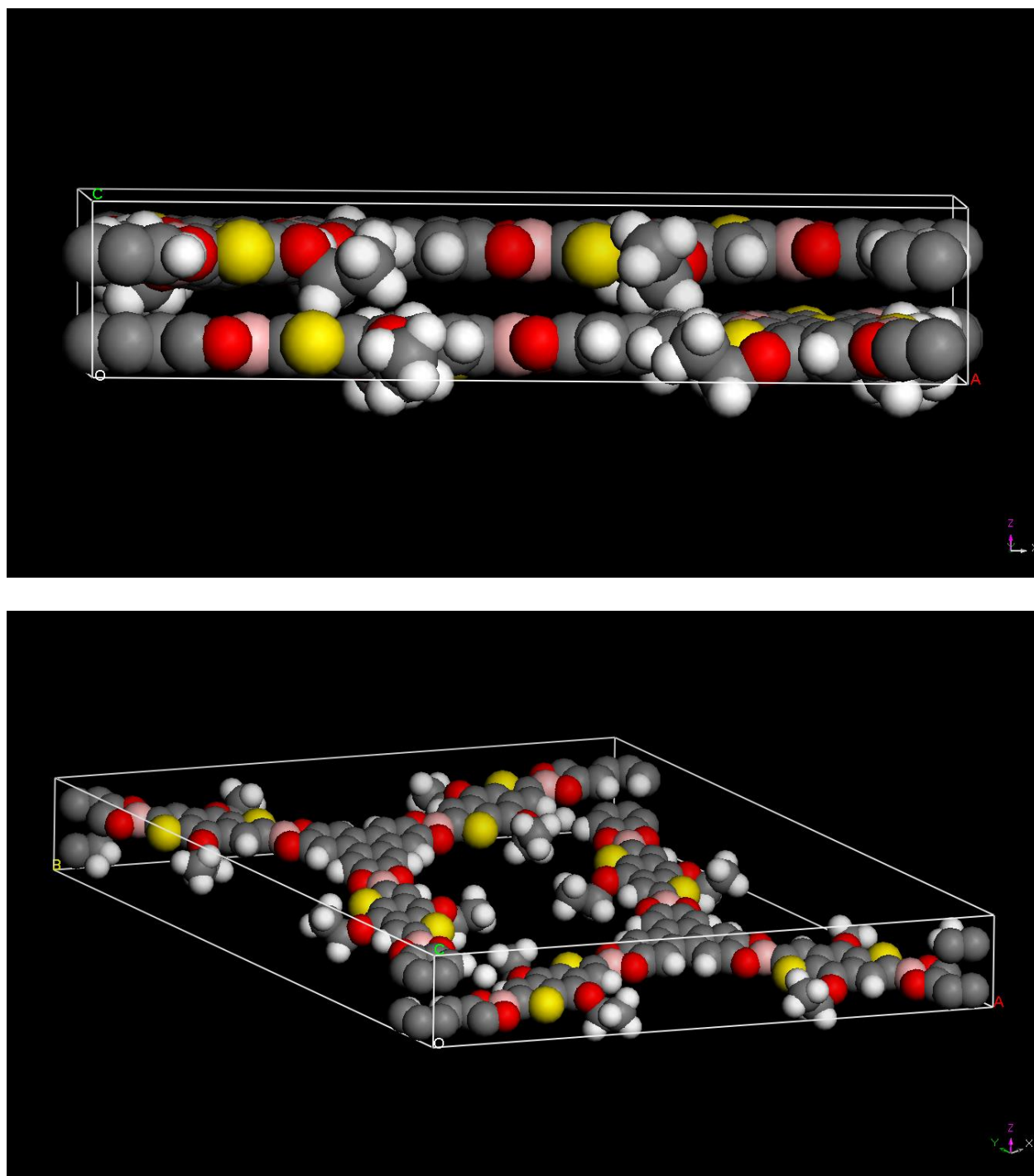
Figure S3.2. Simulation of BDT-OEt COF unit cell in an eclipsed arrangement in the P6 space group viewed along the c-axis with an interlayer distance of 3.65 Å.
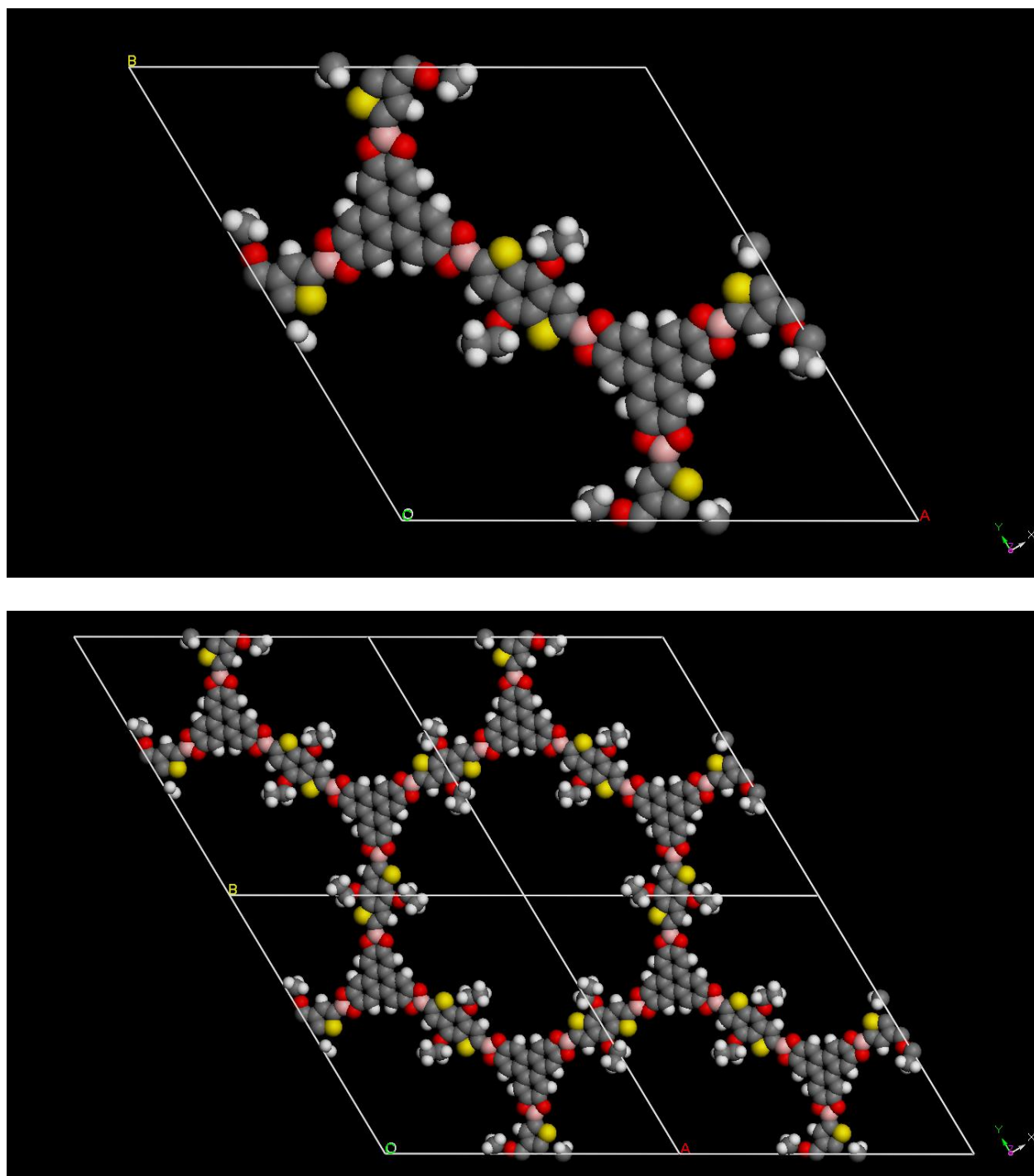
Figure S3.3. Simulation of BDT-OEt COF unit cells calculated in an eclipsed arrangement in the P1 space group. Top: top view on ab plane, bottom: four BDT-OEt COF unit cells fused to form the hexagonal pore.
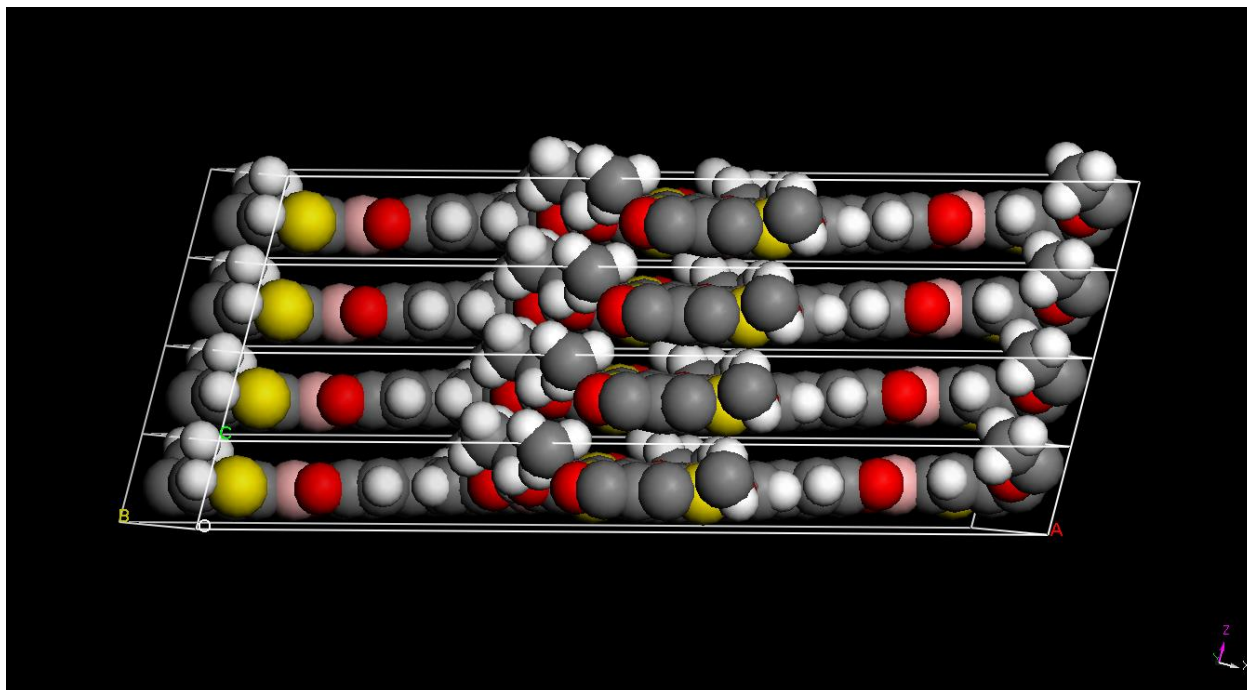
Figure S3.4. Simulation of the BDT-OEt COF unit cell in the P1 space group viewed along the c-axis.
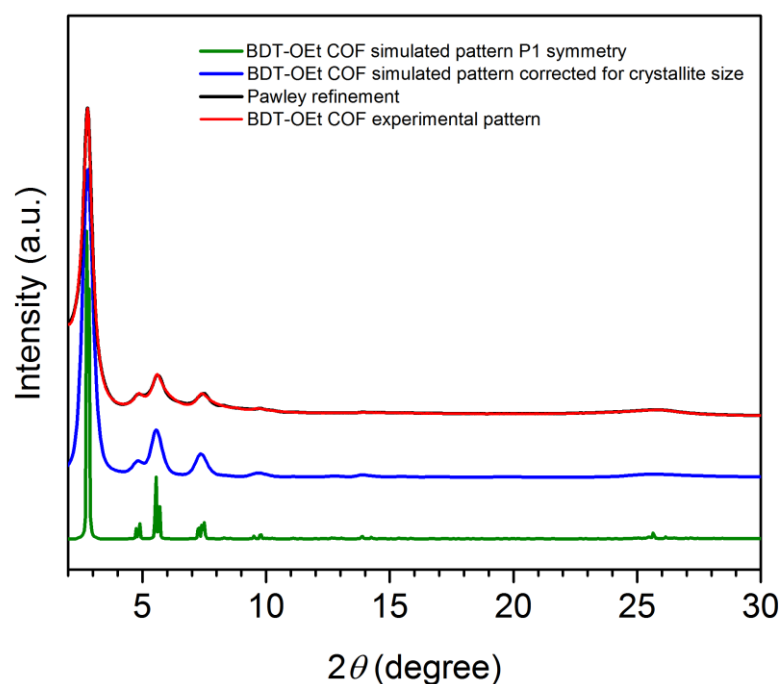
Figure S3.5. XRD patterns of BDT-OEt COF in P1 space group: experimental (red), Pawley refinement (black), simulated pattern corrected for crystallite size (blue), and simulated pattern (green). For Pawley refinement: The refinement parameters Rp and Rwp are 2.87% and 2.16%, respectively, the refined unit cell parameters are a = 37.15Å±0.04, b = 37.17 ±0.04 Å, c = 3.58±0.04 Å; α=90.31°, β=77.44°, γ =120.35°.
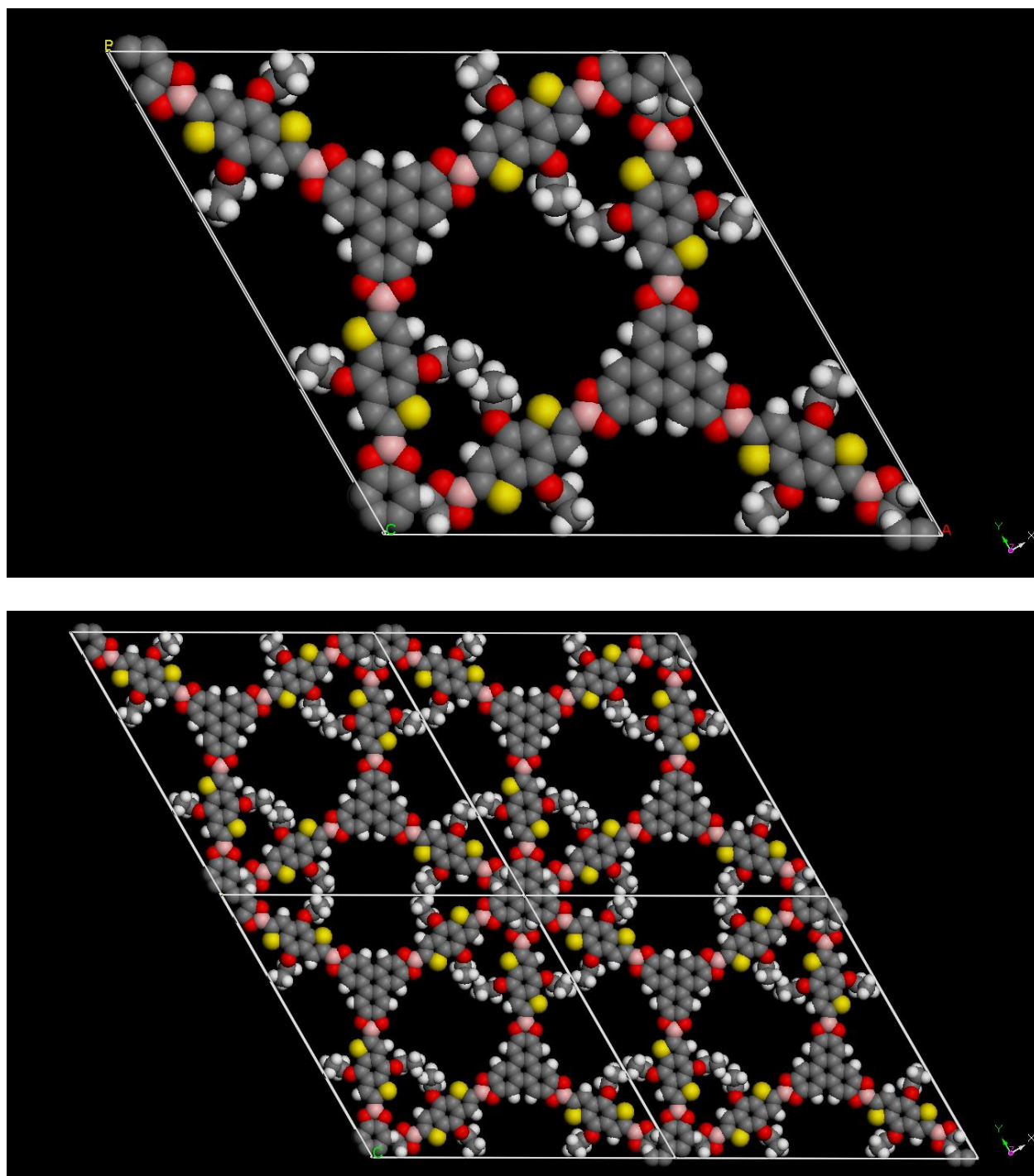
Figure S3.6. Simulation of BDT-OEt COF unit cells calculated in a staggered arrangement with P6$_3$ space group. Top: top view on ab plane, bottom four BDT-OEt COF unit cells fused to form the pore system.

Figure S3.7. Simulation of the BDT-OEt COF unit cell in a staggered arrangement, viewed along the c-axis.
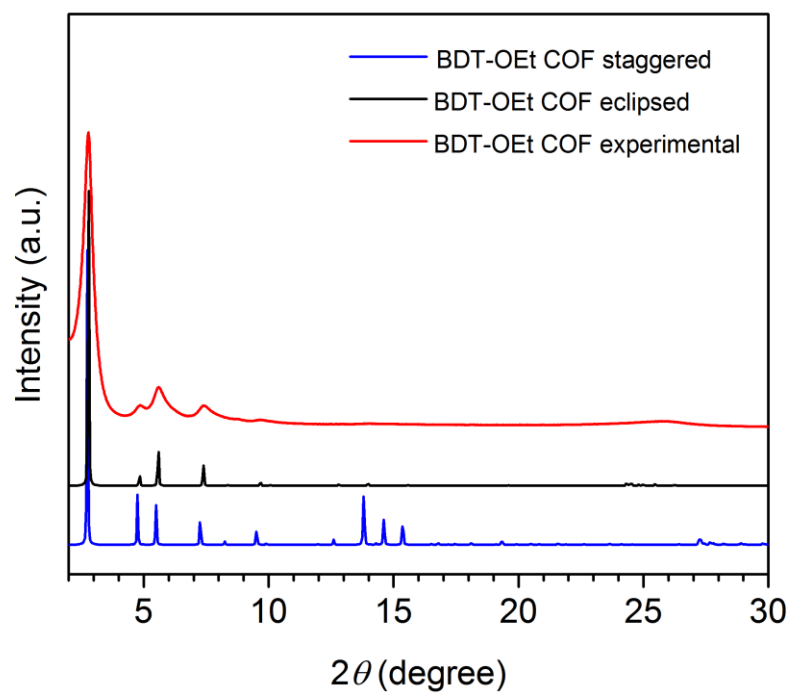
Figure S3.8. XRD patterns of BDT-OEt COF: experimental (red), simulated AA eclipsed arrangement (black), and simulated AB staggered arrangement (blue).
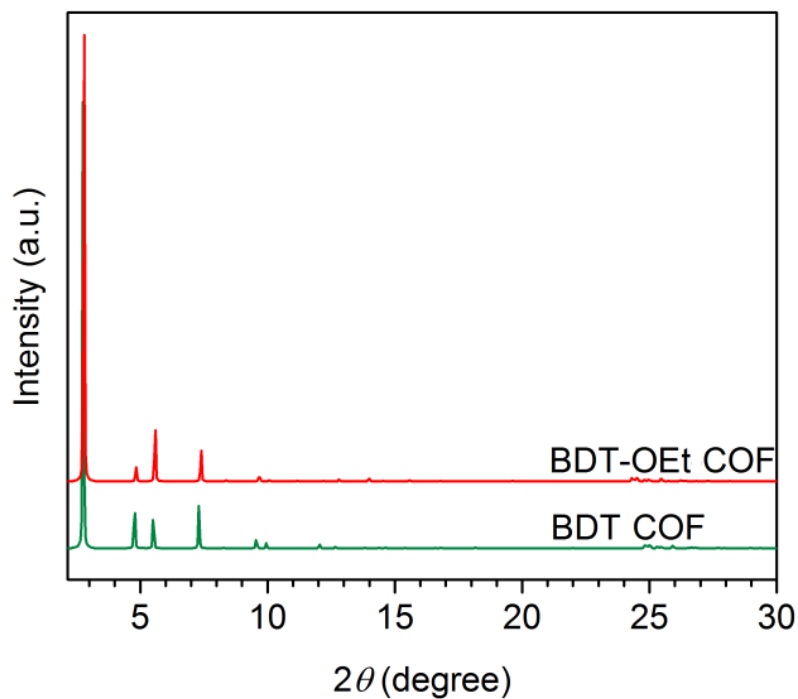
Figure S3.9. Comparison of simulated XRD patterns of BDT COF (green) and BDT-OEt COF (red).

Molecular dynamics simulations
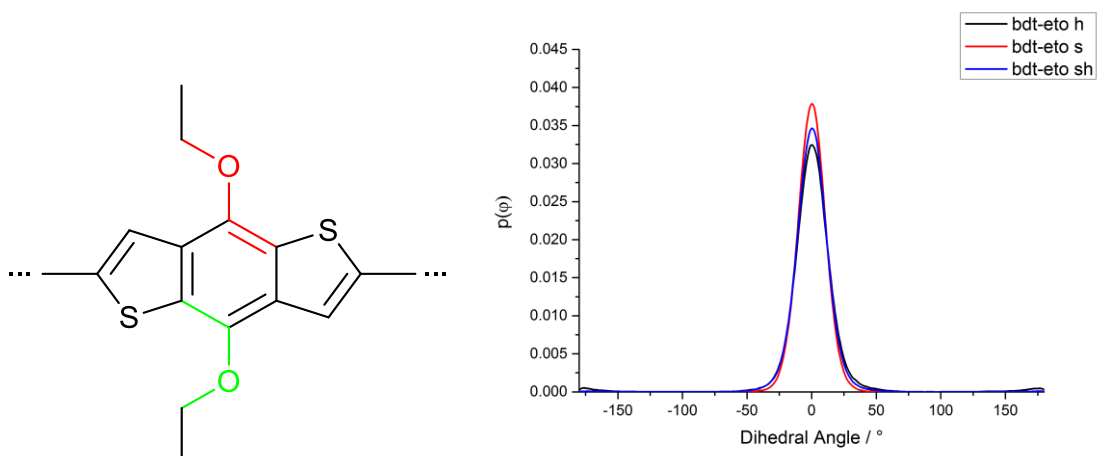
Figure S3.10. Left: Molecular structure of the ethoxy-substituted BDT unit. The possible initial orientations for the dihedral angle are shown in red (facing hydrogen, 180°) and green (facing sulfur, 0°). Right: Probability distribution of the dihedral angle sampled over 10 ns. Almost all dihedrals reorient to face the sulfur atom within the equilibration period of 0.1 ns, independent of the starting orientation (s = sulfur, h = hydrogen, sh = mixed).
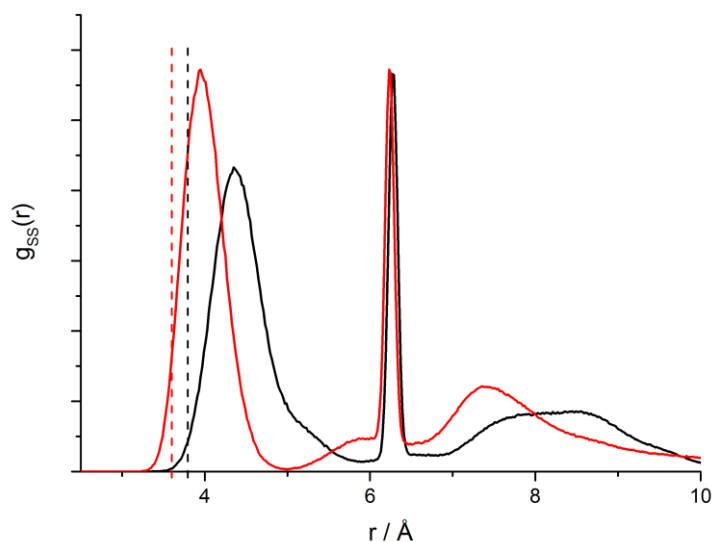
Figure S3.11. Sulfur-sulfur radial distribution functions of the ethoxy substituted (black) and pristine (red) BDT-COF. The vertical, dotted lines indicate the respective average interlayer distance.

Nitrogen sorption
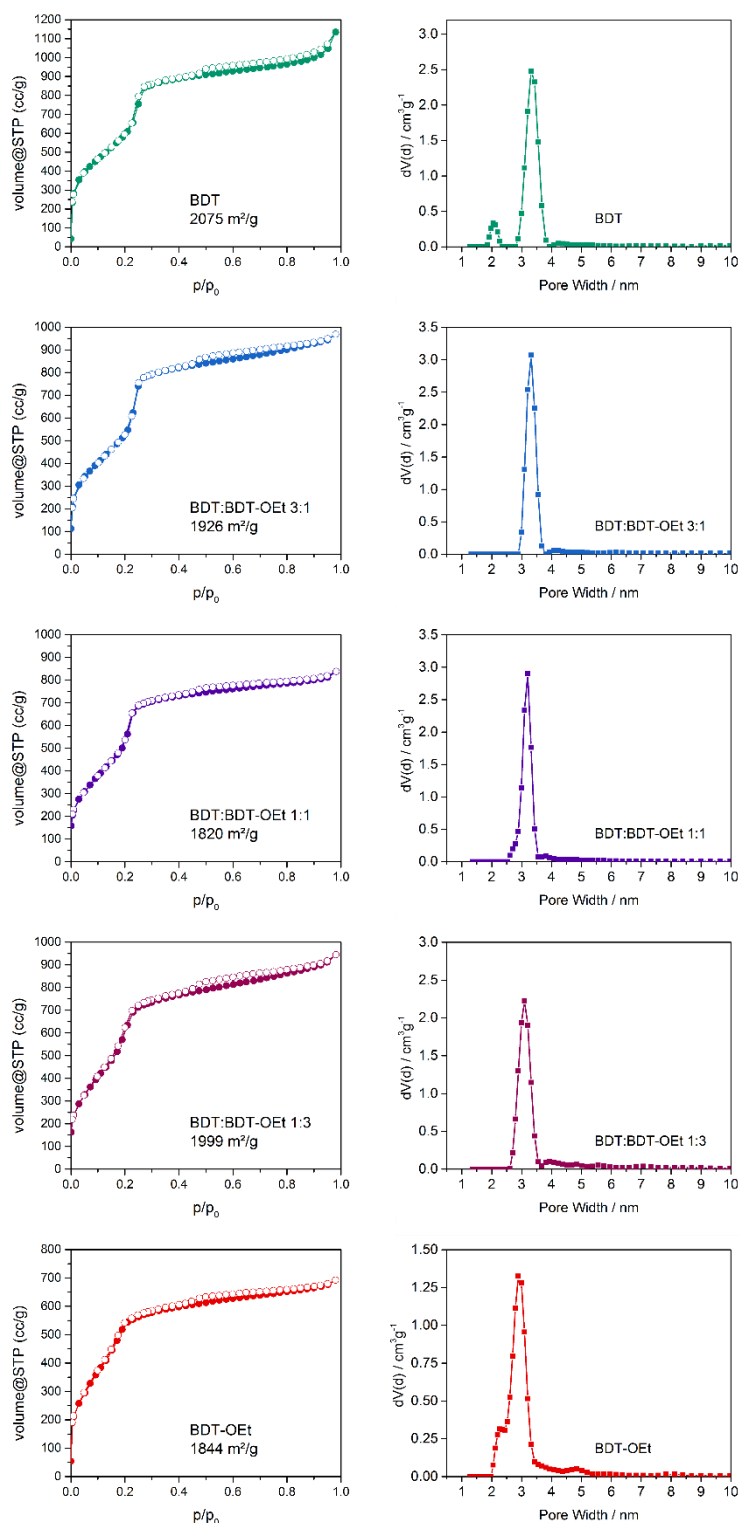
Figure S3.12. Nitrogen sorption isotherms of the COF powders (left) and pore size distributions (right).

SEM micrographs
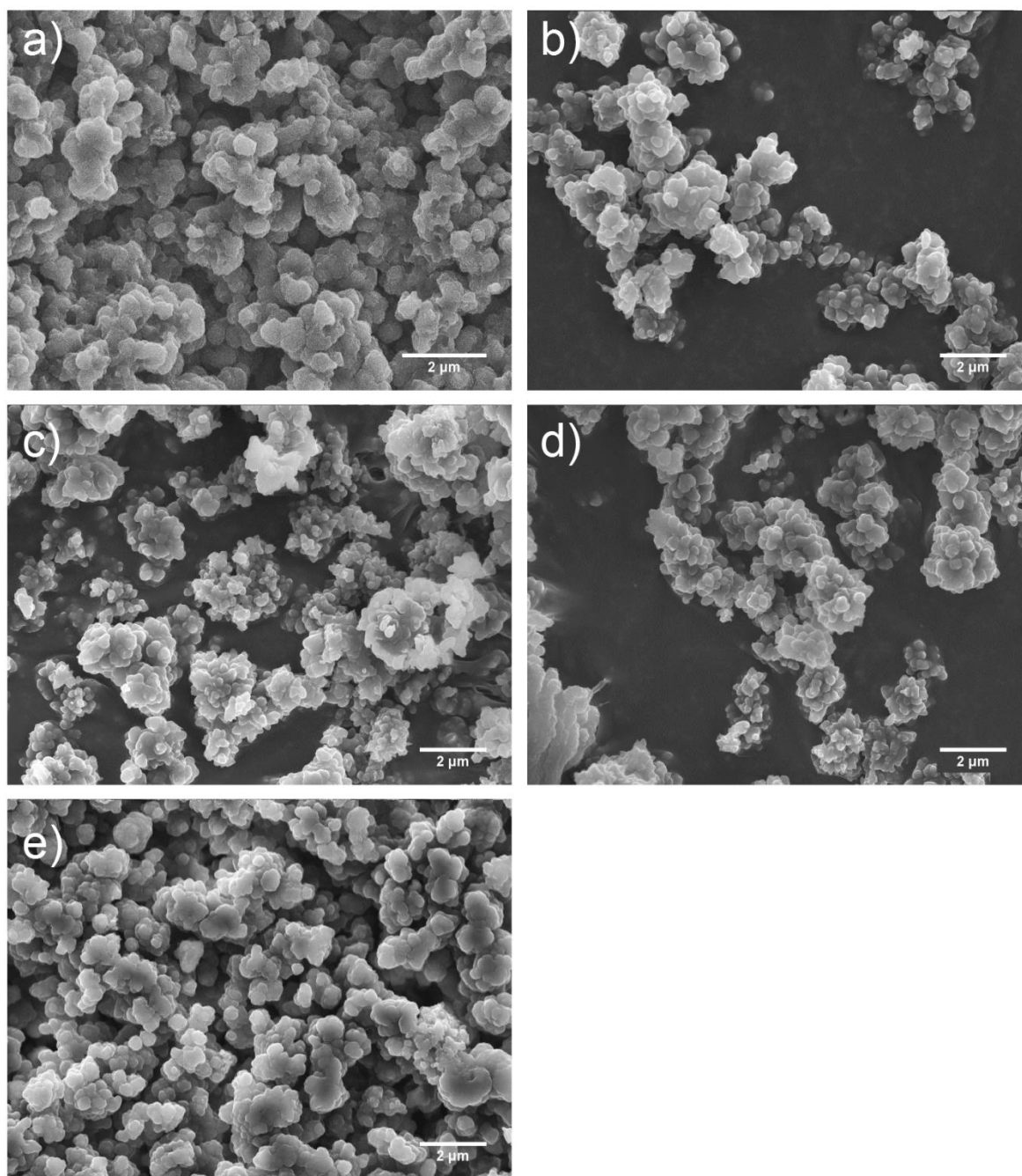
Figure S3.13. SEM micrographs of (a) BDT COF, (b) BDT:BDT-OEt 3:1 COF, (c) BDT:BDT-OEt 1:1 COF, (d) BDT:BDT-OEt 1:3 COF, (e) BDT-OEt COF, respectively.
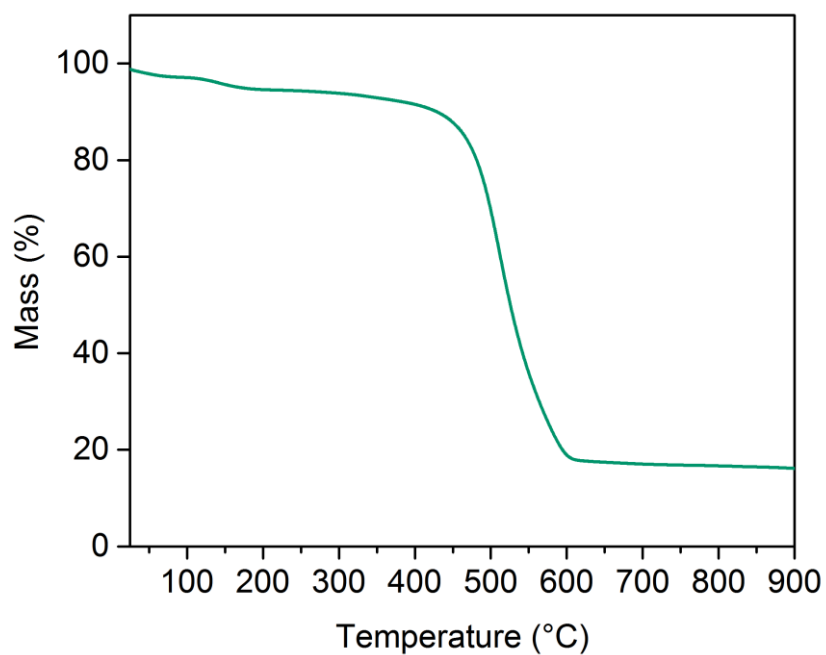
TEM micrographs
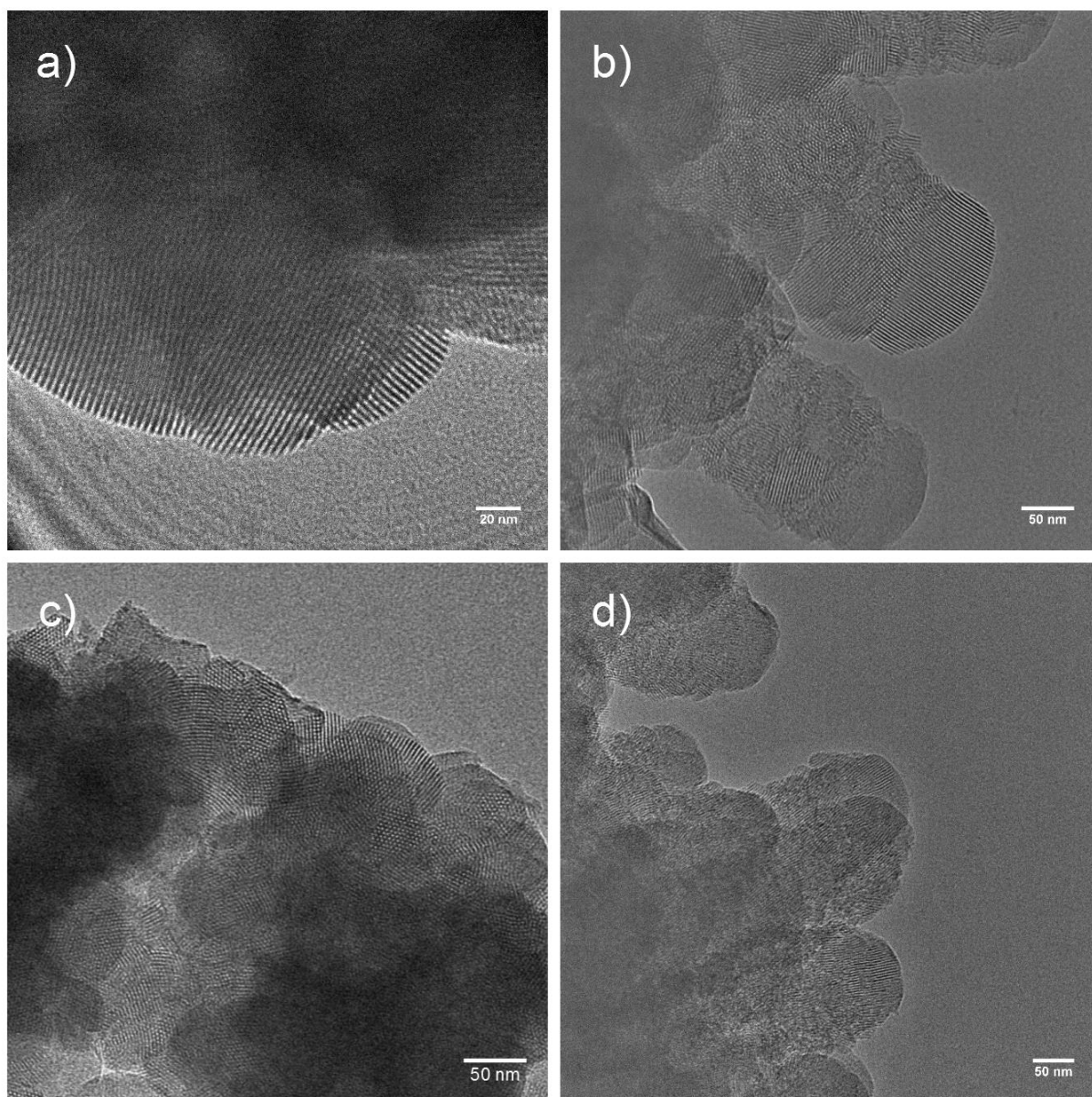
Figure S3.14. TEM micrographs of (a) BDT COF, (b) BDT:BDT-OEt 3:1 COF, (c) BDT:BDT-OEt 1:1 COF, (d) BDT:BDT-OEt 1:3 COF, respectively.

Thermogravimetric analysis

Figure S3.15. TGA trace of BDT COF.
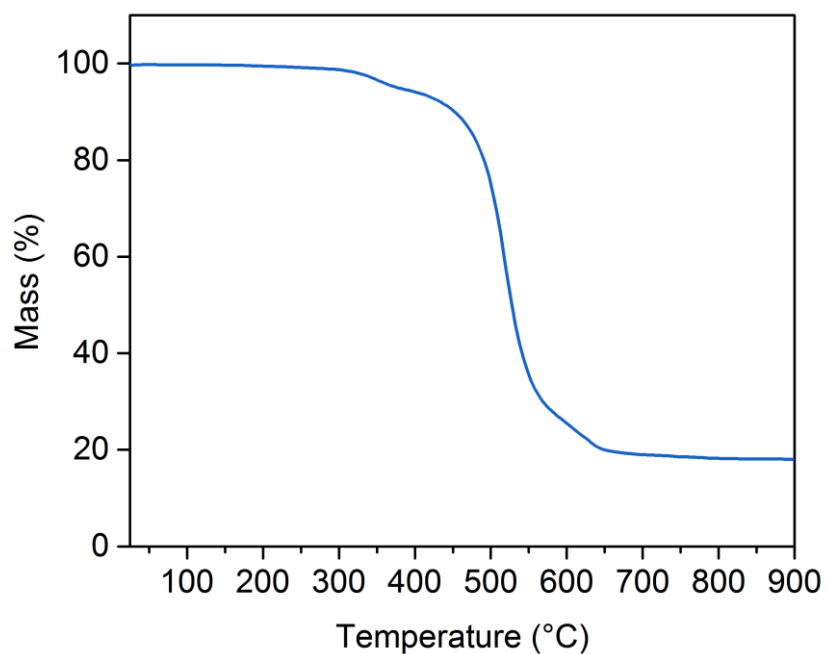
Figure S3.16. TGA trace of BDT:BDT-OEt 3:1 COF.
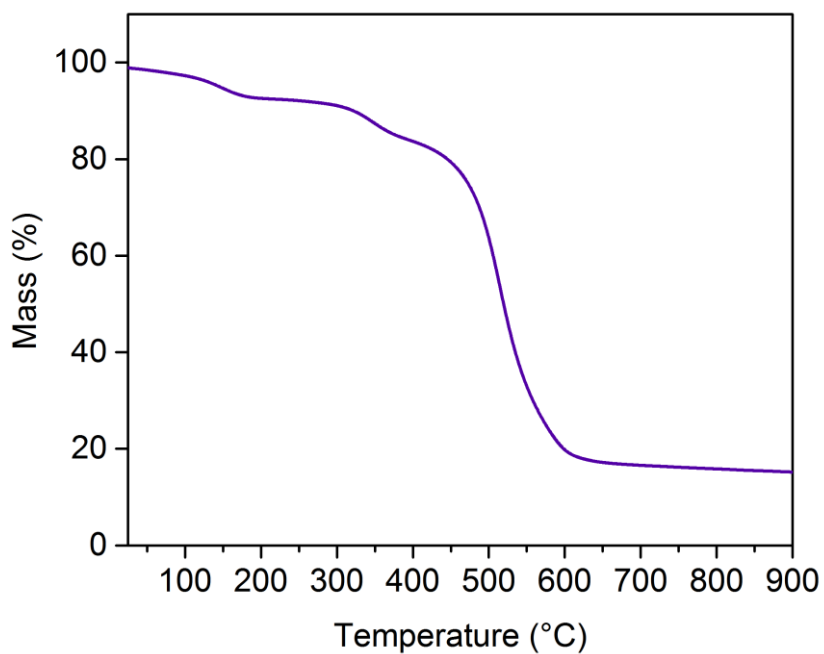
Figure S3.17. TGA trace of BDT:BDT-OEt 1:1 COF.
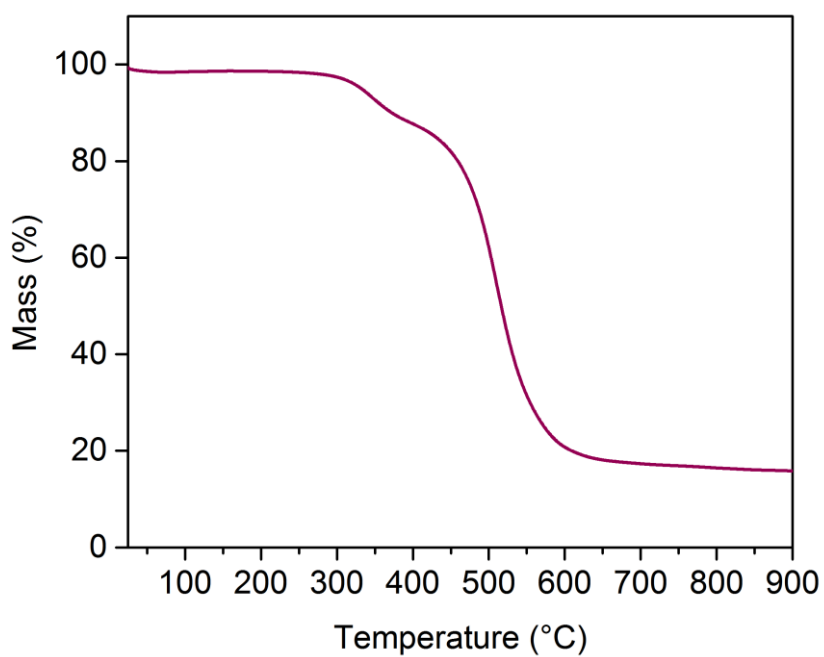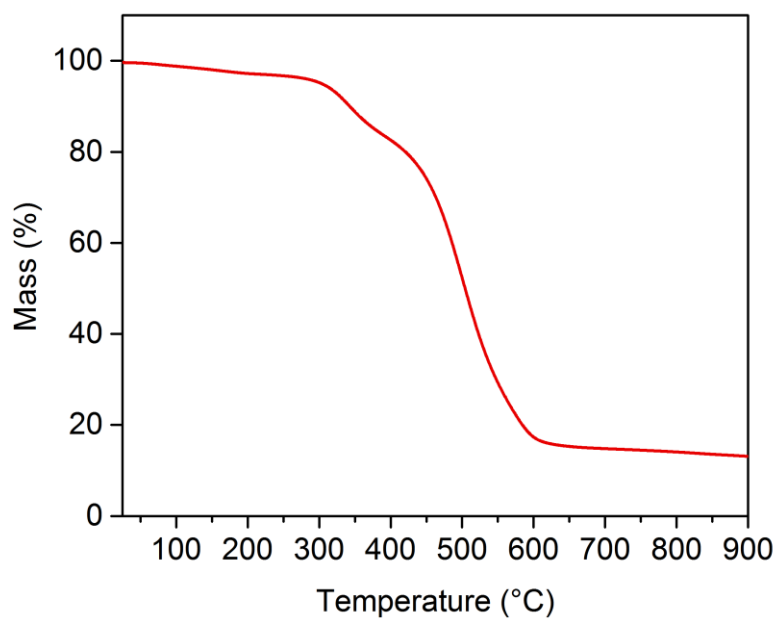

Figure S3.18. TGA trace of BDT:BDT-OEt 1:3 COF.

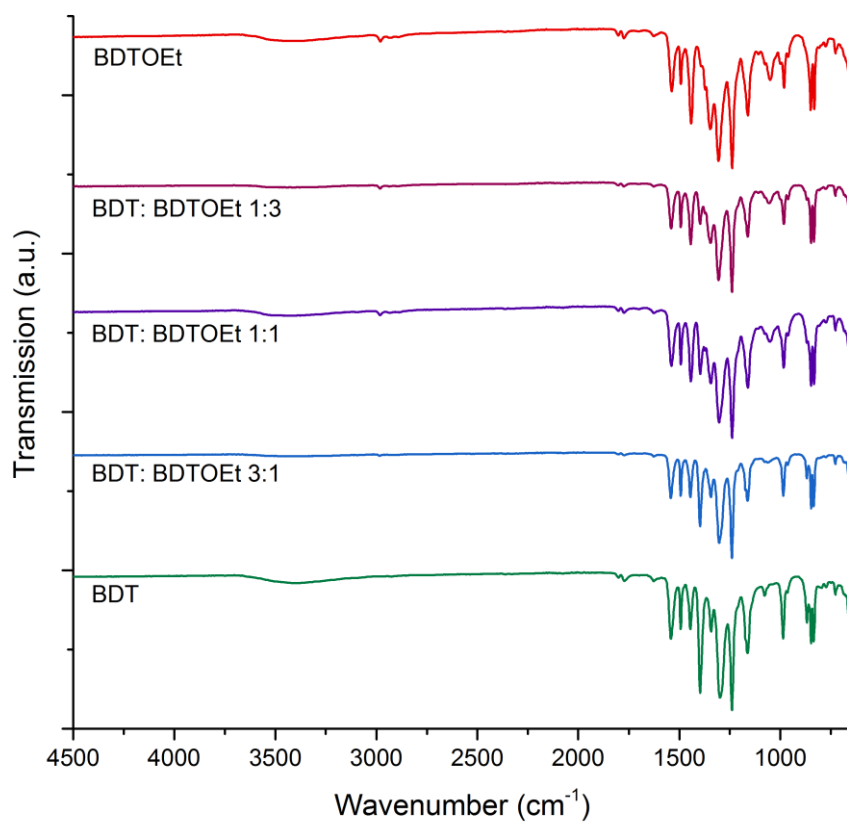Figure S3.19. TGA trace of BDT-OEt COF.

FT-IR spectra

Figure S3.20. FT-IR plots of BDT COF, BDT:BDT-OEt COFs and BDT-OEt COF.
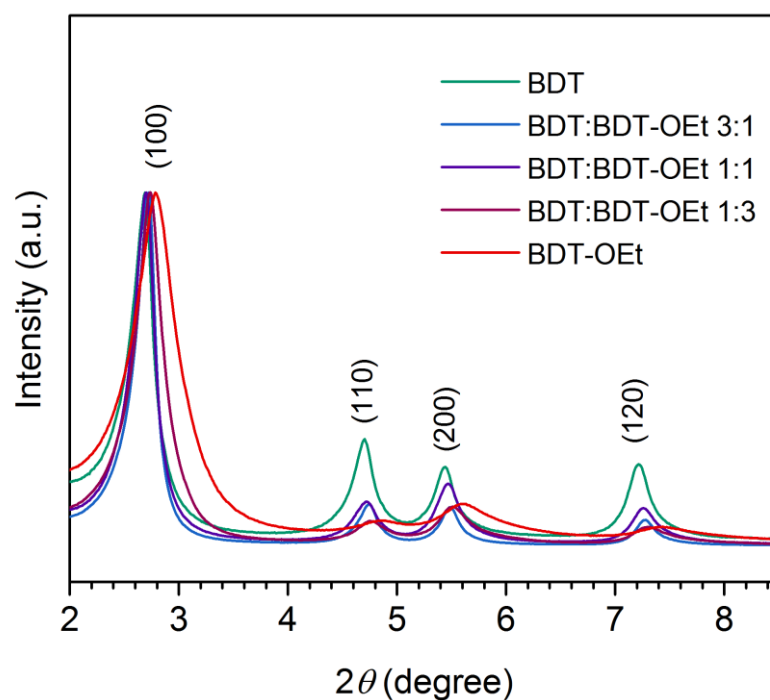
PXRD small angle region

Figure S3.21. PXRD patterns of BDT COF, BDT:BDT-OEt COFs, and BDT-OEt COF: small angle region showing a gradual shift of the reflections corresponding to the ab plane to higher 2 theta values with the higher integrated fraction of BDT-OEt building units.

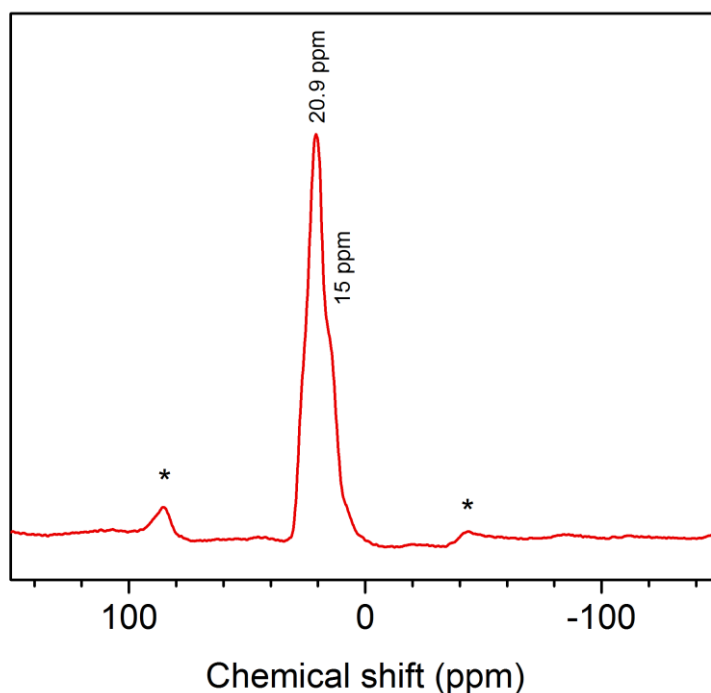### Solid state NMR spectra of BDT-OEt COF

Figure S3.22. ^{11}B ssNMR spectrum of BDT-OEt COF showing a boronic ester peak at 20.9 ppm. The shoulder peak at 15 ppm is attributed to free boronic acid groups present as terminal moieties of the framework. Asterisks indicate spinning side bands.
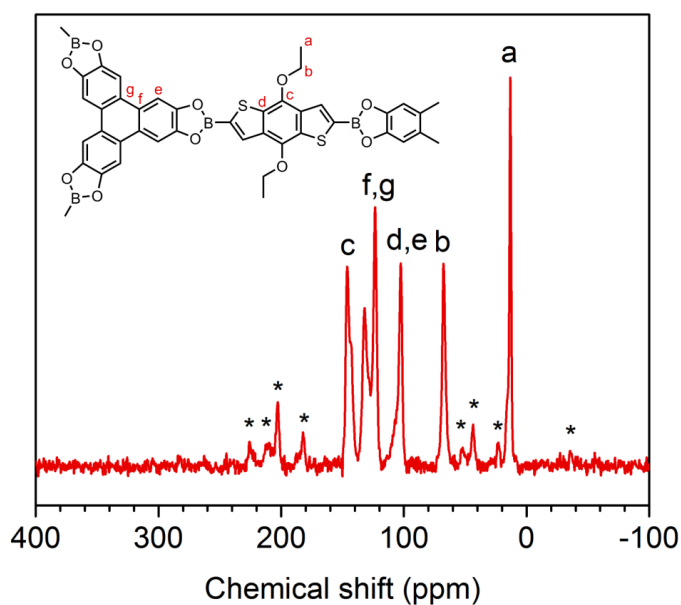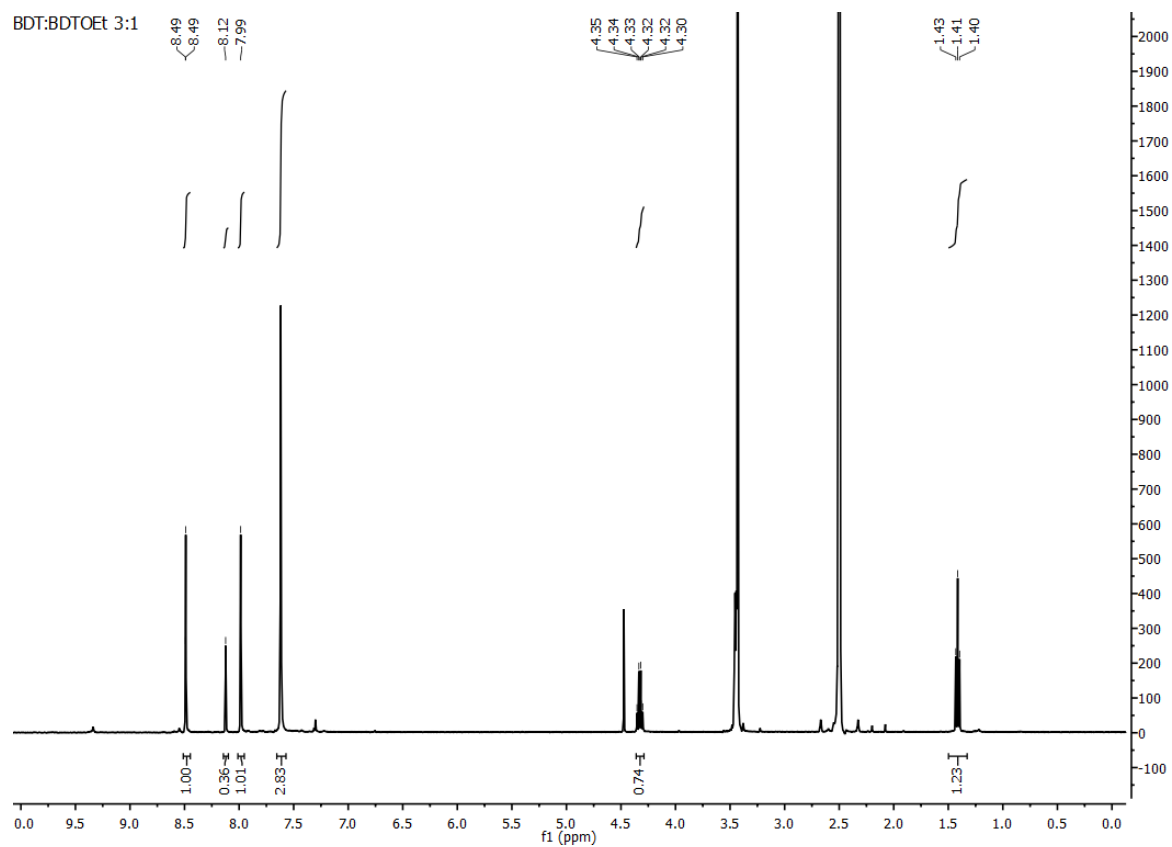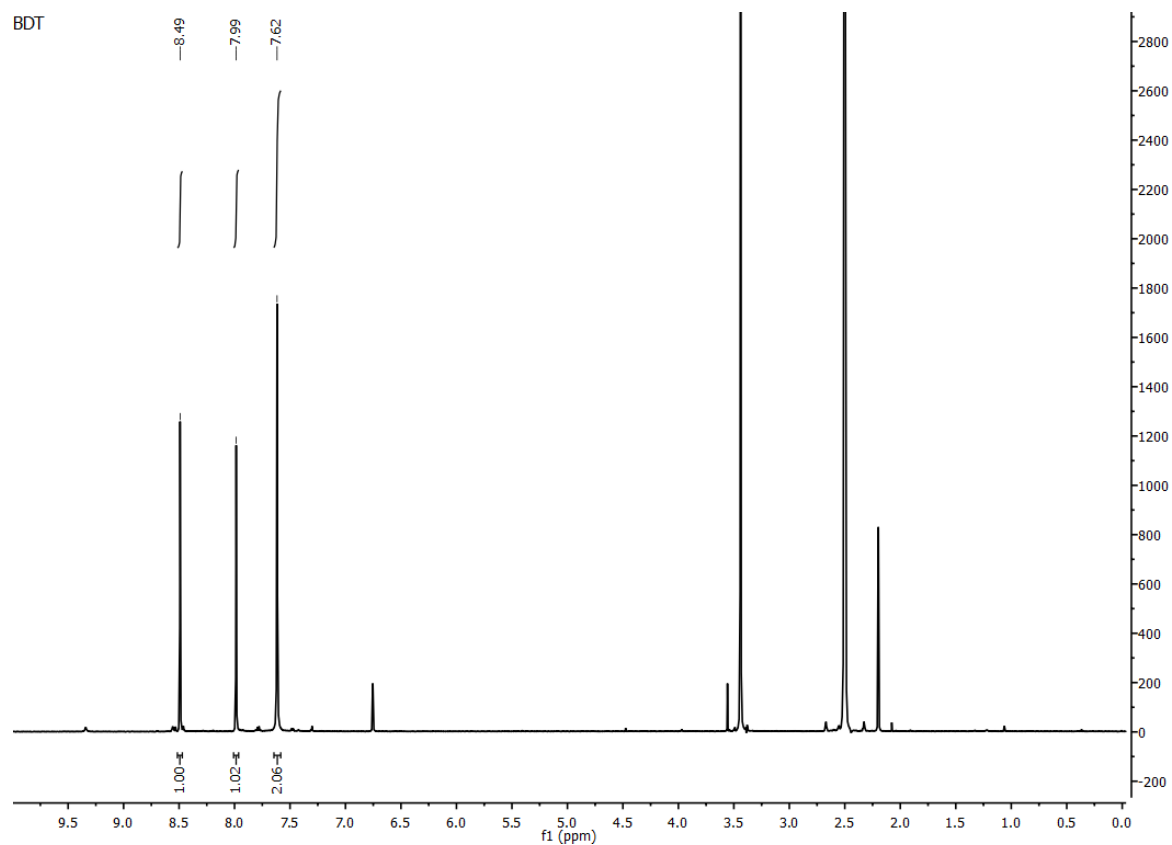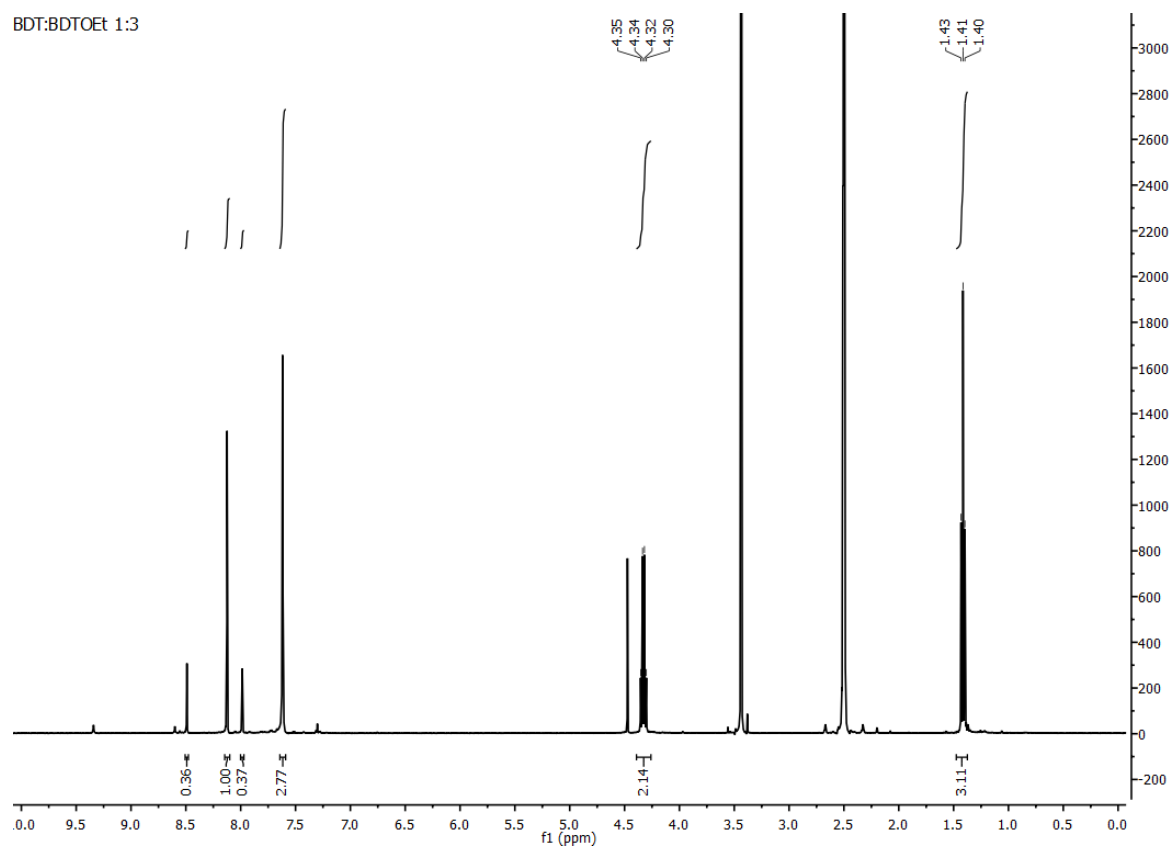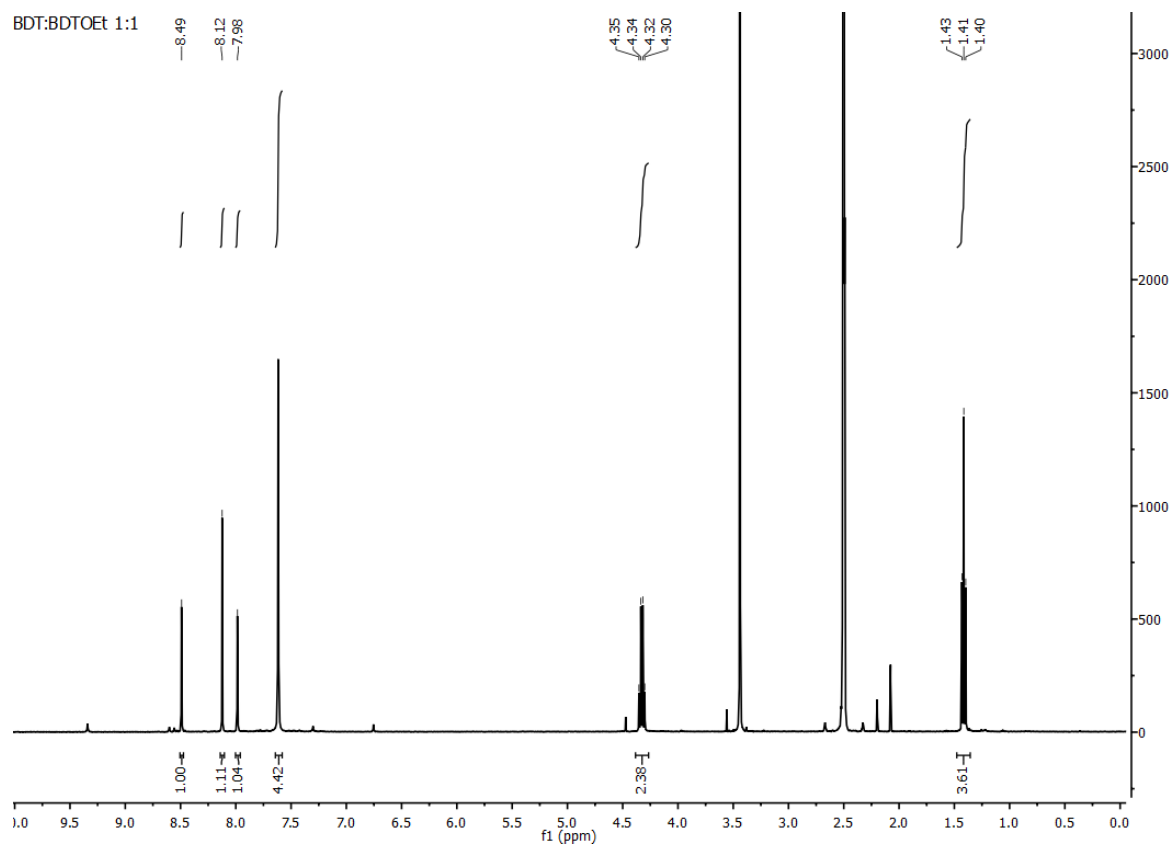

Figure S3.23. 13C ssNMR spectrum of BDT-OEt COF. Asterisks indicate spinning side bands.

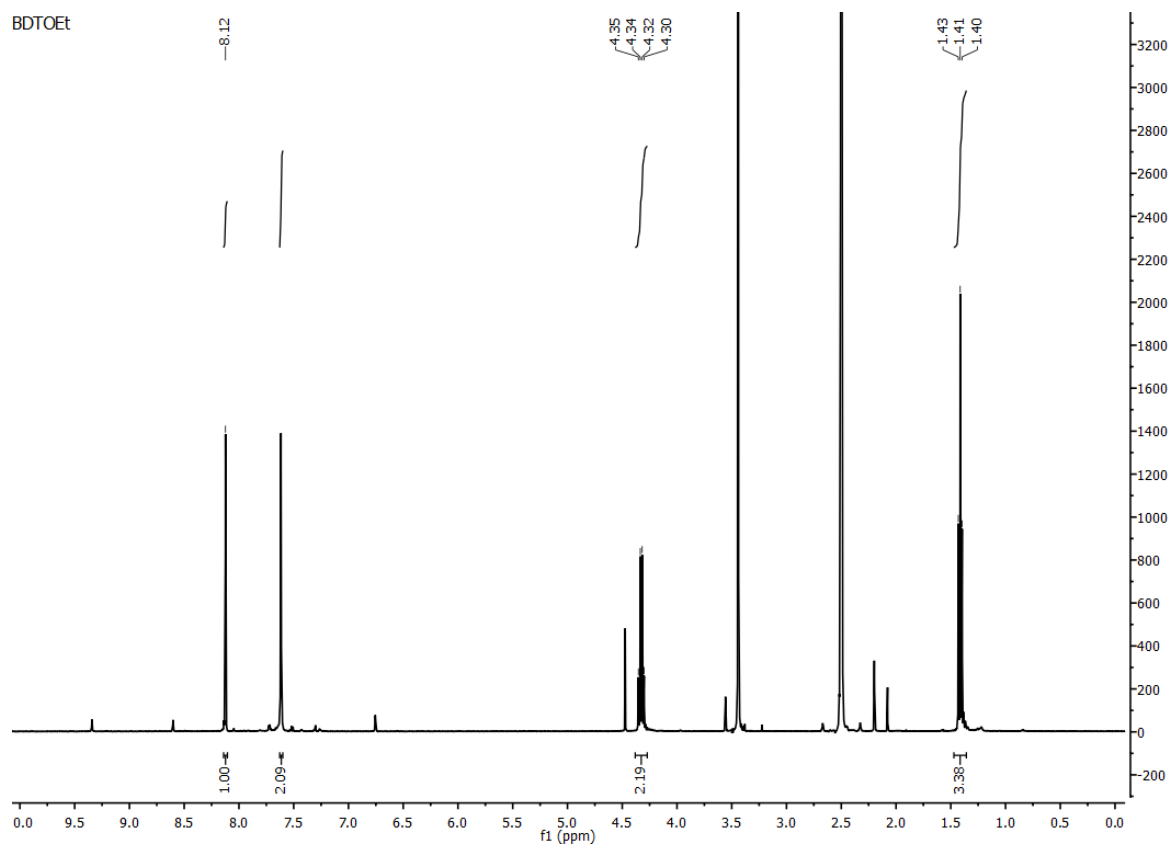## NMR spectra of hydrolysed COFs

BDT:BDTOEt 1:1

BDT:BDTOEt 1:3

BDTOEt

4. Covalent Organic Framework Films through Electrophoretic Deposition - Creating Efficient Morphologies for Catalysis

This chapter is based on the following publication:

4.1. Abstract

The ability to grow covalent organic framework (COF) films allows for studying their properties as solid layers and enables the incorporation of these materials into a variety of functional devices. Here, we report on the fabrication of COF films and coatings by electrophoretic deposition (EPD). We demonstrate that the EPD technique is suitable for depositing COFs featuring two- and three-dimensional structures linked by imine- or boronate ester-bonds, namely BDT-ETTA COF, COF-300 and COF-5. For the deposition, COF nanoparticle suspensions are prepared by dispersing the as-synthesized bulk materials in solvents with low dielectric constants. Subsequently, two electrodes are immersed into the COF particle suspensions and upon inducing electric fields ranging from 100-900 V cm^{-1}, COFs are deposited as films on the positively charged electrode. Through EPD, within two minutes, large-area films of up to 25 cm^2 are obtained on both smooth and corrugated surfaces. COF films prepared by EPD feature an inherent textural porosity and tunable thickness, demonstrated from 400 nm to 24 μm. By governing the deposition parameters such as duration, particle concentration and applied potential, deposits of precise thickness can be produced. Furthermore, co-depositions of several different COFs as well as COF/Pt nanoparticle suspensions are demonstrated. The film morphologies obtained by EPD are shown to be advantageous for catalysis, as demonstrated for sacrificial agent free photoelectrochemical water reduction. Here, BDT-ETTA COF photocathodes show a drastic increased photocurrent density compared to the respective dense and oriented surface-grown films. Typical BDT-ETTA COF/Pt nanoparticle hybrid films exhibit

photocurrent densities of over 100 μA cm^{-2}. The rapid and highly scalable deposition of COF particles as films and coatings through EPD is a versatile addition to the toolbox of COF film fabrication techniques, allowing for the tailoring of COF film architectures for desired functionalities.

4.2.   Introduction

Covalent organic frameworks (COFs) are a novel class of ordered, light-weight organic polymers exhibiting great structural and chemical diversity. COFs are constructed by connecting rigid molecular organic building blocks through condensation polymerization reactions under slightly reversible conditions. Depending on the geometry of the respective COF building blocks, COFs form 2D or 3D porous solids, featuring long-range order, permanent porosity and high surface areas.[1,2] Due to their structural and chemical versatility, COFs have been examined for various applications, such as gas storage,[3] separation,[4–6] catalysis,[7–12] photovoltaics and optoelectronics[13–15] or energy storage.[16–19]

The deposition of COFs onto surfaces as homogenous coatings or as thin films is an important step towards the incorporation of this novel class of materials into a variety of functional platforms.[20] Commonly, COFs are synthesized under solvothermal conditions and precipitate as intergrown nanocrystalline bulk materials, which are difficult to process and to convert into high-quality COF films on surfaces.[21] Exploring routes for processing COF powders and developing techniques which allow for the direct deposition of COFs on substrates as films is hence of great importance. To date, the growth of thin COF films onto surfaces is based mainly on "bottom-up" approaches where the substrates are exposed to a reactive precursor solution. Oriented thin COF films, featuring open channels orthogonal to the substrate surface, are accessible by this so-called *in-situ* approach, where COF powders and films are often forming simultaneously. However, this approach provides limited control over the resulting film thickness.[22–24] In this context, a continuous flow setup was reported, which allowed for a finer tuning of film thickness.[25] A major drawback of the *in-situ* approach is the overall low synthesis yield, defined by the mass ratio of the deposited COF material and the COF bulk precipitate. Facing this challenge, we developed the vapor-assisted conversion (VAC) approach for the deposition of boronate-ester COFs as films exclusively on surfaces. In contrast to the *in-situ* approach, in VAC, precursors in a thin precursor solution layer react to form a COF film on a surface.

This allows for control over the film thickness and morphology, ranging from dense thin films to thick coatings consisting of intergrown particles and interstitial voids.[26] For applications such as catalysis, COF films featuring additional textural porosity and a large interface can be highly beneficial for rapid diffusion of reactants and products in and out of the film and thereby enhancing the catalytic performance.[27] However, a rapid fabrication of such film morphologies applicable to the different COF types in high yields is still lacking.

Electrophoretic deposition (EPD) is an efficient method for the deposition of particles bearing an intrinsic surface charge on an electrode by creating an external electric field.[28] In general, the electric field between two electrodes immersed into a particle suspension in a non-conducting solvent induces a migration of charged particles towards the electrode of opposite charge. The EPD method was adopted for various inorganic and hybrid materials, such as silica,[29] zeolites,[30] metal oxides,[31] quantum dots,[32] carbon nitrides,[33] carbon nanotubes[34] and conducting organic polymers, such as polythiophene or polyanilines.[35,36] Additionally, metal-organic frameworks as well as a covalent-ionic-organic framework, containing a ligand especially tailored with cationic functional groups for the deposition, were reported.[37–40]

Here, we expand the paradigm of EPD into a highly general method for the rapid fabrication of COF films featuring a high textural porosity on conductive surfaces. For the deposition, we utilize various well-characterized bulk COF materials namely COF-5,[41] BDT-ETTA COF[42] and COF-300.[43] Thereby, we demonstrate the versatility of EPD as being applicable for the deposition of both 2D and 3D frameworks of different particle sizes and morphologies, linked by imine or boronate ester bonds. Prior to the deposition, stable COF particle suspensions were prepared by COF powder attrition or simply by immersion in a non-conducting solvent. Through EPD, COF films and coatings were deposited within minutes with control over the film thicknesses ranging from hundreds of nanometers to several micrometers. Furthermore, co-depositions of two different COF materials, as well as a COF/Pt nanoparticle mixture are demonstrated, yielding homogeneous hybrid films. Additionally, the catalytic performance of BDT-ETTA COF and BDT-ETTA COF/Pt films, prepared by EPD, was evaluated for the light-driven electrochemical production of hydrogen and compared to state-of-the-art dense and oriented BDT-ETTA COF films.[42]

Experimental Section

Chemicals. All materials were purchased from Aldrich, Fluka, Acros, Activate Scientific or TCI Europe in the common purities purum, puriss or reagent grade. Materials were used as received without additional purification and handled under air unless denoted. All solvents used were anhydrous and purged with inert gas. 4,4',4'',4'''-(1,1,2,2-ethylenetetrayl)tetrakisaniline (ETTA) and 2,6-benzo[1,2-*b*:4,5-*b*']dithiophene dialdehyde (BDT) were synthesized as reported in literature.[42]

BDT-ETTA COF. Under argon atmosphere BDT (benzo[1,2-*b*:4,5-*b*']dithiophene-2,6-dicarboxaldehyde, 74 mg, 0.30 mmol) and ETTA (1,1,2,2-tetra(*p*-aminophenyl)ethylene, 58.6 mg, 0.15 mmol) were suspended in a mixture of benzyl alcohol and mesitylene (V/V 9:1, 5 mL) in a 25 mL Schott-Duran vial. Acetic acid (6 M, 500 µL) was added to the vessel and the mixture was placed in a pre-heated oven at 120 °C for 3 days. The resulting orange precipitate was suction filtered, soxhlet-extracted with dry THF and dried at reduced pressure.

COF-300. Tetrakis(4-aminophenyl)methane (100 mg, 0.26 mmol) and terephthalaldehyde (60 mg, 0.44 mmol) were suspended in a mixture of 1,4-dioxane (5 mL) and acetic acid (6 M, 500 µL) in a 25 mL Schott-Duran vial. The mixture was subject to a short sonication and placed in a preheated oven at 120 °C for 3 days. The yellow precipitate was suction filtered, soxhlet-extracted with dry THF and dried at reduced pressure.

COF-5. Benzene-1,4-diboronic acid (18.7 mg, 0.113 mmol) and 2,3,6,7,10,11-hexahydroxytriphenylene hydrate (24.3 mg, 0.075 mmol) were placed in a 5 mL microwave vial and 4 mL of a 1,4-dioxane and mesitylene 1:1 mixture was added. The vial was sonicated for 5 min and then placed in the microwave and heated for 3 h at 100 °C. The grey precipitate was suction filtered, subsequently washed with anhydrous acetone and dried at reduced pressure.

COF-300 and COF-5 suspension preparation. COF particle suspensions were prepared by adding the amount to deposit (0.5 mg for COF-5 and, depending on the desired thickness of COF-300 films 0.05 – 0.5 mg of COF-300 (Figure S4.10) of the respective COF into ethyl acetate (10 mL). A brief sonication in an ultrasonic bath was then applied to homogeneously disperse the particles in the solvent. After the treatment, homogeneous COF dispersions colored yellow or grey for COF-300 or COF-5, respectively, were obtained.

82

For COF-5, we observed a severe impact on crystallinity if sonication times exceeded 15 seconds.

BDT-ETTA COF particle attrition and suspension preparation. Prior to deposition, BDT-ETTA COF was subjected to an ultrasound-based attrition process to break up large, intergrown agglomerates. Therefore 5 mg of COF was suspended in 25 mL of deposition solvent and a sonication amplitude of 70% for 30 min was chosen. During the process, the particle suspension was cooled using an ice bath. After the treatment, the suspension was centrifuged at a relative centrifugal force of 7000 g after which the supernatant was used for deposition. Using this process, particle size could be greatly reduced and suspensions stable for more than one week were obtained. The concentration of the produced BDT-ETTA COF suspension was determined by subtracting the weight of the centrifuge COF residue from the initial COF mass. A BDT-ETTA COF concentration of 0.74 mg per 25 mL ethyl acetate, or 0.03 mg mL^{-1}, was determined.

Electrophoretic Deposition. In a typical EPD experiment, two conductive substrates were contacted by alligator clamps to the potentiostat parallel and with the conducting sides facing each other, and with a horizontal distance of 1 cm between the electrodes. Subsequently, the electrodes were dipped into the COF particle suspension (10 mL). The electrode area submerged in the suspension was 1 cm × 1 cm. Then, the desired potential was applied between the electrodes for the respective deposition time (e.g. 900 V for 2 min). After deposition, the applied potential was set to zero and the electrodes were removed from the solvent and subsequently dried under nitrogen flow. For the COF-5 deposition as depicted in Figure 4.1 of the manuscript, 0.5 mg material was used. For the preparation of the large area films two FTO (fluorine-doped tin oxide) substrates (8 cm × 5 cm) were used, where the submerged area used for deposition was 5 cm × 5 cm. For the co-deposition of COF-300 and BDT-ETTA COF, 2 mL of the ultrasound attrited BDT-ETTA COF particle suspension was diluted with 8 mL of ethyl acetate. Then, 0.2 mg of COF-300 was added and the mixture was sonicated in a sonication bath for 1 min for homogenization. The subsequent deposition was carried out on an ITO (indium doped tin oxide) coated glass substrate at 900 V for 2 min. Assuming a complete suspension depletion and employing defined concentrations of both samples afford a ratio of 0.06:0.2 mg/mg for the BDT-ETTA COF and COF-300 codeposition film.

Photoelectrochemical hydrogen production. For the 3 μm thick BDT-ETTA COF films used in PEC-based hydrogen production, 15 mL (7.5 mL for the 1.5 μm thick film) of the BDT-ETTA COF suspension in ethyl acetate, fabricated as described before, were used and deposited on a 1 cm × 1 cm large area of FTO (total dimensions of FTO electrode was 1 cm × 4 cm). Pt nanoparticles were synthesized as reported in literature.[44] A zeta potential of −24.3 mV in water was recorded for the synthesized particles. Subsequently, Pt nanoparticles were isolated through lyophilization under dynamic vacuum. Hereby, Pt nanoparticles of 2–4 nm in diameter were obtained, as measured from TEM micrographs (Figure S4.16). Additionally, the hydrodynamic radii of the citrate capped nanoparticles were determined by dynamic light scattering (DLS) and sizes ranging from 4–9 nm were found (Figure S4.17). For the codeposition, 10 mL of the BDT-ETTA suspension were used, to which 0.15 mg of Pt nanoparticles were added. Then, the mixed suspension was subjected to an additional sonication step (as described in BDT-ETTA COF suspension preparation) for 10 min to homogenize the mixture. The deposition was carried out at 900 V for 2 min on an ITO coated glass substrate. During the deposition, additional Pt particles (0.10 mg in 2 mL ethyl acetate) were steadily added to the deposition suspension by a syringe.

Characterization Methods. PXRD and film XRD patterns were measured on a Bruker D8 Discover instrument equipped with a Lynx Eye detector in Bragg-Brentano geometry and Ni-filtered Cu K$_\alpha$ X-ray radiation. Scanning electron microscopy (SEM) images were recorded on a FEI Helios Nanolab G3 UC microscope at an acceleration voltage of 2.5 kV. Energy dispersive X-ray spectra (EDX) were recorded at 20 kV. Prior to analysis, the samples were coated with carbon. TEM micrographs were obtained from a FEI Titan Themis 60-300 TEM at an acceleration voltage of 300 kV. Electrochemical measurements were performed on a Methrom μAutolabIII/FRA2 instrument. Fourier-transformed infrared (FT-IR) spectra were recorded on a *Thermo Scientific Nicolet* iN10 FT-IR microscope in reflection on a steel substrate. FT-IR spectra of the films were acquired by scratching-off the respective COF deposits. Microwave based COF synthesis was carried out using a Biotage Initiator microwave. Ultrasonic particle attrition was carried out using a Bandelin Sonopuls HD 4100 homogenizer with a TS113 13 mm tip. For electrophoretic deposition (EPD), a Heinzinger LNC 3000 potentiostat was used. Dynamic light scattering (DLS) and zeta potential measurements were recorded using a Malvern Zetasizer instrument at room temperature using 10 mm path length cuvettes. Nitrogen

physisorption data was recorded using a Quantachrome Autosorb iQ system. Prior to the measurement, samples were heated at 120 °C for 6 h under high vacuum. Measurements were performed at 77.35 K. For sorption measurements, the respective materials were obtained by scratching-off the COF deposits from five films.

4.3. Results and Discussion

The central aspect addressed in this study is the development of a general COF film fabrication method, applicable for a variety of structures, providing tunable film thicknesses and textural porosity. Therefore, we established a processing protocol utilizing COF particle suspensions and subsequently EPD for obtaining the desired deposit. We chose well-characterized and -known structures to validate the developed EPD-based protocol as a structure-independent approach. For this purpose, we synthesized highly crystalline 2D and 3D COF bulk materials under solvothermal conditions, namely the imine-linked BDT-ETTA COF and the COF-300, and the boronate ester-based COF-5. [41–43] The isolated COF powders were suspended in a non-conducting and low dielectric constant solvent and subsequently deposited by EPD onto a conductive substrate serving as an electrode. For the deposition, the external electric field between two electrodes allowed for the migration of COF nanoparticles, bearing an intrinsic surface charge, to the electrode of opposite charge.
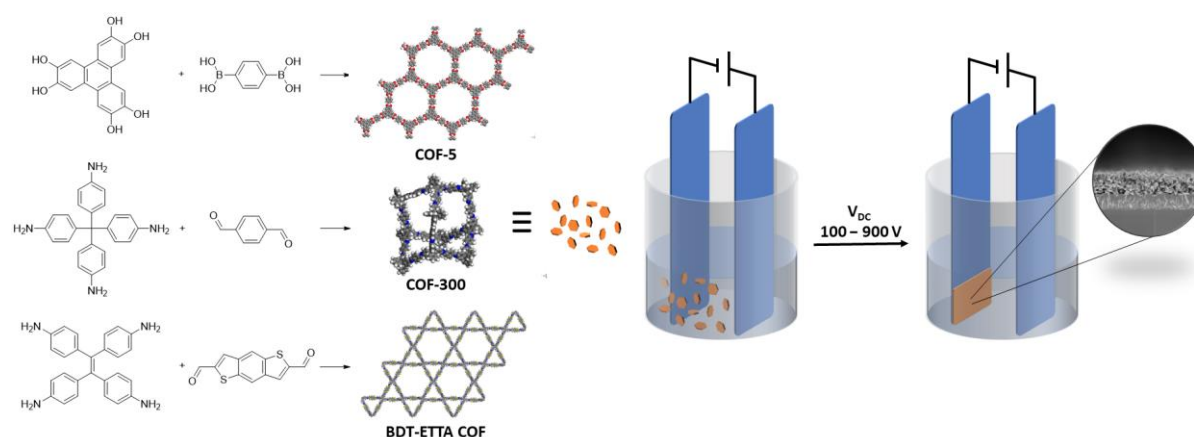
Scheme 4.1: COF building blocks and structures of the resulting frameworks used in the EPD. Schematic presentation of the EPD set-up with a typical COF film SEM cross-section as an inset.

In the EPD setup, two conductive substrates (1 cm x 1 cm), such as FTO, ITO or titanium foil were submerged into a COF particle suspension (Scheme 4.1, Figure S4.1). Untreated COF-5 agglomerates, nanoparticles of BDT-ETTA COF as well as almost micrometer-sized COF-300 single crystallites were suspended in an adequate organic solvent and subsequently deposited using the same deposition protocol. Aprotic, organic solvents of

low polarity, such as ethyl acetate, toluene or anisole (Figure S4.2), were found to be suitable media for the preparation of stable COF particle suspensions and for effective electrophoresis. While COF-5 and COF-300 particles were suspended in the respective solvents without further treatment, the robust BDT-ETTA COF was subjected to an ultrasonic attrition process to disassociate intergrown and agglomerated COF crystals using a 20 kHz ultrasonic disintegrator at high amplitudes. Dynamic light scattering (DLS) measurements of the obtained suspension revealed average particle sizes of about 200 nm (Figure S4.3). This shows that the ultrasonic treatment provided sufficient mechanical force for separating the COF agglomerates into isolated and well-suspended nanocrystals.

The EPD COF films were produced by inducing an electric field of 900 V cm^{-1} between the electrodes for two minutes. Under these conditions, the particles of the different COFs readily migrate to the positively charged electrode, indicating that the COF particles, regardless of their linkage-type, bear an intrinsic negative surface charge. Within seconds, a colored deposit formed on the surface of the submerged electrode and within two minutes a complete discoloration of the suspension was observed, indicating a quantitative deposition of the suspended material. After the deposition, the obtained COF films were dried under an air stream, revealing a continuous, colored deposit on the substrate (Figure 4.1).

Top view scanning electron microscopy (SEM) micrographs of all the examined EPD COF films revealed uniform deposits on the immersed conducting electrode surfaces (Figure 4.1). The deposits consist of closely packed particles of similar size creating interstitial voids. Cross-section SEM micrographs revealed continuous COF deposits on the substrates featuring an even thickness throughout the respective films. Using the deposition conditions of 900 V cm^{-1} and 2 minutes deposition time, a film thickness of 2 µm was obtained for the BDT-ETTA COF suspension. In the cases of the untreated COF-5 and COF-300 suspensions, thicknesses of 14 µm and 6 µm were determined, respectively. Notably, interstitial voids between the particles are apparent throughout the films and therefore, textural porosity is characteristic for all the examined samples. X-ray diffraction (XRD) measurements confirmed that all the deposited films consist of crystalline COF particles, and the obtained diffraction patterns are in excellent agreement with the respective bulk materials (Figure 4.1). Transmission electron microscopy (TEM) analysis of a BDT-ETTA COF film powder removed from the substrate revealed crystalline domains

of about 100 nm without traces of an amorphous phase (Figure S4.4). This observation confirms that the milling process applied to the BDT-ETTA COF suspension is vigorous enough to dissociate the COF aggregates into individual particles without causing structural degradation.
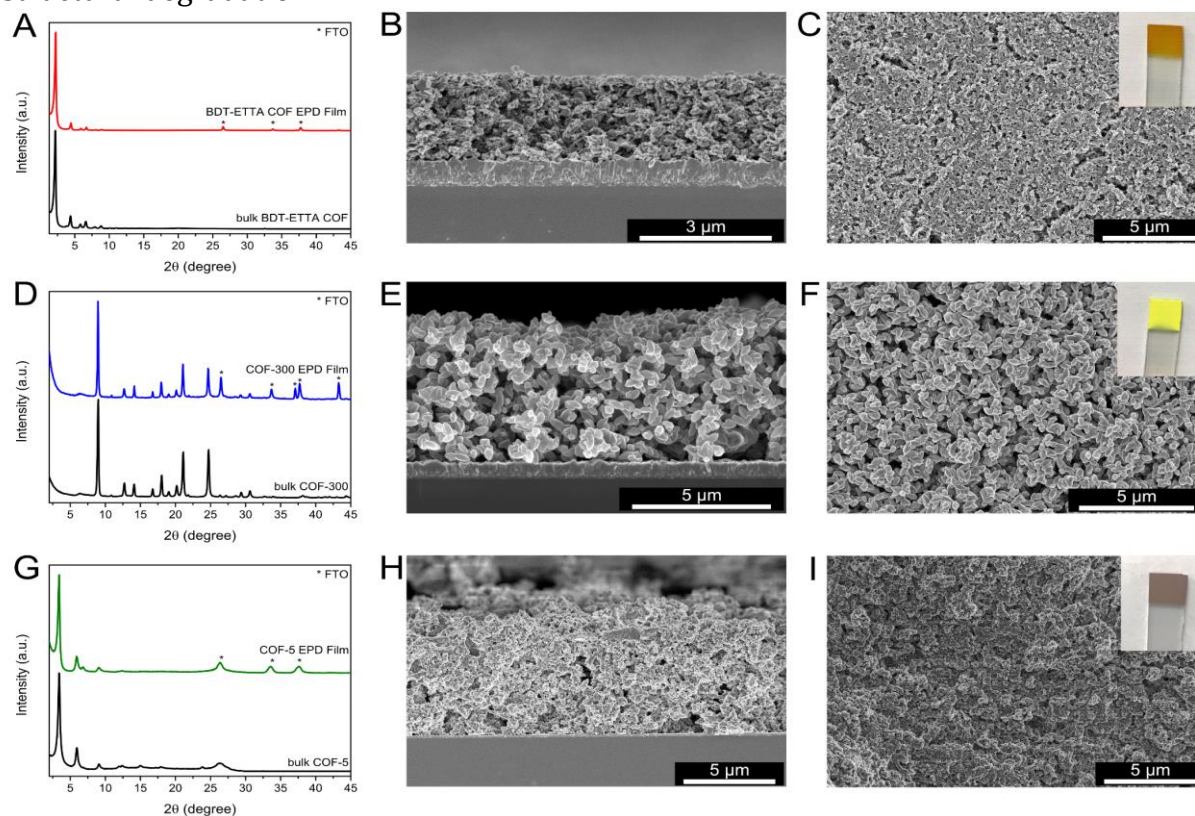

Figure 4.1: (A) XRD of BDT-ETTA COF as EPD film and as bulk material. (B) SEM cross-section and (C) top-view of BDT-ETTA COF film and a photograph of the film as an inset. (D) XRD of COF-300 as EPD film and as bulk material. (E) SEM cross-section and (F) top-view of COF-300 film and a photograph of the film as an inset. (G) XRD of COF-5 as EPD film and as bulk material. (H) SEM cross-section and (I) top-view of COF-5 and a photograph of the film as an inset.

In contrast, the non-treated COF-300 powder consists of relatively uniform individual crystallites of about 500 nm in size. Here, the COF powder was suspended in ethyl acetate without the need for particle attrition to form a stable suspension. Therefore, films deposited from such COF suspensions consist of single COF crystallites and feature structural characteristics of the bulk material (Figure S4.5). These observations indicate that with the COF-300 particles no significant agglomeration occurred in the course of the film deposition. In the case of EPD COF-5 films, intergrown crystallite agglomerates exceeding 100 nm are visible, nevertheless forming a continuous deposit (Figure S4.6). Importantly, the XRD and TEM analyses of the films illustrate the compatibility of the different COF materials with the electrophoretic process, as no electrochemical reaction

or degradation of the framework is observed. Nitrogen physisorption experiments of scratched-off COF film material showed the respective isotherm shapes and confirmed the retention of porosity for all deposited frameworks (Figure S4.7). Additionally, Fourier-transform infrared (FT-IR) spectra of the deposited materials match those of the bulk COF powders. This further indicates that no chemical alteration of the framework occurred during the deposition and emphasizes the compatibility of COFs with the EPD process (Figure S4.8).

The migration of the COF particles to the respective electrode is driven by their intrinsic surface potential. Interestingly, independent of their structure and chemical composition, COFs readily migrate to the positive electrode, indicating negative surface potential. Zeta-potential measurements performed for COF-300 suspensions in ethyl acetate confirmed this observation and revealed a negative particle surface potential of −21 mV. To invert the surface potential through protonation of the terminal amine groups, glacial acetic acid was added to suspensions of COF-300 particles in ethyl acetate. Zeta-potential measurements of the protonated COF-300 particle suspensions revealed a change in the surface potential to 11.9 mV. Notably, acetic acid treated COF-300 particles readily migrated to the opposite, negatively charged electrode during electrophoretic depositions, illustrating the significant role of the terminal functional groups in the EPD process.

To further study the parameters governing the EPD of COF films, we focused our following investigations on COF-300 as the first representative for 3D COF films on conducting substrates and on the photoactive BDT-ETTA COF, serving as a representative for 2D COFs.[42,43] Achieving control of the COF film thickness is essential for applications such as sieving, sensing or optimizing photocatalytic performance.[45] Furthermore, film deposition techniques providing COF film thicknesses of more than several hundred nanometers are rare.[20,24,45] In EPD, the amount of the deposited material is directly proportional to deposition time and the mass of the suspended material.[46] Accordingly, the film thickness can be easily predetermined and systematically adjusted by varying parameters such as deposition time and particle concentrations, thus, enabling a fine control over film thickness. For the deposition of BDT-ETTA COF, we found that adjusting the deposition time allows for controlling and predetermining the film thickness.

To determine the film deposition rate, we fabricated a series of BDT-ETTA COF films using different EPD deposition times, ranging from 5 s to 120 s. The XRD patterns of the film

series showed a linear increase in the COF (100) reflection intensity, relative to a constant FTO reflection intensity (observed at 25.9° 2θ) serving as an internal reference. We attribute this steady intensity increase to a linear increase in film thickness (Figure 4.2A). SEM cross-section analysis revealed a film thickness of about 2 μm corresponding to a deposition time of two minutes. Remarkably, we observed a complete surface coverage and a film thickness of about 400 nm already within 10 s (Figure 4.2B). To calculate the deposition rate, the BDT-ETTA COF film thicknesses, obtained from the SEM analysis, were plotted against the deposition times (Figure S4.9). After an initial time of about 10 seconds during which steady-state conditions are established, we observed a linear dependence of the film thickness on the deposition time with a calculated deposition rate of 16 nm s^{-1}.

Additionally, we investigated the effect of the applied voltage on the growth rate and film homogeneity. For this purpose, BDT-ETTA COF particles were deposited using potentials of 100, 200, 300, 600 and 900 V while keeping the deposition time constant at 2 min. Using these deposition parameters, a steady increase in the COF (100) reflection intensity in the XRD pattern relative to the FTO reflection intensity was observed. This is attributed to the applied higher deposition voltages, indicating a higher mass transfer rate from the suspension to the electrode (Figure S4.10). SEM top-view micrographs of the films deposited at 100, 200 and 300 V cm^{-1} reveal randomly scattered COF particles only partially covering the electrode surface. At 600 V cm^{-1} a nearly continuous film was observed, but in contrast to the film fabricated under the optimal conditions of 900 V cm^{-1}, large cracks protruding the film were still visible (Figure S4.10).

Recently, advanced synthesis approaches for growing single crystals of COFs, in some cases even exhibiting sizes suitable for single crystal XRD analysis, were reported.[47] For boronate ester COFs, such as COF-5, in the form of larger single crystals, size-dependent effects such as prolonged lifetimes of excitons were observed by transient absorption spectroscopy.[48] So far, COF film synthesis methods have not been successfully used for the preparation of films comprising single crystal domains. Here, we found that the as-synthesized near micrometer-sized COF-300 particles are directly dispersible as individual crystallites in the deposition solvent and therefore, a quantitative deposition of COF-300 crystals from the suspension is feasible. For a quantitative deposition, we found that up to 1 mg of COF-300 powder in 10 mL of ethyl acetate yields a stable suspension. The suspended crystallites can directly be deposited on 1 cm^2 of electrode area within 2 minutes at 900 V cm^{-1}, resulting in a film thickness of 24 μm. Assuming a complete

depletion of the particles in the suspension, we can establish a film deposition formula suitable for predetermining film thickness, e.g. 24 μm film thickness per mg COF powder and cm^2 electrode area (24 μm mg^{-1} cm^{-2}) for COF-300 (Figure S4.11).
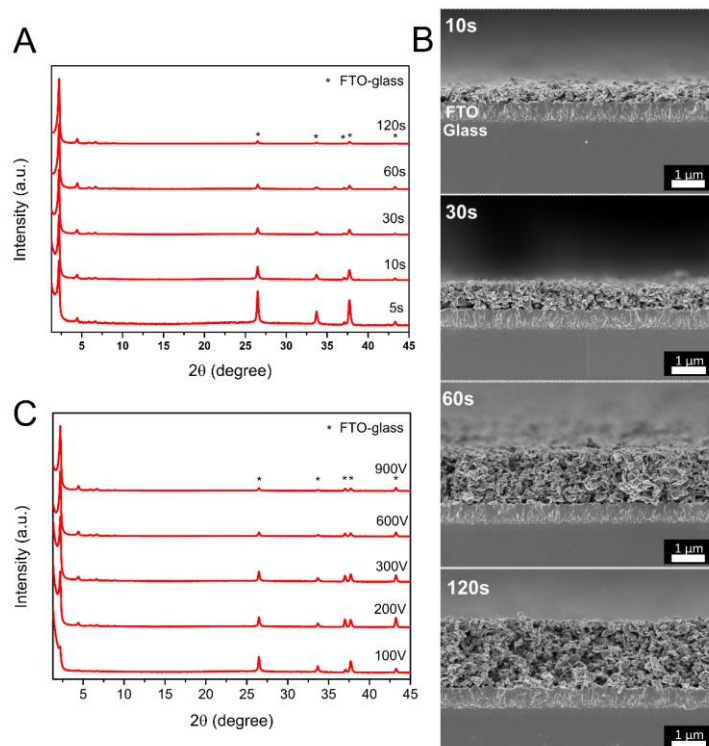

Figure 4.2: (A) XRD film patterns of BDT-ETTA COF films resulting from different deposition times (deposition voltage 900 V). (B) Corresponding SEM cross-sections of BDT- ETTA COF films (deposition voltage 900 V). (C) XRD patterns of BDT-ETTA COF films deposited at different electrode potentials.

The scalability of the EPD process is a central advantage for obtaining coatings on conductive surfaces. To the best of our knowledge, a process that allows for the direct preparation of COF films on surfaces larger than a few cm2 has yet to be reported. To probe the scalability of EPD for COF films, we fabricated a BDT-ETTA COF film on a 5 cm × 5 cm large FTO substrate by increasing the COF and solvent quantities used for the deposition on a 1 cm2 substrate by 25 times, while keeping the deposition time and potential constant at 2 min and 900 V cm−1, respectively. The obtained film features a macroscopic homogeneous deposit similar to deposits on smaller substrates. This confirms that the established COF EPD protocol is indeed highly scalable and applicable to the rapid deposition of COF crystals on large surface (Figure S4.12). In the context of COF film
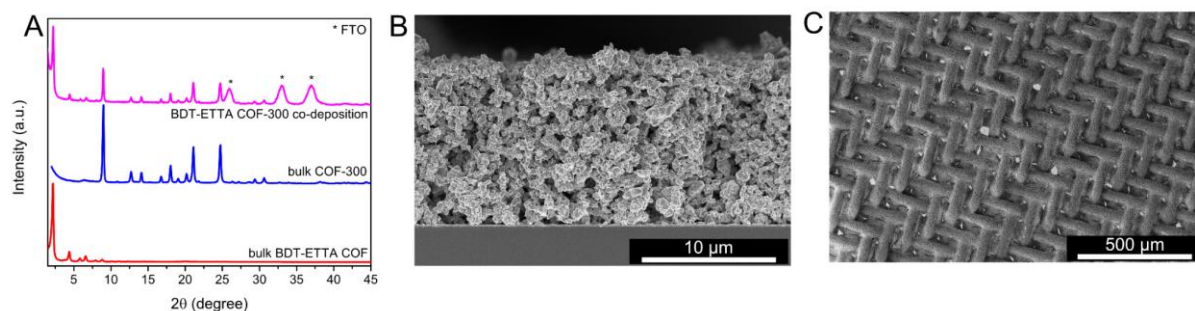
Figure 4.3: (A) XRD pattern of co-deposited COF-300 and BDT-ETTA COF materials compared with the respective bulk PXRD patterns of the individual COFs, and (B) the corresponding SEM cross-section. (C) Deposition of COF-300 on a stainless-steel mesh.

preparation, this versatile deposition technique constitutes a significant improvement over other state-of-the-art methods in terms of deposition yield, growth time, scalability and thickness control. We conclude that COFs are especially suitable for EPD due to faster growth rates and homogeneous film coverages, compared to related materials.[40,49]

The EPD of COF materials opens new perspectives regarding the facile production of films and coatings for applications such as sensing, catalysis or molecular sieving. Here, we demonstrate the feasibility of using EPD for the preparation of COF-based membranes supported by a porous grid. For this purpose, a stainless-steel grid featuring a mesh size of 270 (53 μm pore size) was used as the deposition electrode for COF-300 (Figure 4.3C). Adjusting the mass of the suspended COF and applying EPD for 2 minutes at 900 V cm^{-1} resulted in the formation of a homogeneous coating covering the grid and its cavities, the permeable areas. The deposition on such a mesh demonstrates that EPD can be used for the fabrication of COF coatings not only on flat surfaces but also on corrugated 3D surfaces (Figure 4.3 and S4.13). Harnessing the ability to prepare COF suspensions from synthesized COF powders and developing a deposition formula for high yields, we explored the simultaneous deposition of two structurally distinct COF particles featuring different pore shapes and sizes from a mixed COF crystallite suspension. To this end, we produced a suspension consisting of BDT-ETTA COF and COF-300 particles in ethyl acetate and deposited this COF particle mixture onto FTO at 900 V cm^{-1} and 2 minutes deposition time (for more details see supporting information). The XRD pattern of the obtained film shows the characteristic (100) and the (111) reflections for BDT-ETTA COF and COF-300 at 2.26° and 8.89° 2θ, respectively. Furthermore, higher-order reflections of both COFs with relative intensities similar to the bulk powder are visible, indicating that the COF

long-range order remained intact. This demonstrates the deposition of a mixed 2D/3D COF film consisting of crystallites featuring three pore types (micropores and mesopores in BDT-ETTA COF and micropores in COF-300), exhibiting different chemical environments and dimensions (Figure 4.3A). The homogeneous mixing of the two COFs was confirmed by SEM cross-section micrographs, where both COF morphologies, namely large, oval COF-300 particles and BDT-ETTA COF nanocrystallites, are evenly distributed throughout the film (Figure 4.3B).

Photocatalytic water reduction has become a major interest for potential COF applications. Typically, COF powder is used in combination with a sacrificial agent to facilitate or enable the solar driven hydrogen evolution.[45] Recently, we demonstrated the use of highly oriented thin films of BDT-ETTA COF as photocathodes for the sacrificial agent free photoelectrochemical hydrogen production and provided a detailed characterization of the catalytic properties of the material as a dense and oriented film.[42] This allows for studying the impact of morphology on the performance of EPD BDT-ETTA COF films on the photoelectrochemical (PEC) catalysis performance, already shown for this type of COF. Therefore, we measured light-induced photocurrent generation for these films in a water-splitting setup. A three-electrode setup was used with a BDT-ETTA COF film supported by FTO as the photocathode working electrode, a platinum mesh counter-electrode and a reverse hydrogen electrode (RHE) as a reference electrode. A BDT-ETTA COF film of 3 μm thickness, in a 0.1 M Na_2SO_4 aqueous, nitrogen-purged electrolyte, was measured by linear sweep voltammetry either in the dark or under illumination through
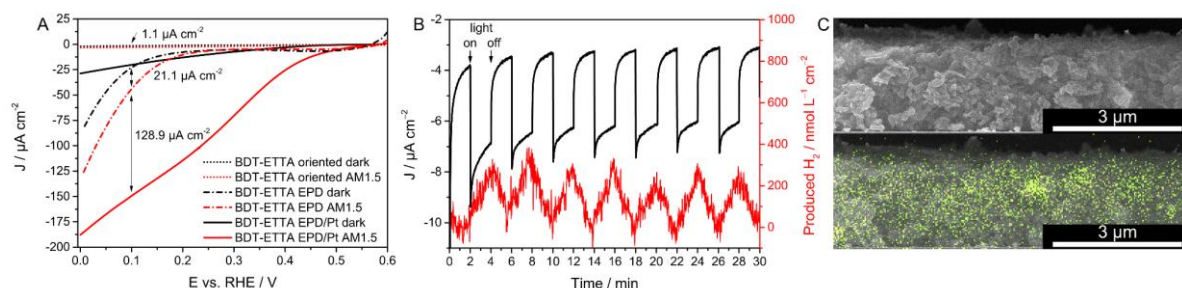

Figure 4.4: (A) PEC linear sweep voltammograms of electrodes coated with BDT-ETTA COF as a dense and oriented film, a 3 μm thick film prepared by EPD, and a COF/Pt nanoparticle hybrid film prepared via EPD. Illumination at AM1.5G. (B) Dynamic hydrogen evolution measurement under chopped AM1.5G illumination of a BDT-ETTA COF electrode at 0.2 V vs. RHE. (C) SEM cross-section generation, a linear potential sweep was carried out in the dark to quantify non-PEC of BDT-ETTA COF and the corresponding EDX elemental mapping of Pt recorded at an electron acceleration voltage of 20 kV.

the substrate by simulated sunlight (AM1.5G, 100 mW cm^{-2}). The measurements were carried out at potentials ranging from 0.6 V to 0 V vs. RHE. Prior to measuring PEC current related electrochemical reactions and film capacitance. PEC measurements of the pristine BDT-ETTA COF film under illumination showed a photocurrent onset at 0.25 V vs. RHE and a high photocurrent density of 21.1 µA cm^{-2} at 0.1 V vs. RHE (Figure 4.4A). The recorded photocurrent density is 19-times higher compared to the value previously reported on dense and oriented thin BDT-ETTA COF films at the same potential.[42] Furthermore, we performed a dynamic hydrogen evolution experiment under chopped illumination with an interval time of two minutes. Here, the dissolved hydrogen gas was quantified using a microsensor, equipped with a hydrogen selective silicone membrane. The measurement was carried out at 0.2 V vs. RHE, close to the photocurrent onset potential, to prove that the observed photocurrent is indeed generated by proton reduction. Upon illumination, an instant current response was observed followed by a typical photocurrent transient. This photocurrent is directly correlated with an increase in the simultaneously recorded hydrogen concentration. In the dark, the recorded current density regresses rapidly and the hydrogen concentration simultaneously declines. This light-on and -off sequence was repeated several times and showed stable current and hydrogen concentration responses over the recorded course of 30 minutes (Figure 4.4B). Subsequently, XRD analysis of this film proved the retention of crystallinity of the active material (Figure S4.15). To investigate whether charge carrier transport efficiently occurs throughout the whole EPD COF film thickness, a film of half the thickness, about 1.5 µm, was used in the same experimental setup. Here, a reduced photocurrent density of 16.7 µA cm^{-2} at 0.1 V vs. RHE was observed (Figure S4.14). This reduction in photocurrent correlates with the reduction of the film thickness, indicating that PEC activity is indeed thickness-dependent, and charge carriers are sufficiently transported throughout the porous film morphology. Furthermore, it illustrates that a tight contact and continuous interface between the active COF material and the electrode are not necessarily prerequisites for effective electrocatalysis. We attribute the overall enhanced performance of the BDT-ETTA COF film prepared by EPD to the greatly enlarged interface between the photoabsorber and medium provided by the textural porosity. This compensates for the decreased areal interaction of the COF with the electrode, obtained by using a dense film. Besides the textural porosity, the inherent porosity of the COF can contribute to its catalytic performance. A stabilized current density output under constant

illumination was recorded for the 1.5 µm thick film by chronoamperometric measurements at 0.1 V vs. RHE, which showed a constant photocurrent density of 14.3 µA cm^{-2} over the course of 10 minutes (Figure S4.14). Next, we focused on the co-deposition of BDT-ETTA COF and an inorganic co-catalyst to facilitate electron charge transfer from the COF photoabsorber towards the aqueous electrolyte, whereby a further improvement of the PEC performance is expected.[50] Platinum nanoparticles sized 2–4 nm were included into the BDT-ETTA COF particle suspension prior to the EPD (Figure S4.16 and S4.17). To prevent a premature depletion of the Pt nanoparticles during deposition, due to their higher mobility under electrophoretic conditions, additional Pt nanoparticle suspension was continuously added to the COF/Pt deposition medium in the course of the deposition process. Hereby, a homogeneous distribution of Pt in the COF film was achieved, confirmed by elemental mapping analysis using energy-dispersive X-ray spectroscopy on a film cross-section in the SEM (Figure 4.4C). Subsequently, the exact same linear potential sweeps measurements were repeated for this COF/Pt hybrid film. Strikingly, a PEC photocurrent density of 128.9 µA cm^{-2} was recorded at 0.1 V vs. RHE for the COF/Pt films, which is an additional 6.1-fold increase with respect to the pristine COF EPD film and 29-times higher than the current density previously reported for dense and oriented thin BDT-ETTA COF film decorated with Pt nanoparticles on the surface.[42] An additional valuable effect of the incorporation of the platinum co-catalyst is an earlier photocurrent onset, which is shifted from 0.25 V to 0.45 V vs. RHE. Moreover, the dark current was strongly reduced. These results show that the COF film morphology plays a pivotal role in determining device performance. We postulate that the nanostructured film exhibiting a large interfacial area allows for an efficient charge separation and transport paths attributed to a direct transfer of electrons from the COF/Pt catalytic center to the surrounding water while holes can travel through the aggregated COF particle pathways towards the transparent conductive oxide (TCO) substrate.[42,51] These separated charge carrier transport pathways enable the use of even thicker COF films. In the case of a dense film, electrons and holes are generated in the bulk film and travel throughout the whole film thickness to reach a catalytic center or the TCO support. Therefore, charge carriers may be more likely to recombine, thus providing an overall limited effective film thickness and photocurrent density. According to these results, we conclude that film morphologies must be carefully chosen and tailored towards the respective application.

4.4.   Conclusion

In conclusion, we demonstrate the preparation of COF films and coatings by depositing COF particles on conducting substrates in an electric field through EPD. Hereby, 2D and 3D imine and boronate-ester linked COFs of different particle sizes and morphologies were deposited on metal, transparent conducting metal oxides or steel meshes. By adjusting the EPD parameters, such as deposition times, particle concentrations, and electrode potentials, film thicknesses could be tuned and predetermined. The obtained films feature an inherent textural porosity with interstitial voids between the deposited particles, thereby allowing for an increased contact to active media for applications such as catalysis. In addition, we showed that through EPD, film composites consisting of mixed COFs can be straightforwardly prepared, enabling encoded functionalities such as multi-pore COF films. Finally, a BDT-ETTA COF film as well as a COF/Pt nanoparticle hybrid film were examined regarding their PEC performance, where a 19- and 117-fold catalytical improvement, respectively, was found over our previously reported dense and oriented BDT-ETTA COF films. To put these results in perspective, it shows that film morphology plays a crucial role for different applications and should be considered in combination with the inherent properties of the COFs. This, as well as the simplicity and generality of the approach, underlines the importance of EPD as an addition to the field of COF film preparation methods. Therefore, we believe that this work will assist in designing high-performance devices for specific applications.

4.5.   References

(1) Diercks, C. S.; Yaghi, O. M. The atom, the molecule, and the covalent organic framework. *Science* **2017**, *355*.

(2) Jin, Y.; Hu, Y.; Zhang, W. Tessellated multiporous two-dimensional covalent organic frameworks. *Nat. Rev. Chem.* **2017**, *1*, 56.

(3) Furukawa, H.; Yaghi, O. M. Storage of hydrogen, methane, and carbon dioxide in highly porous covalent organic frameworks for clean energy applications. *J. Am. Chem. Soc.* **2009**, *131*, 8875–8883.

(4) Sharma, A.; Malani, A.; Medhekar, N. V.; Babarao, R. CO 2 adsorption and separation in covalent organic frameworks with interlayer slipping. *CrystEngComm* **2017**, *19*, 6950–6963.

(5) Fan, H.; Mundstock, A.; Feldhoff, A.; Knebel, A.; Gu, J.; Meng, H.; Caro, J. Covalent Organic Framework-Covalent Organic Framework Bilayer Membranes for Highly Selective Gas Separation. *J. Am. Chem. Soc.* **2018**, *140*, 10094–10098.

(6) Zhang, S.; Zheng, Y.; An, H.; Aguila, B.; Yang, C.-X.; Dong, Y.; Xie, W.; Cheng, P.; Zhang, Z.; Chen, Y. *et al.* Covalent Organic Frameworks with Chirality Enriched by Biomolecules for Efficient Chiral Separation. *Angew. Chem. Int. Ed.* **2018**, *57*, 16754–16759.

(7) Ding, S.-Y.; Gao, J.; Wang, Q.; Zhang, Y.; Song, W.-G.; Su, C.-Y.; Wang, W. Construction of covalent organic framework for catalysis: Pd/COF-LZU1 in Suzuki-Miyaura coupling reaction. *J. Am. Chem. Soc.* **2011**, *133*, 19816–19822.

(8) Sun, Q.; Aguila, B.; Ma, S. A bifunctional covalent organic framework as an efficient platform for cascade catalysis. *Mater. Chem. Front.* **2017**, *1*, 1310–1316.

(9) Lin, S.; Diercks, C. S.; Zhang, Y.-B.; Kornienko, N.; Nichols, E. M.; Zhao, Y.; Paris, A. R.; Kim, D.; Yang, P.; Yaghi, O. M. *et al.* Covalent organic frameworks comprising cobalt porphyrins for catalytic CO_2 reduction in water. *Science* **2015**, *349*, 1208–1213.

(10) Aiyappa, H. B.; Thote, J.; Shinde, D. B.; Banerjee, R.; Kurungot, S. Cobalt-Modified Covalent Organic Framework as a Robust Water Oxidation Electrocatalyst. *Chem. Mater.* **2016**, *28*, 4375–4379.

(11) Thote, J.; Aiyappa, H. B.; Deshpande, A.; Díaz Díaz, D.; Kurungot, S.; Banerjee, R. A covalent organic framework-cadmium sulfide hybrid as a prototype photocatalyst for visible-light-driven hydrogen production. *Chemistry* **2014**, *20*, 15961–15965.

(12) Wang, X.; Chen, L.; Chong, S. Y.; Little, M. A.; Wu, Y.; Zhu, W.-H.; Clowes, R.; Yan, Y.; Zwijnenburg, M. A.; Sprick, R. S. *et al.* Sulfone-containing covalent organic frameworks for photocatalytic hydrogen evolution from water. *Nat. Chem.* **2018**, *10*, 1180–1189.

(13) Dogru, M.; Handloser, M.; Auras, F.; Kunz, T.; Medina, D.; Hartschuh, A.; Knochel, P.; Bein, T. A photoconductive thienothiophene-based covalent organic framework showing charge transfer towards included fullerene. *Angew. Chem. Int. Ed.* **2013**, *52*, 2920–2924.

(14) Bessinger, D.; Ascherl, L.; Auras, F.; Bein, T. Spectrally Switchable Photodetection with Near-Infrared-Absorbing Covalent Organic Frameworks. *J. Am. Chem. Soc.* **2017**, *139*, 12035–12042.

(15) Guo, J.; Xu, Y.; Jin, S.; Chen, L.; Kaji, T.; Honsho, Y.; Addicoat, M. A.; Kim, J.; Saeki, A.; Ihee, H. *et al.* Conjugated organic framework with three-dimensionally ordered stable structure and delocalized π clouds. *Nat. Commun.*, *4*, 2736.

(16) DeBlase, C. R.; Silberstein, K. E.; Truong, T.-T.; Abruña, H. D.; Dichtel, W. R. β-Ketoenamine-linked covalent organic frameworks capable of pseudocapacitive energy storage. *J. Am. Chem. Soc.* **2013**, *135*, 16821–16824.

(17) Chandra, S.; Roy Chowdhury, D.; Addicoat, M.; Heine, T.; Paul, A.; Banerjee, R. Molecular Level Control of the Capacitance of Two-Dimensional Covalent Organic Frameworks: Role of Hydrogen Bonding in Energy Storage Materials. *Chem. Mater.* **2017**, *29*, 2074–2080.

(18) Halder, A.; Ghosh, M.; Khayum M, A.; Bera, S.; Addicoat, M.; Sasmal, H. S.; Karak, S.; Kurungot, S.; Banerjee, R. Interlayer Hydrogen-Bonded Covalent Organic Frameworks as High-Performance Supercapacitors. *J. Am. Chem. Soc.* **2018**, *140*, 10941–10945.

(19) Wang, D.-G.; Li, N.; Hu, Y.; Wan, S.; Song, M.; Yu, G.; Jin, Y.; Wei, W.; Han, K.; Kuang, G.-C. *et al.* Highly Fluoro-Substituted Covalent Organic Framework and Its Application in Lithium-Sulfur Batteries. *ACS Appl. Mater. Interfaces* **2018**.

(20) Wuttke, S.; Medina, D. D.; Rotter, J. M.; Begum, S.; Stassin, T.; Ameloot, R.; Oschatz, M.; Tsotsalas, M. Bringing Porous Organic and Carbon-Based Materials toward Thin-Film Applications. *Adv. Funct. Mater.* **2018**, *28*, 1801545.

(21) Beuerle, F.; Gole, B. Covalent Organic Frameworks and Cage Compounds: Design and Applications of Polymeric and Discrete Organic Scaffolds. *Angew. Chem. Int. Ed.* **2018**, *57*, 4850–4878.

(22) Colson, J. W.; Woll, A. R.; Mukherjee, A.; Levendorf, M. P.; Spitler, E. L.; Shields, V. B.; Spencer, M. G.; Park, J.; Dichtel, W. R. Oriented 2D covalent organic framework thin films on single-layer graphene. *Science* **2011**, *332*, 228–231.

(23) Medina, D. D.; Werner, V.; Auras, F.; Tautz, R.; Dogru, M.; Schuster, J.; Linke, S.; Döblinger, M.; Feldmann, J.; Knochel, P. *et al.* Oriented thin films of a benzodithiophene covalent organic framework. *ACS Nano* **2014**, *8*, 4042–4052.

(24) Wang, H.; He, B.; Liu, F.; Stevens, C.; Brady, M. A.; Cai, S.; Wang, C.; Russell, T. P.; Tan, T.-W.; Liu, Y. Orientation transitions during the growth of imine covalent organic framework thin films. *J. Mater. Chem. C* **2017**, *5*, 5090–5095.

(25) Bisbey, R. P.; DeBlase, C. R.; Smith, B. J.; Dichtel, W. R. Two-dimensional Covalent Organic Framework Thin Films Grown in Flow. *J. Am. Chem. Soc.* **2016**, *138*, 11433–11436.

(26) Medina, D. D.; Rotter, J. M.; Hu, Y.; Dogru, M.; Werner, V.; Auras, F.; Markiewicz, J. T.; Knochel, P.; Bein, T. Room temperature synthesis of covalent-organic framework films through vapor-assisted conversion. *J. Am. Chem. Soc.* **2015**, *137*, 1016–1019.

(27) Zhao, X.; Pachfule, P.; Li, S.; Langenhahn, T.; Ye, M.; Schlesiger, C.; Praetz, S.; Schmidt, J.; Thomas, A. Macro/Microporous Covalent Organic Frameworks for Efficient Electrocatalysis. *J. Am. Chem. Soc.* **2019**, *141*, 6623–6630.

(28) BESRA, L.; LIU, M. A review on fundamentals and applications of electrophoretic deposition (EPD). *Prog. Mater Sci.* **2007**, *52*, 1–61.

(29) Castro, Y.; Ferrari, B.; Moreno, R.; Durán, A. Coatings produced by electrophoretic deposition from nano-particulate silica sol–gel suspensions. *Surf. Coat. Technol.* **2004**, *182*, 199–203.

(30) Seike, T.; Matsuda, M.; Miyake, M. Preparation of FAU type zeolite membranes by electrophoretic deposition and their separation properties. *J. Mater. Chem.* **2002**, *12*, 366–368.

(31) Limmer, S. J.; Seraji, S.; Wu, Y.; Chou, T. P.; Nguyen, C.; Cao, G. Z. Template-Based Growth of Various Oxide Nanorods by Sol–Gel Electrophoresis. *Adv. Funct. Mater.* **2002**, *12*, 59.

(32) Salant, A.; Shalom, M.; Hod, I.; Faust, A.; Zaban, A.; Banin, U. Quantum dot sensitized solar cells with improved efficiency prepared using electrophoretic deposition. *ACS Nano* **2010**, *4*, 5962–5968.

(33) Xu, J.; Shalom, M. Electrophoretic Deposition of Carbon Nitride Layers for Photoelectrochemical Applications. *ACS Appl. Mater. Interfaces* **2016**, *8*, 13058–13063.

(34) Casagrande, T.; Imin, P.; Cheng, F.; Botton, G. A.; Zhitomirsky, I.; Adronov, A. Synthesis and Electrophoretic Deposition of Single-Walled Carbon Nanotube Complexes with a Conjugated Polyelectrolyte. *Chem. Mater.* **2010**, *22*, 2741–2749.

(35) Garate, J.-A.; English, N. J.; Singh, A.; Ryan, K. M.; Mooney, D. A.; MacElroy, J. M. D. Electrophoretic deposition of poly(3-decylthiophene) onto gold-mounted cadmium selenide nanorods. *Langmuir* **2011**, *27*, 13506–13513.

(36) Li, G.; Martinez, C.; Semancik, S. Controlled electrophoretic patterning of polyaniline from a colloidal suspension. *J. Am. Chem. Soc.* **2005**, *127*, 4903–4909.

(37) Han, H.; Yuan, X.; Zhang, Z.; Zhang, J. Preparation of a ZIF-67 Derived Thin Film Electrode via Electrophoretic Deposition for Efficient Electrocatalytic Oxidation of Vanillin. *Inorg. Chem.* **2019**, *58*, 3196–3202.

(38) Feng, J.-F.; Yang, X.; Gao, S.-Y.; Shi, J.; Cao, R. Facile and Rapid Growth of Nanostructured Ln-BTC Metal-Organic Framework Films by Electrophoretic Deposition for Explosives sensing in Gas and Cr 3+ Detection in Solution. *Langmuir* **2017**, *33*, 14238–14243.

(39) Wang, L.; Zeng, C.; Xu, H.; Yin, P.; Chen, D.; Deng, J.; Li, M.; Zheng, N.; Gu, C.; Ma, Y. A highly soluble, crystalline covalent organic framework compatible with device implementation. *Chem. Sci.* **2019**, *10*, 1023–1028.

(40) Hod, I.; Bury, W.; Karlin, D. M.; Deria, P.; Kung, C.-W.; Katz, M. J.; So, M.; Klahr, B.; Jin, D.; Chung, Y.-W. *et al.* Directed growth of electroactive metal-organic framework thin films using electrophoretic deposition. *Adv. Mater.* **2014**, *26*, 6295–6300.

(41) Côté, A. P.; Benin, A. I.; Ockwig, N. W.; O'Keeffe, M.; Matzger, A. J.; Yaghi, O. M. Porous, crystalline, covalent organic frameworks. *Science* **2005**, *310*, 1166–1170.

(42) Sick, T.; Hufnagel, A. G.; Kampmann, J.; Kondofersky, I.; Calik, M.; Rotter, J. M.; Evans, A.; Döblinger, M.; Herbert, S.; Peters, K. *et al.* Oriented Films of Conjugated 2D Covalent Organic Frameworks as Photocathodes for Water Splitting. *J. Am. Chem. Soc.* **2018**, *140*, 2085–2092.

(43) Uribe-Romo, F. J.; Hunt, J. R.; Furukawa, H.; Klöck, C.; O'Keeffe, M.; Yaghi, O. M. A crystalline imine-linked 3-D porous covalent organic framework. *J. Am. Chem. Soc.* **2009**, *131*, 4570–4571.

(44) Wu, G.-W.; He, S.-B.; Peng, H.-P.; Deng, H.-H.; Liu, A.-L.; Lin, X.-H.; Xia, X.-H.; Chen, W. Citrate-capped platinum nanoparticle as a smart probe for ultrasensitive mercury sensing. *Anal. Chem.* **2014**, *86*, 10955–10960.

(45) Wang, H.; Zeng, Z.; Xu, P.; Li, L.; Zeng, G.; Xiao, R.; Tang, Z.; Huang, D.; Tang, L.; Lai, C. *et al.* Recent progress in covalent organic framework thin films: fabrications, applications and perspectives. *Chem. Soc. Rev.* **2019**, *48*, 488–516.

(46) Hamaker, H. C. Formation of a deposit by electrophoresis. *Trans. Faraday Soc.* **1940**, *35*, 279.

(47) Ma, T.; Kapustin, E. A.; Yin, S. X.; Liang, L.; Zhou, Z.; Niu, J.; Li, L.-H.; Wang, Y.; Su, J.; Li, J. *et al.* Single-crystal x-ray diffraction structures of covalent organic frameworks. *Science* **2018**, *361*, 48–52.

(48) Evans, A. M.; Parent, L. R.; Flanders, N. C.; Bisbey, R. P.; Vitaku, E.; Kirschner, M. S.; Schaller, R. D.; Chen, L. X.; Gianneschi, N. C.; Dichtel, W. R. Seeded growth of single-crystal two-dimensional covalent organic frameworks. *Science* **2018**, *361*, 52–57.

(49) Safaei, J.; Mohamed, N. A.; Mohamad Noh, M. F.; Soh, M. F.; Ludin, N. A.; Ibrahim, M. A.; Roslam Wan Isahak, W. N.; Mat Teridi, M. A. Graphitic carbon nitride (g-C 3 N 4) electrodes for energy conversion and storage: a review on photoelectrochemical water splitting, solar cells and supercapacitors. *J. Mater. Chem. A* **2018**, *6*, 22346–22380.

(50) Kemppainen, E.; Bodin, A.; Sebok, B.; Pedersen, T.; Seger, B.; Mei, B.; Bae, D.; Vesborg, P. C. K.; Halme, J.; Hansen, O. *et al.* Scalability and feasibility of photoelectrochemical H 2 evolution: the ultimate limit of Pt nanoparticle as an HER catalyst. *Energy Environ. Sci.* **2015**, *8*, 2991–2999.

(51) Medina, D. D.; Petrus, M. L.; Jumabekov, A. N.; Margraf, J. T.; Weinberger, S.; Rotter, J. M.; Clark, T.; Bein, T. Directional Charge-Carrier Transport in Oriented Benzodithiophene Covalent Organic Framework Thin Films. *ACS Nano* **2017**, *11*, 2706–2713.

4.6. Supporting Information

Deposition of BDT-ETTA COF on FTO, ITO and titanium foil
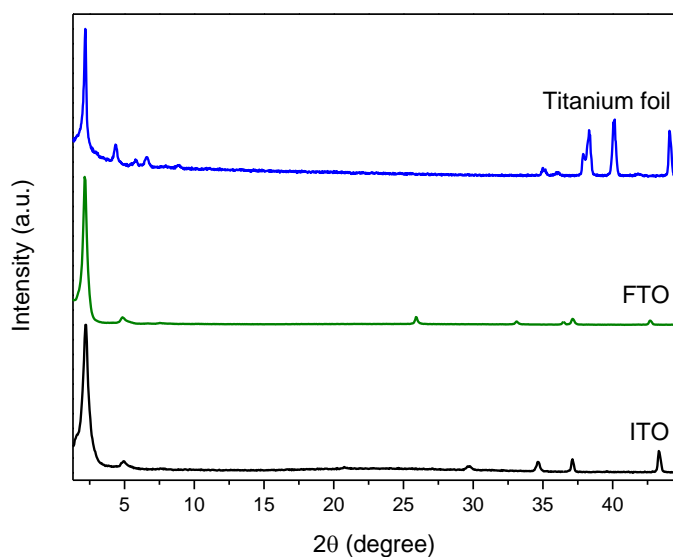
Figure S4.1: Deposition of BDT-ETTA COF on different conducting surfaces, namely titanium foil, glass coated with FTO and glass coated with ITO. All depositions were carried out using 10 mL of BDT-ETTA COF suspension in ethyl acetate at 900 V for 2 min.

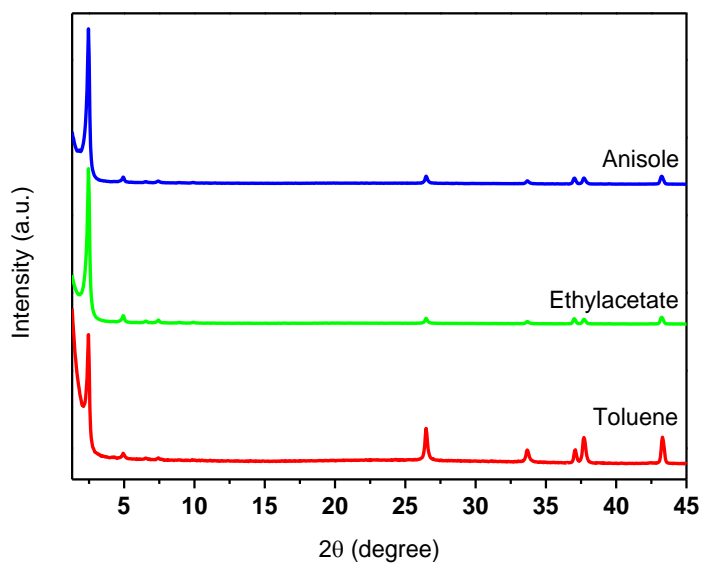## Deposition of BDT-ETTA COF in anisole, ethyl acetate and toluene

Figure S4.2: Deposition of BDT-ETTA COF from different solvents, namely anisole, ethyl acetate and toluene. All depositions were carried out using 10 mL of the respective BDT-ETTA COF suspension at 900 V for 2 min.

DLS Data for ultrasound treated BDT-ETTA COF
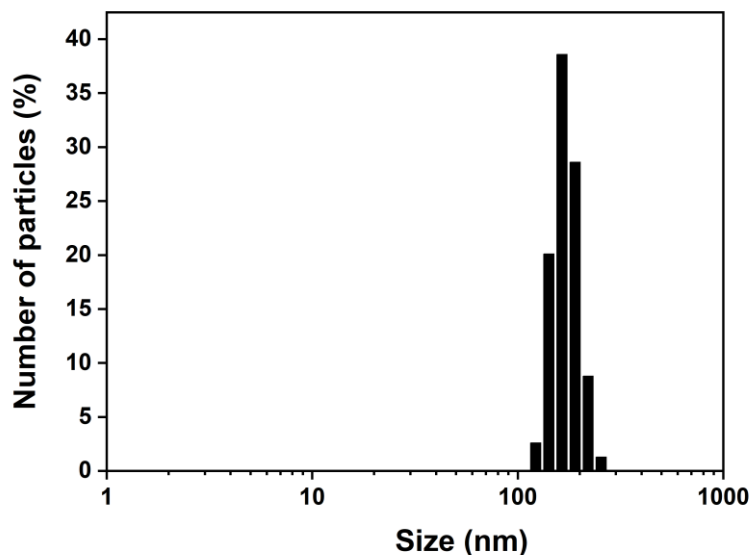
Figure S4.3: Particle size distribution of BDT-ETTA COF after the ultrasonic milling process.

Transmission electron micrographs
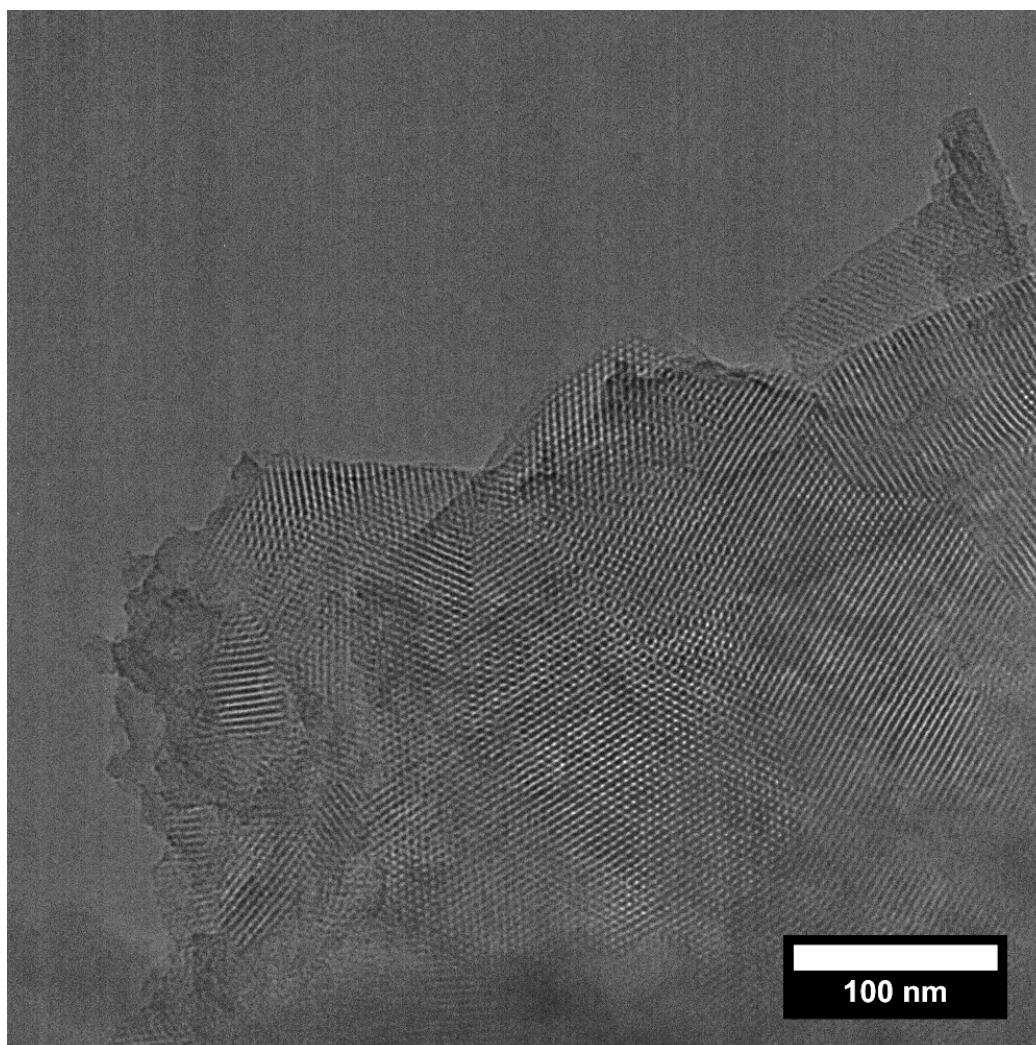
Figure S4.4: TEM image of deposited BDT-ETTA COF particles after the ultrasonic milling
process.
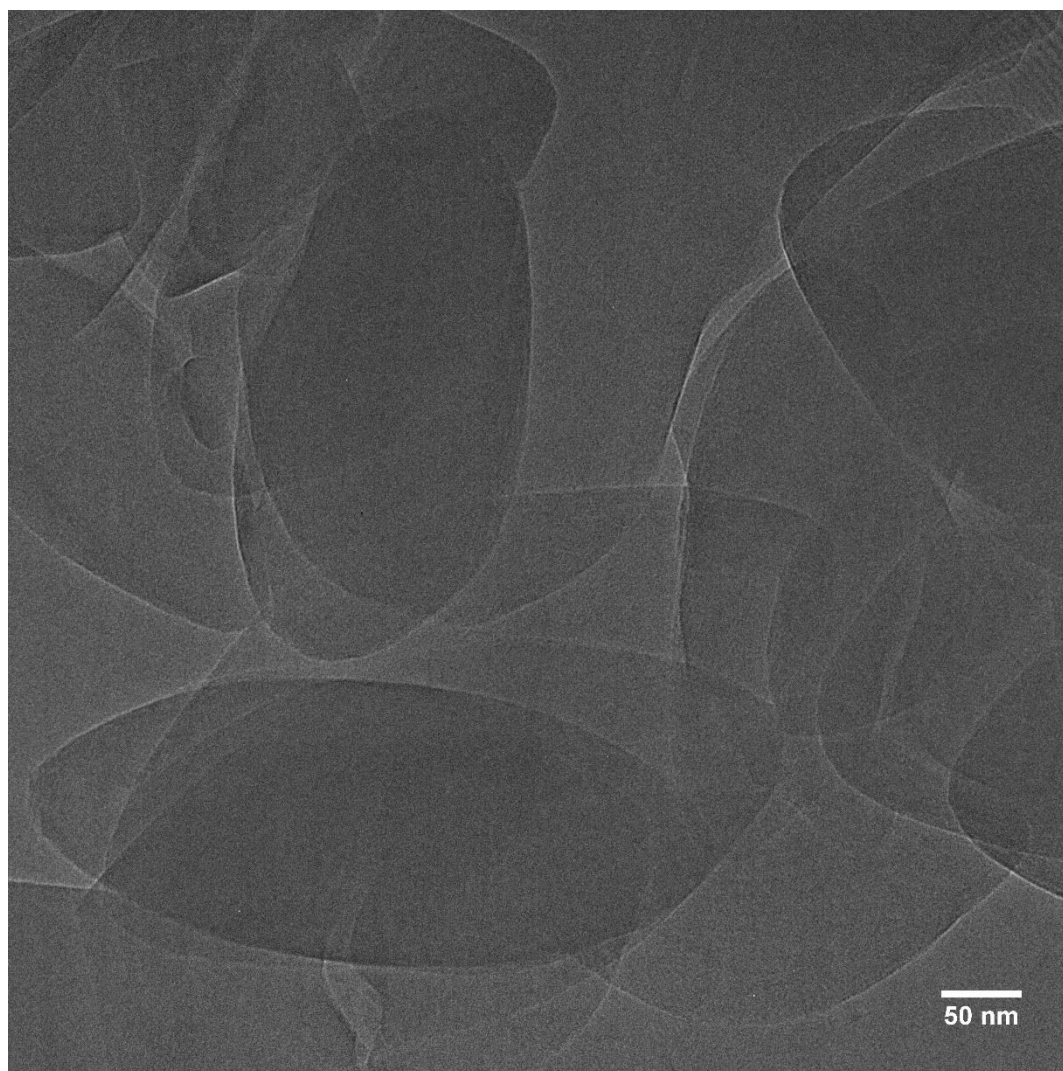
Figure S4.5: TEM image of deposited COF-300 particles.
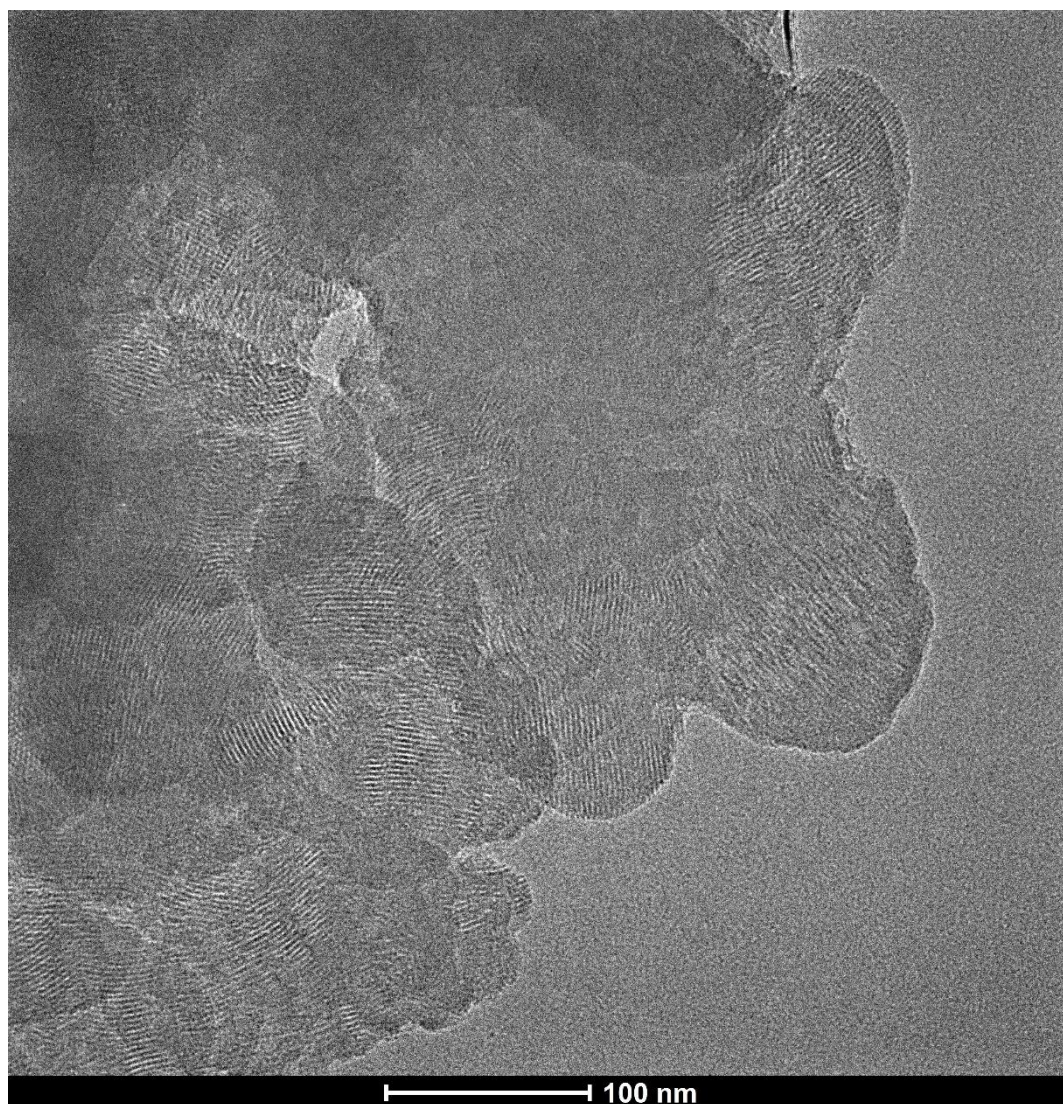
Figure S4.6: TEM image of deposited COF-5.

COF EPD film physisorption
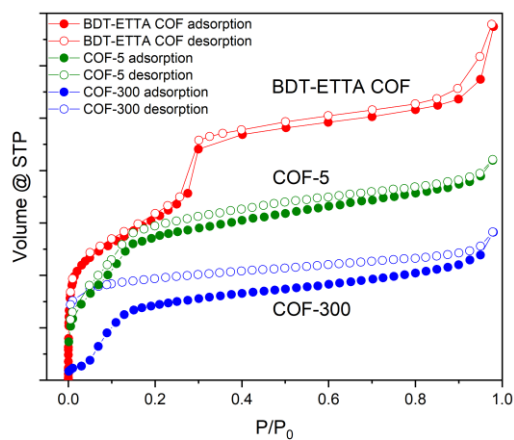
Figure S4.7: Nitrogen physisorption isotherms of scratched-off powder from the respective COF EPD films. Due to the low mass of the scratched-off powders, quantitative nitrogen uptake could not be accurately determined.

Fourier-transform infrared spectroscopy
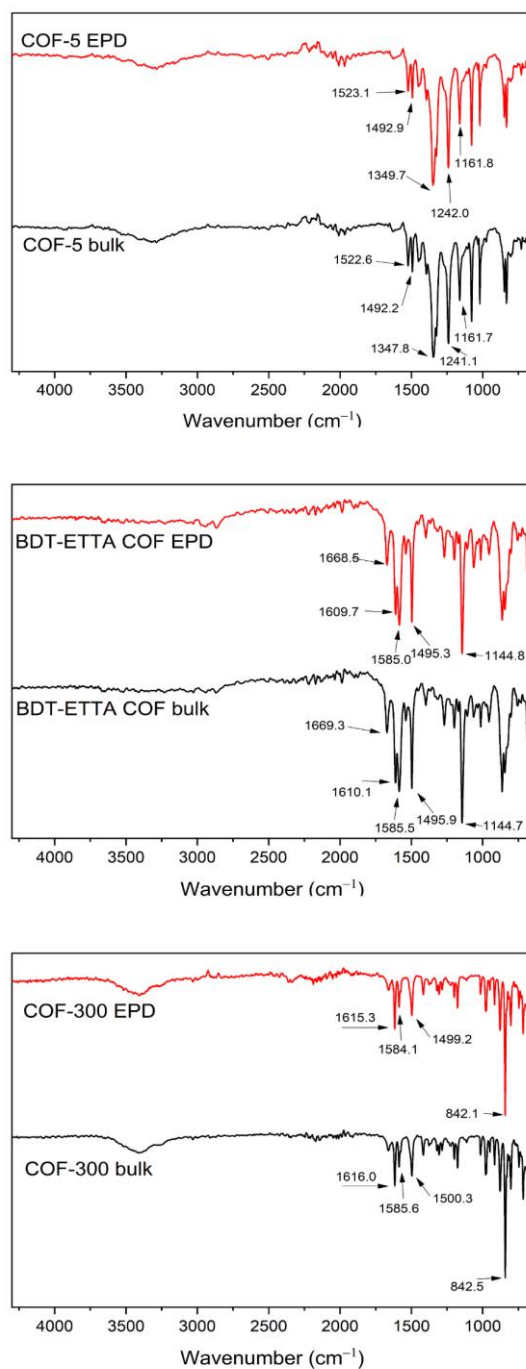
Figure S4.8: FT-IR spectra of the as-synthesized bulk material and as scratched-off EPD film materials. In all three cases IR vibrations are preserved. This indicates that no chemical degradation occurred during the EPD process.

BDT-ETTA COF time-dependent thickness plot
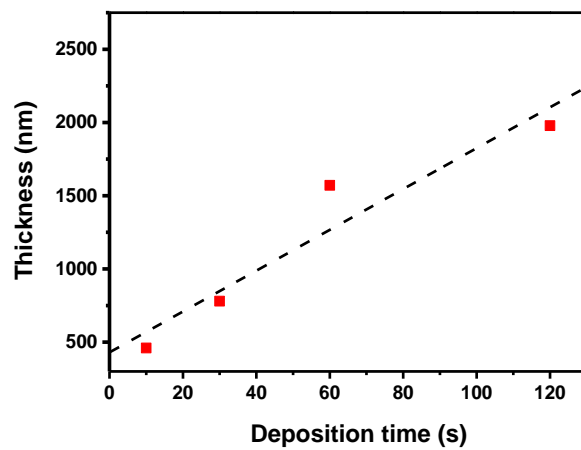
Figure S4.9: Time-dependent thickness plot of BDT-ETTA COF deposited from ethyl acetate at 900 V. Thicknesses obtained from SEM cross-sections.

Voltage dependent deposition of BDT-ETTA COF
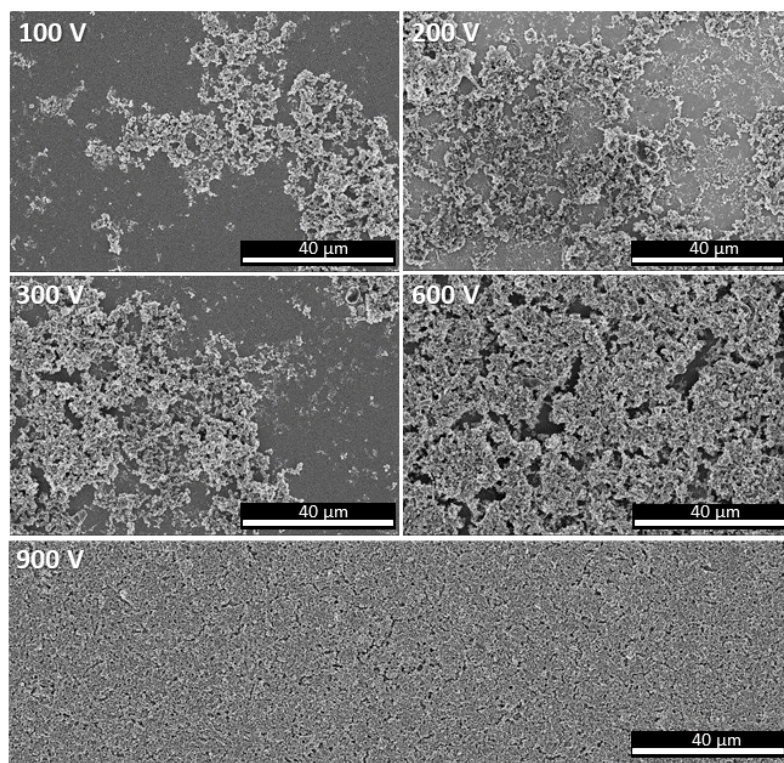
Figure S4.10: SEM top-view images of BDT-ETTA COF deposited at different voltages for 2 min from ethyl acetate.

Mass-dependent deposition of COF-300
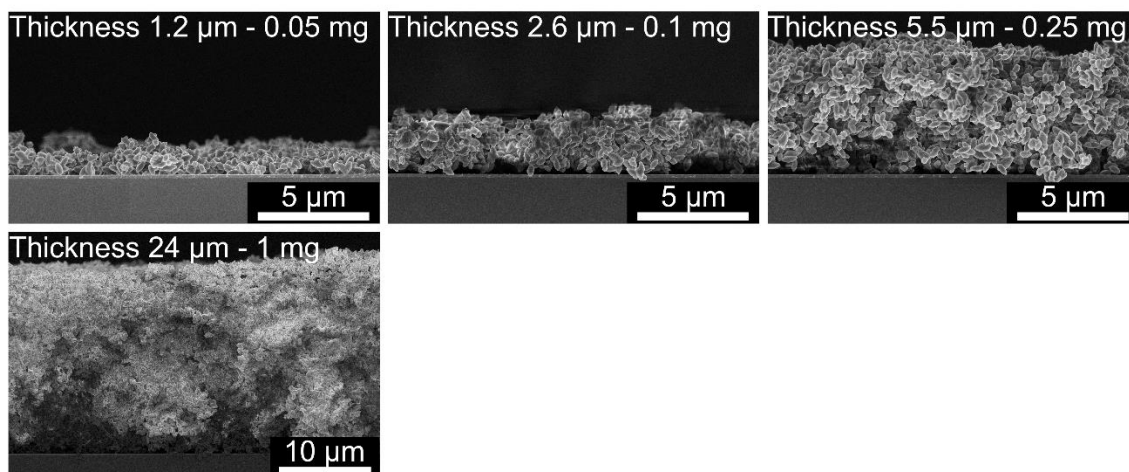
Figure S4.11: SEM cross-section images of depositions of COF-300 using different masses in 10 mL suspension and the resulting film thicknesses. Depositions were carried out at 900 V for 2 min from ethyl acetate.

Large area deposition of BDT-ETTA COF
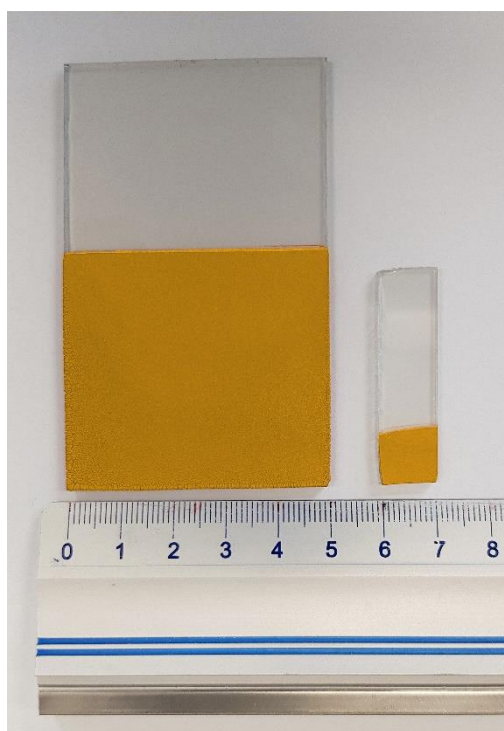
Figure S4.12: Photograph of an EPD of BDT-ETTA COF on 5 cm × 5 cm electrode area as well as a 1 cm × 1 cm film. Both depositions were carried out on FTO at 900 V for 2 min.

SEM Micrographs of BDT-ETTA COF deposited on a porous mesh
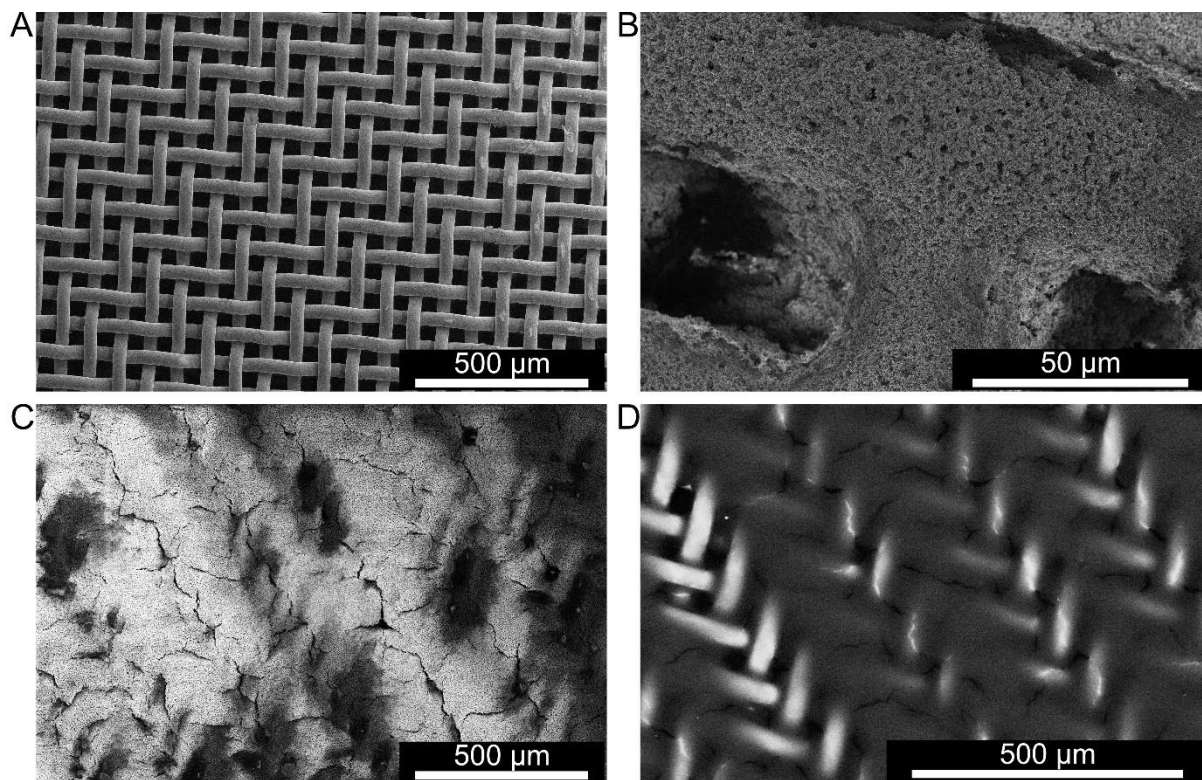
Figure S4.13: SEM top view micrographs of BDT-ETTA COF depositions on a porous steel mesh (mesh size 270). (A) Image of the bare mesh prior to deposition. (B) High magnification of BDT-ETTA COF particles deposited on the mesh. (C) Deposition of BDT-ETTA COF in high concentration on a steel mesh, revealing the complete coverage of the pores. (D) Corresponding back-scattered electron micrograph at 30 kV acceleration voltage, revealing the underlying mesh structure.

Thickness dependent PEC current measurements and chronoamperometry
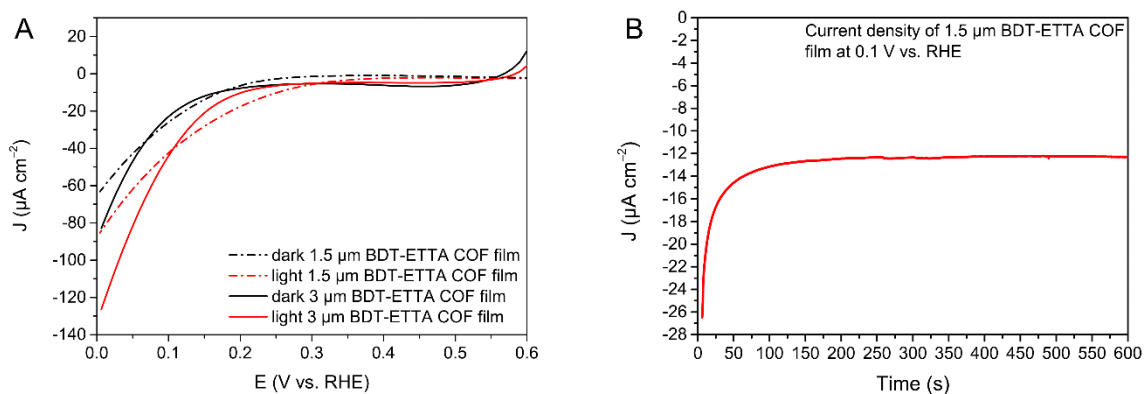
Figure S4.14: (A) Thickness dependent PEC linear sweep voltammograms of electrodes coated with BDT-ETTA COF. Illumination at AM1.5G. (B) Chronoamperometric current density measurement of BDT-ETTA COF under illumination.

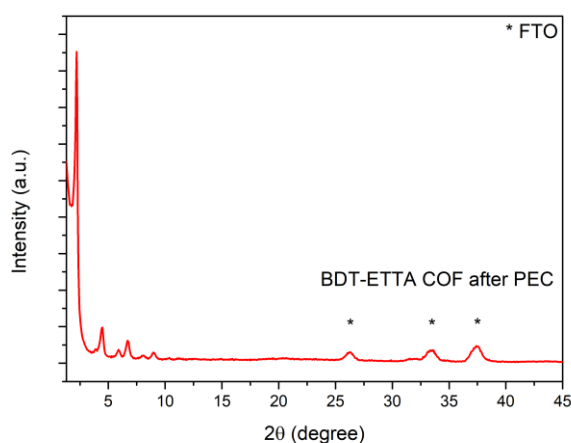## Stability of BDT-ETTA COF after PEC catalysis

Figure S4.15: Stability of BDT-ETTA COF after 30 minutes of chopped illumination at 0.1 V vs. RHE.
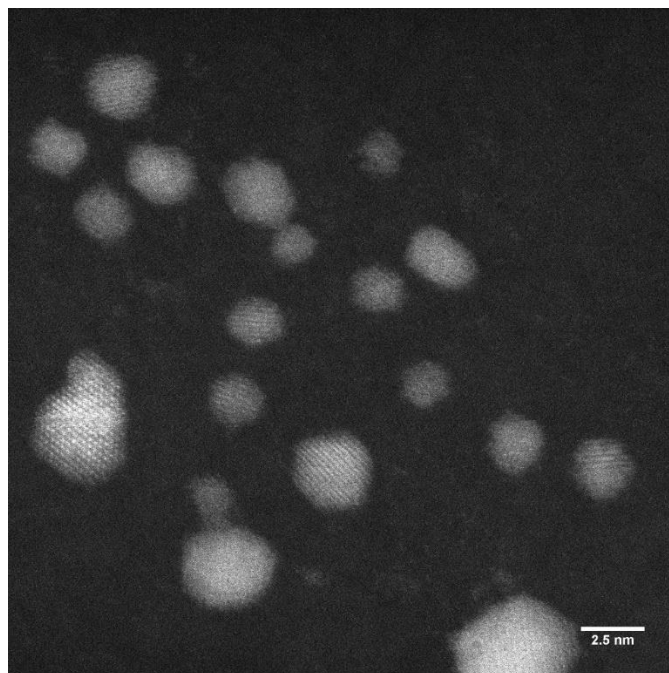
Pt nanoparticles size characterization

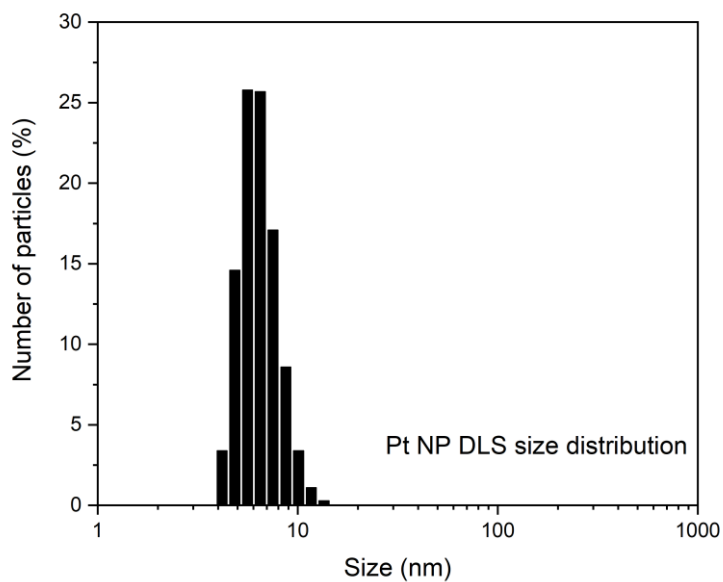Figure S4.16: TEM micrograph of Pt nanoparticles after lyophilization.

Figure S4.17: DLS profile of Pt nanoparticles after lyophilization.

5. High Electrical Conductivities in Doped Wurster-type Covalent Organic Frameworks and Their Thin Films

Julian M. Rotter, Michael Auth, Roman Guntermann, Andre Mähringer, Andreas Sperlich, Vladimir Dyakonov, Dana D. Medina, Thomas Bein, to be submitted.

5.1.   Abstract

Covalent organic frameworks (COFs) are a versatile platform combining attractive properties such as crystallinity, porosity, and chemical and structure modularity which are valuable for various applications. For the incorporation of COFs into optoelectronic devices, high charge carrier transport and intrinsic conductivity are essential. Here, we report the synthesis of WTA and WBDT, two imine-linked COFs, featuring a redox-active Wurster-type motif based on the twisted tetragonal *N,N,N',N'*-tetraphenyl-1,4-phenylenediamine node. By condensing this unit with either terephthalaldehyde (TA) or benzodithiophene dialdehyde (BDT), COFs featuring a dual-pore structure were obtained as highly crystalline materials with large specific surface areas and a mesoporous dual-pore topology. In addition, the experimental high conduction band energies of both COFs render them suitable candidates for oxidative doping. The incorporation of a benzodithiophene linear building block into the COF allowed for high intrinsic macroscopic conductivity. The anisotropic conductivities and isotropic conductivities were probed by van-der-Pauw measurements using oriented films and pressed pellets, respectively. Furthermore, the impact of different dopants such as F_4TCNQ, antimony pentachloride and iodine on the conductivities of the resulting doped COFs was studied. By using the strong organic acceptor F_4TCNQ, long-term stable electrical conductivities as high as 3.67 S m^{-1} were achieved for the anisotropic transport in an oriented film, the highest for any doped COF to date. Interestingly, no significant differences between isotropic and anisotropic charge transport were found in films and pressed pellets. This work expands the list of possible building nodes for electrically conducting COFs from solely highly planar systems to twisted geometries. The achievement of high and stable electrical conductivities extends the range of applications of new COFs in optoelectronics and may ultimately promote the use of COFs in organic (opto-)electronics.

5.2.   Introduction

Covalent organic frameworks (COFs) have attracted great interest in materials science and polymer chemistry due to their highly modular construction principle and the resulting intriguing properties.[1] COFs emerge from condensation reactions of organic molecular building blocks, whereby the resulting covalent bonds form highly cross-linked porous frameworks.[2,3] They feature high crystallinity, high surface areas, and defined pore systems. By adhering to the principles of reticular synthesis, framework geometry and dimensionality, connectivity and porosity can be predetermined.[1] As a result of this modularity, various functionalities can be introduced into these frameworks through the design of their building blocks, thereby offering access to many different applications such as gas storage,[4,5] sensing,[6,7] catalysis,[8–10] charge storage,[11–13] or optoelectronics.[14–17] Besides the intrinsic structure of the building blocks, the type of linkage between them is of great significance. By varying the linkage, either electronically separated or highly conjugated systems can be designed.[2,18,19]

Recently, several two-dimensional (2D) COFs with enhanced electrical conductivity were reported.[20–22] A common feature of these frameworks is the cross-linking of the building blocks with either sp^2-hybridized carbon-carbon or carbon-nitrogen bonds. The π-conjugation of these linkages facilitates the through-bond charge transport by allowing for an increased charge delocalization, and therefore, in-plane conductivity is improved.[23] Another postulated design criterion for conducting COFs is the use of planar π-system geometries enabling a large area π-orbital overlap between successive COF layers. Here, the strong π-system interaction is expected to facilitate the through-space charge transport perpendicular to the layers.[18,21] However, while various orientation-dependent studies of electrical conductivity have been carried out, there is no in-depth systematic investigation of isotropic versus anisotropic conductivity. The previously described two design strategies have been implemented for constructing 2D COF systems based on planar linkers such as pyrene,[10] tetrathiafulvalene,[22] phthalocyanine[21] or fully aromatic pyrazine systems.[24] In these cases, intrinsic conductivities ranging from 10^{-5} to 10^{-3} S m^{-1} were observed. Chemical doping of these systems with oxidants serving as guest-molecules in the pores led to a further increase in electrical conductivity. Remarkably, iodine so far appears to be the most suitable dopant, whereby the conductivity of the reported COFs was increased by two to three orders of magnitude.[22]

We recently reported on photoactive COFs consisting of sterically demanding building blocks bearing significantly out-of-plane rotated phenyl groups such as in tetraphenylethylene. These types of COFs were shown to be suitable for charge transport in photoelectrochemical water splitting catalysis.[8,25] To expand the paradigm of non-planar, electrically conducting COFs, additional features, such as specific doping sites in sterically demanding linker are of high interest. Here, we realize such a geometry with a Wurster-type motif, to obtain COFs based on *N,N,N',N'*-tetraphenyl-1,4-phenylenediamine (**W**), as a tetragonal node.

Wurster-type compounds are electron-rich molecules derived from *N,N,N',N'*-tetramethyl-1,4-phenylenediamine (TMPD).[26] They can be easily oxidized, generating stabilized radical cations within their π-systems.[27] The doping of this motif through oxidation is a well-studied feature, and the hereby generated radical cations show promising stability as conductive organic materials for charge transport or storage.[28–30] Organic salts based on TMPD as the electron donor and tetracyanoquinodimethane (TCNQ) as the electron acceptor show high electrical conductivities.[31]

Herein, we demonstrate that the Wurster motif can be embedded into different COFs, defined by using two different linear linker molecules. We also investigate the intrinsic conductivity of the two resulting Wurster-COFs. By condensing **W** with either terephthalaldehyde (TA) or the linear dialdehyde of benzodithiophene (BDT), conjugated, highly crystalline and porous imine-linked materials were obtained. We discuss the incorporation of the Wurster-type motif, structural aspects of the COF geometries, the resulting electronic properties, and study the effect of different dopants on the electrical conductivity of these novel frameworks.

5.3.   Results and Discussion

Synthesis. The Wurster-type COFs were synthesized under solvothermal conditions by condensing *N,N,N',N'*-tetra(4-aminophenyl)benzene-1,4-diamine (**W**) with the linear aldehydes terephthalaldehyde (TA) or benzodithiophene dialdehyde (BDT) to form imine-linked COFs, namely WTA and WBDT (Figure 5.1a). To this end, the respective building blocks were suspended in a mixture of mesitylene and benzyl alcohol and a catalytic amount of 6 M acetic acid was added to the mixture. The reaction vessel was sealed and heated for three days at 100 °C. Subsequently, the red precipitates were isolated by filtration and washed with the pure solvent mixture used in the reaction. The COFs were then purified using our recently reported supercritical CO_2 extraction protocol to remove residual guest molecules from the pores.[32]
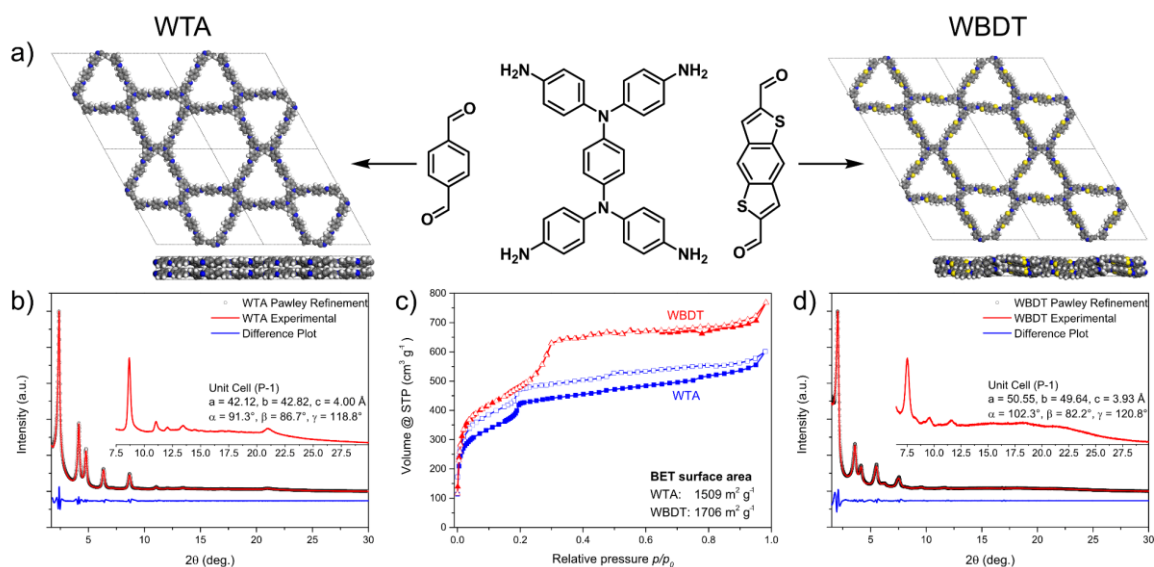

Figure 5.1: a) Schematic presentation of the synthesis of WTA and WBDT from the molecular building blocks. b) PXRD and Pawley refinement of WTA. c) Nitrogen physisorption isotherms of WTA and WBDT. d) PXRD and Pawley refinement of WBDT.

Structural Investigations. Powder X-ray diffraction (PXRD) analysis revealed the formation of highly crystalline materials with well-resolved reflections up to about 22° 2θ (Figure 5.1b, d). To determine the framework topologies of the obtained COFs, several structural models for WTA and WBDT were developed. The combination of the tetragonal **W** building block with TA or BDT should either lead to a tetragonal topology or to a dual-pore, kagome-like topology.[33] Recent reports on tetragonal linkers with similar geometries, like tetraphenylethylene, have shown that kagome-type topologies are

generally preferred.[33,34] Therefore, both structural models were simulated starting with an AA-type, eclipsed layer stacking arrangement, and the associated theoretical PXRD patterns were compared to the experimentally obtained ones. The simulations were carried out using the Forcite module of Materials Studio with the universal force field. Subsequently, the PXRD patterns of the simulated COFs were predicted using the reflex module. The simulations show that the dual-pore kagome structure model is in good agreement with the experimental patterns, and therefore we focused on this model for further modeling (Figure 5.1b, d, and S5.2 and S5.3).

To refine our structure model of the COFs and to gain a deeper understanding of the geometric arrangement of the sterically demanding **W** unit within the framework, we synthesized a molecular fragment by condensing **W** with four monofunctional benzo[*b*]thiophene-2-carboxaldehyde units. Single crystal X-ray analysis of the resulting molecule revealed a counter-clockwise rotation of the triphenylamine moieties, resulting in a chair-like configuration of the molecular fragment (Figure S5.1). This building block geometry is in contrast to the typically propeller-shaped geometries needed for kagome-type structures with hexagonal symmetry. Next, we constructed framework models of WTA and WBDT based on a hexagonal *P*6 space group, where the **W** linker adopts a propeller-like geometry, and the respective triclinic *P*-1 symmetric frameworks, where the **W** geometry is adapted from the single-crystal data. All geometries were optimized using the density functional tight binding plus (DFTB+) code and the 3ob parameter set.[35–37] For both WTA and WBDT it was found that the *P*-1 symmetry is indeed energetically favored by −27.9 or −31.2 kcal/cell, respectively, compared to the hexagonal kagome structures. We can conclude that an apparent kagome, dual-pore structure is present, namely a 2D trihexagonal tiling but only on a higher level of hierarchy, where the atoms are not arranged in hexagonal symmetry. On closer examination, this hexagonal symmetry condition is not preserved on the atomic level, and therefore, according to the symmetry constraints the structures can be only described as kagome-like.

Using the *P*-1 structures, the simulated unit cells were Pawley-refined to match with the experimental ones with very low fitting errors. Additionally, the diffraction patterns were indexed, and the reflections attributed to *hkl* 100, 110, 200, 210, 300, 220, 310, 400, 500 and 001 (by order of appearance) for both COFs (the five strongest reflections for WTA and WBDT are at 2.378, 4.159, 4.795, 6.353, 8.675 ° 2θ and 2.039, 3.586, 4.137, 5.505, 6.215 ° 2θ, respectively). The observed 001 reflections can be directly attributed to the π-

π-stacking distances with *d*-spacing values of 4.00 Å and 3.93 Å for WTA and WBDT, respectively (Figure 5.1b, d).

Physisorption. To determine the internal surface area of the COFs, nitrogen physisorption isotherms were measured. Both COFs exhibit sorption isotherms featuring a mixture of type I and type IVb with two steep nitrogen uptake steps (Figure 5.1c). Here, the first step, at low partial pressure, is characteristic for microporous materials, whereas the second step at higher relative partial pressures reveals additional capillary condensation, indicating the presence of mesopores. The calculated Brunauer, Emmett, Teller (BET) surface areas are 1509 $m^2\,g^{-1}$ and 1706 $m^2\,g^{-1}$ for WTA and WBDT, respectively. Pore sizes were calculated from the nitrogen isotherms using the quenched solid density functional theory (QSDFT) model for 1D cylindrical pores and carbon surfaces. For the COFs, two pore sizes were calculated with 1.76 nm and 2.89 nm (1.78 nm and 2.99 nm from structural simulations) for WTA and 1.79 nm and 3.51 nm (2.12 nm and 3.89 nm from structural simulations) for WBDT (Figure S5.6, S5.7). Additionally, total pore volumes of 1.02 $cm^3\,g^{-1}$ and 1.17 $cm^3\,g^{-1}$ for WTA and WBDT were calculated, respectively. These results confirm the existence of a dual-pore system and strongly support the predicted structures and linker arrangements for WTA and WBDT.
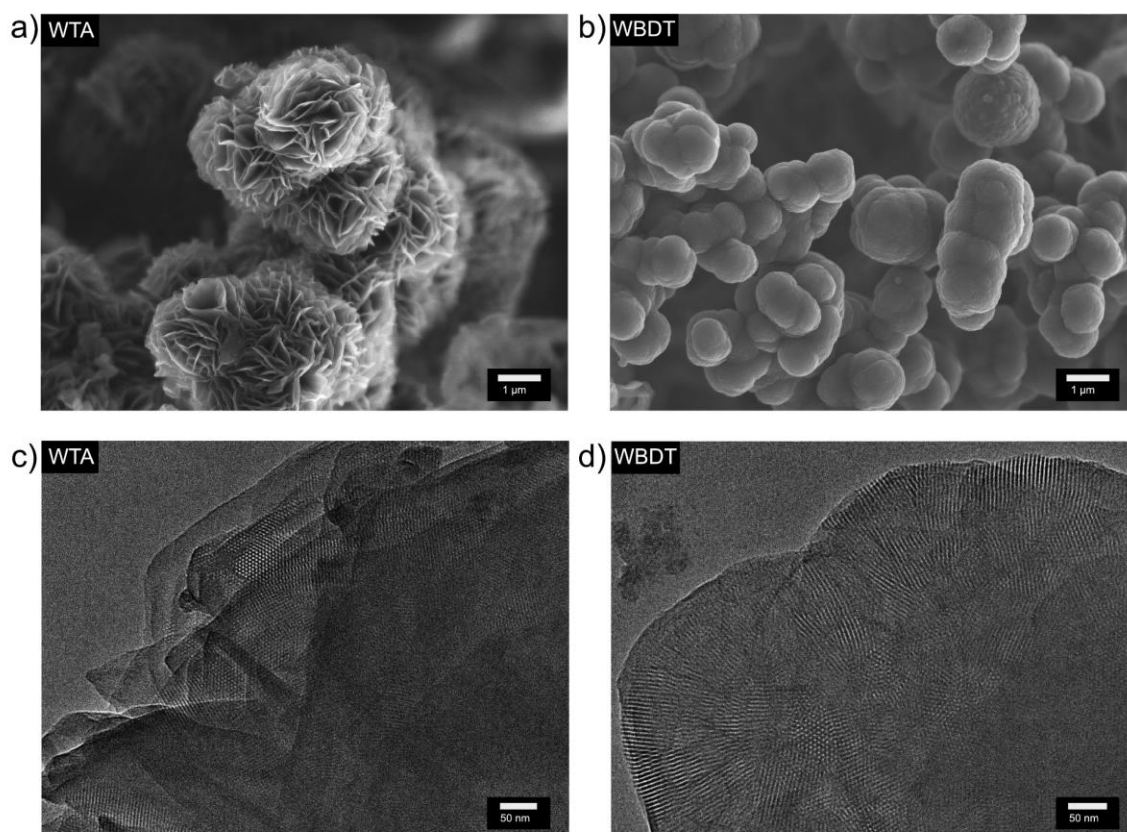
Figure 5.2: a) SEM image of WTA bulk material. b) SEM image of WBDT bulk material. c) TEM image of WTA bulk material. d) TEM image of WBDT bulk material.

Particle Morphology. The morphology of the obtained COFs was assessed by scanning electron microscopy (SEM). WTA powder consists of microparticles of a rosebud-like structure in which platelets intergrow to form larger spherical aggregates of about 2 to 3 μm (Figure 5.2a). In contrast, WBDT powder consists of spherical particles of about 1 μm in size, which intergrow into larger connected structures (Figure 5.2b). Transmission electron microscopy (TEM) clearly shows the channel structures of the two COFs. Domain sizes of about 200 nm and 100 nm can be observed for WTA and WBDT, respectively (Figure 5.2c, d). In both cases, crystal domains where the c-zone axis is oriented parallel to the incident electron beam were detected. This visualises the pseudo-hexagonal pattern generated by the dual-pore arrangement, in excellent agreement with the PXRD and simulation data.
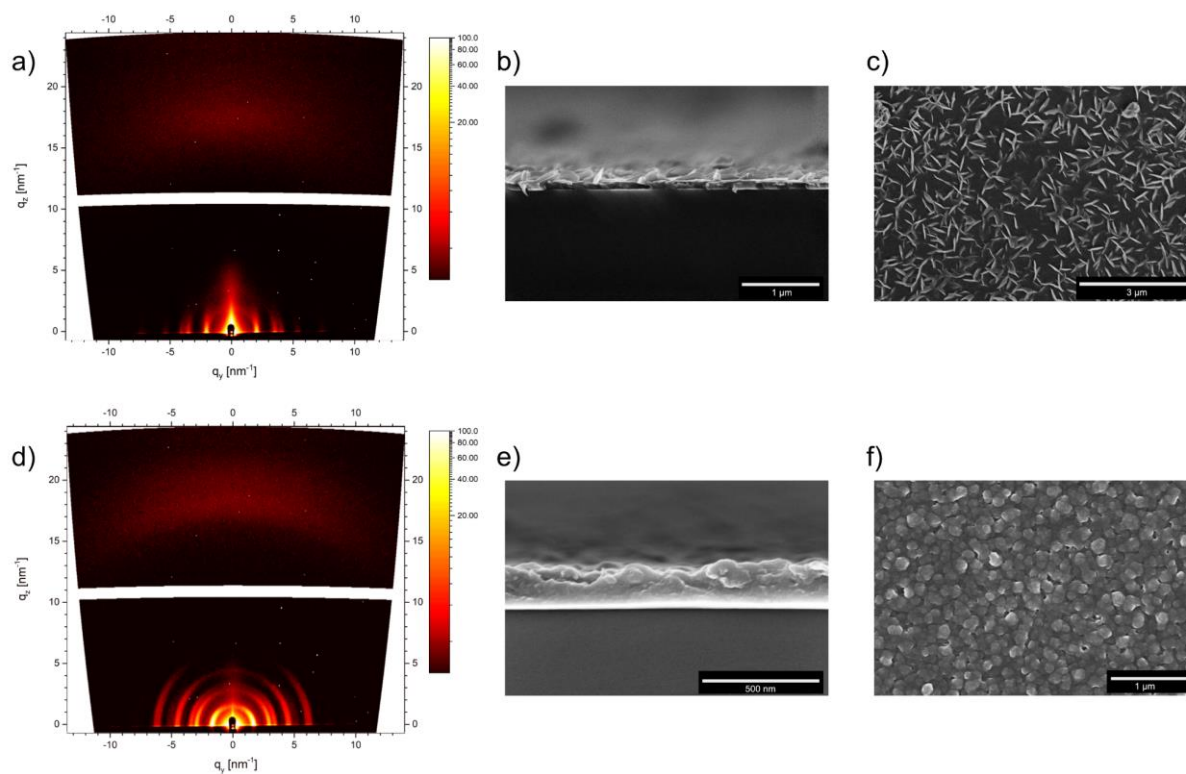
Figure 5.3: a) GIWAXS 2D diffraction pattern of a WTA thin film on glass. b) SEM cross-section image of a WTA thin film with c), the corresponding top-view. d) GIWAXS 2D diffraction pattern of a WBDT thin film on glass. e) SEM cross-section of a WBDT thin film with f), the corresponding top-view.

COF Films. In addition to bulk synthesis, the surface growth of the Wurster-type COFs WTA and WBDT was investigated. In a typical thin film synthesis, a glass substrate was placed horizontally in the COF reaction vessel, and the COF powder synthesis procedure was carried out.[38] After 24 h, the substrate was recovered from the reaction vessel, and the respective COF was obtained as a transparent yet iridescent film on the bottom side of the substrate. To examine the crystallinity of the films, grazing incidence wide-angle X-ray scattering (GIWAXS) images were recorded using an incident angle of 0.22° and a 2D detector. For both COFs, strong X-ray reflections were observed, and the q-values of the respective signals match the ones from the bulk PXRD data (Figure 5.3a, d) (WTA: q_y-values: 1.69, 2.98, 3.41, 4.55, 6.18 nm^{-1}; q_z-value: 15.7 nm^{-1}. WBDT: q_y-values: 1.44, 2.56, 2.90, 3.91, 4.42 nm^{-1}; q_z-value: 16.0 nm^{-1}). Furthermore, the low arching of the in-plane reflections at low q_y-values from 2 – 8 nm^{-1} and the out-of-plane π-stacking reflection at a larger q_z of about 15 nm^{-1} reveal that the COFs deposit as preferentially oriented materials on the substrate, with many of the 1D pores positioned perpendicular to the

substrate. SEM cross-sections of the films show thicknesses of about 80 nm for WTA and 210 nm for WBDT (Figure 5.3b, e). Both materials deposit as dense films without interstitial voids on the substrate. Additionally, thin platelet crystallites sized 100 to 200 nm emerge from the surface of the WTA film. The SEM top-view images reveal densely-packed films covering large areas without apparent cracks. For WTA, thin platelets are visible on the surface, while for WBDT, the film surface is composed of spherical grains of about 50 nm in size (Figure 5.3c, f).
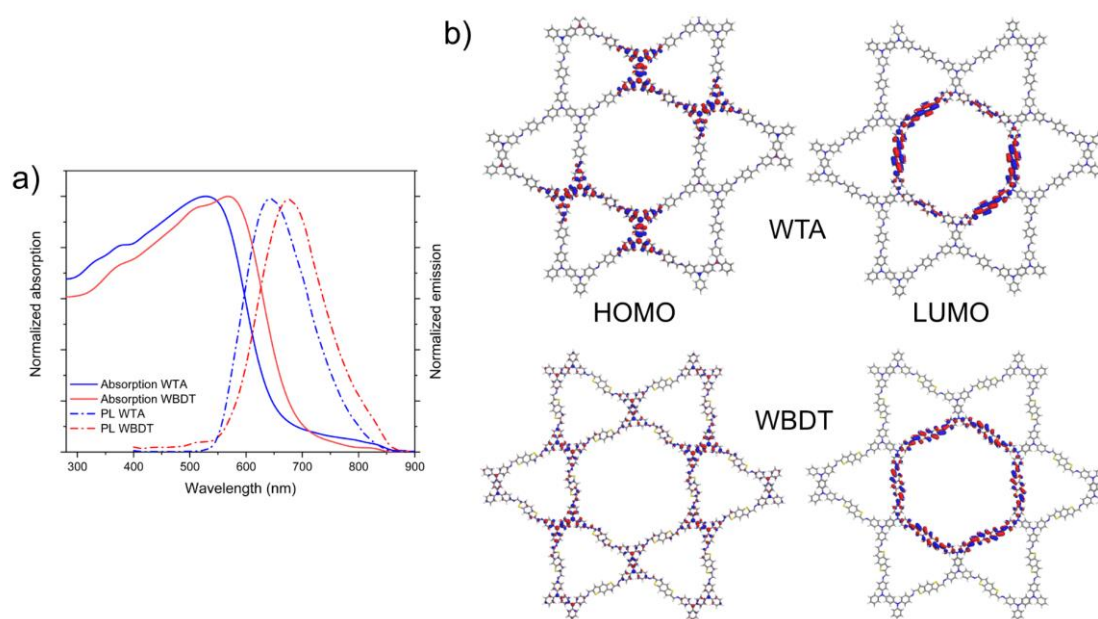
Figure 5.4: UV-vis absorption and PL emission spectra of WTA and WBDT thin films. b) Waveplots of the frontier molecular orbital localizations for WTA and WBDT.

Photophysical Properties. The photophysical properties of the Wurster-type COF films were investigated by means of UV-vis absorption spectroscopy, photoluminescence (PL) and time-correlated single-photon counting (TCSPC) (Figure 5.4a and Figure S5.10, S5.11). Both COFs are red-colored materials and show similar light absorption characteristics with a strong absorption in the visible spectrum. While WTA COF has an absorption onset at about 660 nm, the incorporation of the BDT building block into the COF causes a 40 nm red-shift (Figure 5.4a). Assuming direct optical transitions for both materials, optical band gaps of 1.96 eV and 1.87 eV for WTA and WBDT COFs were calculated using Tauc plots (Figures S5.8, S5.9). PL spectra of the COFs were recorded by exciting the materials with a 378 nm laser light source. The resulting spectra show large stoke-shifts of about 110 nm with PL emission maxima at 641 nm and 673 nm for WTA

and WBDT, respectively, and overall broad emissions ranging from 550 – 850 nm (Figure 5.4a). Fluorescence lifetime decays were obtained by TCSPC using a 378 nm excitation wavelength. The decay curves were subsequently deconvoluted using the instrument response function (IRF) and a biexponential fit. TCSPC data were recorded at the respective PL maxima of the COFs under a nitrogen atmosphere. Here, very short lifetimes of the photoexcited states can be observed. In WTA and WBDT, the major components, 87.6% and 86.5%, decay within 100 ps and 130 ps, respectively, while the minor components decay within 750 ps and 740 ps, respectively (Figures S5.10, S5.11). These very short-lived excited states point to the presence of a push-pull system in the COF, in which electron-donating and -accepting motifs are separated. To probe whether such localization is present, we constructed theoretical model pore systems roughly the size of four unit cells for WTA (924 atoms) and WBDT (1032 atoms) using one layer of their refined structure models. Hydrogen atoms were used to terminate the lattice, and the hydrogen geometries were refined at the same DFTB+ (3ob) level while keeping the remainder of the structure restrained. Subsequently, orbital energies and localizations were calculated using density functional theory (DFT) at the PBE0-def2SVP level.[39] By plotting the localization of the highest occupied molecular orbitals (HOMOs) and lowest unoccupied molecular orbitals (LUMOs) for WTA and WBDT COFs, sharp spatial separations of the respective HOMOs and LUMOs can be observed. For both WTA and WBDT, the HOMO is strongly localized on the six central Wurster-type motifs while the LUMO spans along the inner linear linkers, which form the hexagonal pore (Figure 5.4b). From these calculations, we can conclude that the electron-donating property of the Wurster-motif is preserved within the model systems. Consequently, we propose that the electron-donating- and -accepting parts are partially separated within the imine-linked frameworks, creating a push-pull system as indicated by the TCSPC data.
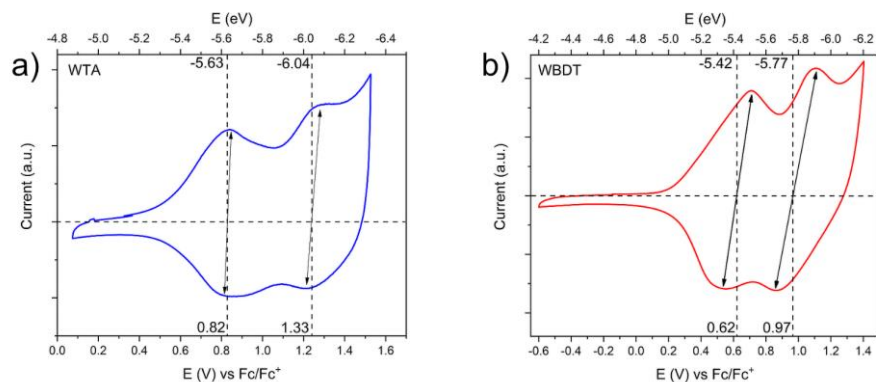
Figure 5.5: Cyclic voltammograms of a) WTA and b) WBDT.

The retention of the electron-rich property of the Wurster-motif in the COFs should lead to valence band edges with high energies. Consequently, the COFs should undergo oxidation at relatively low potentials. Here, we used cyclic voltammetry (CV) to determine the oxidation potentials of WTA and WBDT electrochemically. To this end, we grew the COFs as films on gold-coated glass substrates (modified with a 40 nm thick, conductive gold coating). CV measurements of the respective films were subsequently carried out in a typical three-electrode setup using tetraethylammonium tetrafluoroborate as the electrolyte in argon-purged, anhydrous acetonitrile. The measurements were referenced against the ferrocene/ferrocenium (Fc/Fc$^+$) redox couple. For WTA, two redox couples were found – at 0.82 V and 1.33 V vs. Fc/Fc$^+$. Here, the narrow peak separations of 20 mV for the first and 62 mV for the second redox couple show that the oxidation of WTA is a highly reversible process and that the redox properties typical for Wurster-compounds are retained in the COF (Figure 5.5a).[30]

WBDT shows two redox couples as well, the first at 0.62 V and the second at 0.97 V vs Fc/Fc$^+$. With oxidation-reduction peak separations of 170 mV for the first oxidation step and 220 mV for the second oxidation step, both oxidation steps can be described as quasi-reversible (Figure 5.5b).

With the CV data at hand, the absolute energy of the valence band edge against the vacuum scale can be determined by comparing the oxidation onset potential against the HOMO energy of ferrocene.[40] Consequently, the energy of the conduction band edge can then be assessed by adding the optical band gap energy to the absolute energy of the valence band. The absolute valence band energy is determined by using the first oxidation onset potential and correlating this to the vacuum energy of the ferrocene HOMO energy at 4.8

eV.[40] Thereby, valence band energies of -5.2 eV and -5.0 eV and conduction band energies of -3.24 eV and -3.13 eV can be calculated for WTA and WBDT, respectively. The high conduction band energies of the COFs render the materials as suitable candidates for oxidative doping.

Electrical conductivity. Here, we measured the electrical conductivity of the materials presented as oriented films on glass, and as pressed pellets of bulk materials. The measurements were carried out using a van-der-Pauw four-probe setup with an electrode separation of 5 mm. For WTA, electrical conductivities of $4.91 \cdot 10^{-6}$ S m^{-1} for the pressed pellet and $3.78 \cdot 10^{-6}$ S m^{-1} for the oriented film were determined. In contrast to WTA, the conductivity of WBDT is two to three orders of magnitude higher, with $2.70 \cdot 10^{-4}$ S m^{-1} and $1.64 \cdot 10^{-3}$ S m^{-1} for the pressed pellet and the oriented film, respectively. For WTA, no large difference in conductivity was measured for the oriented film and the pressed pellet. In the case of WBDT, the orientation of the film apparently increased the conductivity by one order of magnitude. We attribute this to the orientation of the crystallites in the film, where charge transport occurs mainly throughout the conjugated 2D layers. We attribute the absence of this effect for WTA to the film morphology, in which individual crystallites protrude from the plane of the oriented film and thus act as barriers and impede charge transport.

COF doping. The measured intrinsic electrical conductivity values of WBDT are among the highest reported for COFs so far.[24] This fact is particularly remarkable since the WBDT COF layer geometry is twisted and non-planar which is in contrast to the assumption that highly planar 2D layers are essential for high conductivities.[21] As Dinca and coworkers have previously reported, it is difficult to precisely compare measured electrical conductivities in molecular frameworks. There it was shown that the respective measuring methods have a great influence on the result and that conductivity values of different methods can often not be compared with each other.[41] Encouraged by the high intrinsic conductivities of our COFs, we turned our attention to the chemical doping of the WBDT framework. As dopants, we chose 2,3,5,6-tetrafluoro-tetracyanoquinodimethane (F$_4$TCNQ) as an organic electron acceptor, antimony pentachloride (SbCl$_5$) as a strong inorganic oxidizer and iodine, which is commonly used for the doping of COFs.[24] Bulk WBDT was doped by adding the material to a solution consisting of acetonitrile and the dopant. As soon as the red COF powder contacted the doping solution, an instant color change to dark grey was observed, indicating a direct reaction of the material with the

respective dopant. To ensure homogeneous doping of the framework, the material was stirred in the solution for one hour. The optimal dopant concentration was determined by using different amounts of F_4TCNQ and recording the resulting conductivities of pressed powder pellets. Thereby, a concentration of 0.3 equivalents of dopant, compared to the calculated number of Wurster-moieties, was determined as the ideal doping level, which was subsequently used for the doping experiments (Figure S5.12). Successful doping was observed with all three dopants, as illustrated by a strong increase in conductivity. While doping with antimony pentachloride and iodine showed an increase in conductivity by two orders of magnitude to $3.09 \cdot 10^{-2}$ S m^{-1} and $4.72 \cdot 10^{-2}$ S m^{-1}, respectively, doping with F_4TCNQ proved to be even more effective, with an increase to $3.67 \cdot 10^{0}$ S m^{-1}. Thin films of WBDT were doped at a level similar to the bulk material by placing them into the solution of the respective dopant. For these experiments, comparable increases in conductivity were observed (see Table 5.1). In addition, bulk WTA was doped with F_4TCNQ to assess whether a similar increase in conductivity can also be observed. Here, the doping caused only a minor increase in conductivity from $4.91 \cdot 10^{-6}$ S m^{-1} to $1.51 \cdot 10^{-5}$ S m^{-1}. Therefore, we postulate that, although both COFs feature a Wurster-type motif, the efficiency of doping is also highly dependent on the linear building block. The integration of the electroactive BDT building block apparently facilitates charge transport, resulting in increased electrical conductivity and allowing for effective doping. Due to the large difference in doping behavior between WTA and WBDT, in the following we focus on the WBDT system.

Table 5.1: Overview of the electrical conductivities measured for WTA and WBT pressed pellets and thin films.

COF system	Pressed pellet	Oriented film
WTA, pristine	$4.91 \cdot 10^{-6}$ S m^{-1}	$3.78 \cdot 10^{-6}$ S m^{-1}
WTA / F_4TCNQ	$1.51 \cdot 10^{-5}$ S m^{-1}	$7.35 \cdot 10^{-5}$ S m^{-1}
WBDT, pristine	$2.70 \cdot 10^{-4}$ S m^{-1}	$1.64 \cdot 10^{-3}$ S m^{-1}
WBDT / F_4TCNQ	$3.67 \cdot 10^{0}$ S m^{-1}	$2.18 \cdot 10^{0}$ S m^{-1}
WBDT / SbCl$_5$	$3.09 \cdot 10^{-2}$ S m^{-1}	$6.86 \cdot 10^{-2}$ S m^{-1}
WBDT / Iodine	$4.72 \cdot 10^{-2}$ S m^{-1}	$1.33 \cdot 10^{-2}$ S m^{-1}

For a doping to be meaningfully used for increasing conductivity, the resulting doping must be permanent and stable. While iodine has been successfully used to increase conductivities by several orders of magnitude for various COFs, the high vapor pressure of iodine hinders long-term doping and the measured conductivities decreased within 24 h after doping.[22] To assess the stability of the doping effect on the WBDT, we conducted time-dependent conductivity measurements of the respective pellets after 1 day, 3 days and 7 days (Figure 5.6a). Here, COFs doped with iodine and antimony pentachloride showed a decline of conductivity within the first 24 h after doping. Subsequently, the conductivity of the iodine-doped material stabilized at about one order of magnitude higher than the pristine COF pellet. In contrast to iodine, the conductivities of antimony pentachloride-doped WBDT continued to decline and fell below the values of the pristine COF pellet within 3 days. Using the organic F_4TCNQ acceptor molecule proved to create doped COFs with stable conductivity over the whole course of the measurement (Figure 5.6a), while also retaining the crystallinity of the COF (Figure S5.13). This result shows that the use of a strong electron acceptor that does not chemically react with the host material is the ideal dopant to generate a highly conductive, stable doped COF.
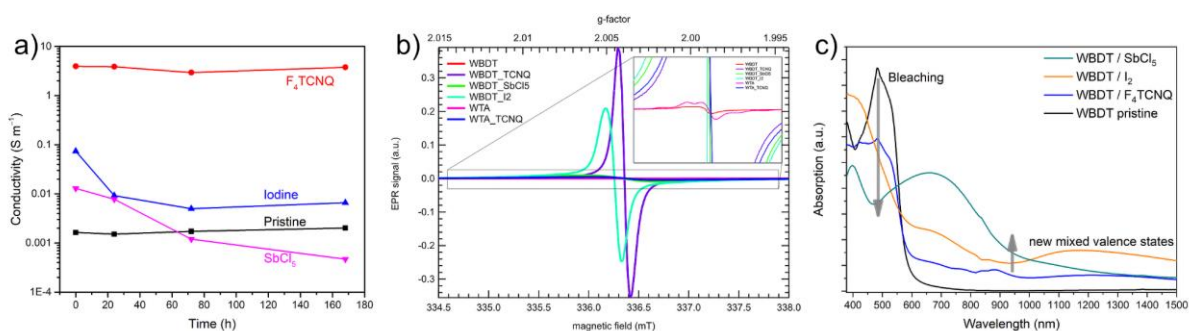
Figure 5.6: a) Time-dependent stability measurements of the conductivity of WBDT with different dopings. b) EPR data of WTA, WBDT and the respective dopings. c) UV-vis-NIR absorption spectra of doped WBDT.

To compare the efficiency of radical charge carrier generation, electron paramagnetic resonance (EPR) spectra were recorded for the doped and pristine WTA and WBDT bulk materials (Figure 5.6b). For the pristine COFs, only minimal amounts of paramagnetic $WTA^{\cdot+}$ and $WBDT^{\cdot+}$ were found, which can be attributed to weakly doped as-synthesized COFs. The existence of a small number of radicals within the pristine materials can be attributed to linker impurities or the oxidation of the COFs in air. Upon doping WTA with F_4TCNQ, an increase by one order of magnitude in paramagnetic intensity can be

observed. For the doping of WBDT, the signal intensity increases by three to four orders of magnitude for iodine and F_4TCNQ, respectively, while antimony pentachloride doping generates only a small amount of paramagnetic species. These observed relative EPR signal intensities are in direct correlation with the changes in the electrical conductivity recorded upon doping. Interestingly, two different species of $WBDT^{\cdot+}$ radical centers are found in the EPR data. The pristine COF, as well as the antimony pentachloride- and F_4TCNQ-doped WBDT, feature a paramagnetic center at g = 2.0044, while the iodine-induced $WBDT^{\cdot+}$ signal appears at g = 2.005 (Figure 5.6b). This suggests that the doped species differ from each other, and that different $WBDT^{\cdot+}$ radical populations are created.

As described previously, the doping is not only reflected in the conductivity but also in a change of color. Therefore, UV-vis-NIR absorption spectra were recorded for the doped WBDT films. A strong bathochromic shift extends the absorption of all doped WBDT materials into the NIR up to 1500 nm (Figure 5.6c). This red-shift is accompanied by significant bleaching in the visible range as compared to the pristine material. Upon doping, very broad absorption bands at around 700 nm emerge, which extend to 900 nm for iodine and F_4TCNQ and to more than 1000 nm for antimony pentachloride. This is in line with the observed immediate and strong color change for the COFs. The new absorption in the NIR is strongest for antimony pentachloride and weakest for F_4TCNQ. The resulting broad and low-intensity NIR absorption is typical for conjugated and doped COFs, where free radical charge carriers are delocalized and generate a mixed-valence state between doped and undoped sites which can be related to the enhanced electrical conductivity.[22]

5.4.   Conclusion

We report two novel, 2D imine-linked COFs based on the electron-rich Wurster-motif, named WTA and WBDT. The highly crystalline materials were analyzed by PXRD refinement and structure modeling. Nitrogen physisorption revealed the existence of dual-pore systems with high surface areas. Additionally, oriented thin films of the COFs were synthesized, which were subsequently used to study the optical properties and electronic energy levels. The macroscopic electrical conductivity of the COFs was studied by means of van-der-Pauw measurements on pressed pellets and oriented thin films grown on glass substrates. Depending on the linear linker in the COF, conductivities of the

pristine materials as high as $1.64 \cdot 10^{-3}$ S m^{-1} were determined. Furthermore, different dopants, as well as different doping concentrations, were investigated to create the radical cation forms of the COFs, and their long-term effect on the electrical conductivity was assessed. The use of F$_4$TCNQ as a strong electron acceptor yielded conductivities as high as $3.67 \cdot 10^0$ S m^{-1}, the highest value for doped imine-linked COFs reported so far. Moreover, the impact of doping on the optical absorption and the formation of radicals in the COF could be correlated with the changes in conductivity. In contrast to previous work in the field of conductive COFs, it could be shown that the high conductivities resulting from doping are stable over time for the organic acceptor molecule F$_4$TCNQ. This stability is of central importance in order to be able to exploit high conductivities by doping permanently.

In the context of electrical conductivity, we discovered that the geometry of the linker can deviate from planarity and show high values. In addition, non-planar COFs have the added value of high-crystallinity and robustness achieved through molecular docking sites. Encoding electrical conductivity in these non-planar systems requires the selection of electroactive building blocks. Increasing the electrical conductivity in these systems through doping is highly dependent on the dopant and we can attribute the long-term stability to a combination of factors e.g., a robust framework and a chemically innocent dopant. We believe that these results will contribute to the development of new strategies for the design of COFs for various applications, such as sensors or optoelectronics.

5.5.   References

 (1) Diercks, C. S.; Yaghi, O. M. The atom, the molecule, and the covalent organic framework. *Science* **2017**, *355*.

 (2) Lohse, M. S.; Bein, T. Covalent Organic Frameworks: Structures, Synthesis, and Applications. *Adv. Funct. Mater.* **2018**, *355*, 1705553.

 (3) Huang, N.; Wang, P.; Jiang, D. Covalent organic frameworks: a materials platform for structural and functional designs. *Nat. Rev. Mater.*, *1*, 1–19.

 (4) Fan, H.; Mundstock, A.; Feldhoff, A.; Knebel, A.; Gu, J.; Meng, H.; Caro, J. Covalent Organic Framework-Covalent Organic Framework Bilayer Membranes for Highly Selective Gas Separation. *JACS* **2018**, *140*, 10094–10098.

 (5) Li, Z.; Feng, X.; Zou, Y.; Zhang, Y.; Xia, H.; Liu, X.; Mu, Y. A 2D azine-linked covalent organic framework for gas storage applications. *Chemical communications (Cambridge, England)* **2014**, *50*, 13825–13828.

(6) Ding, S.-Y.; Dong, M.; Wang, Y.-W.; Chen, Y.-T.; Wang, H.-Z.; Su, C.-Y.; Wang, W. Thioether-Based Fluorescent Covalent Organic Framework for Selective Detection and Facile Removal of Mercury(II). *JACS* **2016**, *138*, 3031–3037.

(7) Li, Z.; Zhang, Y.; Xia, H.; Mu, Y.; Liu, X. A robust and luminescent covalent organic framework as a highly sensitive and selective sensor for the detection of Cu(2+) ions. *Chemical communications (Cambridge, England)* **2016**, *52*, 6613–6616.

(8) Sick, T.; Hufnagel, A. G.; Kampmann, J.; Kondofersky, I.; Calik, M.; Rotter, J. M.; Evans, A.; Döblinger, M.; Herbert, S.; Peters, K.*; et al.* Oriented Films of Conjugated 2D Covalent Organic Frameworks as Photocathodes for Water Splitting. *JACS* **2018**, *140*, 2085–2092.

(9) Wang, X.; Chen, L.; Chong, S. Y.; Little, M. A.; Wu, Y.; Zhu, W.-H.; Clowes, R.; Yan, Y.; Zwijnenburg, M. A.; Sprick, R. S.*; et al.* Sulfone-containing covalent organic frameworks for photocatalytic hydrogen evolution from water. *Nat. Chem.* **2018**, *10*, 1180–1189.

(10) 2D sp2 Carbon-Conjugated Covalent Organic Frameworks for Photocatalytic Hydrogen Production from Water. *Chem* **2019**, *5*, 1632–1647.

(11) DeBlase, C. R.; Silberstein, K. E.; Truong, T.-T.; Abruña, H. D.; Dichtel, W. R. β-Ketoenamine-linked covalent organic frameworks capable of pseudocapacitive energy storage. *JACS* **2013**, *135*, 16821–16824.

(12) Chandra, S.; Roy Chowdhury, D.; Addicoat, M.; Heine, T.; Paul, A.; Banerjee, R. Molecular Level Control of the Capacitance of Two-Dimensional Covalent Organic Frameworks: Role of Hydrogen Bonding in Energy Storage Materials. *Chem. Mater.* **2017**, *29*, 2074–2080.

(13) Halder, A.; Ghosh, M.; Khayum M, A.; Bera, S.; Addicoat, M.; Sasmal, H. S.; Karak, S.; Kurungot, S.; Banerjee, R. Interlayer Hydrogen-Bonded Covalent Organic Frameworks as High-Performance Supercapacitors. *JACS* **2018**, *140*, 10941–10945.

(14) Wang, H.; Zeng, Z.; Xu, P.; Li, L.; Zeng, G.; Xiao, R.; Tang, Z.; Huang, D.; Tang, L.; Lai, C.*; et al.* Recent progress in covalent organic framework thin films: fabrications, applications and perspectives. *Chem. Soc. Rev.* **2019**, *48*, 488–516.

(15) Medina, D. D.; Petrus, M. L.; Jumabekov, A. N.; Margraf, J. T.; Weinberger, S.; Rotter, J. M.; Clark, T.; Bein, T. Directional Charge-Carrier Transport in Oriented Benzodithiophene Covalent Organic Framework Thin Films. *ACS Nano* **2017**, *11*, 2706–2713.

(16) Medina, D. D.; Werner, V.; Auras, F.; Tautz, R.; Dogru, M.; Schuster, J.; Linke, S.; Döblinger, M.; Feldmann, J.; Knochel, P.*; et al.* Oriented thin films of a benzodithiophene covalent organic framework. *ACS Nano* **2014**, *8*, 4042–4052.

(17) Medina, D. D.; Sick, T.; Bein, T. Photoactive and Conducting Covalent Organic Frameworks. *Adv. Energy Mater.* **2017**, *7*, 1700387.

(18) Guo, J.; Xu, Y.; Jin, S.; Chen, L.; Kaji, T.; Honsho, Y.; Addicoat, M. A.; Kim, J.; Saeki, A.; Ihee, H.*; et al.* Conjugated organic framework with three-dimensionally ordered stable structure and delocalized π clouds. *Nat. Commun.*, *4*, 2736.

(19) Calik, M.; Auras, F.; Salonen, L. M.; Bader, K.; Grill, I.; Handloser, M.; Medina, D. D.; Dogru, M.; Löbermann, F.; Trauner, D.*; et al.* Extraction of photogenerated electrons and holes from a covalent organic framework integrated heterojunction. *JACS* **2014**, *136*, 17802–17807.

(20) Li, H.; Chang, J.; Li, S.; Guan, X.; Li, D.; Li, C.; Tang, L.; Xue, M.; Yan, Y.; Valtchev, V.*; et al.* Three-Dimensional Tetrathiafulvalene-Based Covalent Organic Frameworks for Tunable Electrical Conductivity. *JACS* **2019**, *141*, 13324–13329.

(21) Meng, Z.; Stolz, R. M.; Mirica, K. A. Two-Dimensional Chemiresistive Covalent Organic Framework with High Intrinsic Conductivity. *JACS* **2019**, *141*, 11929–11937.

(22) Cai, S.-L.; Zhang, Y.-B.; Pun, A. B.; He, B.; Yang, J.; Toma, F. M.; Sharp, I. D.; Yaghi, O. M.; Fan, J.; Zheng, S.-R.*; et al.* Tunable electrical conductivity in oriented thin films of tetrathiafulvalene-based covalent organic framework. *Chem. Sci.* **2014**, *5*, 4693–4700.

(23) DeBlase, C. R.; Dichtel, W. R. Moving Beyond Boron: The Emergence of New Linkage Chemistries in Covalent Organic Frameworks. *Macromolecules* **2016**, *49*, 5297–5305.

(24) Kim, S.; Choi, H. C. Light-promoted synthesis of highly-conjugated crystalline covalent organic framework. *Commun. Chem.*, *2*, 1–8.

(25) Rotter, J. M.; Weinberger, S.; Kampmann, J.; Sick, T.; Shalom, M.; Bein, T.; Medina, D. D. Covalent Organic Framework Films through Electrophoretic Deposition—Creating Efficient Morphologies for Catalysis. *Chem. Mater.* **2019**, *31*, 10008–10016.

(26) Yamashita, Y.; Tomura, M. Highly polarized electron donors, acceptors and donor–acceptor compounds for organic conductors. *J. Mater. Chem.* **1998**, *8*, 1933–1944.

(27) Zhang, J.; Guo, S.-Z.; Dong, Y.-B.; Rao, L.; Yin, J.; Yu, G.-A.; Hartl, F.; Liu, S. H. Multistep Oxidation of Diethynyl Oligophenylamine-Bridged Diruthenium and Diiron Complexes. *Inorg. Chem.* **2017**, *56*, 1001–1015.

(28) Ghalsasi, P. S.; Cage, B.; Yarger, J. L. Studies on TMPD:TCNB; a donor-acceptor with room temperature paramagnetism and n-pi interaction. *Molecules (Basel, Switzerland)* **2004**, *9*, 808–814.

(29) CHen, C.-J.; Yen, H.-J.; Chen, W.-C.; Liou, G.-S. Novel high-performance polymer memory devices containing (OMe)2tetraphenyl-p-phenylenediamine moieties. *J. Polym. Sci., Part A: Polym. Chem.* **2011**, *49*, 3709–3718.

(30) EL-Mahdy, A. F. M.; Mohamed, M. G.; Mansoure, T. H.; Yu, H.-H.; Chen, T.; Kuo, S.-W. Ultrastable tetraphenyl-p-phenylenediamine-based covalent organic frameworks as platforms for high-performance electrochemical supercapacitors. *Chem. Commun.* [Online early access]. DOI: 10.1039/C9CC08107K. https://pubs.rsc.org/en/content/articlepdf/2019/cc/c9cc08107k.

(31) Staab, H. A.; Hinz, R.; Knaus, G. H.; Krieger, C. Elektron-Donor-Acceptor-Verbindungen, XXXII. Ein Elektron-Donor-Acceptor-Paracyclophan mitN,N,N′,N′-Tetramethyl-p-phenylendiamin- und 7,7,8,8-Tetracyanchinodimethan-Untereinheiten. *Ber.* **1983**, *116*, 2835–2847.

(32) Sick, T.; Rotter, J. M.; Reuter, S.; Kandambeth, S.; Bach, N. N.; Döblinger, M.; Merz, J.; Clark, T.; Marder, T. B.; Bein, T.*; et al.* Switching On and Off Interlayer Correlations and Porosity in 2D Covalent Organic Frameworks. *JACS* [Online early access]. DOI: 10.1021/jacs.9b02800.

(33) Ascherl, L.; Sick, T.; Margraf, J. T.; Lapidus, S. H.; Calik, M.; Hettstedt, C.; Karaghiosoff, K.; Döblinger, M.; Clark, T.; Chapman, K. W.*; et al.* Molecular docking sites designed for the generation of highly crystalline covalent organic frameworks. *Nat. Chem.* **2016**, *8*, 310–316.

(34) Dalapati, S.; Jin, E.; Addicoat, M.; Heine, T.; Jiang, D. Highly Emissive Covalent Organic Frameworks. *JACS* **2016**, *138*, 5797–5800.

(35) Aradi, B.; Hourahine, B.; Frauenheim, T. DFTB+, a sparse matrix-based implementation of the DFTB method. *The journal of physical chemistry. A* **2007**, *111*, 5678–5684.

(36) Gaus, M.; Goez, A.; Elstner, M. Parametrization and Benchmark of DFTB3 for Organic Molecules. *Journal of chemical theory and computation* **2013**, *9*, 338–354.

(37) Gaus, M.; Lu, X.; Elstner, M.; Cui, Q. Parameterization of DFTB3/3OB for Sulfur and Phosphorus for Chemical and Biological Applications. *Journal of chemical theory and computation* **2014**, *10*, 1518–1537.

(38) Wuttke, S.; Medina, D. D.; Rotter, J. M.; Begum, S.; Stassin, T.; Ameloot, R.; Oschatz, M.; Tsotsalas, M. Bringing Porous Organic and Carbon-Based Materials toward Thin-Film Applications. *Adv. Funct. Mater.* **2018**, *28*, 1801545.

(39) Biswal, B. P.; Vignolo-González, H. A.; Banerjee, T.; Grunenberg, L.; Savasci, G.; Gottschling, K.; Nuss, J.; Ochsenfeld, C.; Lotsch, B. V. Sustained Solar H2 Evolution from a Thiazolo5,4-dthiazole-Bridged Covalent Organic Framework and Nickel-Thiolate Cluster in Water. *JACS* **2019**, *141*, 11082–11092.

(40) Cardona, C. M.; Li, W.; Kaifer, A. E.; Stockdale, D.; Bazan, G. C. Electrochemical considerations for determining absolute frontier orbital energy levels of conjugated polymers for solar cell applications. *Advanced materials (Deerfield Beach, Fla.)* **2011**, *23*, 2367–2371.

(41) Sun, L.; Park, S. S.; Sheberla, D.; Dincă, M. Measuring and Reporting Electrical Conductivity in Metal-Organic Frameworks: Cd2(TTFTB) as a Case Study. *JACS* **2016**, *138*, 14772–14782.

5.6.　Supporting Information

Chemicals

All materials were purchased from Aldrich, Fluka, Acros or TCI Europe in the common purities purum, puriss or reagent grade. Materials were used as received without additional purification and handled under air unless denoted. All solvents used were anhydrous and purged with inert gas.

Methods and Instruments

Nuclear magnetic resonance spectra were recorded on Bruker AV 400 and AV 400 TR spectrometers. Proton chemical shifts are expressed in parts per million (δ scale) and are calibrated using residual non-deuterated solvent peaks as an internal reference (e.g., DMSO-d_6: 2.50).

Powder X-ray diffraction measurements were performed on a Bruker D8 Discover diffractometer using Ni-filter Cu K$_\alpha$ radiation and a position sensitive LynxEye detector in Bragg-Brentano geometry.

Nitrogen sorption isotherms were recorded on a Quantachrome Autosorb 1 instrument at 77 K within pressure ranges of p/p_0 = 0.001 to 0.98. Samples for physisorption were directly taken from supercritical CO_2 activation. Prior to the measurements, the samples were heated for 12 h at 100 °C under high vacuum. For the evaluation of the surface area the BET method was applied within a p/p_0 range of 0.05 to 0.3. Pore size distributions were calculated using the QSDFT absorption model with a carbon kernel for cylindrical pores.

Ultraviolet–Vis–infrared absorption spectra were recorded on a Perkin-Elmer Lambda 1050 spectrometer equipped with a 150 mm integration sphere.

Photoluminescence and time-correlated single photon counting measurements were carried out using a FluoTime 300 from PicoQuant GmbH. Samples were excited using a 378 nm laser source pulsed at 40 MHz and a fluence of 300 nJ cm^{-2} / pulse.

Scanning electron microscopy images were recorded with an FEI Helios NanoLab G3 UC scanning electron microscope equipped with a field emission gun operated at 3 kV. Prior to the measurements, the samples were sputtered with carbon.

Transmission electron microscopy were recorded with an FEI Titan Themis 60 - 300 equipped with a field emission gun operated at 300 kV.

Electrochemical measurements were performed on a Methrom µAutolabIII/FRA2 instrument using a three-electrode setup with a Pt-wire counter-electrode and a silver wire as a pseudo reference electrode under argon atmosphere. Measurements were carried out in dry acetonitrile

with tetrabutyl ammonium tetrafluoro borate (1 M) as the electrolyte. After recording CV data, the measurement was repeated after a small amount of ferrocene was added to the sample. The position of the redox couple from Fc/Fc$^+$ was then used as the reference system.

Van-der-Pauw measurements were carried out using an ECOPIA Model HMS 3000 setup. The samples were contacted with gold plated spring electrodes with an electrode separation of 5 mm. Powder pellets were pressed by using 20 mg of COF material and pressing into a cylindrical pellet with a circle diameter of 1 cm under a pressure of 8000 kPa.

Theoretical Calculations

The initial structures of the COFs were initially built using the Forcite module of Accelrys Material Studio 6.0 using the Universal Force Field as implemented. Pawley refinements were carried using the Reflex module of PXRD using the Howard-profile fitting function. DFTB+ calculations were carried out using the DFTB+ code with the 3ob parameter set.[1] DFT calculations on the model pore systems were carried out using Gaussian 16 with the PBE0 functional and the def2SVP basis set on standard convergence criteria.

Synthesis of WTA

WTA-COF
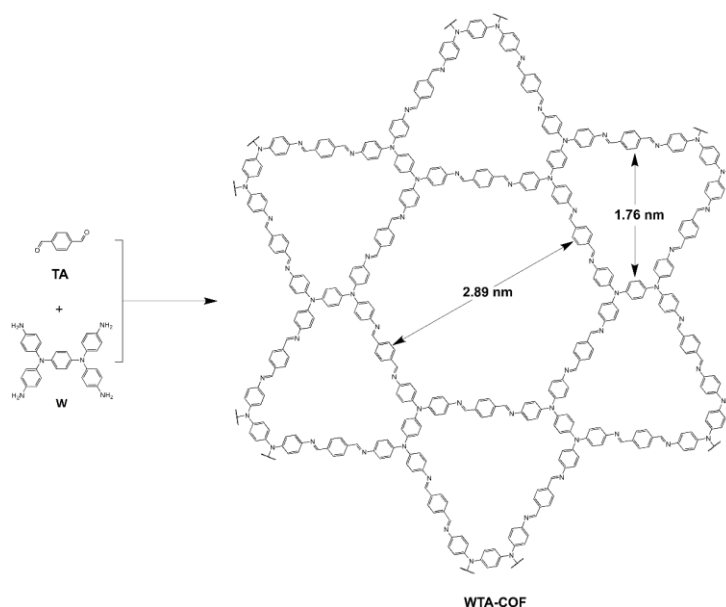
In a 5 mL culture tube, a solid mixture of terephthalaldehyde (**TA**, 0.025 mmol, 3.4 mg) and *N,N,N',N'*-tetrakis(4-aminophenyl)-1,4-phenylenediamine (**W**, 0.013 mmol, 6.0 mg) was suspended in 1 mL mesitylene and benzyl alcohol (1:1 V:V). The loading of the culture tube was carried out in an argon filled glovebox. Subsequently, 50 µL of acetic acid (6M) was added.

Then, the culture tube was tightly sealed and heated at 100 °C for 72 h in an oven. The resulting dark red suspension was filtrated hot and the isolated powder was washed with 10 mL of tetrahydrofuran (THF). The obtained red microcrystalline product was dried under vacuum and subsequently activated with supercritical CO_2 at 110 bar and 40 °C for 1 hour.

Synthesis of WBDT
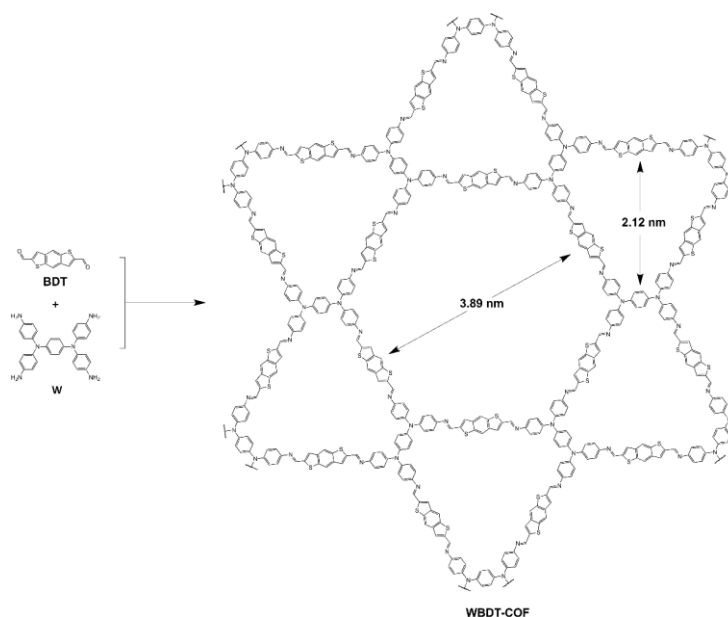
In a 5 mL culture tube, a solid mixture of benzodithiophene-2,6-dicarboxaldehyde (**BDT**, 0.025 mmol, 6.26 mg) and *N,N,N',N'*-tetrakis(4-aminophenyl)-1,4-phenylenediamine (**W**, 0.013 mmol, 6.0 mg) was suspended in 1 mL mesitylene and benzyl alcohol (1:1 V:V). The loading of the culture tube was carried out in an argon filled glovebox. Subsequently, 50 μL of acetic acid (6M) was added. Then, the culture tube was tightly sealed and heated at 100 °C for 72 h in an oven. The resulting dark red suspension was filtrated hot and the isolated powder was washed with 10mL of tetrahydrofuran (THF). The obtained red microcrystalline product was dried under vacuum and subsequently activated with supercritical CO_2 at 110 bar and 40 °C for 1 hour.

Synthesis of WTA thin films

In a 25 mL Schott duran glass bottle, a solid mixture of terephthalaldehyde (**TA**, 0.1 mmol, 13.6 mg) and *N,N,N',N'*-tetrakis(4-aminophenyl)-1,4-phenylenediamine (**W**, 0.052 mmol, 24.0 mg) was suspended in 4 mL mesitylene and benzyl alcohol (1:1 V:V). The loading of the reaction vessel was carried out in an argon filled glovebox. 200 μL of acetic acid (6 M) was added. A substrate holder with two horizontally orientated substrates (1.5 cm × 1.5 cm) was placed into the suspension. The reaction vessel was tightly sealed and heated at 100 °C for 12 h in an oven. Then, the substrate holder was taken from the vessel and the substrates from the holder. The

upper sides of the substrates were cleaned from COF precipitates by wiping the surface with an aceton wetted cotton tip. Subsequently, the bottom sides of the subtrates were washed with THF and dried under vacuum.

Synthesis of WBDT thin films

In a 25 mL Schott duran glass bottle, a solid mixture of benzodithiophene-2,6-dicarboxaldehyde (**BDT**, 0.1 mmol, 25.04 mg) and *N,N,N',N'*-tetrakis(4-aminophenyl)-1,4-phenylenediamine (**W**, 0.052 mmol, 24.0 mg) was suspended in 4 mL mesitylene and benzyl alcohol (1:1 V:V). The loading of the reaction vessel was carried out in an argon filled glovebox. 200 µL of acetic acid (6M) was added. A substrate holder with two horizontally orientated substrates (1.5 cm × 1.5 cm) was placed into the suspension. The reaction vessel was tightly sealed and heated at 100 °C for 12 h in an oven. Then, the substrate holder was taken from the vessel and the substrates from the holder. The upper sides of the substrates were cleaned from COF precipitates by wiping the surface with an aceton wetted cotton tip. Subsequently, the bottom sides of the subtrates were washed with THF and dried under vacuum.

Synthesis of the WBDT molecular fragment and single crystal growth
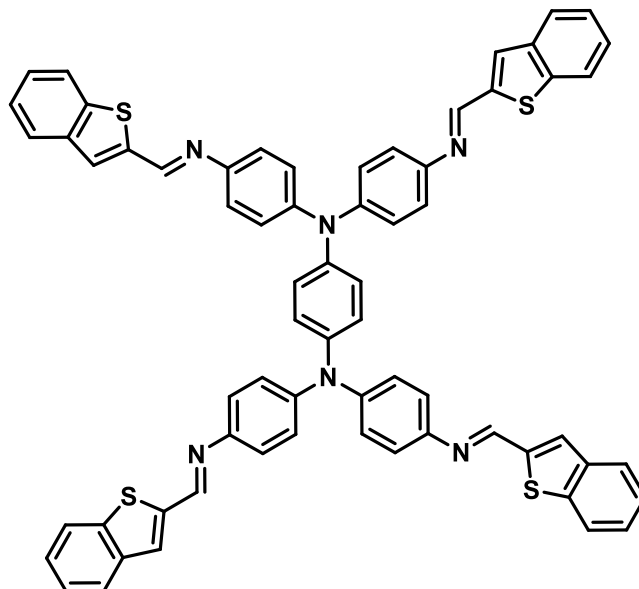
In a 5 mL culture tube, a solid mixture of benzothiophene-2-carboxaldehyde (0.25 mmol, 62.6 mg) and *N,N,N',N'*-tetrakis(4-aminophenyl)-1,4-phenylenediamine (**W**, 0.05 mmol, 23.0 mg) was suspended in 4 mL of CHCl₃. The culture tube was sealed and heated for 24 h at 60 °C. Subsequently, the reaction was cooled to room temperature and the resulting precipitate was collected by filtration and washed with methanol (20 mL). The dark red material was dried under vacuum.

^{1}H NMR (400 MHz, DMSO-d_6) δ (ppm): 8.50 (4H), 7.79 (8H), 7.45 (8H), 7.32 (8H), 7.30 (4H), 7.18 (8H), 7.14 (4H).

MS-EI: calculated (m/z): $C_{66}H_{44}N_6S_4$ 1048.2510, found 1048.2478.

Single crystals were grown by dissolving 5 mg of the WBDT molecular fragment in dichloromethane (10 mL) in a 25 mL screw-capped vial equipped with a septum. A needle was pierced through the septum to allow a slow evaporation of the solvent at room temperature. After 5 days, red platelet-like crystals were obtained, which were removed from solution directly prior to single-crystal analysis.
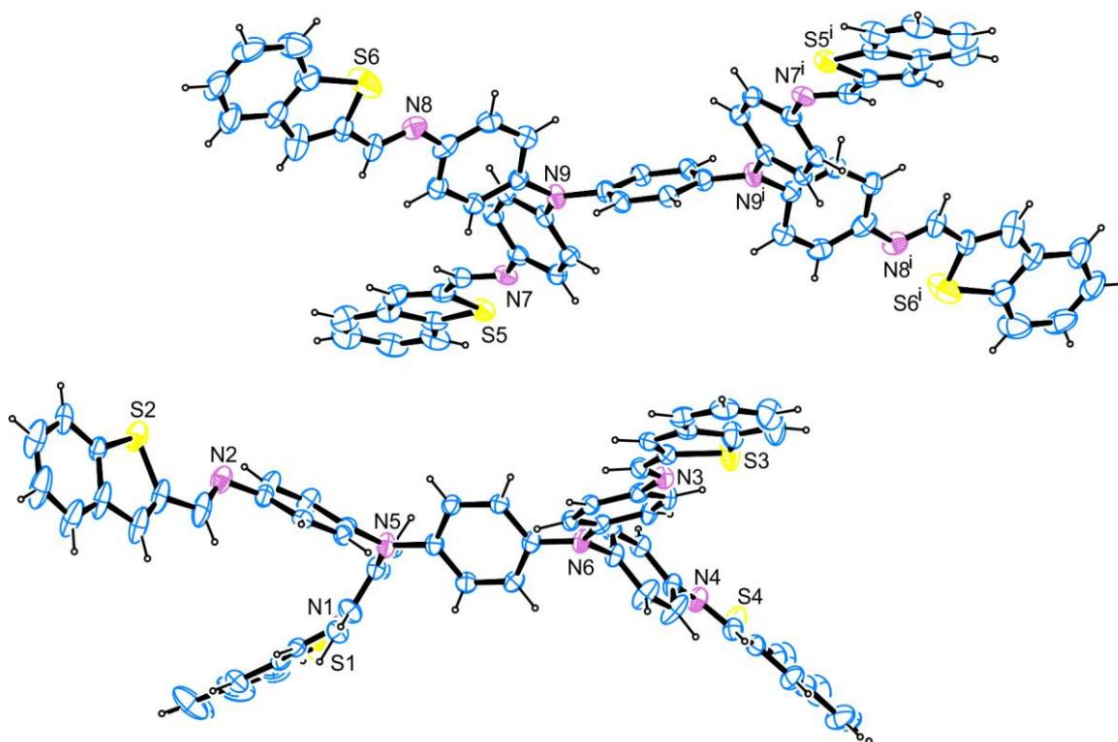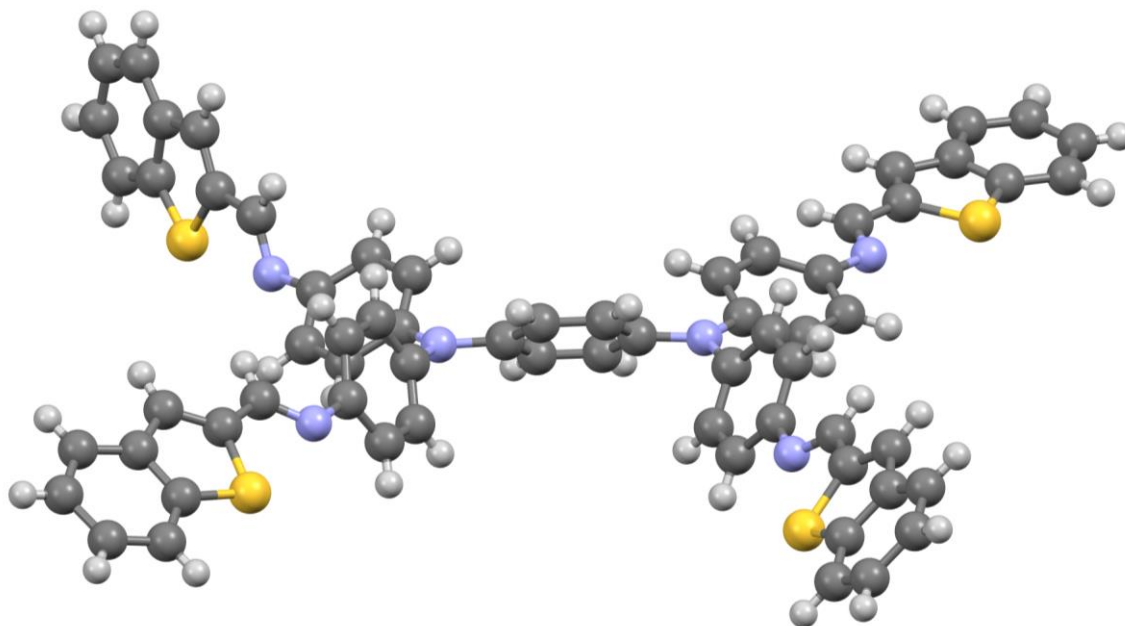
Figure S5.1: The molecular arrangement of the WBDT molecular fragment, obtained from single crystal data in ORTEP and stick-ball representation.

Table S5.1: Summary of the single crystal data of the WBDT molecular fragment.

net formula	$C_{67.55}H_{47.10}Cl_{3.09}N_6S_4$
M_r/g mol^{-1}	1180.73
crystal size/mm	$0.090 \times 0.070 \times 0.020$
T/K	106.(2)
radiation	Mo K$_\alpha$
diffractometer	'Bruker D8 Venture TXS'
crystal system	triclinic
space group	'P -1'
a/Å	13.8855(6)
b/Å	17.9904(7)
c/Å	19.1860(7)

$\alpha/°$	77.1720(10)
$\beta/°$	78.2210(10)
$\gamma/°$	69.1000(10)
$V/\text{Å}^3$	4324.4(3)
Z	3
calc. density/g cm^{-3}	1.360
μ/mm^{-1}	0.357
absorption correction	Multi-Scan
transmission factor range	0.96–0.99
refls. measured	58603
R_{int}	0.0538
mean $\sigma(I)/I$	0.0600
θ range	2.337–25.350
observed refls.	10556
x, y (weighting scheme)	0.1012, 10.3561
hydrogen refinement	Constr.
Refls. in refinement	15789
parameters	1321
restraints	406
$R(F_{\text{obs}})$	0.0811
$R_{\text{w}}(F^2)$	0.2308
S	1.023
shift/error$_{\text{max}}$	0.001
max electron density/e Å^{-3}	1.274

142

min electron density/e Å^{-3} -1.050

There are several disordered parts in this structure. All methylene chloride molecules are disordered. Split models have been applied. SADI instructions have been used to restrain all C-Cl and all Cl-Cl distances to similar values. All but one of the CH_2Cl_2 moieties have been refined isotropically. The SIMU restraint has been used to refine the U_{ij} of adjacent atoms (to a distance of 0.8 A) similarly. The SAME instruction has been applied to obtain good bond geometries in two disordered branches of the macromolecules using well-refined branches as model. ISOR and FLAT restraints have been used to improve vibration ellipsoids and geometry, respectively.

The figure above does not show the methylene chloride molecules and the minor parts of disordered sections.

Symmetry code i = 2-x, 1-y, 1-z.

Simulated tetragonal structure of WTA
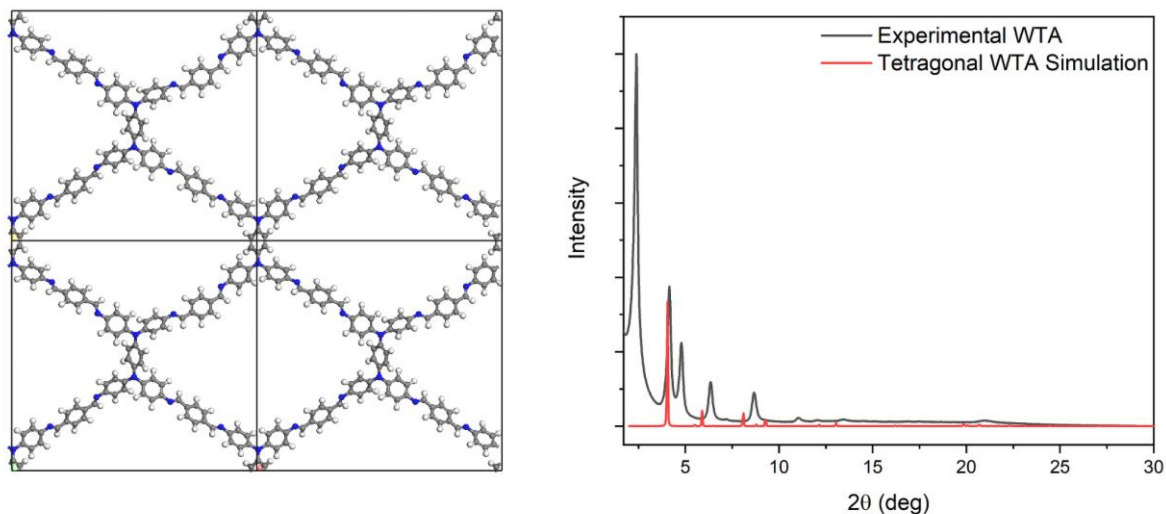
Figure S5.2: Simulated tetragonal structure of WTA and the corresponding calculated PXRD pattern vs. the experimentally obtained one.

Simulated tetragonal structure of WBDT
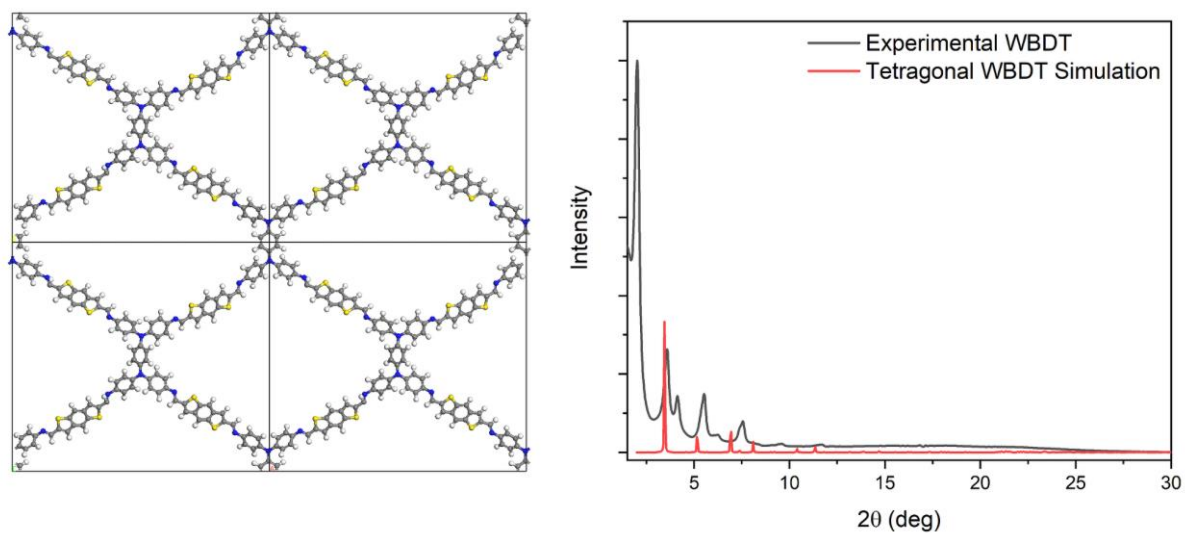
Figure S5.3: Simulated tetragonal structure of WBDT and the corresponding calculated PXRD pattern vs. the experimentally obtained one.

Hexagonal kagome vs. kagome-like arrangement of WTA
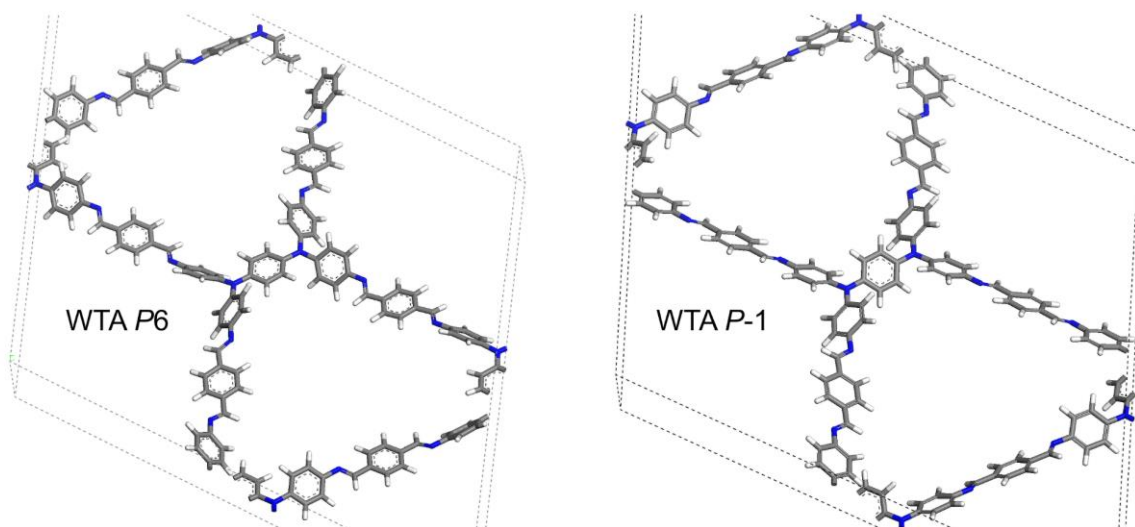
Figure S5.4: Representation of the geometric arrangement of the central W unit in WTA in a hexagonal P6 symmetry and in P-1 symmetry.

Hexagonal kagome vs. kagome-like arrangement of WBDT
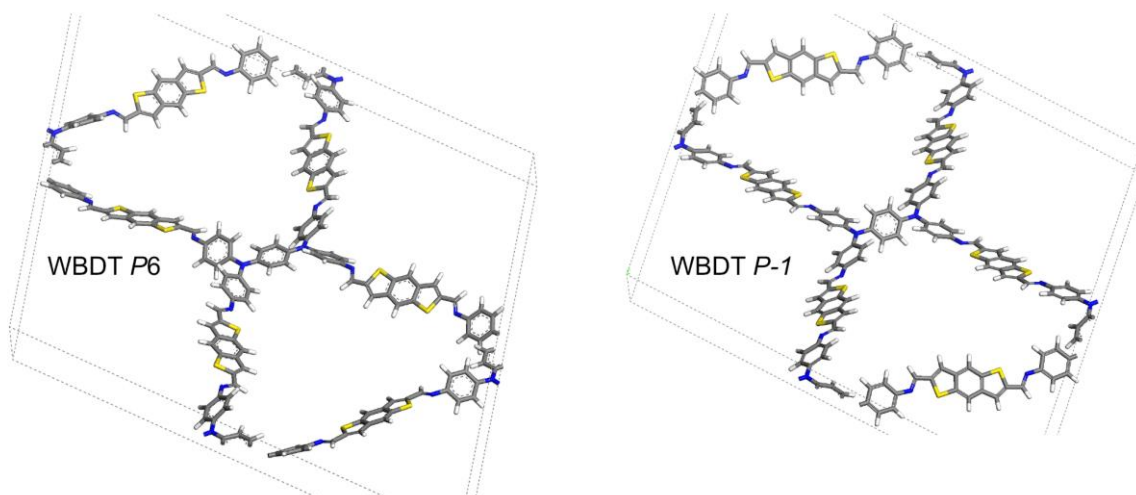
Figure S5.5: Representation of the geometric arrangement of the central W unit in WBDT in a hexagonal P6 symmetry and in P-1 symmetry.

Pore size distribution of WTA
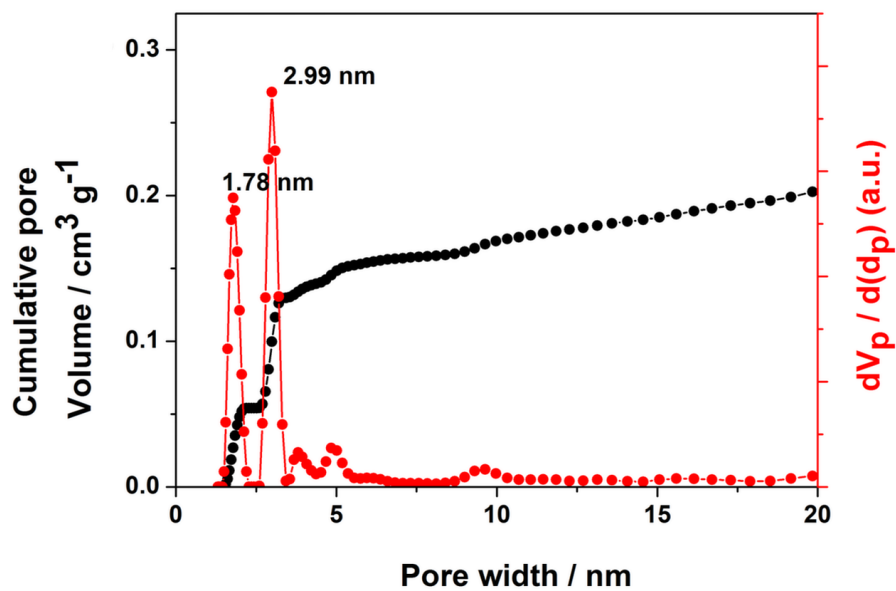
Figure S5.6: Pore size distribution and cumulative pore volume profiles of WTA obtained by QSDFT calculations on the N_2 adsorption curve.

Pore size distribution of WBDT
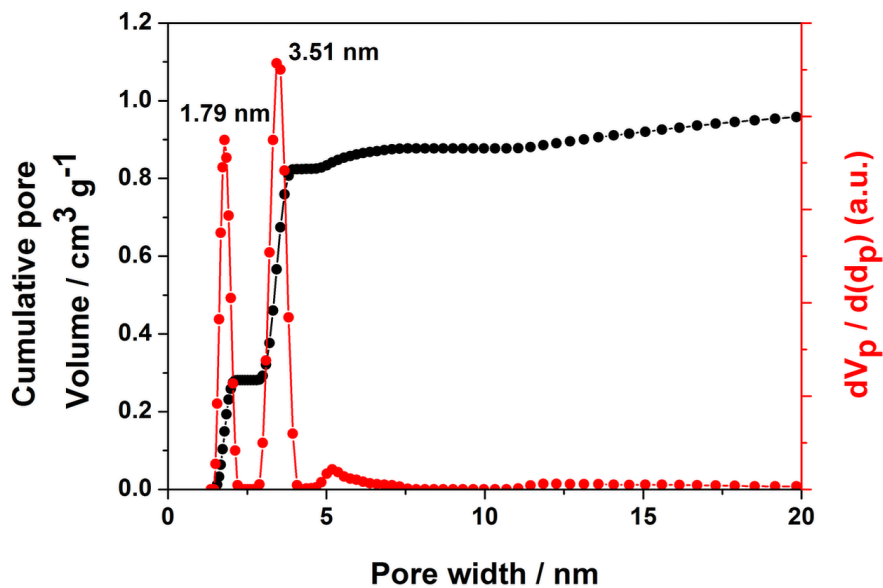
Figure S5.7: Pore size distribution and cumulative pore volume profiles of WBDT obtained by QSDFT calculations on the N₂ adsorption curve.

Tauc plot of WTA
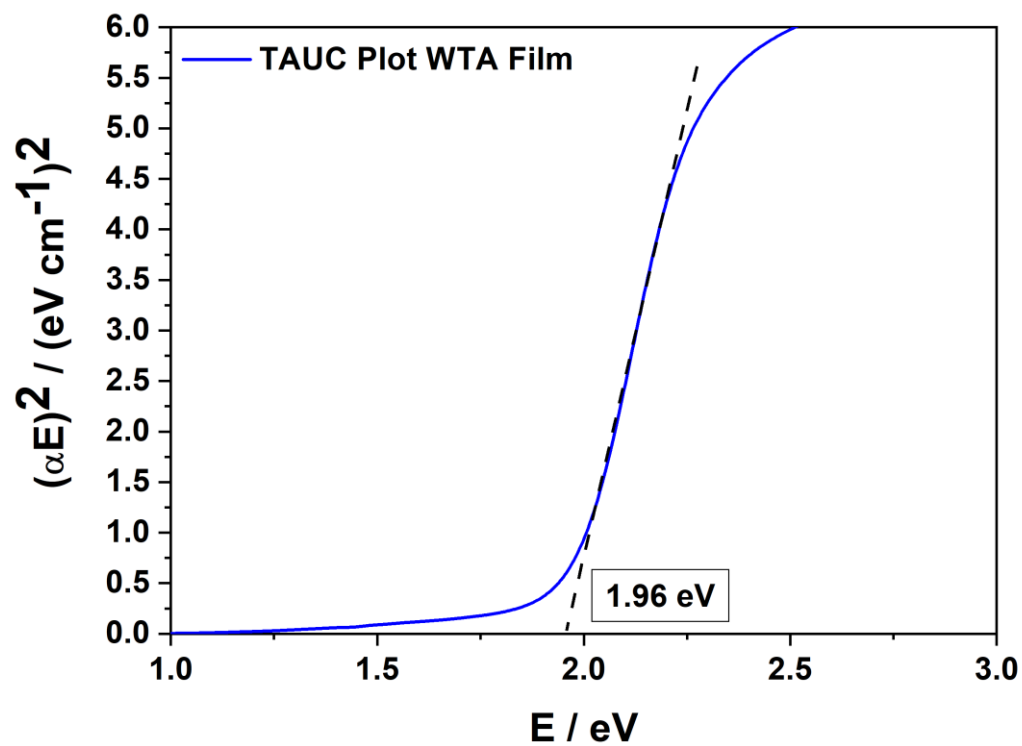
Figure S5.8: Tauc plot of the UV-vis absorption data of WTA.

Tauc plot of WBDT
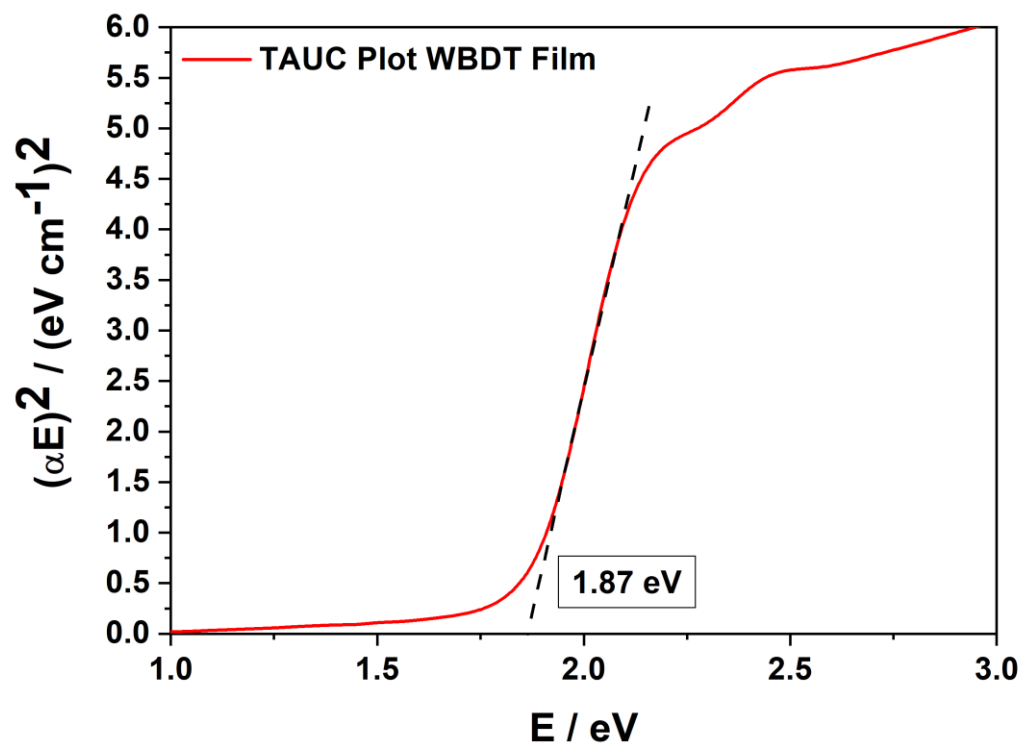
Figure S5.9: Tauc plot of the UV-vis absorption data of WBDT.

TCSPC decay data for WTA

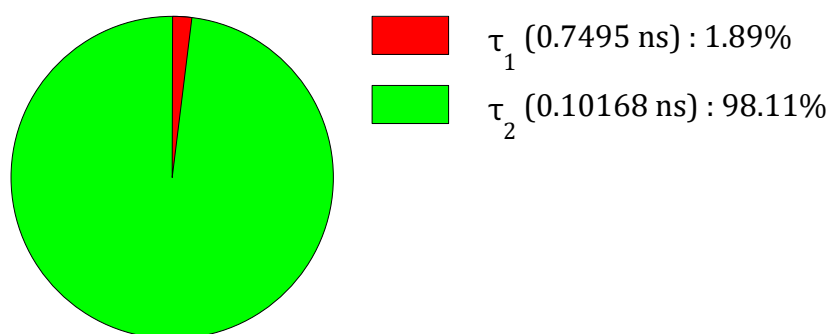| Parameter	Value	Conf. Lower	Conf. Upper	Conf. Estimation
A_1 [Cnts]	1066	-103	+103	Fitting
τ_1 [ns]	0.7495	-0.0496	+0.0496	Fitting
A_2 [Cnts]	55350	-1660	+1660	Fitting
τ_2 [ns]	0.10168	-0.00197	+0.00197	Fitting
Bkgr. Dec [Cnts]	110.0	---	---	<none>
Bkgr. IRF [Cnts]	18.9	---	---	<none>
Shift IRF [ns]	0.345887	-0.000602	+0.000602	Fitting
A Scat [Cnts]	641580	-6740	+6740	Fitting

Average Lifetime:

$\tau_{Av.1}$=0.1822 ns (intensity weighted)

$\tau_{Av.2}$=0.1139 ns (amplitude weighted)

Fractional Intensities of the Positive Decay Components:

τ_1 (0.7495 ns) : 12.43%

τ_2 (0.10168 ns) : 87.57%

Fractional Amplitudes of the Positive Decay Components:

τ_1 (0.7495 ns) : 1.89%

τ_2 (0.10168 ns) : 98.11%

Figure S5.10: Fitted Decay and Exponential Components for WTA.

TCSPC PL decay data for WBDT

Parameter	Value	Conf. Lower	Conf. Upper	Conf. Estimation
A_1 [Cnts]	1066	-103	+103	Fitting
τ_1 [ns]	0.7495	-0.0496	+0.0496	Fitting
A_2 [Cnts]	55350	-1660	+1660	Fitting
τ_2 [ns]	0.10168	-0.00197	+0.00197	Fitting
Bkgr. Dec [Cnts]	110.0	---	---	<none>
Bkgr. IRF [Cnts]	18.9	---	---	<none>
Shift IRF [ns]	0.345887	-0.000602	+0.000602	Fitting
A Scat [Cnts]	641580	-6740	+6740	Fitting

Average Lifetime:

$\tau_{Av.1}$=0.1822 ns (intensity weighted)

$\tau_{Av.2}$=0.1139 ns (amplitude weighted)

Fractional Intensities of the Positive Decay Components:

τ_1 (0.7495 ns) : 12.43%

τ_2 (0.10168 ns) : 87.57%

Fractional Amplitudes of the Positive Decay Components:

τ_1 (0.7495 ns) : 1.89%

τ_2 (0.10168 ns) : 98.11%

Figure S5.11: Fitted Decay and Exponential Components for WTA.

F$_4$TCNQ dopant concentration
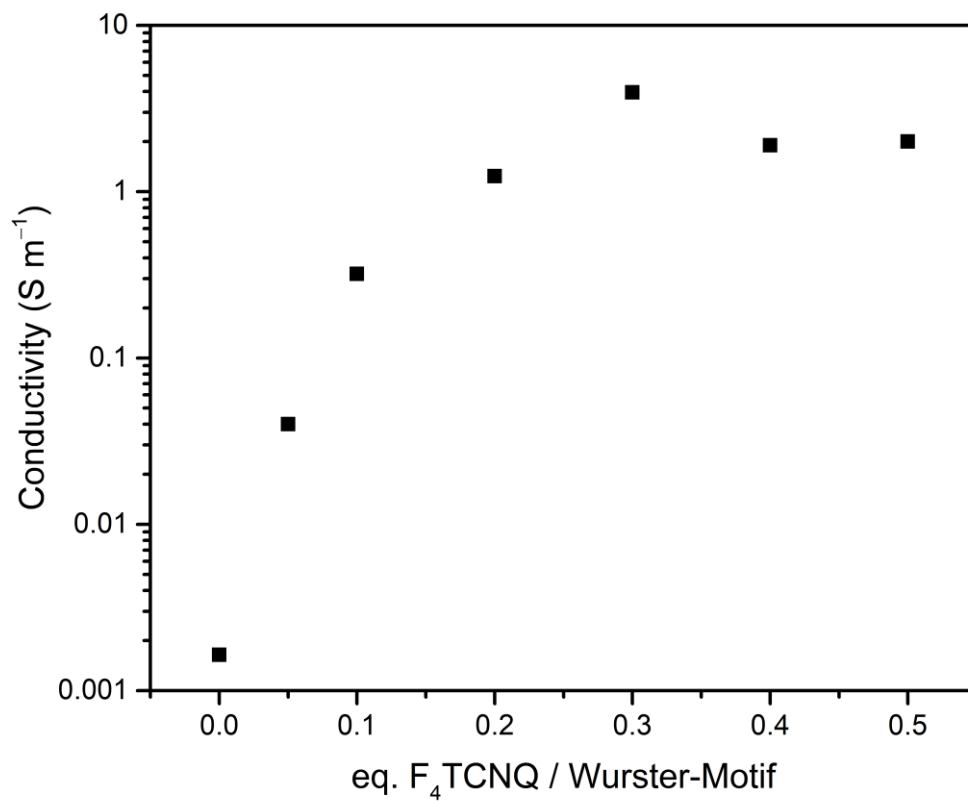
Figure S5.12: F$_4$TCNQ concentration-dependent electrical conductivities of WBDT.

PXRD of pristine WBDT vs. F$_4$TCNQ-doped WBDT
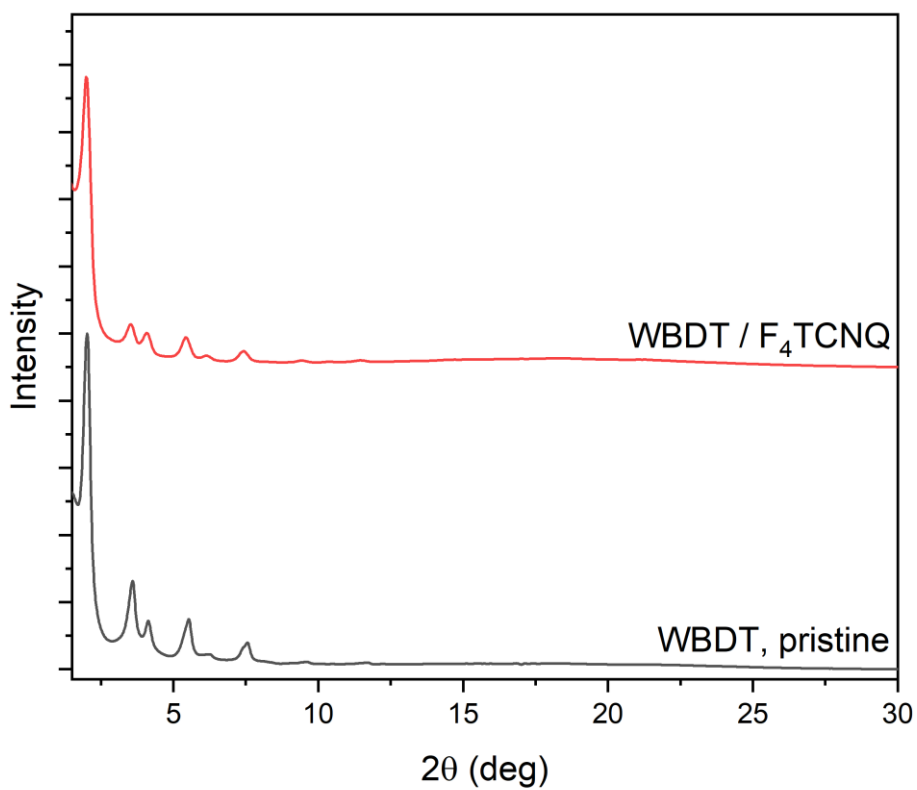
Figure S5.13: PXRD of pristine WBDT in comparison to F$_4$TCNQ-doped WBDT.

Structural parameters of WTA

Unit Cell Parameters (P-1)

a = 42.12, b = 42.82, c = 4.00 Å

α = 91.3°, β = 86.7°, γ = 118.8°

Table S5.2: Fractional coordinates for WTA.

N1	N	0.56807	100.117	0.47259
C2	C	0.53414	100.065	0.48675
C3	C	0.50375	0.97391	0.66456
H4	H	0.50603	0.95338	0.80155
C5	C	0.47045	0.97327	0.67718
H6	H	0.44783	0.95221	0.82277
N7	N	0.57398	0.87287	0.50853
C8	C	0.56912	0.96878	0.47503
C9	C	0.54211	0.93803	0.32626
H10	H	0.52029	0.93912	0.19965
C11	C	0.54268	0.90605	0.33261
H12	H	0.52125	0.88312	0.20962
C13	C	0.57069	0.90348	0.48614
C14	C	0.5979	0.93435	0.63096
H15	H	0.61969	0.9329	0.75493
C16	C	0.59712	0.9662	0.62746
H17	H	0.61844	0.98932	0.74836
C18	C	0.55091	0.84221	0.39954
H19	H	0.52575	0.83712	0.27411
C20	C	0.39932	0.96613	0.53681
C21	C	0.36758	0.96295	0.70525
H22	H	0.36795	0.98565	0.83773
C23	C	0.33546	0.93107	0.70855
H24	H	0.31119	0.92925	0.84221
C25	C	0.33339	0.90089	0.54395
C26	C	0.36533	0.90376	0.38211
H27	H	0.3654	0.88103	0.2532
C28	C	0.39746	0.9357	0.37839
H29	H	0.42153	0.93696	0.24628
N30	N	0.29973	0.87024	0.56212
C31	C	0.29195	0.84209	0.38907
H32	H	0.31153	0.83958	0.20396
N33	N	0.56395	0.567	0.48736
C34	C	0.53201	0.53359	0.49375

C35	C	0.46968	0.49584	0.34229
H36	H	0.44645	0.49326	0.21118
C37	C	0.50088	0.5286	0.33649
H38	H	0.50093	0.55047	0.20148
N39	N	0.30219	0.43331	0.55131
C40	C	0.40189	0.43175	0.52473
C41	C	0.39694	0.45865	0.68764
H42	H	0.41926	0.48021	0.81528
C43	C	0.36381	0.45817	0.69159
H44	H	0.3606	0.47931	0.82062
C45	C	0.33404	0.4309	0.53396
C46	C	0.33865	0.40346	0.37841
H47	H	0.31631	0.38147	0.25431
C48	C	0.37189	0.40404	0.37326
H49	H	0.37461	0.38266	0.24415
C50	C	0.27393	0.41352	0.38746
H51	H	0.2721	0.3922	0.21113
C52	C	0.24218	0.41882	0.42695
C53	C	0.2441	0.44806	0.60843
C54	C	0.21416	0.45334	0.64861
H55	H	0.21614	0.47615	0.79332
C56	C	0.1812	0.42968	0.50774
C57	C	0.17929	0.40049	0.32536
C58	C	0.20925	0.39517	0.28567
H59	H	0.20728	0.37236	0.141
C60	C	0.56117	0.59855	0.49227
C61	C	0.58769	0.62956	0.32652
H62	H	0.6109	0.62966	0.18808
C63	C	0.58488	0.66048	0.33234
H64	H	0.60561	0.68398	0.1957
C65	C	0.55477	0.66114	0.49619
C66	C	0.52771	0.63	0.65446
H67	H	0.50436	0.6302	0.78744
C68	C	0.53133	0.59961	0.65921
H69	H	0.51028	0.57618	0.79328
N70	N	0.54956	0.69079	0.48322
C71	C	0.57435	0.72227	0.54939
H72	H	0.60122	0.72778	0.6412
C73	C	0.56827	0.75276	0.51297
C74	C	0.53712	0.74889	0.3638
C75	C	0.53154	0.77787	0.32634
H76	H	0.50726	0.77438	0.2061
C77	C	0.55682	0.81171	0.43806
C78	C	0.58791	0.81552	0.58827
C79	C	0.59361	0.7866	0.62375

H80	H	0.61792	0.79007	0.74324
N81	N	0.00549	0.56852	0.52085
C82	C	0.00281	0.53436	0.51062
C83	C	0.02825	0.52794	0.32203
H84	H	0.05046	0.54926	0.17518
C85	C	0.02549	0.49443	0.31146
H86	H	0.04564	0.49075	0.15642
N87	N	0.14367	0.69002	0.45561
C88	C	0.04004	0.59919	0.50487
C89	C	0.07015	0.59901	0.6395
H90	H	0.06712	0.57512	0.76159
C91	C	0.10417	0.62885	0.61926
H92	H	0.12706	0.62815	0.72885
C93	C	0.10898	0.6606	0.47822
C94	C	0.0791	0.66103	0.3429
H95	H	0.08254	0.68501	0.21822
C96	C	0.04542	0.63068	0.3514
H97	H	0.023	0.63165	0.2354
C98	C	0.14971	0.72113	0.54655
H99	H	0.12786	0.72613	0.66572
C100	C	0.19336	0.78465	0.64917
C101	C	0.18599	0.75181	0.50591
C102	C	0.21408	0.74922	0.32187
H103	H	0.20856	0.72385	0.20647
C104	C	0.24832	0.77851	0.28171
C105	C	0.25583	0.81126	0.42841
C106	C	0.22774	0.81378	0.61346
H107	H	0.23332	0.83913	0.72998
C108	C	0.02644	0.42832	0.45812
C109	C	0.02764	0.3996	0.2922
H110	H	0.00379	0.37937	0.17051
C111	C	0.05909	0.39671	0.276
H112	H	0.0594	0.37425	0.14391
C113	C	0.09077	0.42226	0.42357
C114	C	0.08981	0.45138	0.58384
H115	H	0.1137	0.47222	0.70061
C116	C	0.0583	0.45413	0.60195
H117	H	0.05851	0.47682	0.73349
N118	N	0.12111	0.41718	0.39226
C119	C	0.14995	0.43565	0.55347
H120	H	0.15284	0.45693	0.73506
H121	H	0.26959	0.46655	0.72058
H122	H	0.15385	0.38198	0.21265
H123	H	0.51734	0.72269	0.27437
H124	H	0.60763	0.84171	0.67857

H125	H	0.17183	0.78714	0.79505
H126	H	0.26976	0.77609	0.13374

Structural parameters of WBDT

Unit Cell Parameters (*P*-1)

a = 50.55, b = 49.64, c = 3.93 Å

α = 102.3°, β = 82.2°, γ = 120.8°

Table S5.3: Fractional coordinates for WBDT.

N1	N	0.55374	0.99687	-0.60032
C2	C	0.52694	0.99856	-0.55079
C3	C	0.50431	0.9766	-0.37176
H4	H	0.50775	0.95834	-0.26936
C5	C	0.47802	0.97806	-0.32231
H6	H	0.4611	0.96102	-0.17751
S7	S	0.56531	0.84115	-0.48225
N8	N	0.55291	0.88478	-0.64731
C9	C	0.55336	0.96869	-0.61445
C10	C	0.52759	0.94343	-0.72101
H11	H	0.50758	0.94559	-0.79244
C12	C	0.5273	0.91583	-0.7372
H13	H	0.50692	0.89656	-0.81845
C14	C	0.55252	0.91227	-0.64593
C15	C	0.57803	0.93733	-0.53323
H16	H	0.59771	0.93479	-0.45944
C17	C	0.57861	0.96509	-0.52136

H18	H	0.59869	0.98428	-0.43224
C19	C	0.53669	0.86342	-0.82589
H20	H	0.52182	0.86542	-1.00479
C21	C	0.53994	0.83649	-0.77446
C22	C	0.52782	0.80856	-0.89572
H23	H	0.51147	0.80152	-1.07651
C24	C	0.41887	0.97625	-0.34965
C25	C	0.39763	0.97539	-0.15227
H26	H	0.40252	0.99595	-0.03827
C27	C	0.3711	0.94893	-0.09736
H28	H	0.35549	0.94916	0.05724
C29	C	0.36489	0.92251	-0.23177
C30	C	0.38506	0.92317	-0.43853
H31	H	0.38111	0.90359	-0.56207
C32	C	0.41181	0.9496	-0.49561
H33	H	0.42776	0.95014	-0.65923
S34	S	0.2414	0.8349	0.32396
N35	N	0.31609	0.88778	0.0643
C36	C	0.2983	0.86168	-0.0272
H37	H	0.30467	0.85348	-0.23181
C38	C	0.2683	0.83701	0.06684
C39	C	0.25625	0.81046	-0.08154
H40	H	0.26749	0.80476	-0.24972
N41	N	0.55388	0.55424	-0.49343
C42	C	0.52687	0.52702	-0.49671
C43	C	0.47469	0.49789	-0.36069
H44	H	0.45507	0.49603	-0.24683

C45	C	0.5014	0.52471	-0.3578
H46	H	0.50272	0.54391	-0.24176
S47	S	0.28988	0.45744	0.32772
N48	N	0.33435	0.44555	0.49764
C49	C	0.41826	0.44603	0.49583
C50	C	0.41405	0.4695	0.35706
H51	H	0.4328	0.48814	0.24117
C52	C	0.38624	0.46891	0.36173
H53	H	0.38306	0.48715	0.25415
C54	C	0.36183	0.44526	0.50778
C55	C	0.3661	0.42192	0.64671
H56	H	0.34755	0.40313	0.75992
C57	C	0.39377	0.42232	0.64061
H58	H	0.39708	0.40427	0.75278
C59	C	0.31278	0.42949	0.67778
H60	H	0.31472	0.41507	0.86249
C61	C	0.28571	0.43224	0.62199
C62	C	0.25781	0.41973	0.74669
H63	H	0.25118	0.40335	0.92866
C64	C	0.23872	0.43064	0.60577
C65	C	0.25341	0.45192	0.36921
C66	C	0.2386	0.46534	0.20682
H67	H	0.24976	0.48158	0.02454
C68	C	0.20907	0.45786	0.27955
C69	C	0.19442	0.43661	0.51632
C70	C	0.20916	0.42306	0.67776
H71	H	0.198	0.40686	0.86042
C72	C	0.55294	0.58182	-0.49046
C73	C	0.57562	0.60613	-0.33761
H74	H	0.59343	0.60302	-0.21865
C75	C	0.57538	0.63351	-0.33323
H76	H	0.59341	0.65192	-0.21386
C77	C	0.55242	0.63763	-0.48156
C78	C	0.52974	0.61335	-0.63476
H79	H	0.51176	0.61633	-0.7501
C80	C	0.52982	0.58584	-0.63782
H81	H	0.51199	0.56724	-0.76009

S82	S	0.53925	0.70892	-0.67797
N83	N	0.55166	0.66488	-0.49642
C84	C	0.56703	0.68657	-0.31776
H85	H	0.58113	0.68494	-0.12895
C86	C	0.5641	0.71344	-0.38114
C87	C	0.57644	0.74152	-0.2628
H88	H	0.59258	0.74843	-0.08024
C89	C	0.56572	0.76043	-0.41147
C90	C	0.5447	0.74543	-0.64619
C91	C	0.53144	0.76003	-0.81534
H92	H	0.5154	0.74858	-0.9964
C93	C	0.53896	0.78974	-0.7516
C94	C	0.56007	0.80474	-0.51755
C95	C	0.57336	0.79018	-0.34886
H96	H	0.58939	0.80158	-0.16763
C97	C	0.02094	0.52108	0.69036
H98	H	0.0371	0.53714	0.84593
C99	C	0.02231	0.49469	0.64116
H100	H	0.03943	0.4902	0.75515
S101	S	0.15423	0.70685	-0.125
N102	N	0.09957	0.66077	-0.10778
C103	C	0.02281	0.58013	-0.32738
C104	C	0.05129	0.5873	-0.43623
H105	H	0.05352	0.57185	-0.58489
C106	C	0.07644	0.6139	-0.36165
H107	H	0.09834	0.61897	-0.44748
C108	C	0.07402	0.63416	-0.17333
C109	C	0.04549	0.62711	-0.06862

H110	H	0.04269	0.64247	0.07407
C111	C	0.02038	0.60069	-0.14267
C112	C	0.10041	0.67784	0.10428
H113	H	0.08156	0.6719	0.25709
C114	C	0.12833	0.70534	0.12721
C115	C	0.13851	0.73048	0.2955
H116	H	0.12464	0.73349	0.45343
C117	C	0.16848	0.75241	0.22041
C118	C	0.18027	0.74227	-0.00739
C119	C	0.20902	0.76011	-0.11437
H120	H	0.21769	0.75207	-0.29008
C121	C	0.22653	0.78857	0.00259
C122	C	0.21478	0.79878	0.2277
C123	C	0.1859	0.78078	0.33872
H124	H	0.17683	0.78853	0.51371
C125	C	0.03143	0.44681	0.4072
C126	C	0.03419	0.42138	0.51286
H127	H	0.01429	0.40148	0.59831
C128	C	0.0618	0.42149	0.51472
H129	H	0.06382	0.40174	0.5978
C130	C	0.08748	0.44668	0.40428
C131	C	0.08487	0.47222	0.30341
H132	H	0.10473	0.49238	0.22577
C133	C	0.05736	0.47233	0.30539
H134	H	0.05555	0.49236	0.2245
S135	S	0.15826	0.43169	0.56375
N136	N	0.11454	0.44552	0.41008
C137	C	0.13589	0.46102	0.22625
H138	H	0.13391	0.4757	0.04395
C139	C	0.16253	0.45727	0.27273
C140	C	0.19018	0.46922	0.14302
H141	H	0.19686	0.48574	-0.03768
N142	N	0.99684	1.55341	0.59983
C143	C	0.99869	1.52683	0.55075
H144	H	0.99841	1.59543	0.9461

References

(1) Aradi, B.; Hourahine, B.; Frauenheim, T. DFTB+, a sparse matrix-based implementation of the DFTB method. J. Phys. Chem. *A* **2007**, *111*, 5678–5684.

6. On-Surface Synthesis of Highly Oriented Thin Metal-Organic Framework Films through Vapor-Assisted Conversion

This chapter is based on the following publication:

6.1.   Abstract

Controlled on-surface film growth of porous and crystalline frameworks is a central requisite for incorporating these materials into functional platforms and operational devices. Here, we present the synthesis of thin zirconium-based metal-organic framework (MOF) films by vapor-assisted conversion (VAC). We established protocols adequate for the growth of UiO-66, UiO-66(NH_2), UiO-67, and UiO-68(NH_2) as well as the porous interpenetrated Zr-organic framework (PPPP-PIZOF-1) as highly oriented thin films. Through the VAC approach, precursors in a cast solution layer on a bare gold substrate are reacting to form a porous continuous MOF film, oriented along the [111] crystal axis by an exposure to a solvent vapor under elevated temperatures of 100 °C and 3 h reaction times. It was found that the concentration of dicarboxylic acid, and modulator, the droplet volume and the reaction time are vital parameters to be controlled for obtaining oriented MOF films. Using VAC for the MOF film growth on gold surfaces modified with thiol SAMs as well as on a bare silicon surface yielded oriented MOF films rendering the VAC process robust towards chemical surface variations. Ethanol sorption experiments show that a substantial part of the material pores is accessible. Thereby, the practical VAC method is an important addition to the tool-box of thin MOF film synthesis methods. We expect that the VAC approach will provide new horizons in the formation of highly defined functional thin MOF films for numerous applications.

6.2.   Introduction

Recent advances in the fabrication of porous thin films have enabled significant progress in a variety of fields including catalysis, sensor technology, sieving platforms and electronics. Metal-organic frameworks (MOFs) are particularly intriguing candidates for the growth of crystalline porous films.[1-5] MOFs consist of a periodic array of inorganic nodes connected by organic units featuring well-defined structures, precise chemical compositions, surface areas and pore sizes.[6-11] Due to their crystalline nature, the growth of thin films of these materials permits, in principle, a specific crystal orientation and, thereby, an oriented pore system relative to a surface.[12] This oriented growth mainly relies on the use of chemically modified surfaces[13] and conditions that support reversible crystal assembly, hence allowing the growing crystal to anneal as it moves towards the energy minimum in the structure-energy landscape.

Several methods have been reported for the growth of oriented thin MOF films.[12, 14-21] However, to date, these methods are suitable only for the synthesis of a small number of MOF topologies. Among these methods, the liquid-phase epitaxy (SURMOF) approach[17-18] stands out offering some degree of structural and chemical diversity for oriented thin MOF films while maintaining the lattice type.[22] That being said, the synthesis of oriented thin films, applicable to a large variety of MOFs while maintaining porosity and crystallinity as main features, is still a challenge.

Here, we report the preparation of oriented thin MOF films using vapor-assisted conversion (VAC). This method is a variation of the well-known,[23] dry-gel conversion (DGC) and steam-assisted conversion (SAC) reported for the bulk and film syntheses of zeolites and other related compounds such as zeolitic imidazolate frameworks.[24-30] Recently, VAC has been introduced as a gentle and efficient way to obtain covalent organic framework (COF) films.[31] This method is based on the conversion of precursors in a cast solution layer into a continuous crystalline and porous film by exposure to a vapor of specific composition at moderate temperatures. Adding to this portfolio, we seek to prove that VAC is a powerful MOF film synthesis approach by showing that a series of Zr-based MOFs are grown on-surface as thin and highly oriented films. The well-known isoreticular series of zirconium-based UiO-type (Universitetet i Oslo) frameworks was selected for this study due to the diversity in the organic units which can be integrated into the framework such as phenyl, biphenyl and terphenyl dicarboxylate.[32-33] Further elongation of the linker
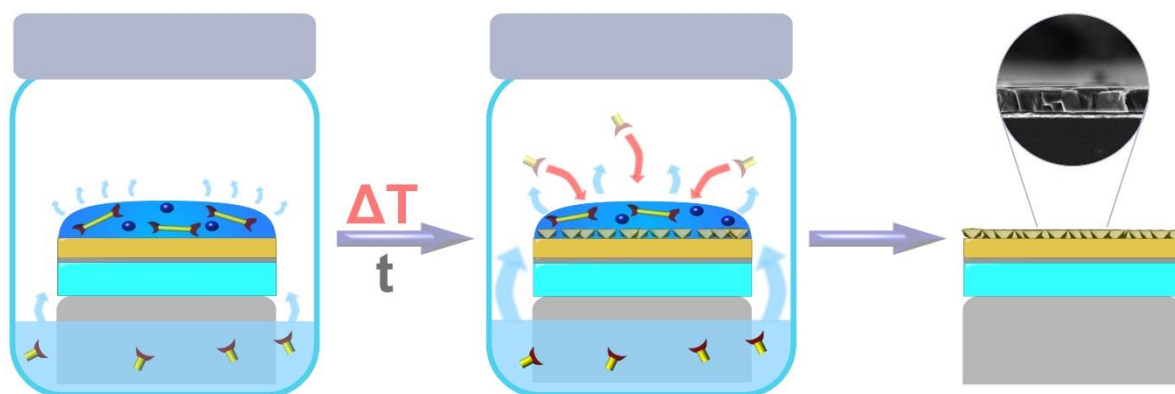
Figure 6.1. Schematic representation of the vapor-assisted conversion process for the fabrication of oriented MOF films.

to quaterphenyl dicarboxylate results in a structure-type consisting of two UiO-frameworks that interpenetrate each other, the so called porous interpenetrated Zr-organic framework (PIZOF).[34-35] To the best of our knowledge, no film of an interpenetrated MOF has ever been reported. Controlling the orientation of UiO as well as PIZOF crystals adds a new level of surface control to the target design of thin MOF films.

6.3.   Results and discussion

Oriented thin films of UiOs. We started the thin film syntheses through VAC with Zr-based MOFs consisting of linkers without and with amino groups as substituents, namely UiO-66, UiO-66(NH_2), UiO-67, and UiO-68(NH_2). For the experiments, $ZrOCl_2$, the dicarboxylic acid, and the modulator acetic acid were dissolved in DMF giving the precursor solution (for details see SI). In a glass vessel containing, as the vapor source, a mixture of DMF and acetic acid (5.25:1 v/v), a substrate (1.0 cm × 1.3 cm and 2.5 cm × 2.5 cm), providing a bare gold surface, was placed on a glass platform (Figure 6.1). A droplet (50 µL) of the precursor solution was deposited on the gold surface. Then, the vessel was sealed and placed in an oven preheated to 100 °C. After keeping the vessel at this temperature for 3 h, it was removed from the oven. The substrate was taken out of the vessel and dried under reduced pressure, revealing an iridescent film on the gold surface (Figure S6.60-62).

The operation of a VAC process was confirmed by a series of control experiments on the formation of UiO-66(NH_2) films in the absence of a vapor source and with DMF or acetic acid as the sole vapor sources. These experiments revealed that for the UiO topology a

vapor source of a particular composition is necessary for the formation of highly crystalline films. All synthesis attempts in the absence of a vapor source resulted in films of low or moderate crystallinity (Figure S6.5).

The films obtained by VAC were studied with X-ray diffraction (XRD) analysis and scanning electron microscopy (SEM). Strikingly, the diffraction patterns (Figures 6.2a-c, S3a) show only a few reflections which are in very good agreement with the reported XRD data of the UiO structures.[32-33, 36] The observed reflections indicate a high degree of crystallite orientation with the [111] axes aligned normal to the gold surface and rotational freedom around these axes. To gain further information on the degree of crystallite orientation across the substrate, we applied 2D grazing-incidence wide-angle X-ray scattering (GIWAXS) at different positions of the UiO-66(NH$_2$) film. Using this technique, the displayed in- and out-of-plane reflections up to the fourth order (Figure 6.2e and S57) confirm a high degree of crystallite orientation throughout the film. Top-view SEM images of the oriented UiO-66, -66(NH$_2$), -67, -68(NH$_2$) films reveal a high surface coverage with MOF crystallites (Figures 6.3a and c, S6.18, S6.3–S6.4). High magnifications show densely packed intergrown octahedral crystallites of uniform size forming a continuous film. In the case of UiO-68(NH$_2$) films, we find sporadic MOF octahedrons on top of the thin film (Figure S6.4). This is ascribed to a secondary nucleation process. Furthermore, the SEM images of UiO-66, -66(NH$_2$) and -67 show highly oriented crystallites exposing almost exclusively the facets attributed to the (111) plane. Low magnification SEM Z-contrast imaging of the UiO-66(NH$_2$) film reveals full surface coverage extending to the edge of the substrate (Figure S6.53). Cross-section SEM analyses show densely-packed films with thicknesses of about 200 nm, 235 nm, 440 nm and 1.3 μm for UiO-66, -66(NH$_2$), -67 and -68(NH$_2$), respectively (Figures 6.3b and d, S6.18, S6.3–S6.4). In all cases, the films display good contact to the gold layer indicating favorable interactions with the substrate. SEM cross-section analysis of the UiO-66(NH2) film revealed similar thicknesses in the central and edge areas, which establishes an even coverage of the MOF film across the whole substrate (Figure S6.56).
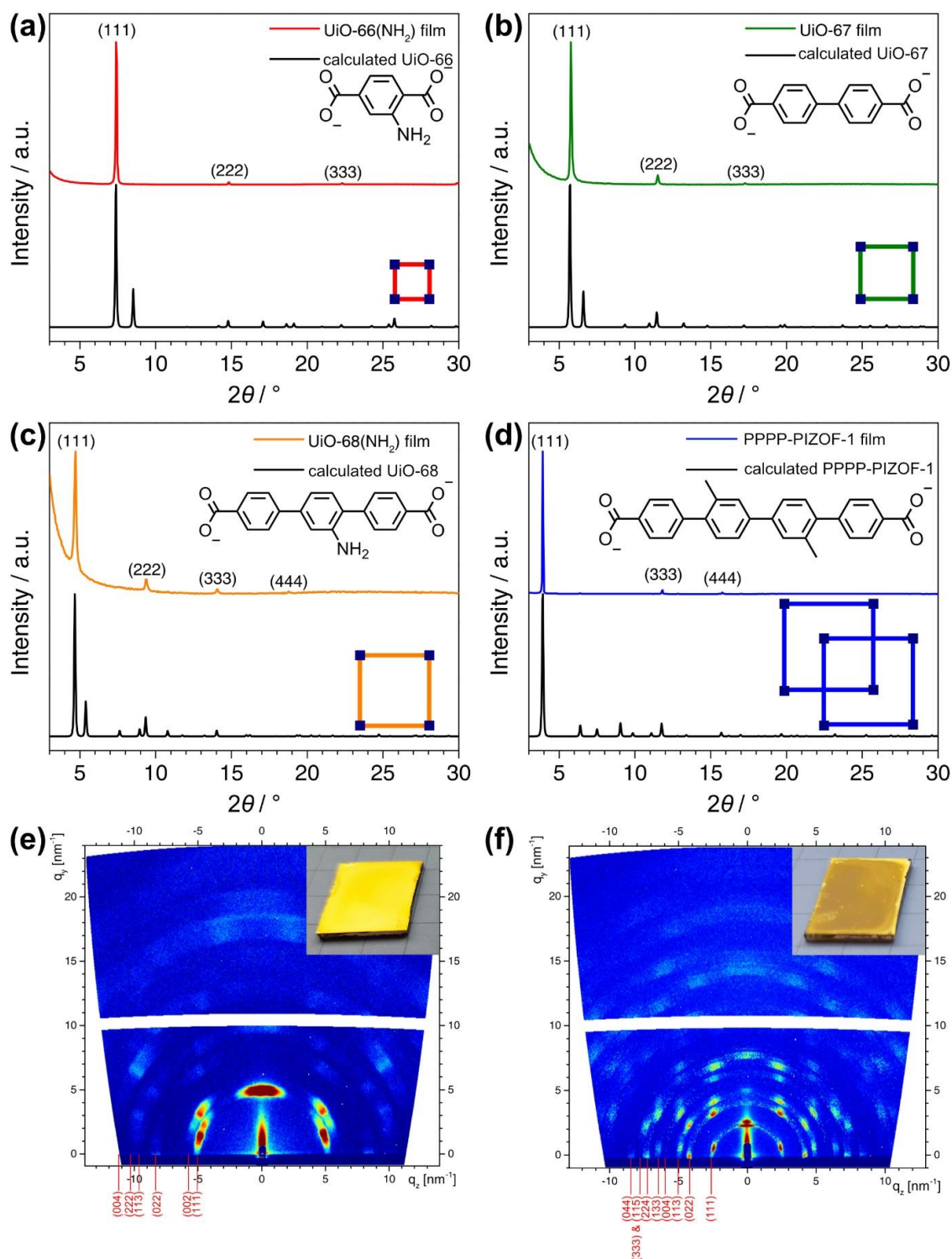
Figure 6.2. (a–d) XRD of UiO-66(NH₂), -67, -68(NH₂) and PPPP-PIZOF-1 films obtained by VAC, plotted in color together with the simulated diffraction patterns of unsubstituted MOFs plotted in black. The structural formulae of the used dicarboxylates are also indicated. (e) and (f) 2D GIWAXS patterns of UiO-66(NH₂) and PPPP-PIZOF-1 reveal a high degree of orientation (in red the Miller indexes according to the set of planes). Photographs of the respective MOF films are shown as insets.
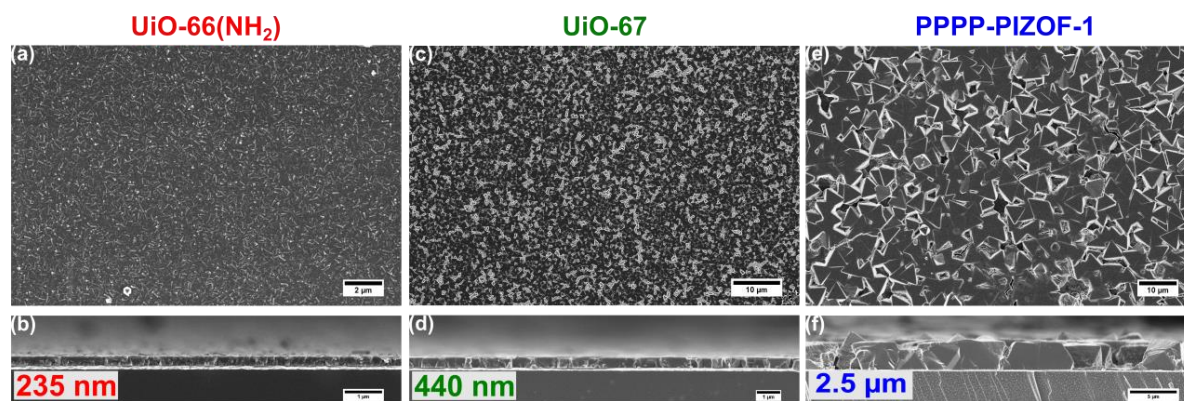
Figure 6.3. (a) Top-view SEM micrograph of UiO-66(NH₂) film depicting the dense surface coverage. (b) Cross-section SEM image of UiO-66(NH₂) presenting the uniform film thickness (see also Figure S6.18). (c) Top-view SEM micrograph of UiO-67 film depicting the dense surface morphology. (d) Cross-section SEM image of UiO-67 presenting the uniform film thickness (see also Figure S6.3). (e) Top-view SEM micrograph of PPPP-PIZOF-1 film showing large intergrown crystallites. (f) Cross-section SEM image of the PPPP-PIZOF-1 crystal layer (see also Figure S6.20).

Moreover, atomic force microscopy (AFM) surface scans of the UiO-66(NH₂) film (Figure S6.2) indicate a smooth faceted surface topography of oriented crystallites with a similar RMS roughness of 7.4 nm at the edge and center of the substrate. These observations demonstrate the power of the VAC deposition method, providing highly homogenous, macroscopic coverage and oriented thin UiO films across the entire substrate.

Oriented thin films of a PIZOF. Next, we turned our attention to the synthesis of a thin film of the MOF PPPP-PIZOF-1 using VAC. The synthesis was carried out using the protocol developed for the preparation of oriented UiO thin films. However, no acetic acid in the precursor solution was present to achieve sufficient solubility of the linkers and, thereby, a suitable reactivity for the MOF formation (Figure S6.6). Similar to the UiO films, the XRD pattern of the PPPP-PIZOF-1 film reveals a high degree of crystallite orientation with the 111 set of crystal planes being parallel to the surface (Figure 6.2d). GIWAXS investigations of the film confirm the formation of PPPP-PIZOF-1, a MOF with two-fold interpenetration (Figure 6.2f) which is, to the best of our knowledge, the first report on an oriented film of an interpenetrated MOF. In addition, the GIWAXS patterns reveal a high degree of crystallite orientation and the investigations obtained at different sites of the film show the homogeneity of the crystallite orientation over the area examined (Figure S6.57). The SEM micrographs of the PPPP-PIZOF-1 film (Figures 6.3e and S6.20) show a high areal coverage with large, intergrown octahedral crystals. The oriented octahedral crystals of

170

uniform size expose well-defined facets with an edge length of about 5.4 μm. In contrast to the continuous surface coverage in case of the UiO films, here the large crystals yielded a loosely packed layer. A homogenous packing of the PPPP-PIZOF-1 crystals is obtained within 200 μm from the edge of the substrate. By calculating the exposed gold area, we obtained a total surface coverage of about 93% (for further details see SI, Figures S6.54, 6.55). Cross-section SEM images illustrate a PPPP-PIZOF-1 layer exhibiting a film thickness of about 2.5 μm (Figures 6.3f and S6.20). The single PPPP-PIZOF-1 layer features individual crystals that are well connected to the substrate.

With respect to our previous report on the growth of 2D COF films by VAC,[31] here the additional important aspect of crystallite orientation on the surface was realized. Although, VAC was applied for related framework classes, MOF and COF, the different crystal growth mechanisms and crystal interactions with the substrate can strongly affect the final film properties. In contrast to other solution-based thin film deposition technologies such as dip-coating and in-situ growth, where only a small fraction of the precursor solution is ultimately deposited on the surface as the final film, in the VAC process all of the precursor molecules in the precursor solution cast on the surface, under conditions allowing for high reaction yields, convert to the desired MOF film (Figure S6.58). This is a striking and unique feature of the VAC method, which renders it extremely attractive when dealing with precious linker molecules.

The impact of the precursor and modulator concentrations on the MOF film growth. To attain further insight into and control over film formation via VAC, we investigated the impact of precursor and modulator concentrations on the crystallinity, crystallite size and orientation by conducting alterations in the synthesis. Control over the MOF crystallite orientation in films is crucial for expanding the scope of their applications. Previous reports emphasized the beneficial role of a modulator for obtaining highly crystalline MOF materials[35, 37] and preferential crystallite orientation in films.[38-39] To this end, we focused on the synthesis of UiO-66(NH$_2$) and PPPP-PIZOF-1 films as model systems for the different topologies.
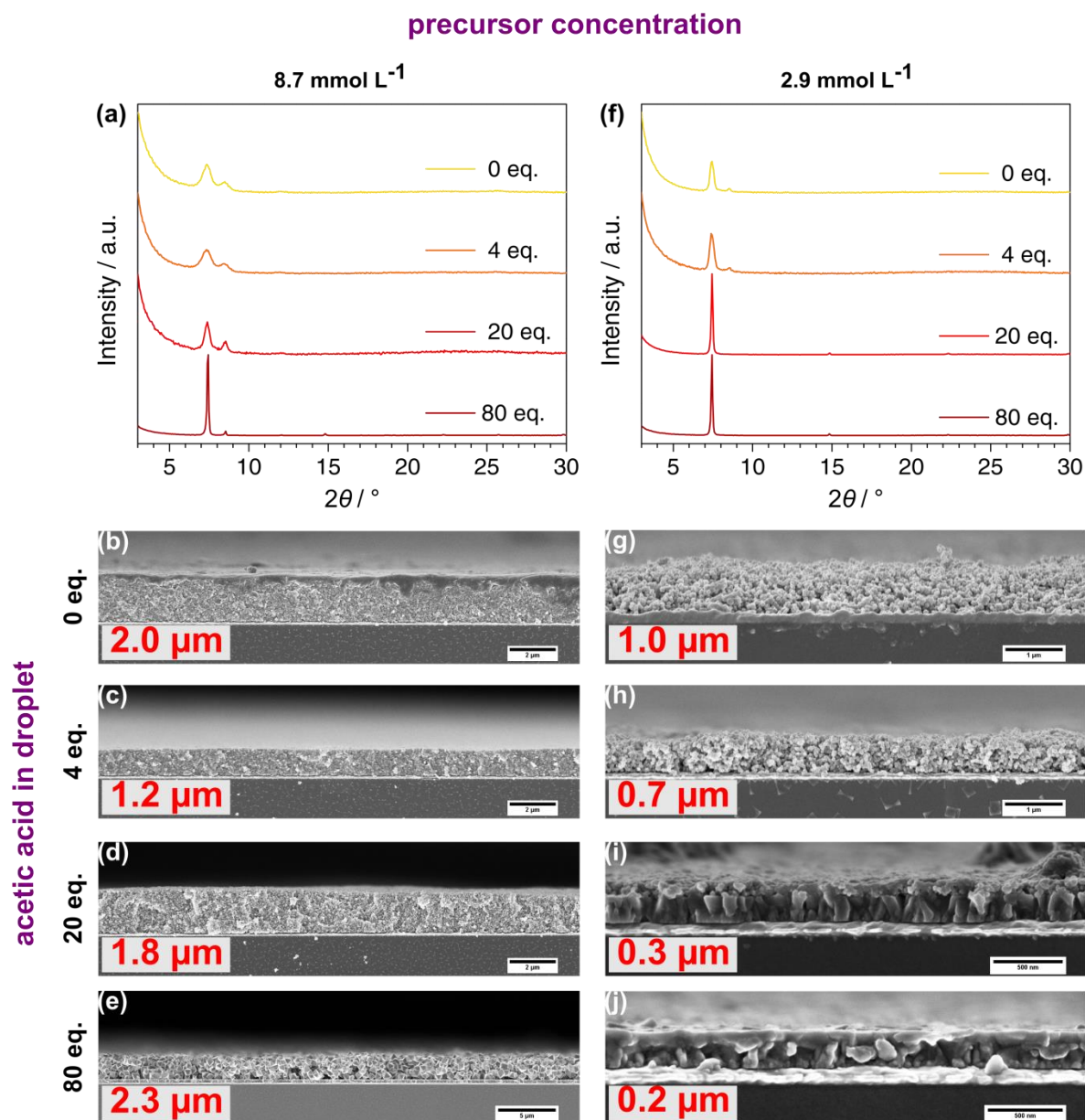
Figure 6.4. XRD patterns and cross-section SEM images of UiO-66(NH$_2$) films obtained for (a–e) high (see also Figures S6.7–S6.12) and (f–j) low (see also Figures S6.13–S6.18) precursor concentrations with amounts of acetic acid ranging from 0–80 molar equivalents relative to the precursor.

In the VAC process, control over crystallite orientation in UiO-66(NH$_2$) films was achieved by simply changing the precursor and modulator concentrations (Figure 6.4). Overall, densely packed non-oriented UiO-66(NH$_2$) films with no preferential orientation formed at a precursor concentration of 8.7 mmol L-1 (Figures 6.4a–e and S6.7–S6.12), whereas oriented thin films were obtained by applying a much lower precursor concentration of 2.9 mmol L-1 in combination with high modulator amounts of at least 20 eq. (Figures
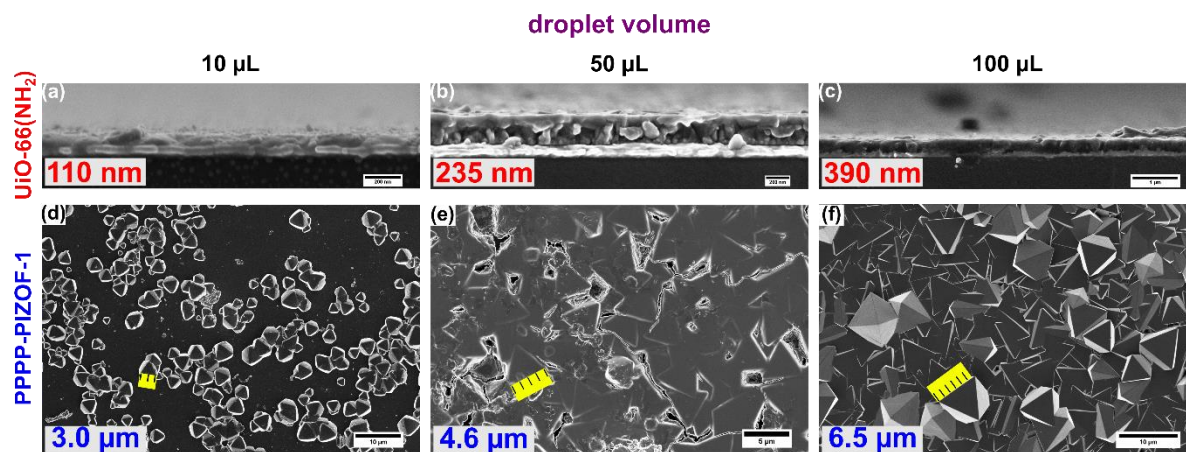
Figure 6.5. (a−c) Shows cross-section SEM images of UiO-66(NH₂) films obtained with different droplet volumes, showing the increase of the film thickness with increasing droplet volume (see also Figures S6.18, S6.24−S6.25). (d−f) Shows top-view SEM images of PPPP-PIZOF-1 films obtained with different droplet volumes, showing the increase of the crystal size and increase in surface coverage with increasing droplet volume (see also Figures S6.27−S6.29).

6.4f−j and S13−S18). Interestingly, a combination of the high precursor concentration of 8.7 mmol L-1 with a high modulator amount of 80 eq. yielded a dense thin UiO-66(NH₂) film of 300 nm thickness with a thick layer of randomly distributed crystals on top of it (Figures 6.4e and S6.12). This indicates that two individual processes are taking place under these conditions, namely homogenous nucleation in the droplet volume, along with a heterogeneous nucleation initiated by the gold surface. The amount of acetic acid in the precursor solution also influences the crystallite size. With more equivalents of acetic acid the crystal size increased as revealed by the X-ray reflection widths (Figures 6.4a, f, S6.7 and S6.13). These results point to the importance of controlled nucleation and crystal growth obtained by including a modulator under the VAC conditions for achieving highly crystalline and oriented UiO films.

In the case of PPPP-PIZOF-1, the film growth is highly precursor concentration dependent, and a decrease from 8.7 to 2.9 mmol L-1 hinders the crystallization process and thereby the formation of an ordered MOF film, regardless of the presence or absence of acetic acid in the precursor solution (Figures S6.19–S6.22). Furthermore, in contrast to the synthesis of UiO films, acetic acid in the precursor solution is detrimental to crystallization (Figure S6.19). However, the presence of acetic acid in the vapor source is needed (Figure S6.6). A slow diffusion of acetic acid from the vapor into the reaction droplet is apparently necessary to allow the formation of highly oriented MOF films (Figure S6.6). This hints

towards a link between the MOF crystallization rate and the degree of crystallinity and crystallite orientation in the films. Tuning the rates of nucleation and crystal growth to a certain degree by acetic acid as a modulator enables, in principle, the formation of a crystalline, highly oriented film.[33, 37, 39]

The impact of the droplet volume on the MOF film growth. Tuning of the UiO-66(NH$_2$) film thickness was achieved by casting droplet volumes of 10, 50 and 100 µL onto the gold surface (Figures 6.5a–c and S6.18, S6.23–S6.25). Uniformly oriented films with thicknesses of 110, 235 and 390 nm were obtained, respectively (Figure 6.5a–c). In the case of PPPP-PIZOF-1 (Figures 6.5d–f and S6.26–S6.29), the droplet volume of 10 µL led to a low surface coverage with loosely packed but well-defined octahedral crystals with 3.0 µm edge length adhering to the surface through the (111) facet (Figures 6.5d and S6.27) whereas the larger droplet volumes of 50 µL and 100 µL led to the formation of a densely packed film consisting of oriented octahedral single crystals with edge lengths of 4.6 µm and 6.5 µm, respectively (Figures 6.5e–f and S6.28–S6.29). These results are consistent with a larger reservoir of building units in the larger droplet allowing for larger crystal sizes and thicker films.

The impact of reaction temperature and reaction time on the MOF film growth. The MOF films discussed so far were synthesized at 100 °C. A temperature increase to 120 °C resulted in randomly distributed and non-oriented PPPP-PIZOF-1 crystallites (Figures S6.35–S6.36). In contrast, the UiO-66(NH2) film obtained at 120 °C features oriented crystallites (Figures S6.30–S6.31).

We found that a reaction time of only 3 h is sufficient for the formation of the MOF films, whereas reaction times shorter than 3 h led to the formation of non-crystalline deposit (Figures S6.33-S6.34, S6.39–S6.40). The combination of lower temperatures and longer reaction times were studies as well. In the case of PPPP-PIZOF-1 (Figure S6.35–S6.38) a lower temperature of 80 °C in combination with a reaction time of 12 h yielded oriented films, however, with a broader crystallite size distribution than in the films obtained at 100 °C. A further temperature decrease to 60 °C continued the trend of increasing crystallite size distribution and a decrease in surface coverage and orientation was observed. Similar experiments for UiO-66(NH$_2$) at 80 °C and 12 h resulted in non-oriented material with considerably decreased crystallinity (Figure S6.30-S6.32).

MOF film growth on different surfaces. To further illustrate the potential of MOF film synthesis via VAC, we included other surfaces but bare gold in our study: gold surfaces modified with different thiol-SAMs featuring −COOH, −CH2OH and −CH3 as terminal functional groups as indicated by contact angle measurements (Figure S6.1), and a bare silicon surface. Interestingly, on all substrates, regardless of their chemical character, UiO-66(NH2) and PPPP-PIZOF-1 films with a high degree of crystallite orientation with the alignment of the [111] axis normal to the surface were obtained (Figures S6.41–S6.50). The UiO-66(NH2) films are homogeneous and dense (Figures S6.42–S6.45) whereas the PPPP-PIZOF-1 films exhibit loosely-packed, large crystals (Figures S6.47–S6.50). Interestingly, on a silicon surface both, UiO-66(NH2) and PPPP-PIZOF-1, feature film morphology (Figures S6.45 and S6.50): in the case of UiO-66(NH2) (Figure S6.45) a layer of randomly distributed crystals are found on top of a dense film, whereas in the case of PPPP-PIZOF-1 large crystals with a good areal coverage are formed. For these cubic MOF systems, the adhesion energy of the nuclei apparently selectively favors nucleation and growth via the (111) facet at all of the interfaces investigated, in a similar fashion as for the oriented growth of MOF crystals on SAM modified surfaces.[12, 14, 16]

Accessible pores of the MOF films. Pore accessibility is a key feature of porous thin films. It is of paramount significance for applications such as on-chip molecular confinement and host-guest interactions. To determine the porosity, UiO-66(NH2) and PPPP-PIZOF-1 were grown as oriented films on quartz crystal microbalance (QCM) chips
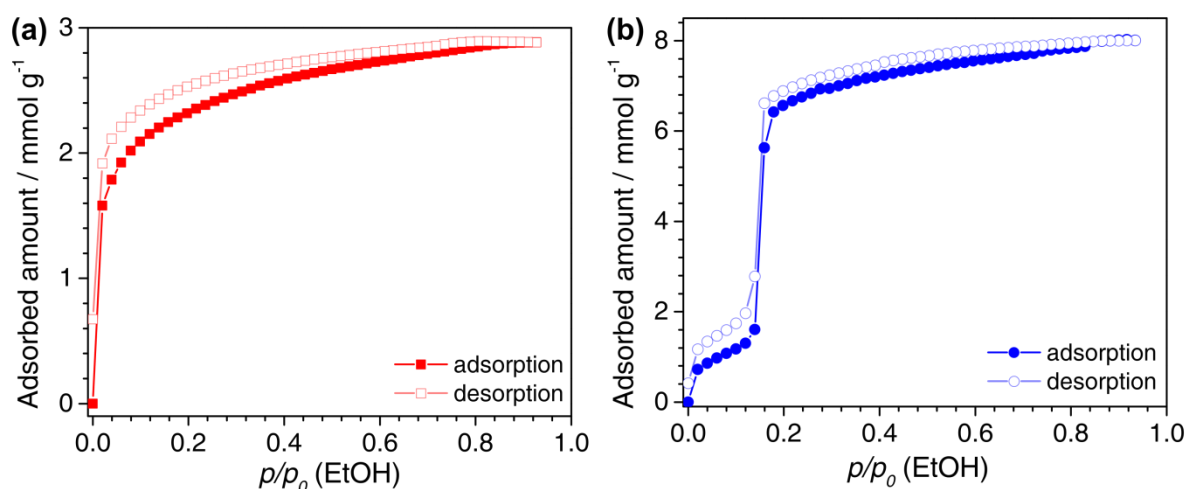
Figure 6.6. Ethanol sorption isotherms of activated MOF films: (a) UiO-66(NH2) and (b) PPPP-PIZOF-1.

(Figures S6.51–S6.52). Physisorption studies were carried out using ethanol as the sorptive at 25 °C. Prior to sorption analysis, the MOF films were activated by heating the substrates to 120 °C for 12 h under nitrogen flow. The UiO-66(NH$_2$) film featured a microporous characteristic Type I(a) isotherm (Figure 6.6a) with a steep ethanol uptake at low relative pressures (p/p0 = 0–0.02) indicating a highly defined microporous structure. Sorption analysis of a PPPP-PIZOF-1 film showed a Type IV(b) isotherm (Figure 6.6b), which is typical for structures classified to be at the transition between micro- and mesoporosity, with a pronounced pore filling step at higher partial pressure (p/p0 = 0.14–0.16) featuring a narrow pore size distribution and an overall higher uptake as compared to UiO-66(NH$_2$). Here, the adsorbed amount of ethanol at a relative pressure of p/p0 = 0.99 for UiO-66(NH$_2$) and PPPP-PIZOF-1 was calculated to be 0.17 cm3 g−1 and 0.47 cm3 g−1, respectively, based on the density of liquid ethanol at room temperature. Additionally, we determined the volumetric EtOH sorption at 20 ºC of highly crystalline UiO-66(NH$_2$) and PPPP-PIZOF-1 powders (Figure S6.59). For both MOFs, highly defined EtOH isotherms were obtained whose shapes are in very good agreement with that of the isotherms obtained for the thin films. This validates our conclusion regarding well-defined accessible pores and a narrow pore size distribution in the MOF films This demonstrates that the thin MOF films obtained via VAC exhibit accessible pores, making them well suited to accommodate guest molecules.

6.4. Conclusion

Summarizing, we report the growth of highly oriented thin films of UiO-66(NH$_2$), UiO-67, UiO-68(NH$_2$) and even of an interpenetrated MOF, the PPPP-PIZOF-1, on a variety of substrates - bare gold, gold surface modified with thiol SAMs, and bare silicon - by applying vapor-assisted conversion (VAC). The obtained MOF films exhibit a high degree of crystallinity and crystal orientation and extend to large area where the MOF crystallites are intergrown, forming almost flawless tile patterns. A detailed study regarding the parameters governing the MOF film formation, including modulator equivalents, precursor concentration, temperature and reaction time reveals a link between the rate of the crystallization and the formation of the oriented MOF films. Tuning the crystallization process by including a modulator led to highly crystalline and oriented films. Remarkably, only a reaction time of 3 h and a temperature of 100 °C are required for the formation of the oriented MOF films. Both, UiO-66(NH$_2$) and PPPP-PIZOF-1 films show considerable

ethanol uptake at room temperature, rendering these MOF films as functional materials suitable for on-chip host-guest studies. Based on the above, we introduce the VAC process as a versatile, gentle, and efficient method for the synthesis of highly crystalline and oriented thin MOF films. Based on the work presented here, we envision that VAC protocols will be generated for many further MOF topologies, which so far were not deposited as homogenous, porous, thin films and macroscopic coatings. As such, VAC is an important addition to the tool-box of film deposition technologies for porous frameworks.

6.5. References

(1)   Stassen, I.; Styles, M.; Grenci, G.; Van Gorp, H.; Vanderlinden, W.; De Feyter, S.; Falcaro, P.; De Vos, D.; Vereecken, P.; Ameloot, R., *Nat. Mater.* **2016,** *15* (3), 304-310.

(2)   Falcaro, P.; Okada, K.; Hara, T.; Ikigaki, K.; Tokudome, Y.; Thornton, A. W.; Hill, A. J.; Williams, T.; Doonan, C.; Takahashi, M., *Nat Mater* **2017,** *16* (3), 342-348.

(3)   Liu, J.; Zhou, W.; Liu, J.; Howard, I.; Kilibarda, G.; Schlabach, S.; Coupry, D.; Addicoat, M.; Yoneda, S.; Tsutsui, Y.; Sakurai, T.; Seki, S.; Wang, Z.; Lindemann, P.; Redel, E.; Heine, T.; Wöll, C., *Angew. Chem. Int. Ed.* **2015,** *54* (25), 7441-5.

(4)   Lausund, K. B.; Nilsen, O., *Nat. Commun.* **2016,** *7*, 13578.

(5)   Uzarevic, K.; Wang, T. C.; Moon, S. Y.; Fidelli, A. M.; Hupp, J. T.; Farha, O. K.; Friscic, T., *Chem. Commun.* **2016,** *52* (10), 2133-6.

(6)   Furukawa, H.; Cordova, K. E.; O'Keeffe, M.; Yaghi, O. M., *Science* **2013,** *341* (6149), 1230444.

(7)   Férey, G., *Chem. Soc. Rev.* **2008,** *37* (1), 191-214.

(8)   Meek, S. T.; Greathouse, J. A.; Allendorf, M. D., *Adv. Mater.* **2011,** *23* (2), 249-267.

(9)   Seoane, B.; Castellanos, S.; Dikhtiarenko, A.; Kapteijn, F.; Gascon, J., *Coord. Chem. Rev.* **2016,** *307*, 147-187.

(10)   Jiang, J.; Zhao, Y.; Yaghi, O. M., *J. Am. Chem. Soc.* **2016,** *138* (10), 3255-3265.

(11)   Cook, T. R.; Zheng, Y.-R.; Stang, P. J., *Chem. Rev.* **2013,** *113* (1), 734-777.

(12)   Biemmi, E.; Scherb, C.; Bein, T., *J. Am. Chem. Soc.* **2007,** *129* (26), 8054-8055.

(13)   Zhuang, J.-L.; Terfort, A.; Wöll, C., *Coord. Chem. Rev.* **2016,** *307*, 391-424.

(14)   Zacher, D.; Baunemann, A.; Hermes, S.; Fischer, R. A., *J. Mater. Chem.* **2007,** *17* (27), 2785-2792.

(15)   Hermes, S.; Schröder, F.; Chelmowski, R.; Wöll, C.; Fischer, R. A., *J. Am. Chem. Soc.* **2005,** *127* (40), 13744-13745.

(16)   Schoedel, A.; Scherb, C.; Bein, T., *Angew. Chem. Int. Ed.* **2010,** *49* (40), 7225-7228.

(17)   Shekhah, O.; Wang, H.; Kowarik, S.; Schreiber, F.; Paulus, M.; Tolan, M.; Sternemann, C.; Evers, F.; Zacher, D.; Fischer, R. A.; Wöll, C., *J. Am. Chem. Soc.* **2007,** *129* (49), 15118-15119.

(18)   Shekhah, O.; Wang, H.; Zacher, D.; Fischer, R. A.; Wöll, C., *Angew. Chem. Int. Ed.* **2009,** *48* (27), 5038-5041.

(19)   Makiura, R.; Motoyama, S.; Umemura, Y.; Yamanaka, H.; Sakata, O.; Kitagawa, H., *Nat. Mater.* **2010,** *9* (7), 565-571.

(20)   Makiura, R.; Kitagawa, H., *Eur. J. Inorg. Chem.* **2010,** *2010* (24), 3715-3724.

(21)   Motoyama, S.; Makiura, R.; Sakata, O.; Kitagawa, H., *J. Am. Chem. Soc.* **2011,** *133* (15), 5640-5643.

(22)   Liu, J.; Lukose, B.; Shekhah, O.; Arslan, H. K.; Weidler, P.; Gliemann, H.; Brase, S.; Grosjean, S.; Godt, A.; Feng, X.; Mullen, K.; Magdau, I. B.; Heine, T.; Woll, C., *Sci. Rep.* **2012,** *2*, 921.

(23)   Xu, W.; Dong, J.; Li, J.; Li, J.; Wu, F., *J. Chem. Soc. Chem. Commun.* **1990,** (10), 755-756.

(24)   Matsukata, M.; Ogura, M.; Osaki, T.; Hari Prasad Rao, P. R.; Nomura, M.; Kikuchi, E., *Top. Catal.* **1999,** *9* (1), 77-92.

(25)   Möller, K.; Yilmaz, B.; Jacubinas, R. M.; Müller, U.; Bein, T., *J. Am. Chem. Soc.* **2011,** *133* (14), 5284-5295.

(26)   Majano, G.; Mintova, S.; Ovsitser, O.; Mihailova, B.; Bein, T., *Microporous Mesoporous Mater.* **2005,** *80* (1–3), 227-235.

(27)   Tatsumi, T.; Jappar, N., *J. Phy. Chem. B* **1998,** *102* (37), 7126-7131.

(28)   Rao, P. R. H. P.; Matsukata, M., *Chem. Commun.* **1996,** (12), 1441-1442.

(29)   Changjean, W.-C.; Chiang, A. S. T.; Tsai, T.-C., *Thin Solid Films* **2013,** *529*, 327-332.

(30)   Shi, Q.; Chen, Z.; Song, Z.; Li, J.; Dong, J., *Angew. Chem. Int. Ed.* **2011,** *50* (3), 672-675.

(31)   Medina, D. D.; Rotter, J. M.; Hu, Y.; Dogru, M.; Werner, V.; Auras, F.; Markiewicz, J. T.; Knochel, P.; Bein, T., *J. Am. Chem. Soc.* **2015,** *137* (3), 1016-1019.

(32)   Cavka, J. H.; Jakobsen, S.; Olsbye, U.; Guillou, N.; Lamberti, C.; Bordiga, S.; Lillerud, K. P., *J. Am. Chem. Soc.* **2008,** *130* (42), 13850-13851.

(33)   Schaate, A.; Roy, P.; Godt, A.; Lippke, J.; Waltz, F.; Wiebcke, M.; Behrens, P., *Chem. - Eur. J.* **2011,** *17* (24), 6643-6651.

(34)   Lippke, J.; Brosent, B.; von Zons, T.; Virmani, E.; Lilienthal, S.; Preuße, T.; Hülsmann, M.; Schneider, A. M.; Wuttke, S.; Behrens, P.; Godt, A., *Inorg. Chem.* **2017,** *56* (2), 748-761.

(35)   Schaate, A.; Roy, P.; Preuße, T.; Lohmeier, S. J.; Godt, A.; Behrens, P., *Chem. - Eur. J.* **2011,** *17* (34), 9320-9325.

(36)   Garibay, S. J.; Cohen, S. M., *Chem. Commun.* **2010,** *46* (41), 7700-7702.

(37)   Wißmann, G.; Schaate, A.; Lilienthal, S.; Bremer, I.; Schneider, A. M.; Behrens, P., *Microporous Mesoporous Mater.* **2012,** *152*, 64-70.

(38)   Zhang, C.; Zhao, Y.; Li, Y.; Zhang, X.; Chi, L.; Lu, G., *Chem. - Asian J.* **2016,** *11* (2), 207-210.

(39)   Miyamoto, M.; Kohmura, S.; Iwatsuka, H.; Oumi, Y.; Uemiya, S., *CrystEngComm* **2015,** *17* (18), 3422-3425.

6.6.   Supporting Information

a. X-ray diffraction (XRD)

X-ray diffraction analyses were performed on a Bruker D8 diffractometer in Bragg-Brentano geometry with Ni-filtered Cu K_α ($\lambda = 1.54060$ Å) radiation operating at 40 kV and 30 mA with a position-sensitive detector (LynxEye).

Two-dimensional grazing-incident wide angle X-ray scattering (2D GIWAXS) data were collected using an Anton-Paar Saxspace system equipped with a Cu K_α microfocus source operated at 50 kV and 1 mA and an Eiger Dectris R 1M 2D detector.

b. Scanning electron microscopy (SEM)

SEM images were recorded on a FEI Helios NanoLab G3 UC electron microscope with an acceleration voltage of 2 kV from a field emission gun for morphological investigations and 5 kV for Z-contrast imaging. For the cross-section analysis, substrates were partially cut and broken manually to reveal fresh cross-section. Prior to SEM analysis all the samples were coated with a thin carbon layer by carbon fiber flash evaporation at high vacuum. EDX spectra were recorded using an Oxford Instruments X-Max 80 detector.

c. Quartz crystal microbalance (QCM)

The samples were activated prior to the measurement by heating the QCM-chips to 120 °C for 12 h under a nitrogen flow of 600 mL min^{-1}. QCM experiments were performed using a flow controlling system. For dosing the gases a gas flow controller (F-201-C-RBA-33-V, Bronkhorst Hi-Tec) was used. The liquid was dosed by a liquid mass flow controller (L01-RBA-11-O, Bronkhorst Hi-Tec), which was connected to an ethanol reservoir and through a nitrogen flow the ethanol was directed to the controlled evaporation mixer. The controllers were connected to a controlled evaporation mixer (W-101A-110-P, Bronkhorst Hi-Tec), where the carrier gas and the ethanol were combined and heated above the boiling point of the ethanol. For the calculation of the individual vapor pressures and settings of the flow controller Bronkhorst's Fluidat software was used.[1]

d. Contact angle measurements

Contact angle measurements were performed on an attension from Biolin Scientific. A droplet of water was placed on the substrate, while recording the images. The image analysis was carried out with the software "one attension" using a Young-Laplace analysis mode and an air-to-water interface.

e. Atomic force microscopy (AFM)

AFM measurements were performed using a NANOINK atomic force microscope in tapping mode with a scan rate of 0.2 Hz, a proportional gain of 50 and an integral gain of 32.

f. Volumetric EtOH sorption

Volumetric EthOH sorption experiments were carried out using a Quantachrome autosorb iQ instrument. Measurements were performed at 20 °C. The bulk material was activated under dynamic vacuum at 120 °C for 6 h prior to the analysis.

Synthetical Details

a. General

Acetic acid (analytical grade, Sigma-Aldrich), acetone (technical grade), terephthalic acid (P diacid, 99%, Sigma-Aldrich), 2-aminoterephthalic acid (P(NH$_2$) diacid; 99%, Sigma-Aldrich), biphenyl-4,4′-dicarboxylic acid (PP diacid; 97%, Sigma-Aldrich), *N,N*-dimethylformamide (anhydrous, synthesis grade, Fischer Scientific), ethanol (absolute, technical grade), gold pellets (Au; 99.99%, Kurt J. Leske Company Ltd), Hellmanex III (Hellma, Sigma-Aldrich), hexadecane-1-thiol (99%, Fluka), 16-mercaptohexadecanoic acid (99%, Sigma-Aldrich), 16-mercaptohexadecan-1-ol (99%, Frontier Scientific) methanol (technical grade), 2-propanol (technical grade and Chromasolv, Sigma-Aldrich), titanium pellets (Ti; 99.99%, Neyco), zirconyl dichloride octahydrate (ZrOCl$_2$•8H$_2$O; ≥99.5%, Sigma-Aldrich).

2′-Amino-1,1′:4′,1′′-terphenyl-4,4′′-dicarboxylic acid (PP(NH_2)P diacid)[2] and 2′,3′′-dimethyl-[1,1′:4′,1′′:4′′,1′′′]-quaterphenyl-4,4′′′-dicarboxylic acid (PP(2-Me)P(3-Me)P diacid)[3] were prepared as reported.

b. Substrates

The preparation of the gold-substrates is based on the procedure described by Hinterholzinger *et al.*[4] Seven microscope glass slides (Menzel, 76 mm x 26 mm) in a support made of Teflon were cleaned by ultrasonic treatment in acetone, followed by sequential washing steps with 2-propanol, a 1:100 mixture of Hellmanex III and water, water and finally 2-propanol (Chromasolv). Oxygen plasma cleaning (Diener electronic, Plasma-Surface-Technology) for 30 min was conducted, previous to the mounting of the glass slides in a vacuum deposition unit installed in a glove box (MBraun Labmaster Pro SP) equipped with an Inficon SQC-310C deposition controller. A layer of 10 nm of titanium and then a layer of 100 nm of gold were thermally deposited under high vacuum onto the microscope glass slides. Afterwards, the microscope slides were cut into 1.3 cm x 1 cm pieces. These substrates were either directly used for MOF film preparation or were used to prepare surface modified substrates. For surface modification the cut substrates were cleaned for 10 min in an ultrasonic bath, first in ethanol and then in methanol. Six pieces were immersed in a solution of a thiol (50 mmol) - 16-mercaptohexadecanoic acid (14.4 mg) or 16-mercaptohexadecan-1-ol (13.7 mg) or 1-hexadecanethiol (12.9 mg) - in ethanol (50 mL) at room temperature for 3 days. The SAM-functionalized substrates were washed with ethanol and afterwards stored in ethanol until their utilization in MOF film synthesis. Before film synthesis, the SAM-functionalized substrates were dried under a stream of nitrogen. The surface modification was proven by contact angle measurements (Figure S6.1).

The silicon-wafers (Si[100]; Ø 20 cm; 0.6 cm thick) from Siegert Wafer were cut into 1.3 cm x 1.0 cm pieces. The 10.000015 MHz QCM-chips (quartz XA 1600 with gold contacts) were purchased from KVG Quartz Crystal Technology GmbH and used without further cleaning.
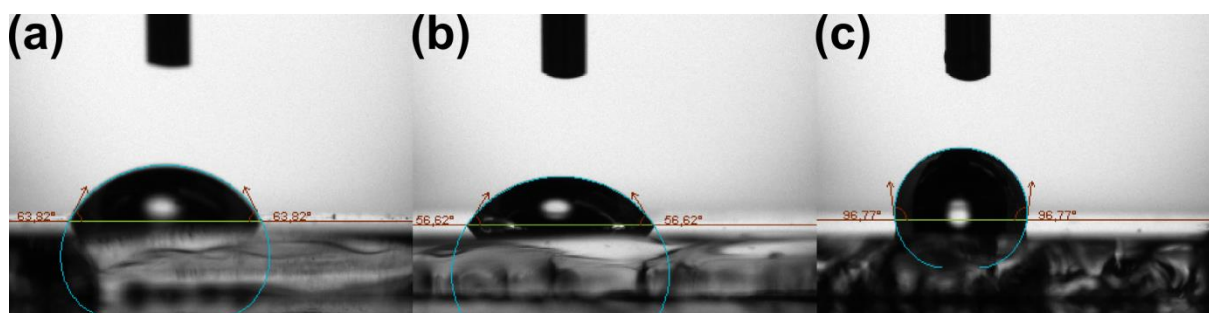
Figure S6.1: Contact angle measurements for gold surfaces modified with (a) 16-mercaptohexadecanoic acid (b) 16-mercaptohexadecan-1-ol and (c) hexadecane-1-thiol giving as contact angles 63.82°, 56.62°, and 96.77°, respectively.

c. Film formation *via* vapor-assisted conversion (VAC)

For the film formation using VAC, a glass bottle (Schott Duran, borosilicate 3.3, ISO4796, 100 mL) with a PBT cap equipped with a Teflon seal was used. The bottom part of the bottle was filled with 14 Raschig-rings (10 mm x 10 mm, soda-lime glass) to obtain an elevated flat platform for the substrate. A mixture of DMF and acetic acid was filled into the bottle. Afterwards, a substrate (1.3 cm x 1 cm) was placed on top of the Raschig-rings and fully coated with a drop of a freshly prepared MOF precursor solution. The bottle was closed and was transferred into a preheated oven where it was kept for the specified time (Tables S1-4). Afterwards the bottle was removed from the oven and were allowed to cool down for 10 min before the substrate was removed and dried under reduced pressure (2 x 10^{-3} bar).

For the precursor solution, $ZrOCl_2 \cdot 8H_2O$ was dissolved in DMF by ultrasonic treatment. If desired, acetic acid was added to this solution. The dicarboxylic acid was added to the solution and dissolved by applying ultrasonic treatment.

Table S6.1: Conditions for the synthesis of UiO-66(NH₂) films.

	Exp.	Precursor solution				Droplet volume	Substrate	Temperature	Reaction time	Vapor source	
		ZrOCl₂•8H₂O	*P(NH₂) diacid*	*acetic acid*	*DMF*					*DMF*	*acetic acid*
variation of precursor and modulator concentration	1	2.8 mg 8.7 mmol L⁻¹	1.6 mg 8.7 mmol L⁻¹	0 µL 0 mmol L⁻¹	1 mL	50 µL	gold	100 °C	3 h	4.2 mL	0.8 mL
	2	2.8 mg 8.7 mmol L⁻¹	1.6 mg 8.7 mmol L⁻¹	2 µL 35 mmol L⁻¹	1 mL	50 µL	gold	100 °C	3 h	4.2 mL	0.8 mL
	3	2.8 mg 8.7 mmol L⁻¹	1.6 mg 8.7 mmol L⁻¹	10 µL 175 mmol L⁻¹	1 mL	50 µL	gold	100 °C	3 h	4.2 mL	0.8 mL
	4	2.8 mg 8.7 mmol L⁻¹	1.6 mg 8.7 mmol L⁻¹	20 µL 350 mmol L⁻¹	1 mL	50 µL	gold	100 °C	3 h	4.2 mL	0.8 mL
	5	2.8 mg 8.7 mmol L⁻¹	1.6 mg 8.7 mmol L⁻¹	40 µL 700 mmol L⁻¹	1 mL	50 µL	gold	100 °C	3 h	4.2 mL	0.8 mL
	6	0.93 mg 2.9 mmol L⁻¹	0.52 mg 2.9 mmol L⁻¹	0 µL 0 mmol L⁻¹	1 mL	50 µL	gold	100 °C	3 h	4.2 mL	0.8 mL
	7	0.93 mg 2.9 mmol L⁻¹	0.52 mg 2.9 mmol L⁻¹	0.7 µL 12 mmol L⁻¹	1 mL	50 µL	gold	100 °C	3 h	4.2 mL	0.8 mL
	8	0.93 mg 2.9 mmol L⁻¹	0.52 mg 2.9 mmol L⁻¹	3.3 µL 58 mmol L⁻¹	1 mL	50 µL	gold	100 °C	3 h	4.2 mL	0.8 mL
	9	0.93 mg 2.9 mmol L⁻¹	0.52 mg 2.9 mmol L⁻¹	6.6 µL 116 mmol L⁻¹	1 mL	50 µL	gold	100 °C	3 h	4.2 mL	0.8 mL
	10	0.93 mg 2.9 mmol L⁻¹	0.52 mg 2.9 mmol L⁻¹	13.3 µL 232 mmol L⁻¹	1 mL	50 µL	gold	100 °C	3 h	4.2 mL	0.8 mL
variation of droplet	11	0.93 mg 2.9 mmol L⁻¹	0.52 mg 2.9 mmol L⁻¹	13.3 µL 232 mmol L⁻¹	1 mL	10 µL	gold	100 °C	3 h	4.2 mL	0.8 mL

volume	**12**	0.93 mg 2.9 mmol L^{-1}	0.52 mg 2.9 mmol L^{-1}	13.3 µL 232 mmol L^{-1}	1 mL	50 µL	gold	100 °C	3 h	4.2 mL	0.8 mL
	13	0.93 mg 2.9 mmol L^{-1}	0.52 mg 2.9 mmol L^{-1}	13.3 µL 232 mmol L^{-1}	1 mL	100 µL	gold	100 °C	3 h	4.2 mL	0.8 mL
variation of the type of substrate	**14**	0.93 mg 2.9 mmol L^{-1}	0.52 mg 2.9 mmol L^{-1}	13.3 µL 232 mmol L^{-1}	1 mL	50 µL	HS-(CH$_2$)$_{15}$-CO$_2$H	100 °C	3 h	4.2 mL	0.8 mL
	15	0.93 mg 2.9 mmol L^{-1}	0.52 mg 2.9 mmol L^{-1}	13.3 µL 232 mmol L^{-1}	1 mL	50 µL	HS-(CH$_2$)$_{16}$-OH	100 °C	3 h	4.2 mL	0.8 mL
	16	0.93 mg 2.9 mmol L^{-1}	0.52 mg 2.9 mmol L^{-1}	13.3 µL 232 mmol L^{-1}	1 mL	50 µL	HS-(CH$_2$)$_{15}$-CH$_3$	100 °C	3 h	4.2 mL	0.8 mL
	17	0.93 mg 2.9 mmol L^{-1}	0.52 mg 2.9 mmol L^{-1}	13.3 µL 232 mmol L^{-1}	1 mL	50 µL	Si-wafer	100 °C	3 h	4.2 mL	0.8 mL
	18	0.93 mg 2.9 mmol L^{-1}	0.52 mg 2.9 mmol L^{-1}	13.3 µL 232 mmol L^{-1}	1 mL	50 µL	QCM-chip	100 °C	3 h	4.2 mL	0.8 mL

variation of the reaction temperature	**19**	0.93 mg 2.9 mmol L^{-1}	0.52 mg 2.9 mmol L^{-1}	13.3 µL 232 mmol L^{-1}	1 mL	50 µL	gold	120 °C	3 h	4.2 mL	0.8 mL
	20	0.93 mg 2.9 mmol L^{-1}	0.52 mg 2.9 mmol L^{-1}	13.3 µL 232 mmol L^{-1}	1 mL	50 µL	gold	80 °C	12 h	4.2 mL	0.8 mL
variation of the reaction time	**21**	0.93 mg 2.9 mmol L^{-1}	0.52 mg 2.9 mmol L^{-1}	13.3 µL 232 mmol L^{-1}	1 mL	50 µL	gold	100 °C	1 h	4.2 mL	0.8 mL
control experiments	**22**	2.8 mg 8.7 mmol L^{-1}	1.6 mg 8.7 mmol L^{-1}	13.3 µL 232 mmol L^{-1}	1 mL	50 µL	gold	100 °C	3 h	4.2 mL	0.8 mL
	23	2.8 mg 8.7 mmol L^{-1}	1.6 mg 8.7 mmol L^{-1}	0 µL 0 mol L^{-1}	1 mL	50 µL	gold	100 °C	3 h	4.2 mL	0.8 mL
	24	2.8 mg 8.7 mmol L^{-1}	1.6 mg 8.7 mmol L^{-1}	13.3 µL 232 mmol L^{-1}	1 mL	50 µL	gold	100 °C	3 h	5.0 mL	-
	25	2.8 mg 8.7 mmol L^{-1}	1.6 mg 8.7 mmol L^{-1}	0 µL 0 mol L^{-1}	1 mL	50 µL	gold	100 °C	3 h	5.0 mL	-
	26	2.8 mg 8.7 mmol L^{-1}	1.6 mg 8.7 mmol L^{-1}	13.3 µL 232 mmol L^{-1}	1 mL	50 µL	gold	100 °C	3 h	-	5.0 mL
	27	2.8 mg 8.7 mmol L^{-1}	1.6 mg 8.7 mmol L^{-1}	13.3 µL 232 mmol L^{-1}	1 mL	50 µL	gold	100 °C	3 h	-	-

Table S6.2: Conditions for the synthesis of PPPP−PIZOF-1 films.

	Exp.	Precursor solution				Droplet volume	Substrate	Temperature	Reaction time	Vapor source	
		ZrOCl₂•8H₂O	*PP(2-Me)P(3-Me)P diacid*	*acetic acid*	*DMF*					*DMF*	*acetic acid*
variation of precursor and modulator concentration	**28**	2.8 mg 8.7 mmol L^{-1}	3.7 mg 8.7 mmol L^{-1}	0 µL 0 mmol L^{-1}	1 mL	50 µL	gold	100 °C	3 h	4.2 mL	0.8 mL
	29	2.8 mg 8.7 mmol L^{-1}	3.7 mg 8.7 mmol L^{-1}	2 µL 35 mmol L^{-1}	1 mL	50 µL	gold	100 °C	3 h	4.2 mL	0.8 mL
	30	2.8 mg 8.7 mmol L^{-1}	3.7 mg 8.7 mmol L^{-1}	10 µL 175 mmol L^{-1}	1 mL	50 µL	gold	100 °C	3 h	4.2 mL	0.8 mL
	31	2.8 mg 8.7 mmol L^{-1}	3.7 mg 8.7 mmol L^{-1}	20 µL 350 mmol L^{-1}	1 mL	50 µL	gold	100 °C	3 h	4.2 mL	0.8 mL
	32	2.8 mg 8.7 mmol L^{-1}	3.7 mg 8.7 mmol L^{-1}	40 µL 700 mmol L^{-1}	1 mL	50 µL	gold	100 °C	3 h	4.2 mL	0.8 mL
	33	0.93 mg 2.9 mmol L^{-1}	1.2 mg 2.9 mmol L^{-1}	0 µL 0 mmol L^{-1}	1 mL	50 µL	gold	100 °C	3 h	4.2 mL	0.8 mL
	34	0.93 mg 2.9 mmol L^{-1}	1.2 mg 2.9 mmol L^{-1}	0.7 µL 12 mmol L^{-1}	1 mL	50 µL	gold	100 °C	3 h	4.2 mL	0.8 mL
	35	0.93 mg 2.9 mmol L^{-1}	1.2 mg 2.9 mmol L^{-1}	3.3 µL 58 mmol L^{-1}	1 mL	50 µL	gold	100 °C	3 h	4.2 mL	0.8 mL
	36	0.93 mg 2.9 mmol L^{-1}	1.2 mg 2.9 mmol L^{-1}	6.6 µL 116 mmol L^{-1}	1 mL	50 µL	gold	100 °C	3 h	4.2 mL	0.8 mL
	37	0.93 mg 2.9 mmol L^{-1}	1.2 mg 2.9 mmol L^{-1}	13.3 µL 232 mmol L^{-1}	1 mL	50 µL	gold	100 °C	3 h	4.2 mL	0.8 mL

variation of droplet volume	38	2.8 mg 8.7 mmol L^{-1}	3.7 mg 8.7 mmol L^{-1}	0 μL 0 mmol L^{-1}	1 mL	10 μL	gold	100 °C	3 h	4.2 mL	0.8 mL
	39	2.8 mg 8.7 mmol L^{-1}	3.7 mg 8.7 mmol L^{-1}	0 μL 0 mmol L^{-1}	1 mL	50 μL	gold	100 °C	3 h	4.2 mL	0.8 mL
	40	2.8 mg 8.7 mmol L^{-1}	3.7 mg 8.7 mmol L^{-1}	0 μL 0 mmol L^{-1}	1 mL	100 μL	gold	100 °C	3 h	4.2 mL	0.8 mL

variation of the type of substrate	**41**	2.8 mg 8.7 mmol L^{-1}	3.7 mg 8.7 mmol L^{-1}	0 µL 0 mmol L^{-1}	1 mL	50 µL	HS-(CH$_2$)$_{15}$-CO$_2$H	100 °C	3 h	4.2 mL	0.8 mL
	42	2.8 mg 8.7 mmol L^{-1}	3.7 mg 8.7 mmol L^{-1}	0 µL 0 mmol L^{-1}	1 mL	50 µL	HS-(CH$_2$)$_{16}$-OH	100 °C	3 h	4.2 mL	0.8 mL
	43	2.8 mg 8.7 mmol L^{-1}	3.7 mg 8.7 mmol L^{-1}	0 µL 0 mmol L^{-1}	1 mL	50 µL	HS-(CH$_2$)$_{15}$-CH$_3$	100 °C	3 h	4.2 mL	0.8 mL
	44	2.8 mg 8.7 mmol L^{-1}	3.7 mg 8.7 mmol L^{-1}	0 µL 0 mmol L^{-1}	1 mL	50 µL	Si-wafer	100 °C	3 h	4.2 mL	0.8 mL
	45	2.8 mg 8.7 mmol L^{-1}	3.7 mg 8.7 mmol L^{-1}	0 µL 0 mmol L^{-1}	1 mL	50 µL	QCM-chip	100 °C	3 h	4.2 mL	0.8 mL
variation of the reaction temperature	**46**	2.8 mg 8.7 mmol L^{-1}	3.7 mg 8.7 mmol L^{-1}	0 µL 0 mmol L^{-1}	1 mL	50 µL	gold	120 °C	3 h	4.2 mL	0.8 mL
	47	2.8 mg 8.7 mmol L^{-1}	3.7 mg 8.7 mmol L^{-1}	0 µL 0 mmol L^{-1}	1 mL	50 µL	gold	80 °C	12 h	4.2 mL	0.8 mL
	48	2.8 mg 8.7 mmol L^{-1}	3.7 mg 8.7 mmol L^{-1}	0 µL 0 mmol L^{-1}	1 mL	50 µL	gold	60 °C	12 h	4.2 mL	0.8 mL
variation of the reaction time	**49**	2.8 mg 8.7 mmol L^{-1}	3.7 mg 8.7 mmol L^{-1}	0 µL 0 mmol L^{-1}	1 mL	50 µL	gold	100 °C	1 h	4.2 mL	0.8 mL
control experiments	**50**	2.8 mg 8.7 mmol L^{-1}	3.7 mg 8.7 mmol L^{-1}	40 µL 700 mmol L^{-1}	1 mL	50 µL	gold	100 °C	3 h	4.2 mL	0.8 mL
	51	2.8 mg 8.7 mmol L^{-1}	3.7 mg 8.7 mmol L^{-1}	0 µL 0 mol L^{-1}	1 mL	50 µL	gold	100 °C	3 h	4.2 mL	0.8 mL
	52	2.8 mg 8.7 mmol L^{-1}	3.7 mg 8.7 mmol L^{-1}	40 µL 700 mol L^{-1}	1 mL	50 µL	gold	100 °C	3 h	5.0 mL	-
	53	2.8 mg 8.7 mmol L^{-1}	3.7 mg 8.7 mmol L^{-1}	0 µL 0 mol L^{-1}	1 mL	50 µL	gold	100 °C	3 h	5.0 mL	-

54	2.8 mg	3.7 mg	0 μL	1 mL	50 μL	gold	100 °C	3 h	-	5.0 mL
	8.7 mmol L^{-1}	8.7 mmol L^{-1}	0 mol L^{-1}							
55	2.8 mg	3.7 mg	0 μL	1 mL	50 μL	gold	100 °C	3 h	-	-
	8.7 mmol L^{-1}	8.7 mmol L^{-1}	0 mol L^{-1}							

Table S6.3: Conditions for the synthesis of UiO-67 film.

Exp.	Precursor solution				Droplet volume	Substrate	Temperature	Reaction time	Vapor source	
	$ZrOCl_2 \bullet 8H_2O$	PP diacid	acetic acid	DMF					DMF	acetic acid
56	0.71 mg	0.53 mg	24.5 µL	1 mL	50 µL	gold	100 °C	3 h	4.2 mL	0.8 mL
	2.2 mmol L^{-1}	2.2 mmol L^{-1}	427 mmol L^{-1}							

Table S6.4: Conditions for the synthesis of UiO-68(NH2) film.

Exp.	Precursor solution				Droplet volume	Substrate	Temperature	Reaction time	Vapor source	
	$ZrOCl_2 \bullet 8H_2O$	PP(NH$_2$)P diacid	acetic acid	DMF					DMF	acetic acid
57	5.6 mg	5.8 mg	98 µL	1 mL	50 µL	gold	100 °C	3 h	4.2 mL	0.8 mL
	17.4 mmol L^{-1}	17.4 mmol L^{-1}	1.7 mol L^{-1}							

Table S6.5: Conditions for the synthesis of UiO-66 film.

Exp.	Precursor solution				Droplet volume	Substrate	Temperature	Reaction time	Vapor source	
	$ZrOCl_2 \bullet 8H_2O$	P diacid	acetic acid	DMF					DMF	acetic acid
58	0.93 mg	0.475 mg	13.3 µL	1 mL	50 µL	gold	100 °C	3 h	4.2 mL	0.8 mL
	2.9 mmol L^{-1}	2.9 mmol L^{-1}	232 mmol L^{-1}							

2. AFM analysis of an oriented UiO-66(NH₂) film
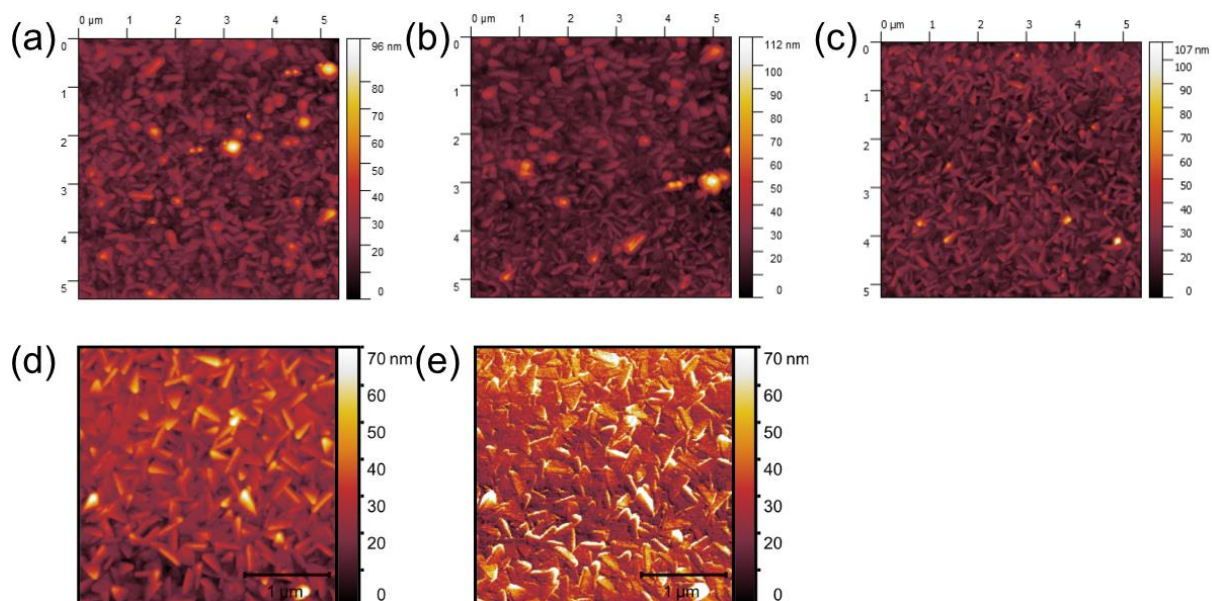
Figure S6.2: AFM topological images of 5.2 × 5.2 μm at 0.5 mm from edge (a) and (b) and of the center (c) area of a UiO-66(NH₂) film (Exp. 10). (d) and (e) magnified 3 × 3 μm area as topological and phase images of (c).

3. Influence of the reaction parameters on film formation

a. MOF with UiO topology
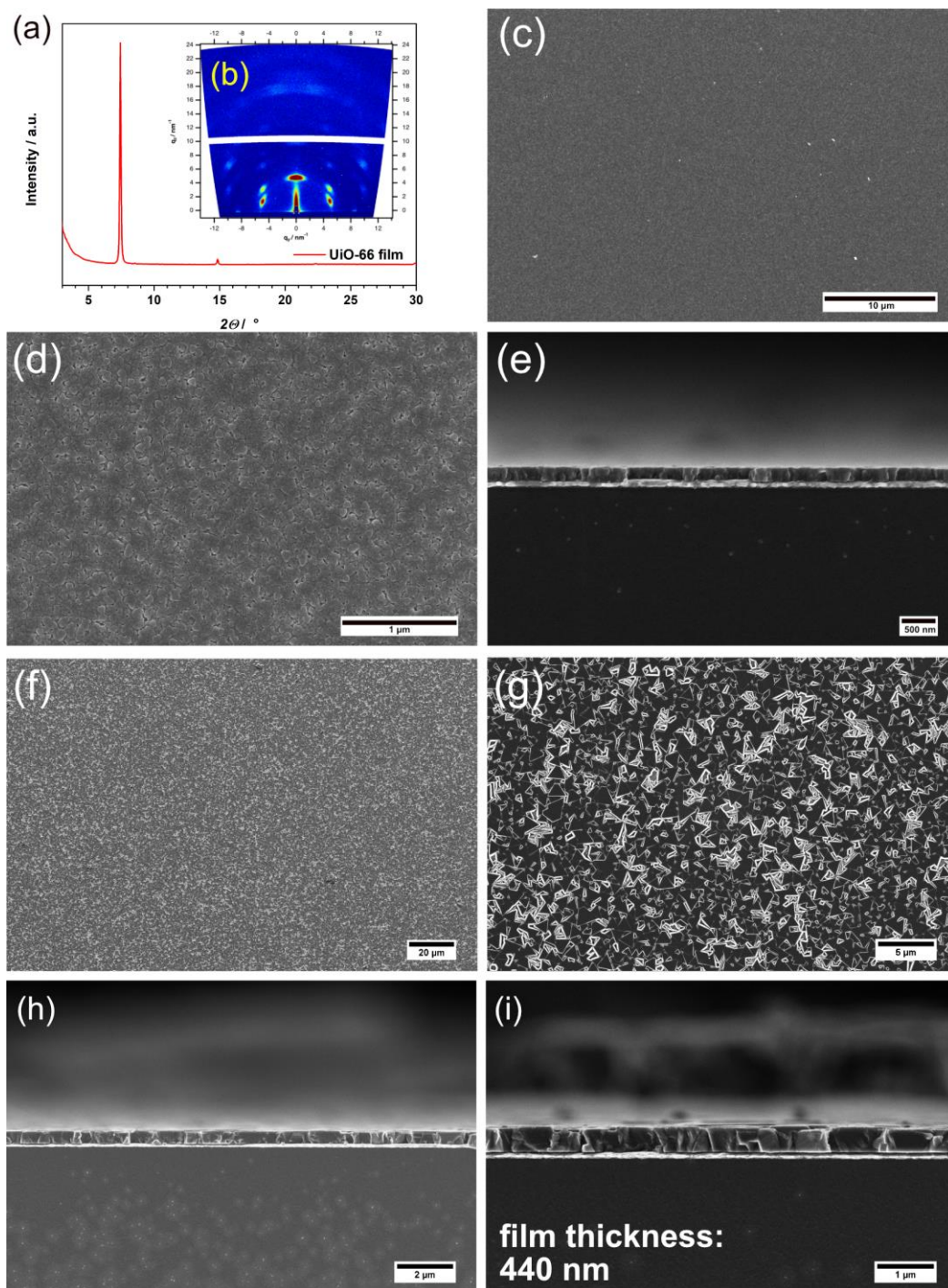
Figure S6.3: (a) XRD pattern of UiO-66 film obtained by VAC and (b) the corresponding 2D GIWAXS pattern (Exp. 58). Top-view (c, d) and cross-section (e) SEM images of the UiO-66 film, showing an oriented film with a thickness of about 200 nm. Top-view (f, g) and cross-section (h, i) SEM images of the UiO-67 film (Exp. 56), showing an oriented film with a thickness of about 440 nm.
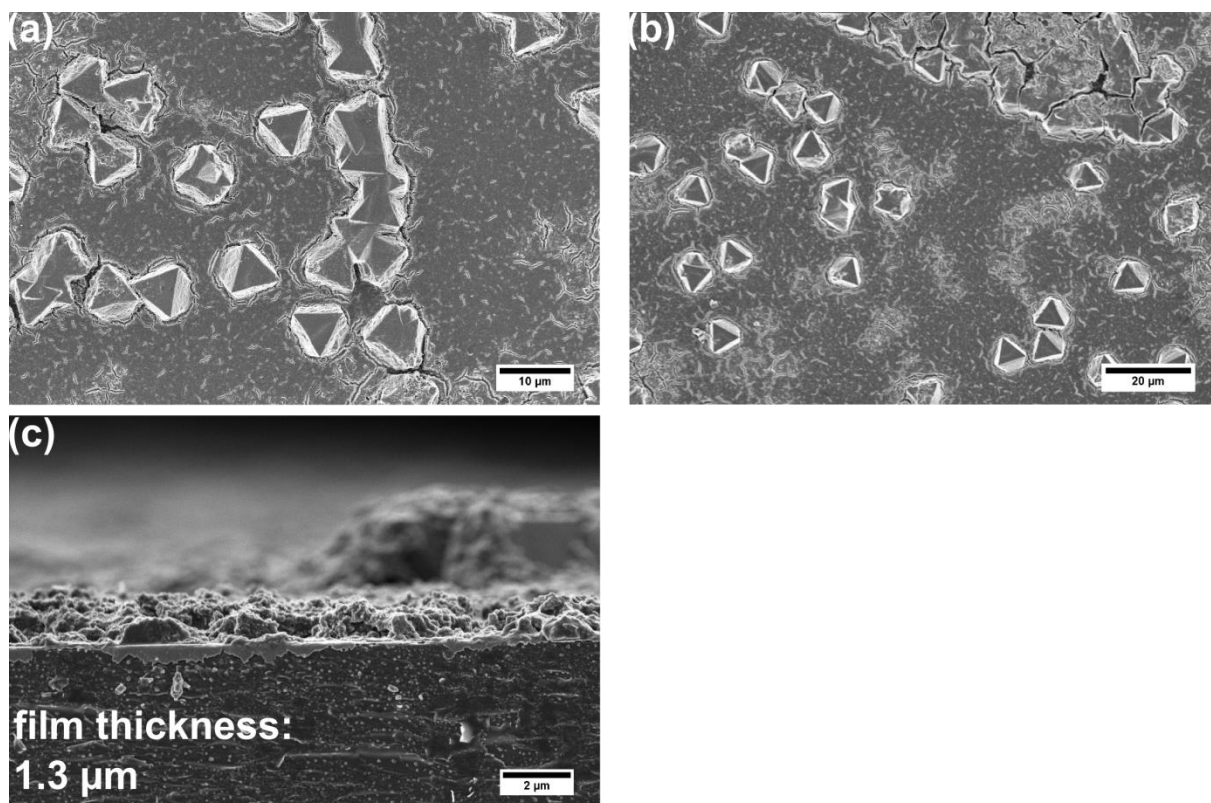
Figure S6.4: Top-view (a, b) and cross-section (c) SEM images of the UiO-68(NH$_2$) film (Exp. 57), showing a film with a thickness of about 1.3 µm and randomly distributed crystals on top of this film.

.

b. Control experiments

i. UiO-66(NH₂)
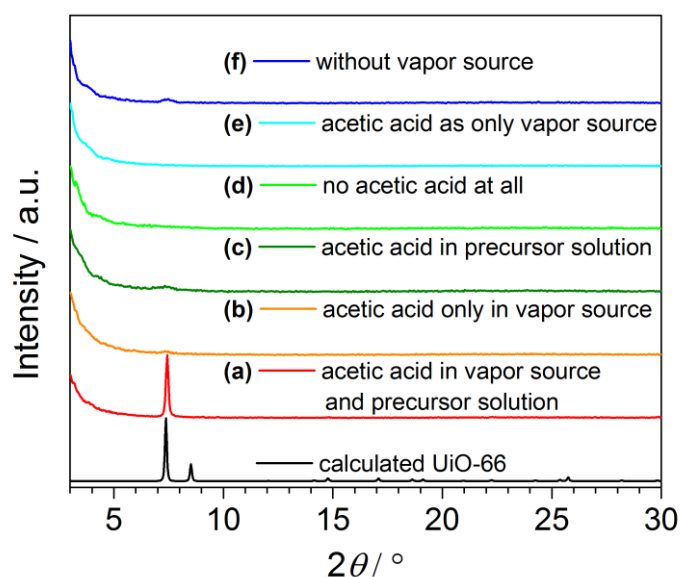
Figure S6.5: XRD patterns of UiO-66(NH₂) films that were obtained under different synthesis conditions and the PXRD pattern calculated for UiO-66 (black): (a) acetic acid and DMF as components of the vapor source and the precursor solution (Exp. 22); (b) acetic acid present only in the vapor source (Exp. 23); (c) acetic acid present only in the precursor solution (Exp. 24); (d) no acetic acid present at all (Exp. 25); (e) acetic acid as the only vapor source component (Exp. 26); (f) without any vapor source (Exp. 27).

ii. PPPP–PIZOF-1
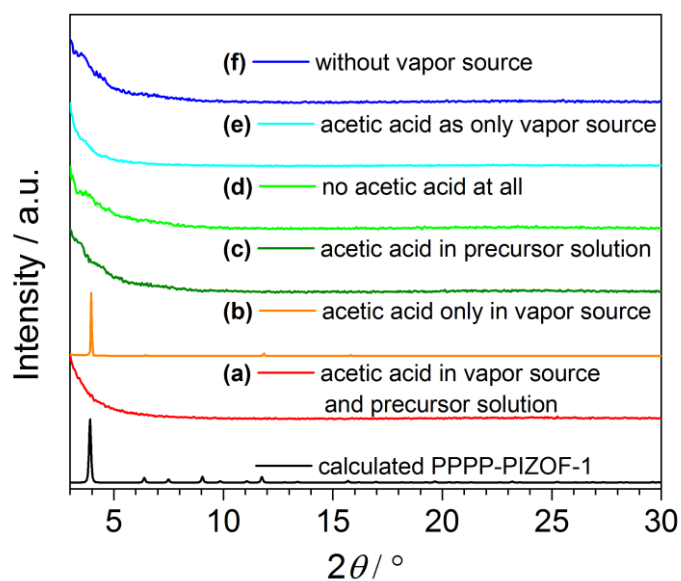
Figure S6.6: XRD patterns of PPPP–PIZOF-1 films that were obtained under different synthesis conditions and the PXRD pattern calculated for PPPP–PIZOF-1 (black): (a) acetic acid and DMF as components of the vapor source and precursor solution (Exp. 50); (b) acetic acid present only in the vapor source (Exp. 51) or (c) acetic acid present only in the precursor solution (Exp. 52); (d) no acetic acid present at all (Exp. 53); (e) acetic acid as the only vapor source component (Exp. 54); (f) without any vapor source (Exp. 55).

c. **The impact of the precursor and modulator concentrations on the MOF film growth**
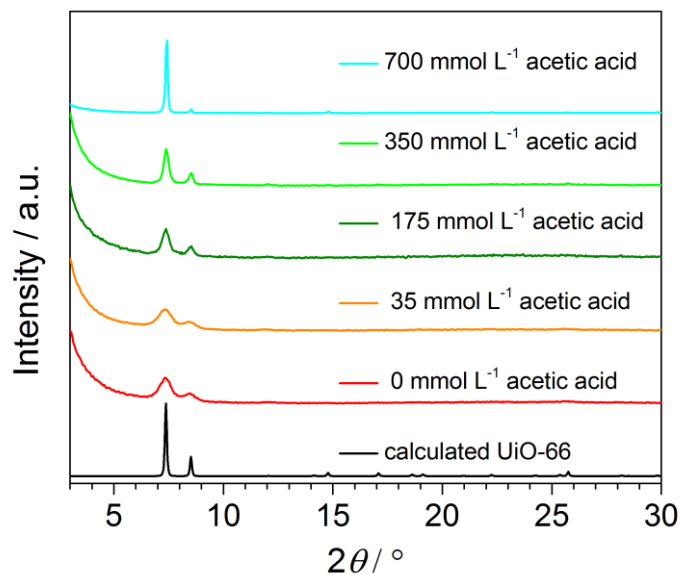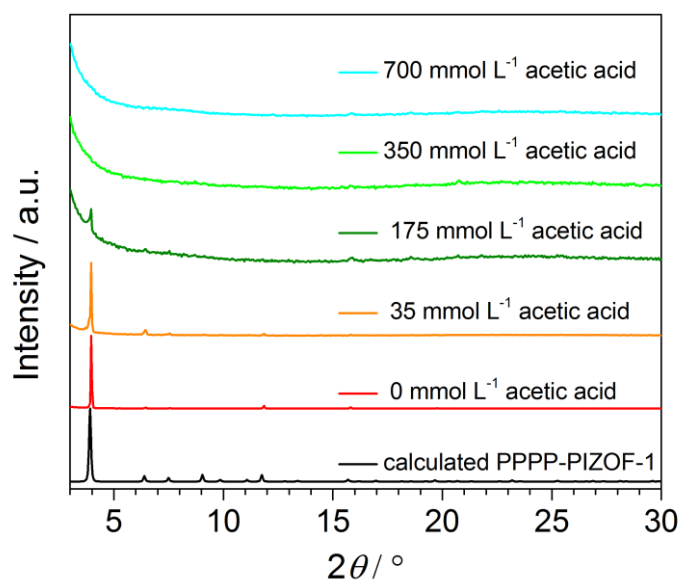
    i. **UiO-66(NH₂)**

Figure S6.7: Calculated PXRD pattern of UiO-66 and XRD patterns of the UiO-66(NH₂) films obtained from solutions with a precursor concentration of 8.7 mmol L-1 at acetic acid concentrations in the precursor solution ranging from 0−700 mmol L-1 which correspond to 0, 4, 20, 40 and 80 mol. equiv. related to ZrOCl2•8H2O (Exp. 1-5). The corresponding SEM images are shown in Figures S6.8-S6.12.
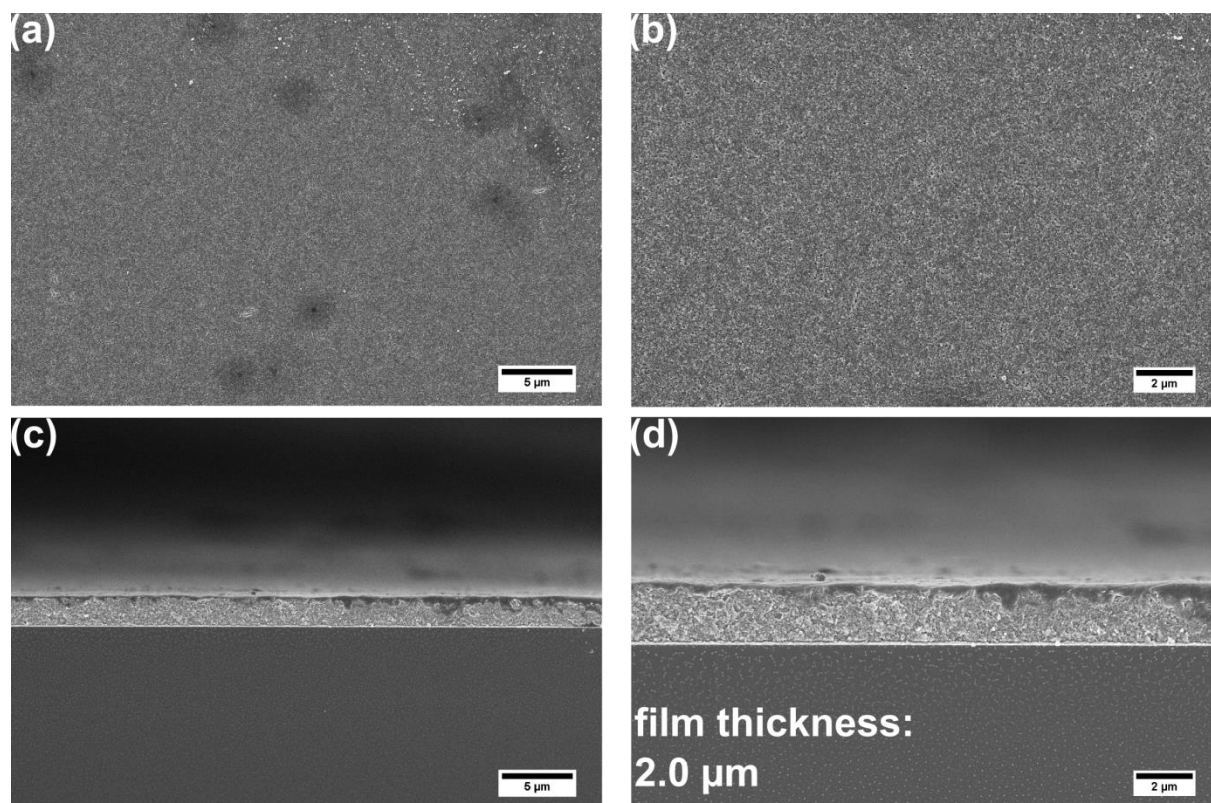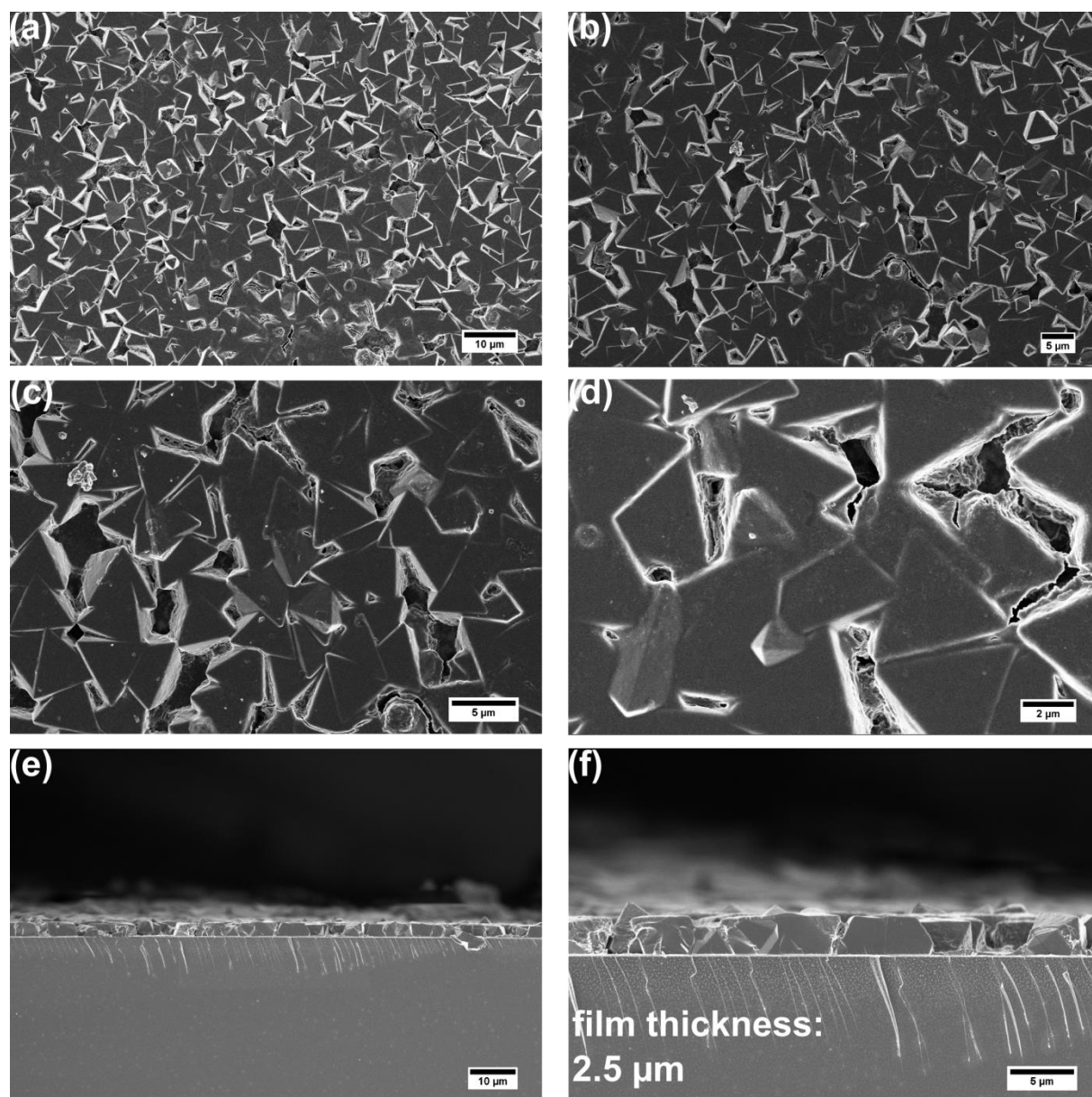
Figure S6.8: Top-view (a, b) and cross-section (c, d) SEM images of the UiO-66(NH$_2$) film obtained without acetic acid in the precursor solution (Exp. 1) showing a dense film with a thickness of about 2.0 μm consisting of MOF nanoparticles. The corresponding XRD is provided in Figure S6.7.
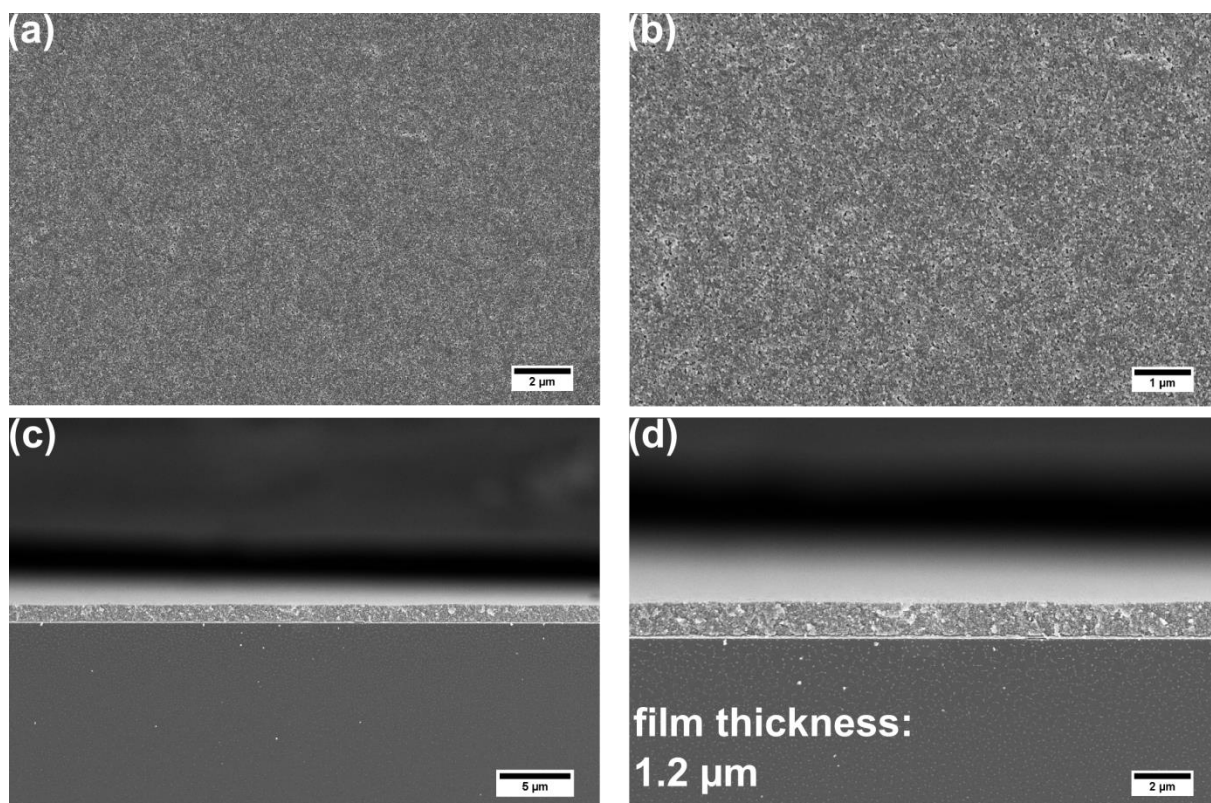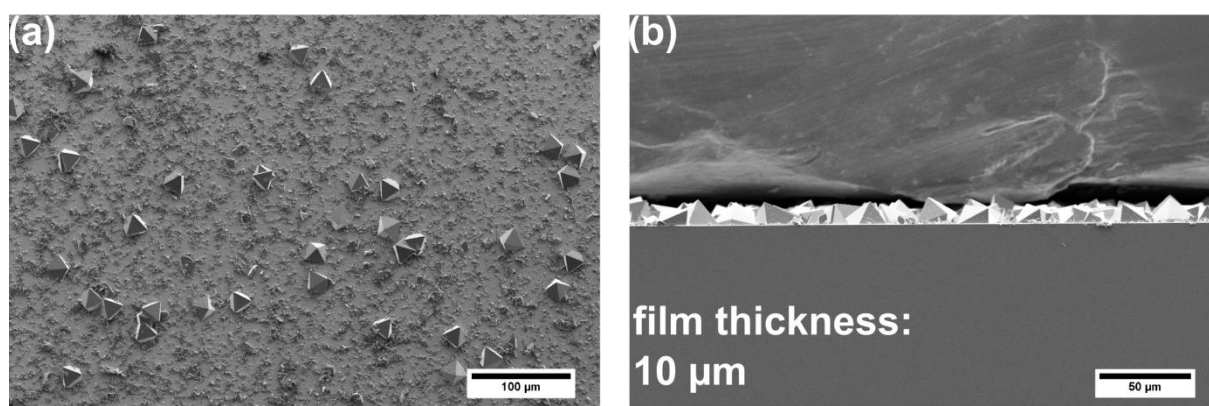
Figure S6.9: Top-view (a, b) and cross-section (c, d) SEM images of the UiO-66(NH$_2$) film obtained with 35 mmol L-1 acetic acid in the precursor solution (Exp. 2) showing a dense film with a thickness of about 1.2 µm consisting of MOF nanoparticles. The corresponding XRD is provided in Figure S6.7.
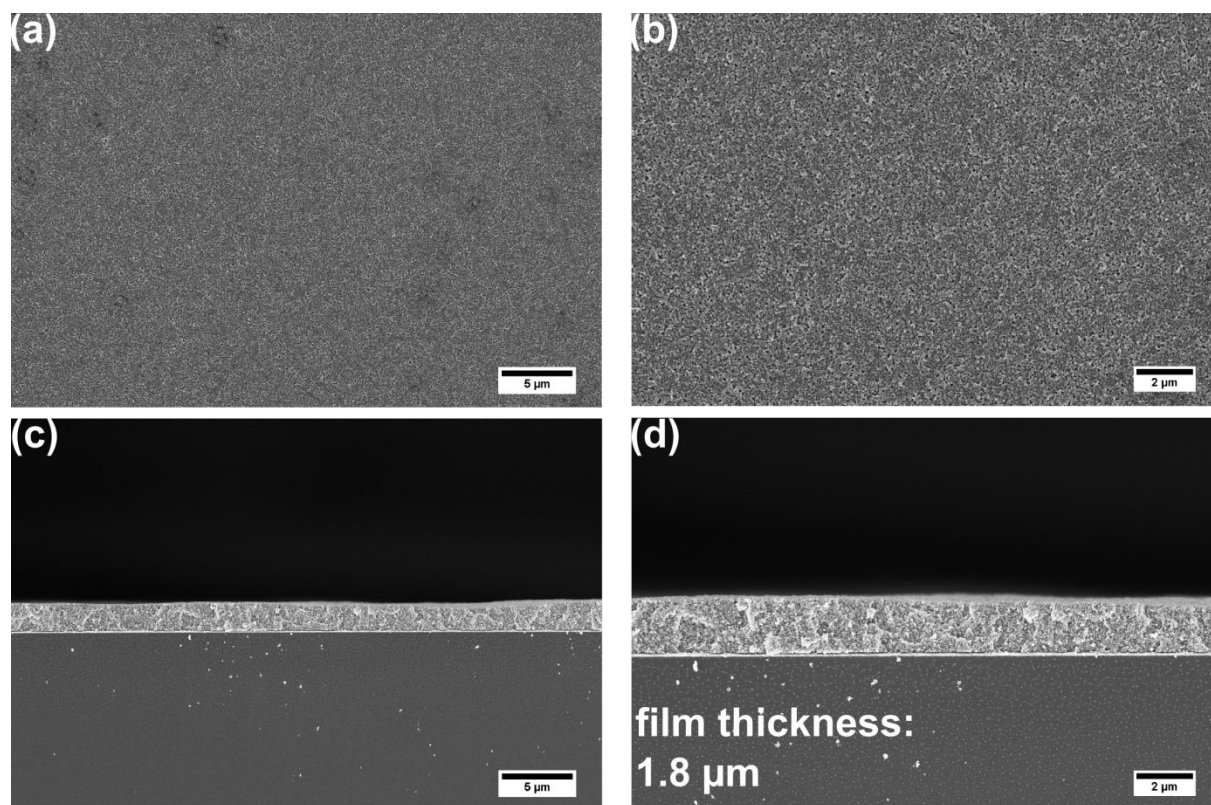
Figure S6.10: Top-view (a, b) and cross-section (c, d) SEM images of the UiO-66(NH$_2$) film obtained with 175 mmol L-1 acetic acid in the precursor solution (Exp. 3) showing a dense film with a thickness of about 1.8 µm consisting of MOF nanoparticles. The corresponding XRD is provided in Figure S7.
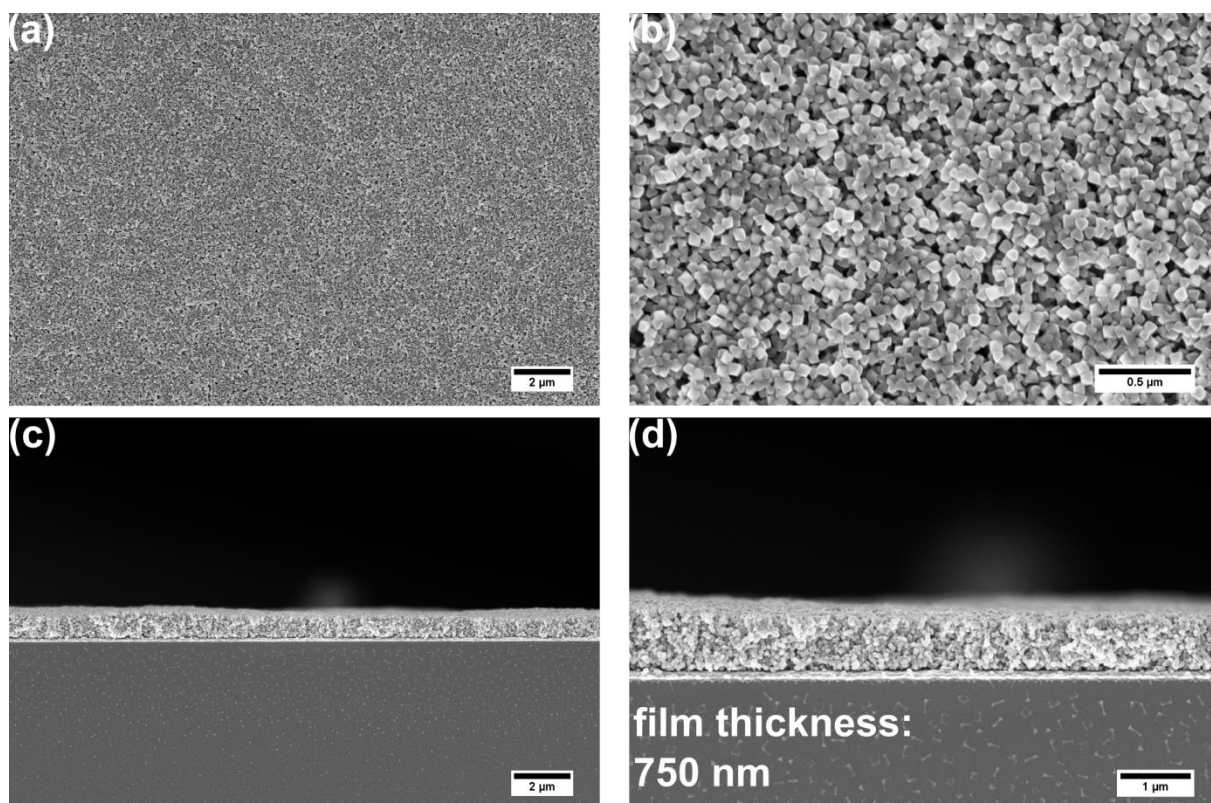
Figure S6.11: Top-view (a, b) and cross-section (c, d) SEM images of the UiO-66(NH$_2$) film obtained with 350 mmol L-1 acetic acid in the precursor solution (Exp. 4) showing a dense film with a thickness of about 750 nm consisting of MOF nanoparticles. The corresponding XRD is provided in Figure S6.7.
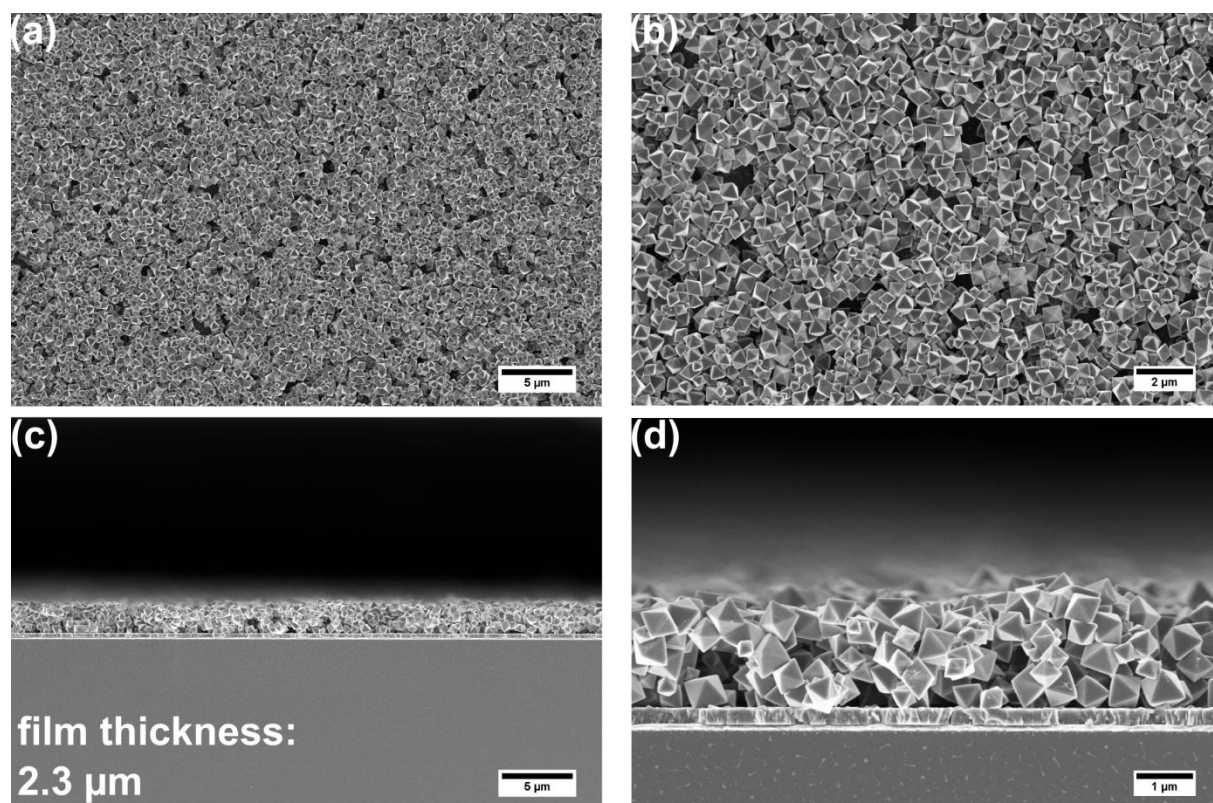
Figure S6.12: Top-view (a, b) and cross-section (c, d) SEM images of the UiO-66(NH$_2$) film obtained with 700 mmol L-1 acetic acid in the precursor solution (Exp. 5) showing a dense film with a thickness of about 2.3 µm consisting of MOF crystals and underneath a MOF film of about 300 nm thickness. The corresponding XRD is provided in Figure S6.7.
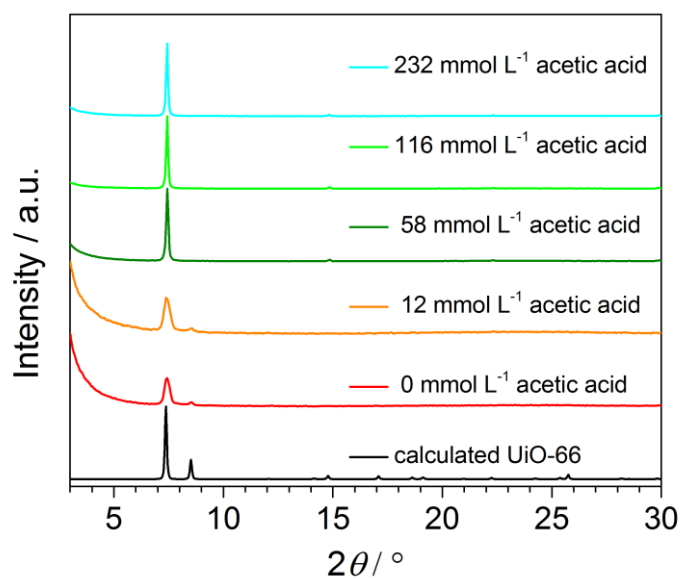
Figure S6.13: Calculated PXRD pattern of UiO-66 and XRD patterns of the UiO-66(NH$_2$) films obtained from solutions with a precursor concentration of 2.9 mmol L-1 at acetic acid concentrations in the precursor solution ranging from 0–232 mmol L-1 which correspond to 0, 4, 20, 40 and 80 mol. equiv. related to ZrOCl2•8H2O (Exp. 6-10). The corresponding SEM images are shown in Figures S6.14-S6.18.
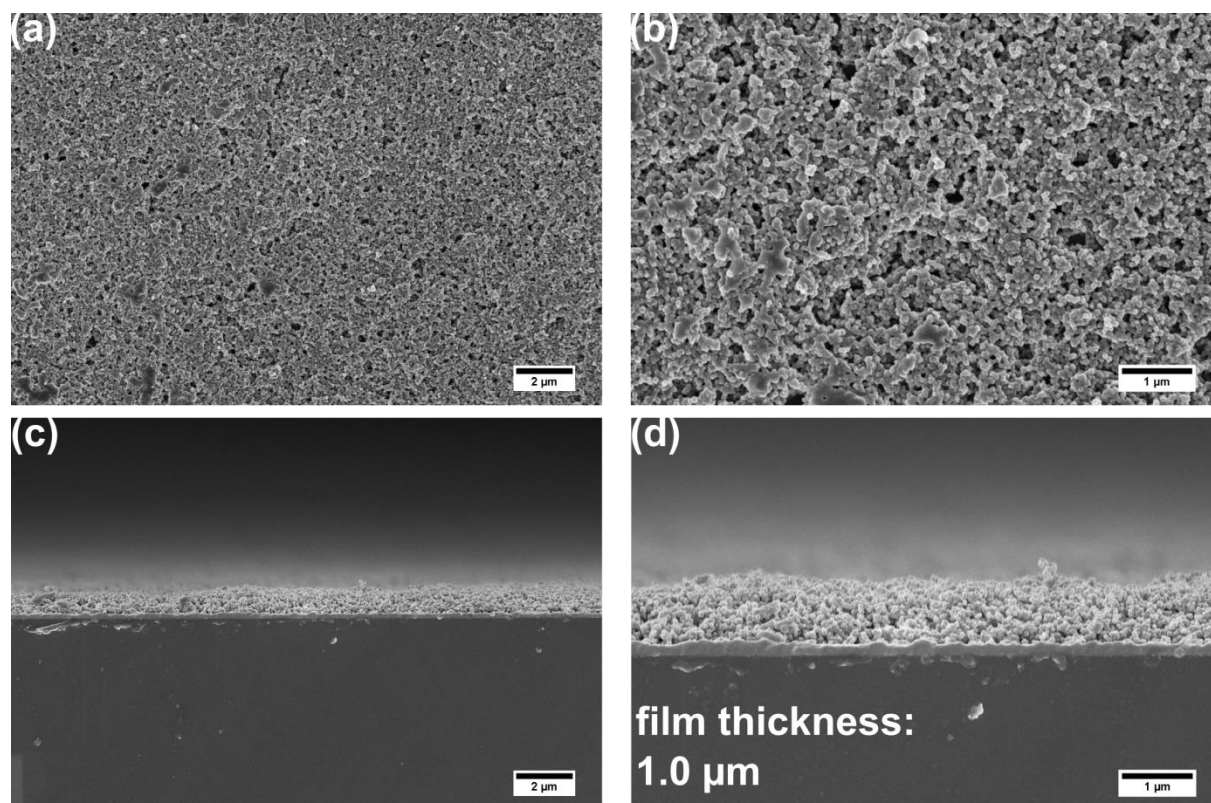
Figure S6.14: Top-view (a, b) and cross-section (c, d) SEM images of the UiO-66(NH$_2$) film, obtained without acetic acid in the precursor solution (Exp. 6) showing a dense film with a thickness of about 1.0 μm consisting of MOF nanoparticles. The corresponding XRD is provided in Figure S6.13.
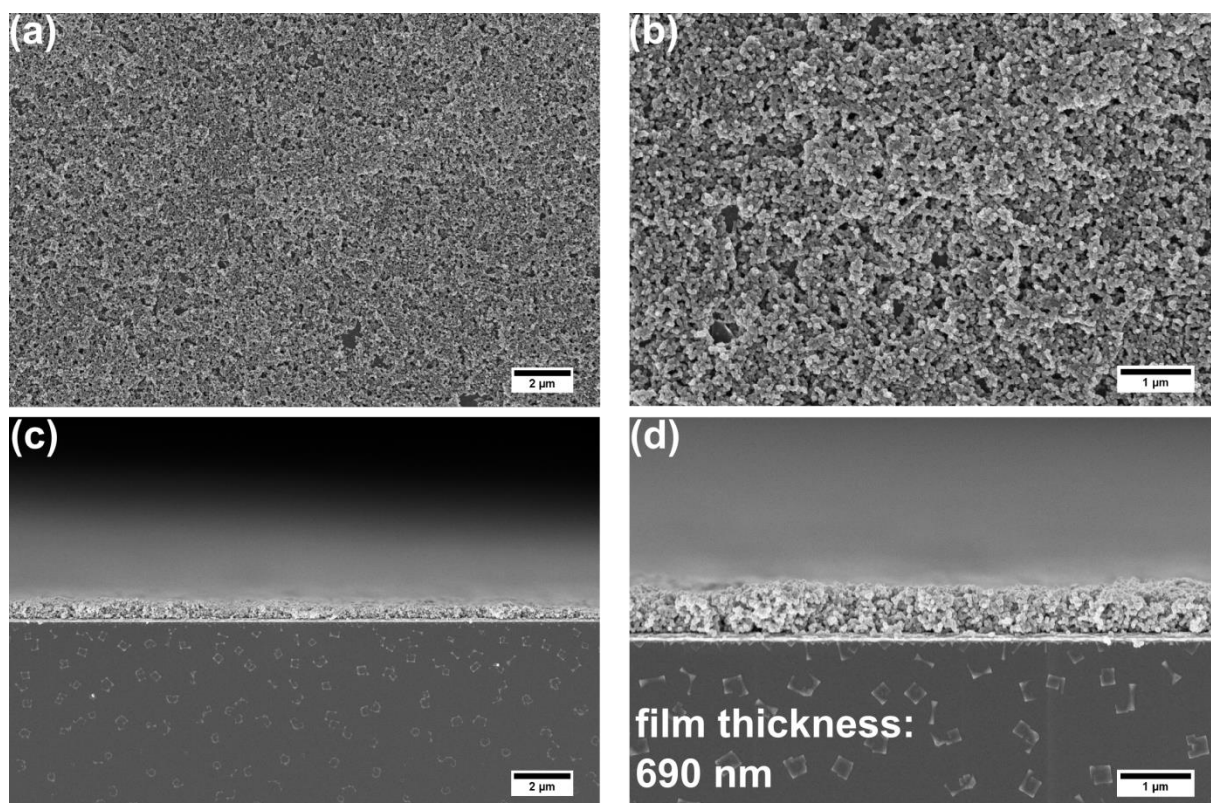
Figure S6.15: Top-view (a, b) and cross-section (c, d) SEM images of the UiO-66(NH$_2$) film obtained with 12 mmol L-1 acetic acid in the precursor solution (Exp. 7) showing a dense film with a thickness of about 690 nm consisting of MOF nanoparticles. The corresponding XRD is provided in Figure S6.13.
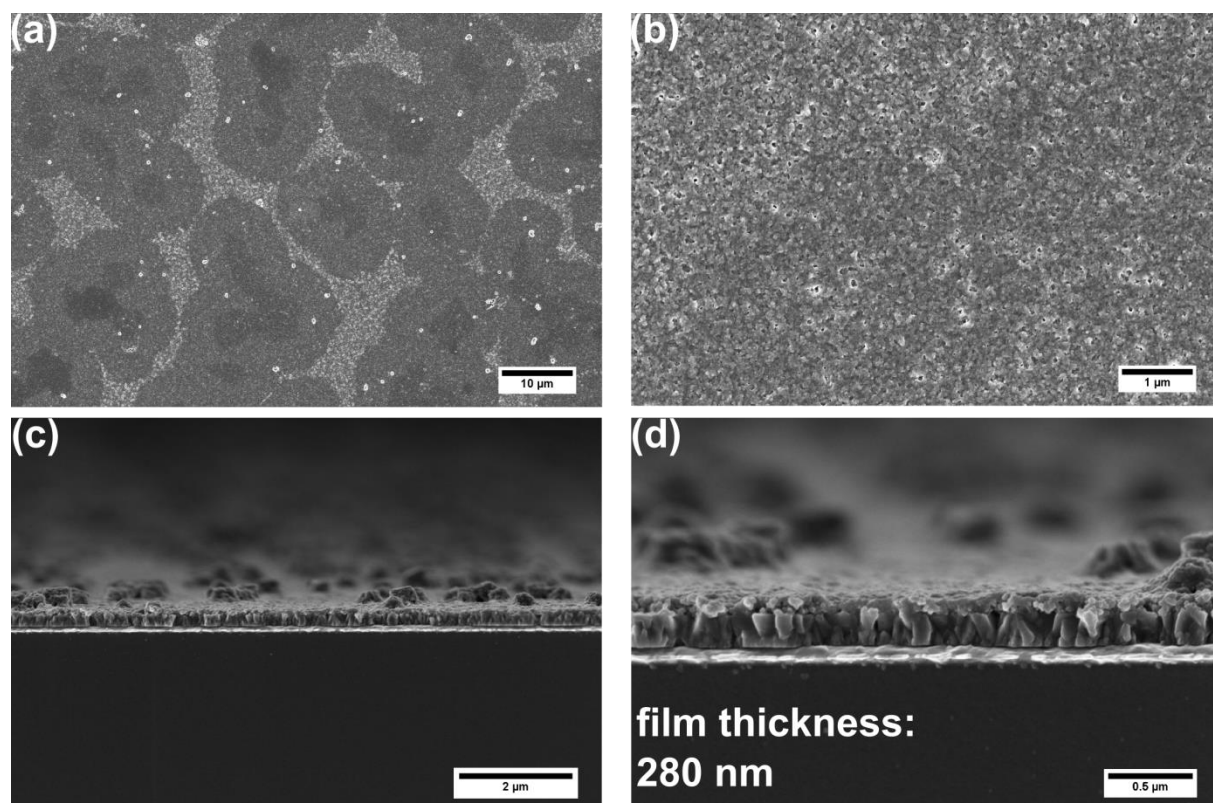
Figure S6.16: Top-view (a, b) and cross-section (c, d) SEM images of the UiO-66(NH$_2$) film obtained with 58 mmol L-1 acetic acid in the precursor solution (Exp. 8) showing a dense film with a thickness of about 280 nm consisting of MOF crystallites. The corresponding XRD is provided in Figure S6.13.
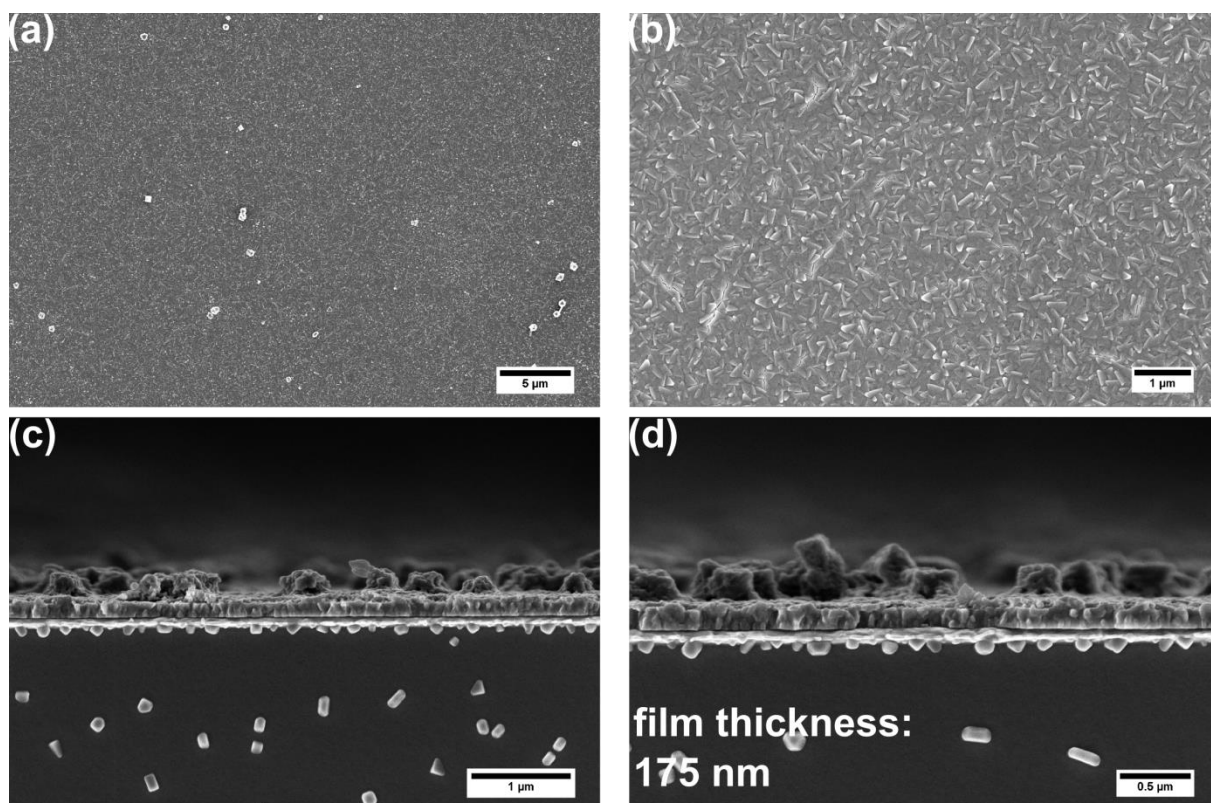
Figure S6.17: Top-view (a, b) and cross-section (c, d) SEM images of the UiO-66(NH$_2$) film obtained with 116 mmol L-1 acetic acid in the precursor solution (Exp. 9) showing a dense film with a thickness of about 175 nm consisting of MOF crystallites and randomly distributed MOF crystals on top of the film. The corresponding XRD is provided in Figure S6.13.
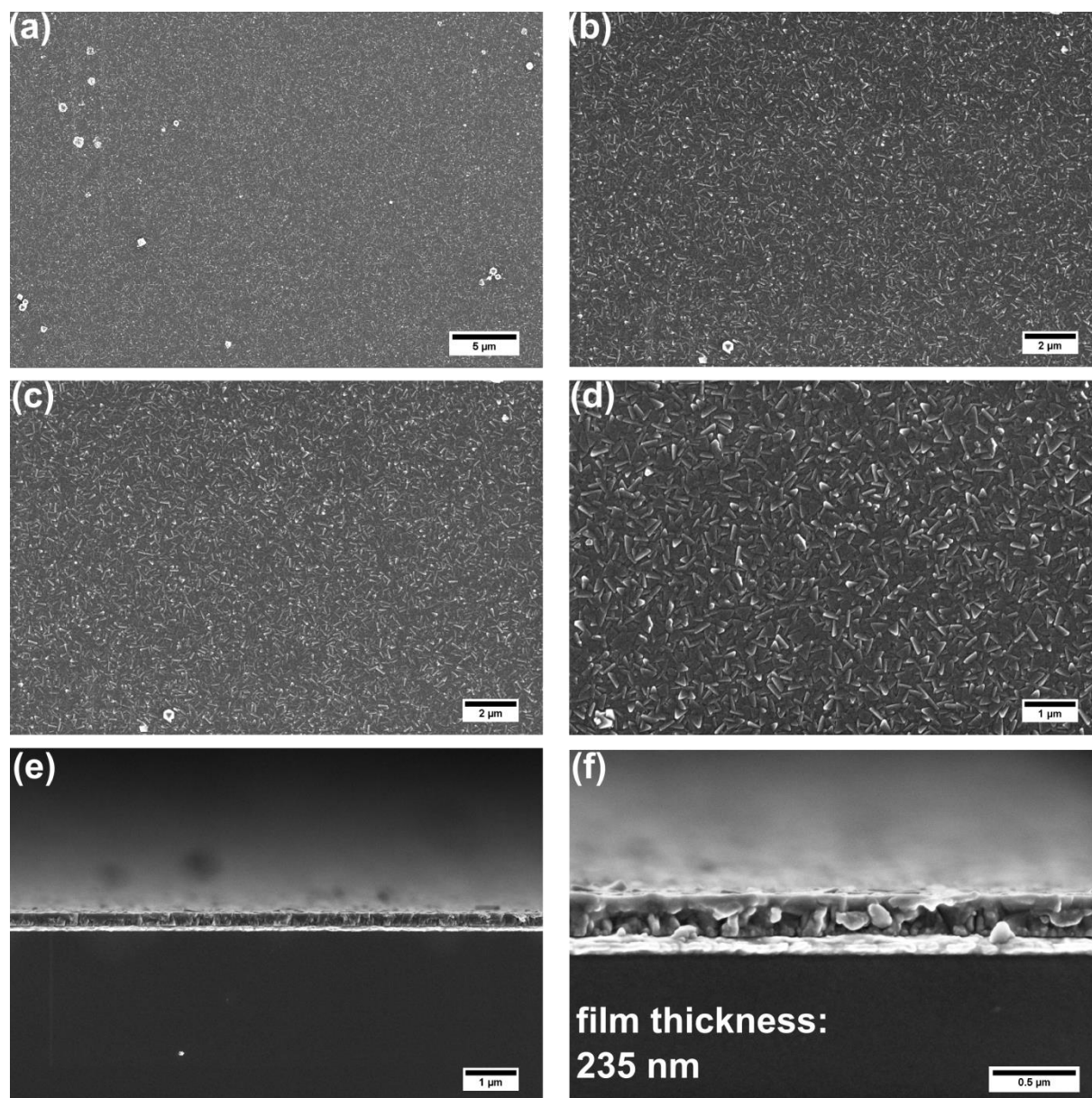
Figure S6.18: Top-view (a-d) and cross-section (e, f) SEM images of the UiO-66(NH$_2$) film obtained with 232 mmol L-1 acetic acid in the precursor solution (Exp. 10) showing a dense film with a thickness of about 235 nm consisting of MOF crystallites. The corresponding XRD is provided in Figure S6.13.

ii. PPPP–PIZOF-1

Figure S6.19: Calculated PXRD pattern of PPPP–PIZOF-1 and XRD patterns of the PPPP–PIZOF-1 films obtained from solutions with a precursor concentration of 8.7 mmol L-1 at acetic acid concentrations in the precursor solution ranging from 0–700 mmol L-1 which correspond to 0, 4, 20, 40 and 80 mol. equiv. related to ZrOCl2•8H2O (Exp. 28-32). The corresponding SEM images are shown in Figures S6.20, S6.21.

Figure S6.20: Top-view (a-d) and cross-section (e, f) SEM images of the PPPP–PIZOF-1 film obtained without acetic acid in the precursor solution (Exp. 28) showing a film with a thickness of about 2.5 µm consisting of MOF crystals. The corresponding XRD is provided in Figure S6.19.

Figure S6.21: Top-view (a) and cross-section (b) SEM images of the PPPP−PIZOF-1 film obtained with 35 mmol L-1 acetic acid in the precursor solution (Exp. 29) showing a layer of randomly distributed MOF crystallites with a thickness of about 10 μm. The corresponding XRD is provided in Figure S6.19.
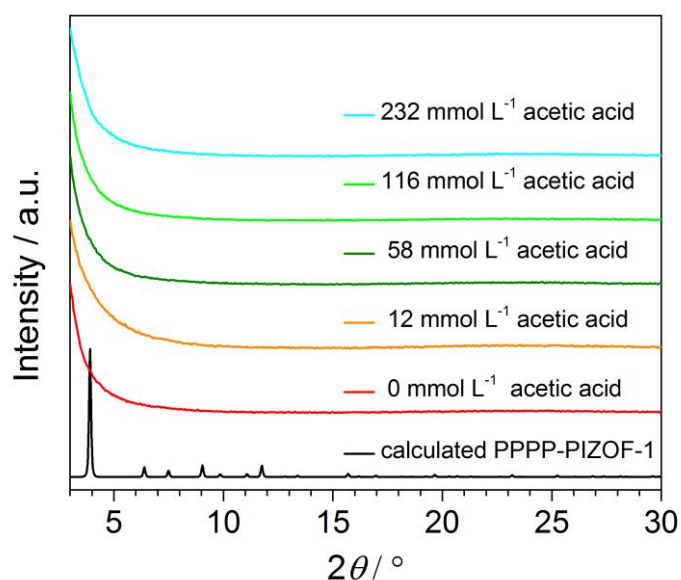
Figure S6.22: Calculated PXRD pattern of PPPP−PIZOF-1 and XRD patterns of the PPPP−PIZOF-1 films obtained from solutions with a precursor concentration of 2.9 mmol L-1 at acetic acid concentrations in the precursor solution ranging from 0−232 mmol L-1 which correspond to 0, 4, 20, 40 and 80 mol. equiv. related to ZrOCl2•8H2O (Exp. 33-37).

d. The impact of the droplet volume on the MOF film growth
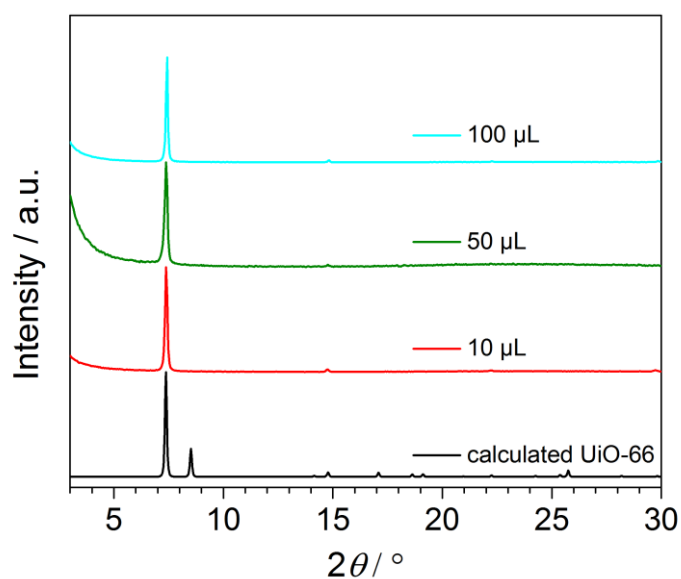
i. UiO-66(NH$_2$)

Figure S6.23: Calculated PXRD pattern of UiO-66 and XRD patterns of the UiO-66(NH2) films obtained by using droplet volumes ranging from 10–100 µL (Exp. 11-13). The corresponding SEM images are shown in Figures S6.18, S6.24, S6.25.

.
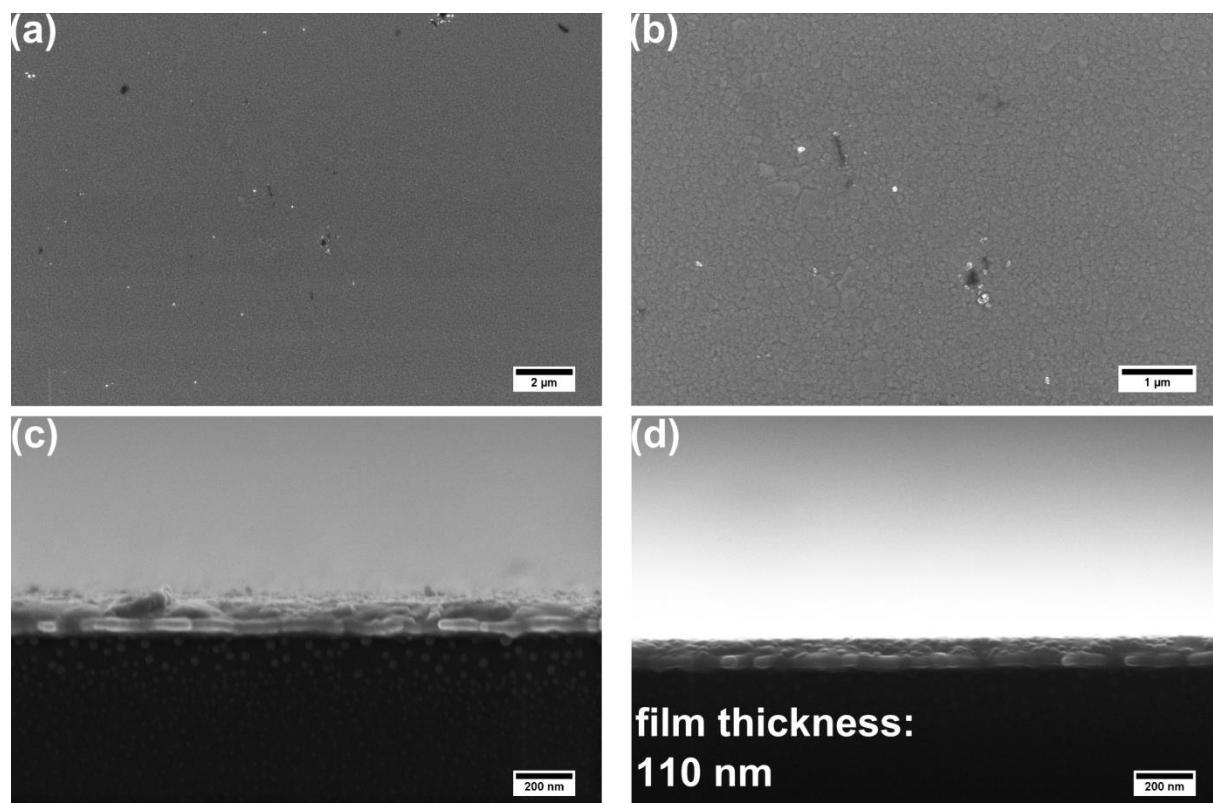
Figure S6.24: Top-view (a, b) and cross-section (c, d) SEM images of the UiO-66(NH2) film obtained with a droplet volume of 10 µL (Exp. 11) showing a dense film with a thickness of about 110 nm. The corresponding XRD is provided in Figure S6.23.
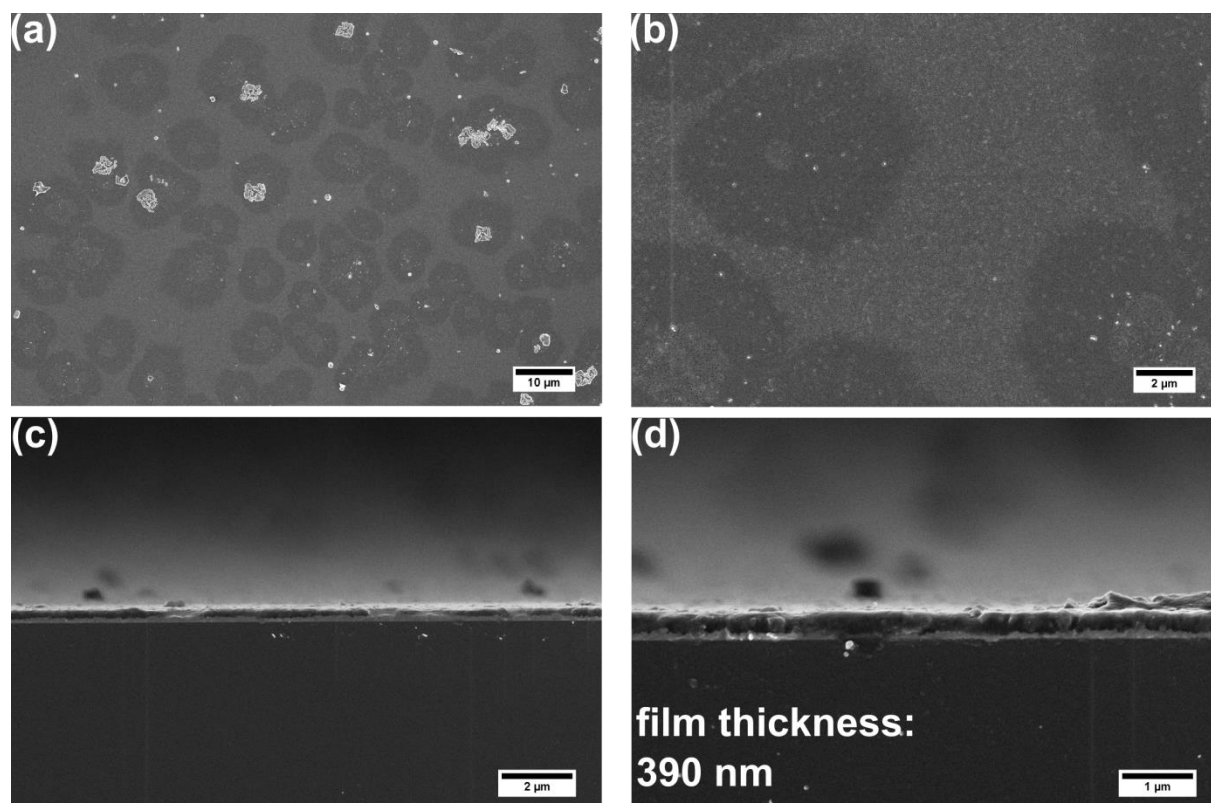
Figure S6.25: Top-view (a, b) and cross-section (c, d) SEM images of the UiO-66(NH2) film obtained with a droplet volume of 100 µL (Exp. 13) showing a dense film with a thickness of about 390 nm. The corresponding XRD is provided in Figure S6.23.
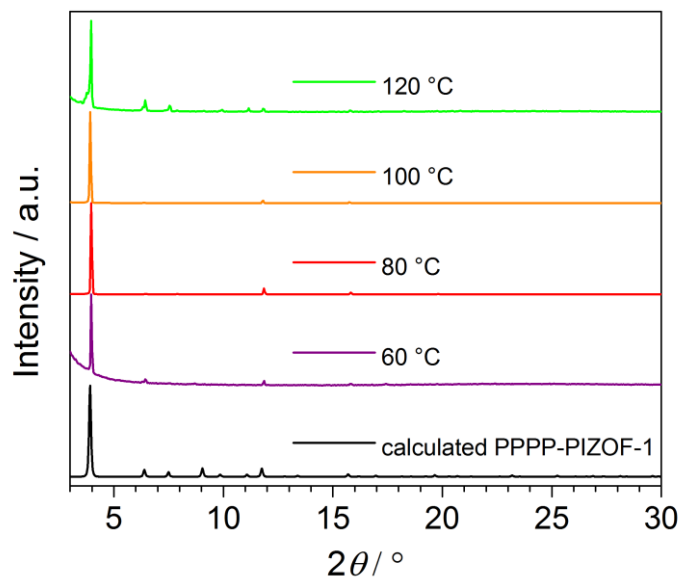
ii. PPPP–PIZOF-1
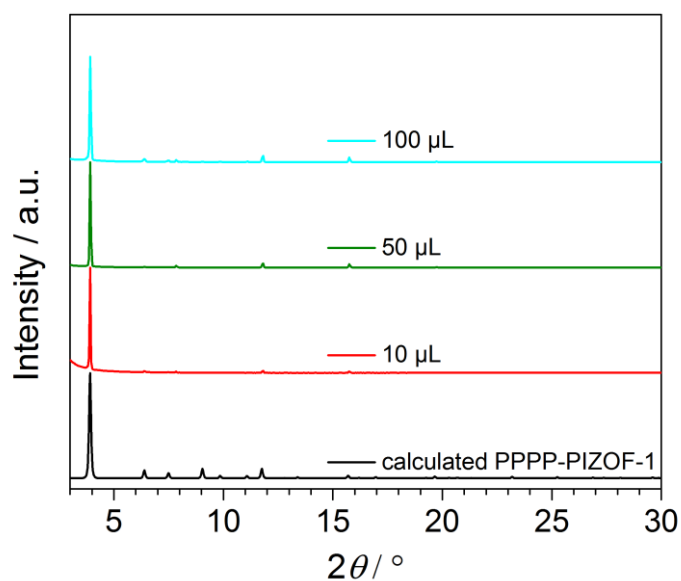
Figure S6.26: Calculated PXRD pattern of PPPP–PIZOF-1 and XRD patterns of the PPPP–PIZOF-1 films obtained by using droplet volumes ranging from 10–100 µL (Exp. 38-40). The corresponding SEM images are shown in Figures S6.27-S6.29.
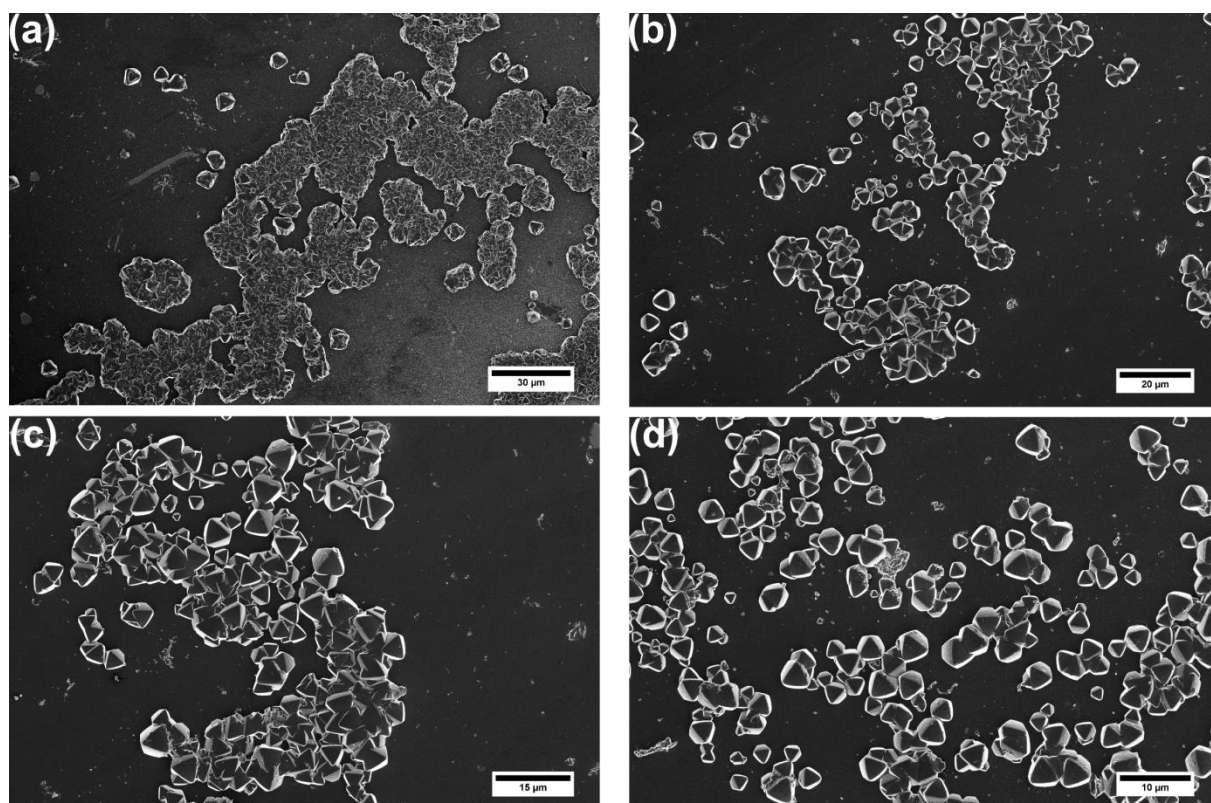
Figure S6.27: Top-view SEM images of the PPPP–PIZOF-1 film obtained with a droplet volume of 10 µL (Exp. 38) showing oriented crystals with an edge length of about 3.0 µm. The corresponding XRD is provided in Figure S6.26.
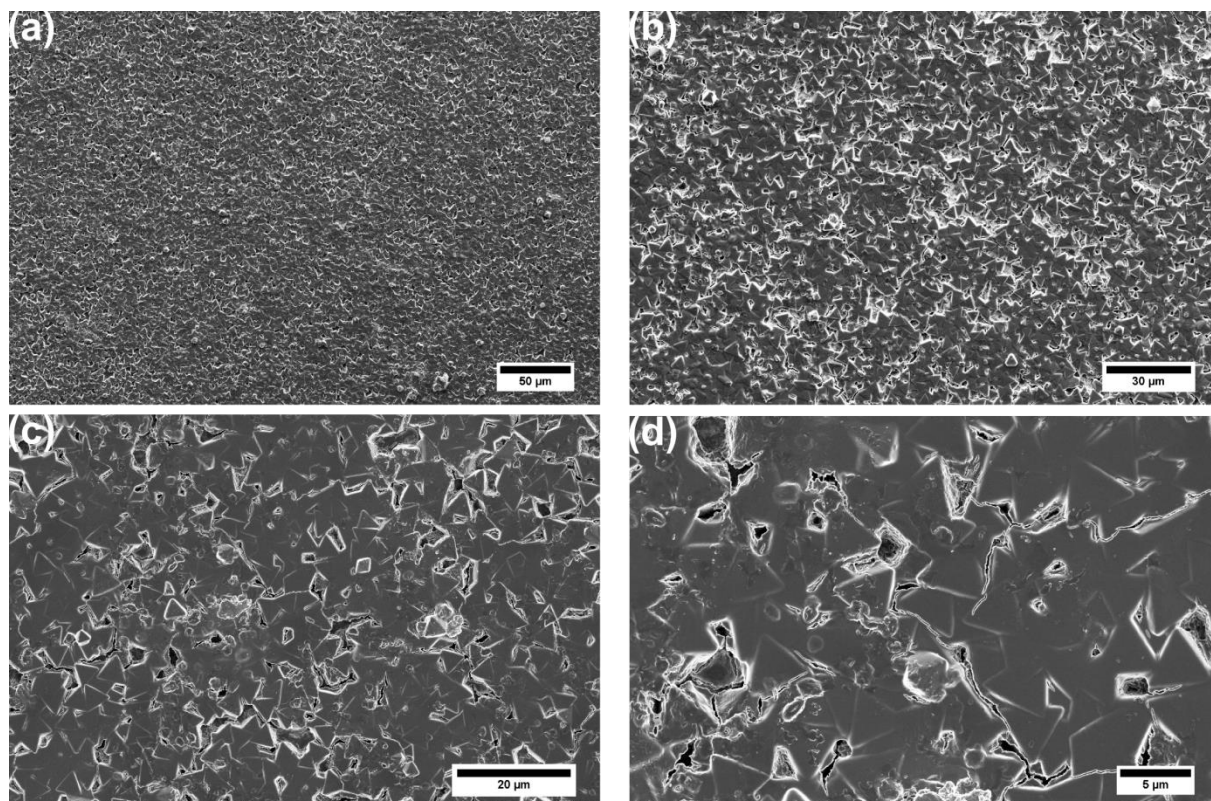
Figure S6.28: Top-view SEM images of the PPPP–PIZOF-1 film obtained with a droplet volume of 50 μL (Exp. 39) showing oriented crystals with an edge length of about 4.6 μm. The corresponding XRD is provided in Figure S6.26.
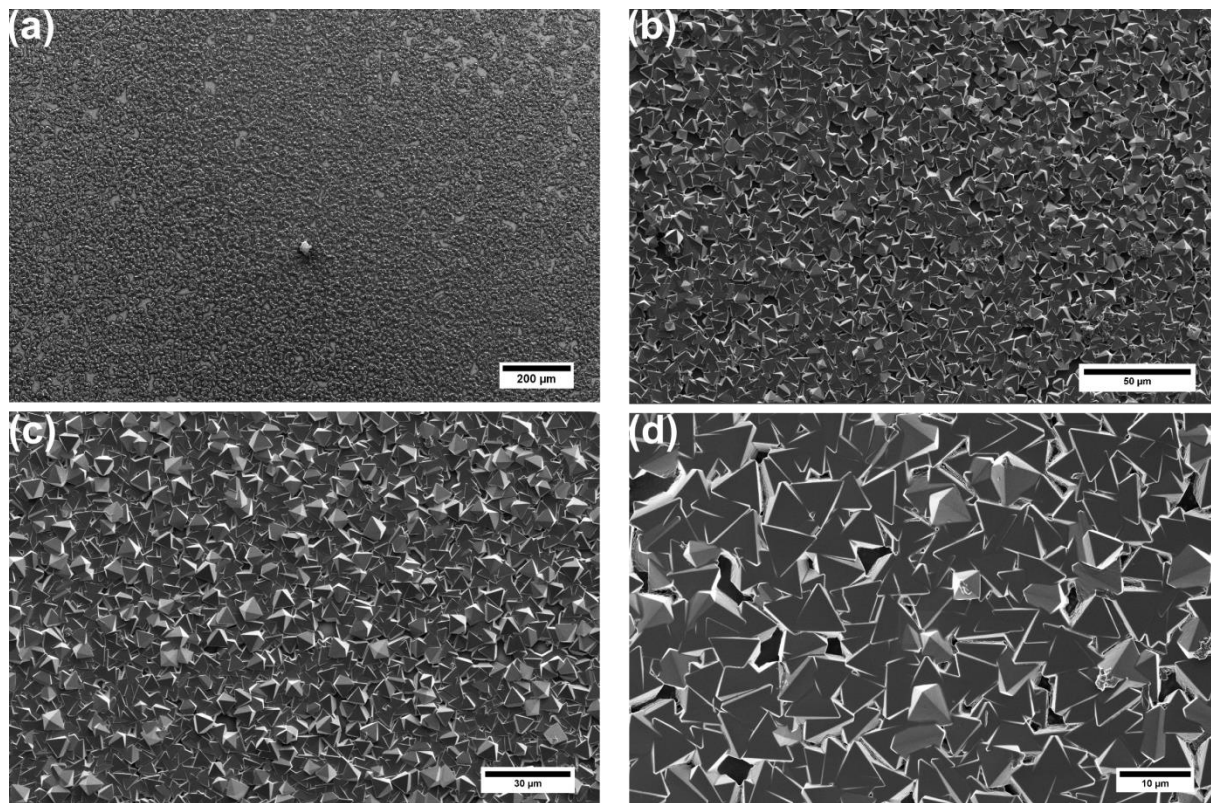
Figure S6.29: Top-view SEM images of the PPPP–PIZOF-1 film obtained with a droplet volume of 100 μL (Exp. 40) showing oriented crystals with an edge length of about 6.5 μm. The corresponding XRD is provided in Figure S6.26.

e. Impact of reaction temperature and reaction time on the MOF film growth
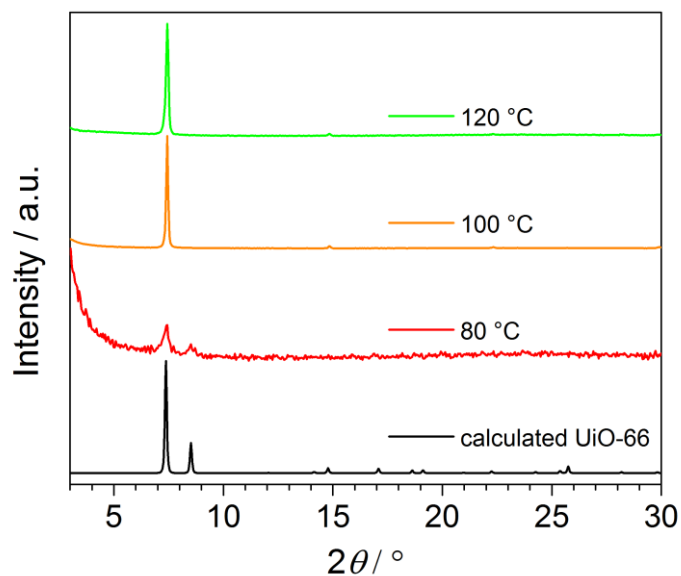
i. UiO-66(NH₂)

Figure S6.30: Calculated PXRD pattern of UiO-66 and XRD patterns of UiO-66(NH2) films obtained at a reaction temperature of 120 °C (Exp. 19), 100 °C (Exp. 10), and 80 °C (Exp. 20). The corresponding SEM images are shown in Figure S6.18, S6.31 and S6.32.
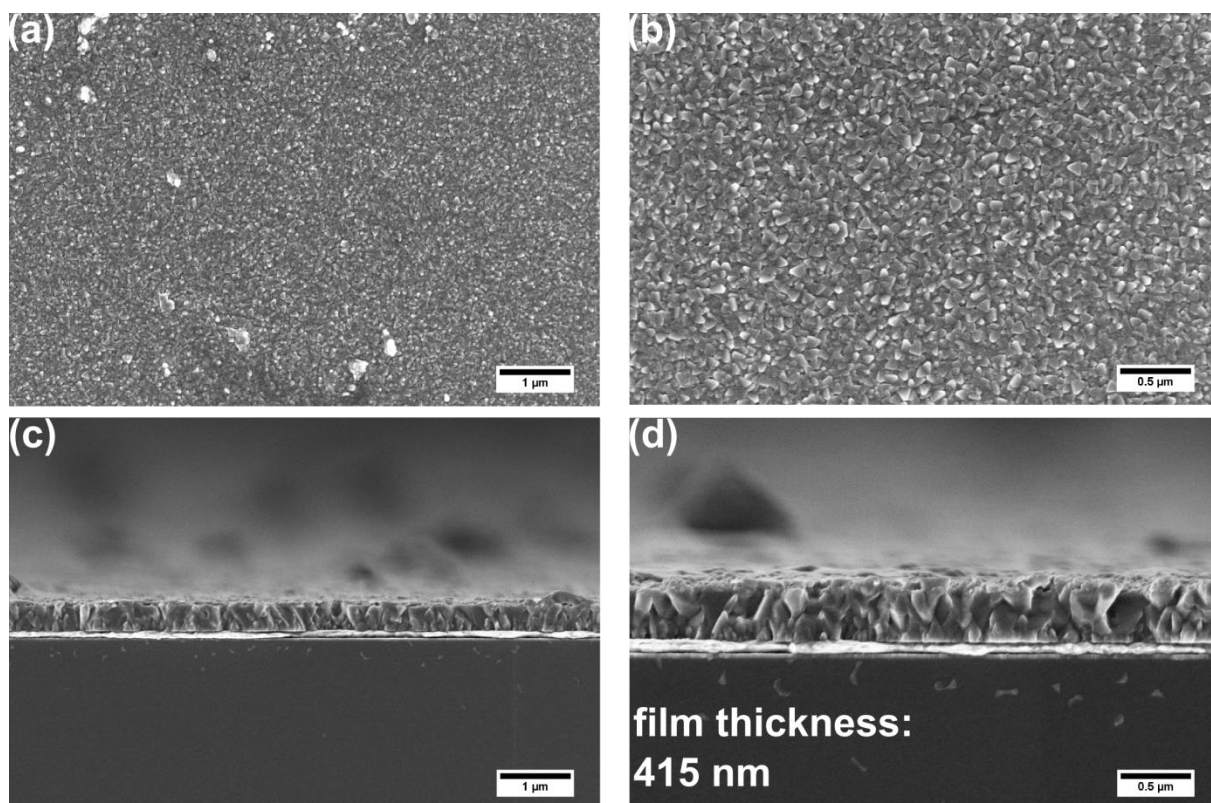
Figure S6.31: Top-view (a, b) and cross-section (c, d) SEM images of the UiO-66(NH2) film obtained at a reaction temperature of 120 °C (Exp. 19) showing a dense film with a thickness of about 415 nm consisting of MOF nanoparticles. The corresponding XRD is provided in Figure S6.30.
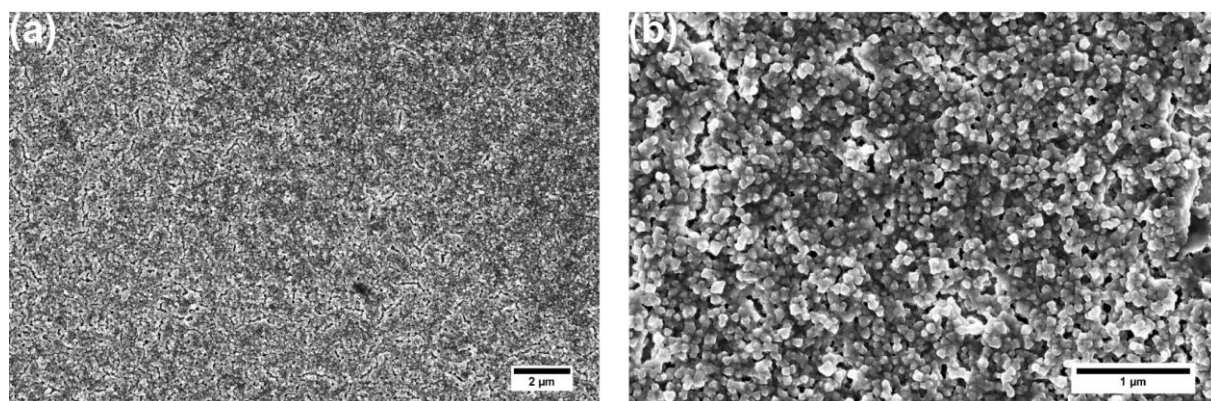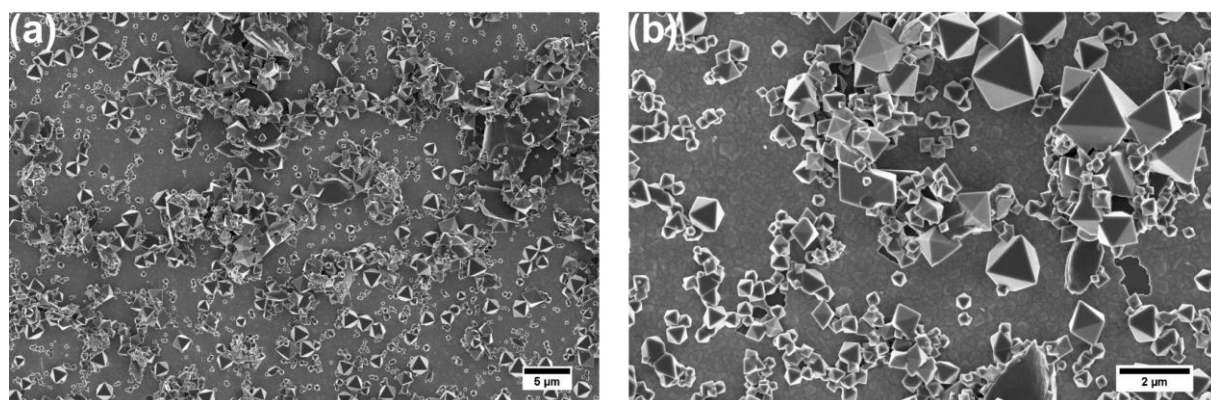

Figure S6.32: Top-view (a, b) SEM images of the UiO-66(NH2) film obtained at a reaction temperature of 80 °C (Exp. 20) showing a dense film. The corresponding XRD is provided in Figure S6.30.
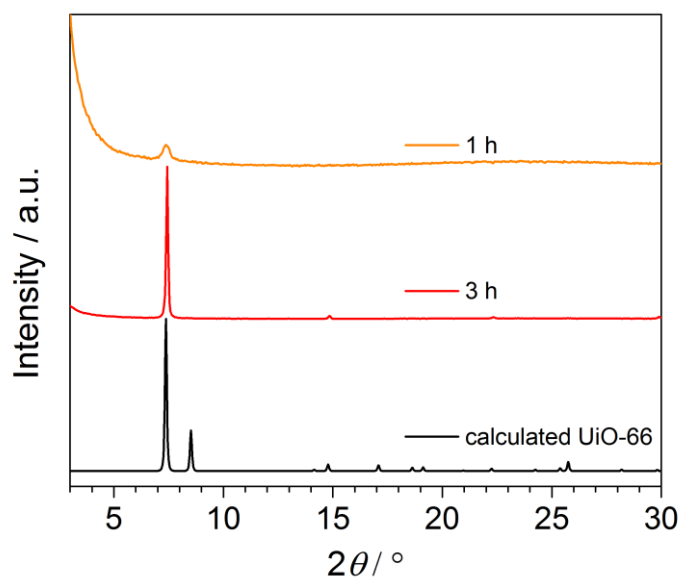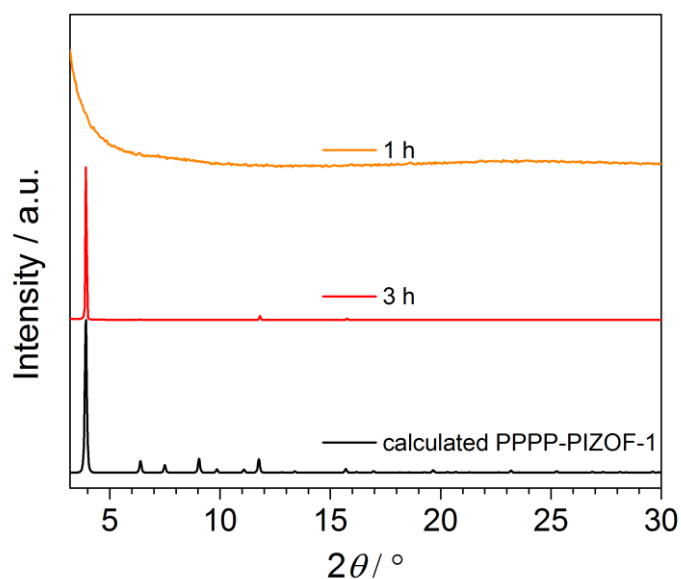
Figure S6.33: Calculated PXRD pattern of UiO-66 and XRD patterns of UiO-66(NH2) films obtained with a reaction time of 1 h (Exp. 21) or 3 h (Exp. 10). The corresponding SEM images are shown in Figures S6.18 and S6.34.
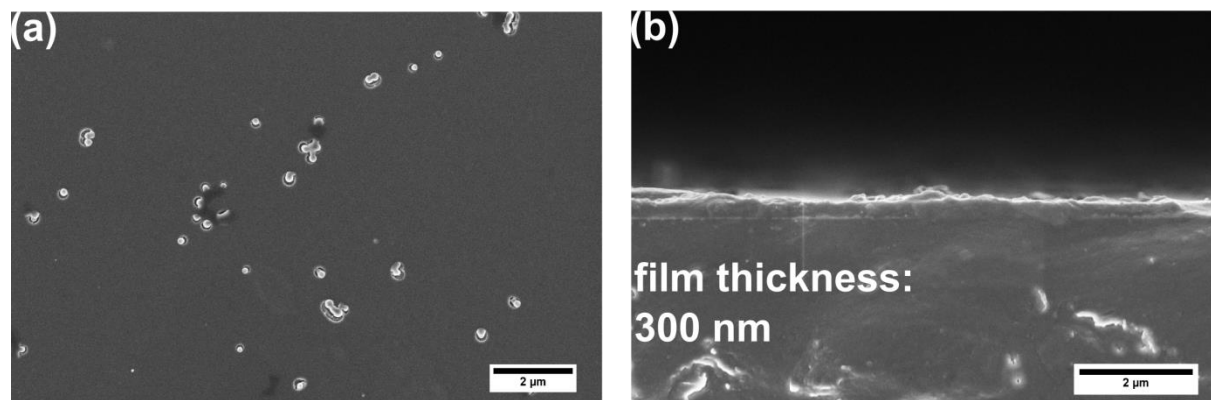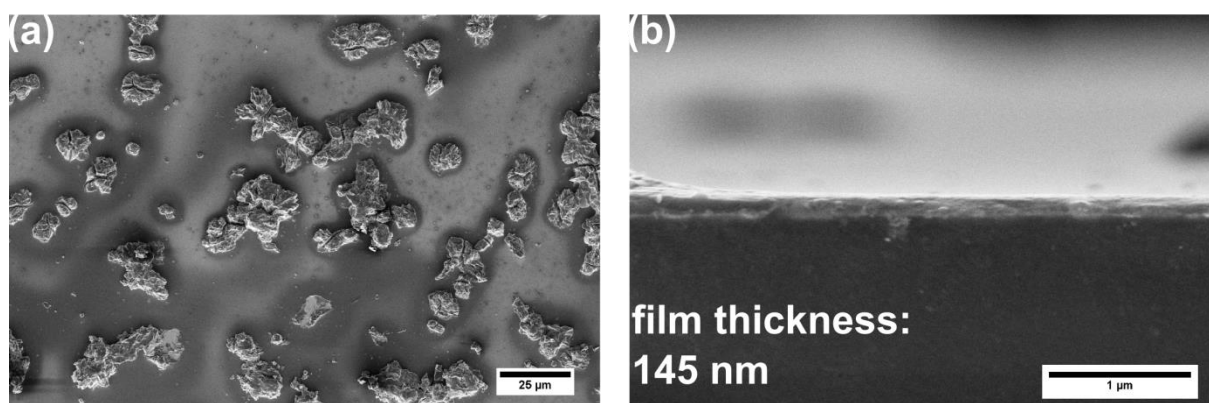

Figure S6.34: Top-view (a) and cross-section (b) SEM images of the UiO-66(NH2) film obtained with a reaction time of 1 h (Exp. 21), showing a film with a thickness of about 300 nm. The corresponding XRD is provided in Figure S6.32.

ii. PPPP–PIZOF-1

Figure S6.35: Calculated PXRD pattern of PPPP–PIZOF-1 and XRD patterns of PPPP–PIZOF-1 films obtained at a reaction temperature of 120 °C (Exp. 46), 100 °C (Exp. 28), 80 °C (Exp. 47), and 60 °C (Exp. 48). The corresponding SEM images are shown in Figures S6.20, S6.36-S6.38.
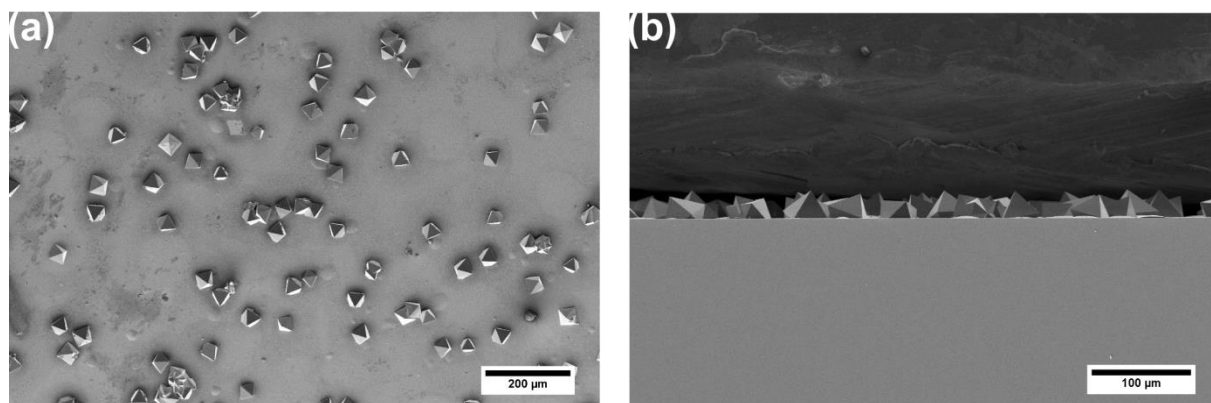
Figure S6.36: Top-view (a) and cross-section (b) SEM images of the PPPP–PIZOF-1 film obtained at a reaction temperature of 120 °C (Exp. 46), showing crystals loosely distributed on the surface. The corresponding XRD is provided in Figure S6.35.
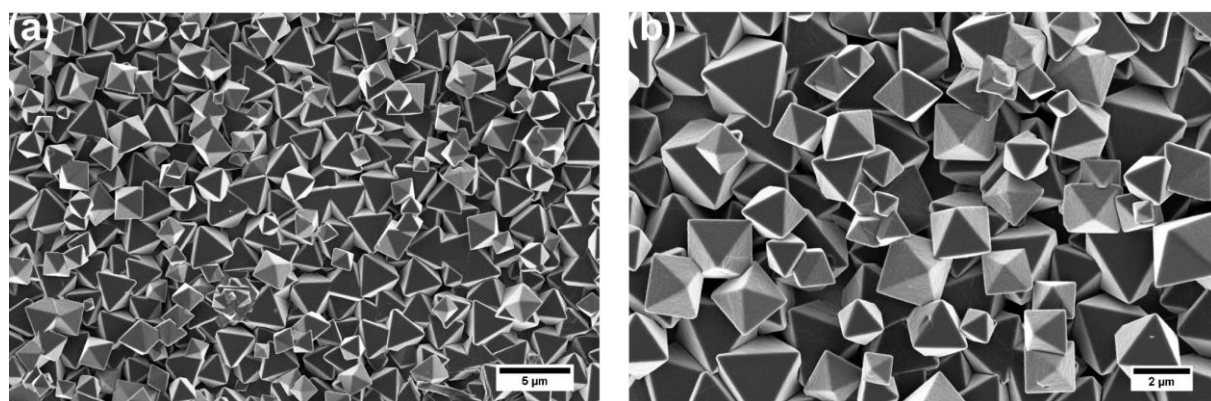
Figure S6.37: Top-view (a, b) SEM images of the PPPP–PIZOF-1 film obtained at a reaction temperature of 80 °C (Exp. 47), showing crystals distributed on the surface. The corresponding XRD is provided in Figure S6.35.

Figure S6.38: Top-view (a, b) SEM images of the PPPP–PIZOF-1 film obtained at a reaction temperature of 60 °C (Exp. 48), showing crystals distributed on the surface. The corresponding XRD is provided in Figure S6.35.

Figure S6.39: Calculated PXRD pattern of PPPP−PIZOF-1 and XRD patterns of PPPP−PIZOF-1 films obtained at a reaction time of 1 h (Exp. 49) or 3 h (Exp. 28). The corresponding SEM images are shown in Figures S6.20 and S6.40.

Figure S6.40: Top-view (a) and cross-section (b) SEM images of the PPPP−PIZOF-1 film obtained with a reaction time of 1 h (Exp. 49) showing an amorphous film with a thickness of about 145 nm. The corresponding XRD is provided in Figure S6.39.

f. MOF film growth on different substrates

i. UiO-66(NH₂)
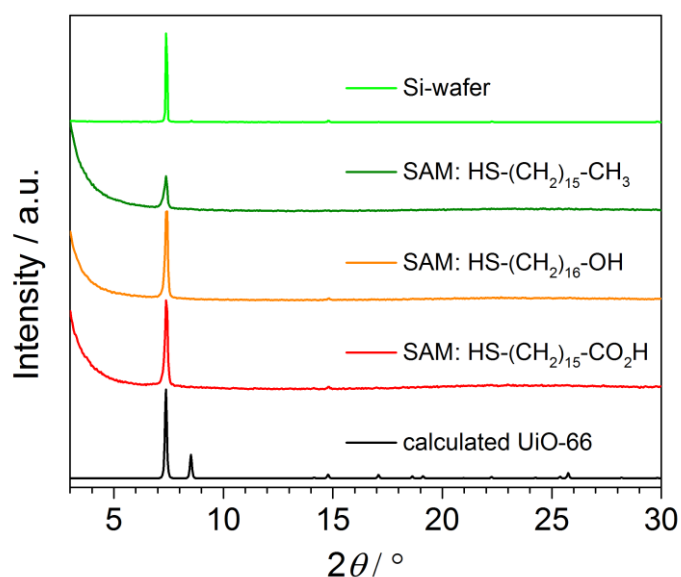
Figure S6.41: Calculated PXRD pattern of UiO-66 and XRD patterns of UiO-66(NH$_2$) films obtained on SAM-modified gold surfaces (Exp. 14-16) and bare silicon surface (Exp. 17). The formulas of the thiols used for the formation of the SAMs are shown in the Figure. The corresponding SEM images are shown in Figures S6.42-S6.45.
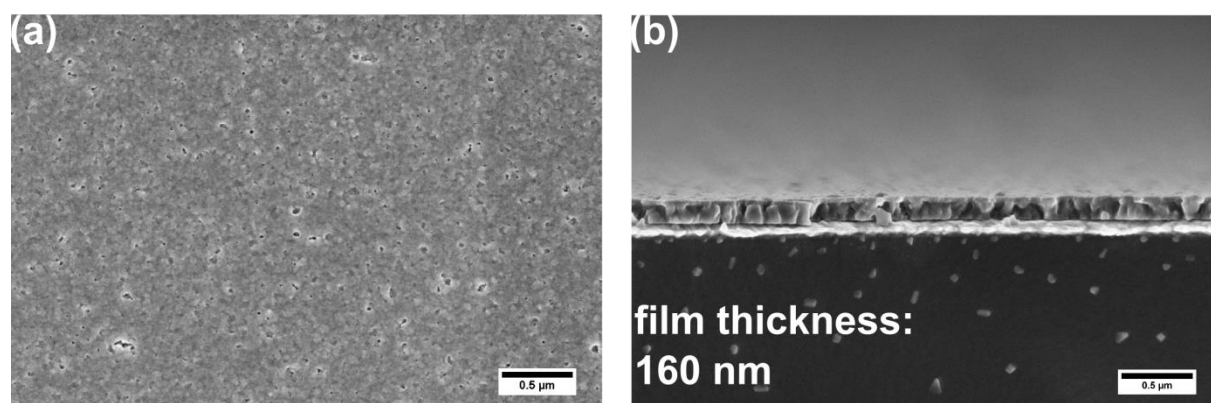
Figure S6.42: Top-view (a) and cross-section (b) SEM images of the UiO-66(NH$_2$) film obtained on a gold surface modified with HS-(CH$_2$)15-CO$_2$H (Exp. 14). The images reveal an oriented film with a thickness of about 160 nm. The corresponding XRD is provided in Figure S6.41.
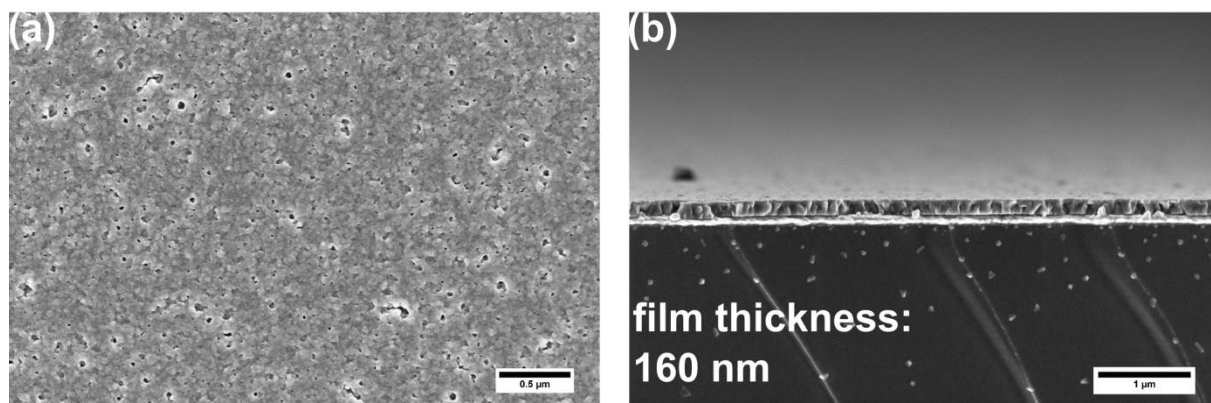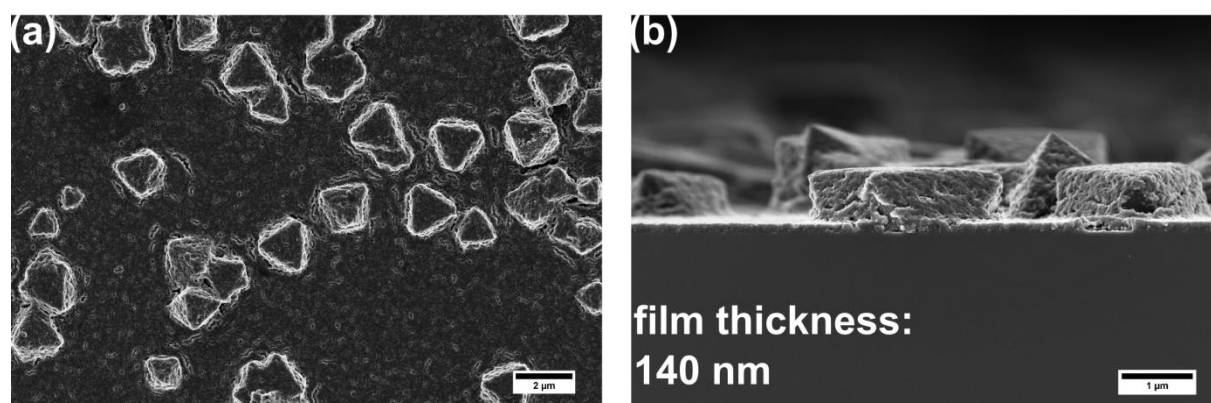
Figure S6.43: Top-view (a) and cross-section (b) SEM images of the UiO-66(NH$_2$) film obtained on a gold surface modified with HS-(CH$_2$)16-OH (Exp. 15). The images reveal an oriented film with a thickness of about 160 nm. The corresponding XRD is provided in Figure S6.41.
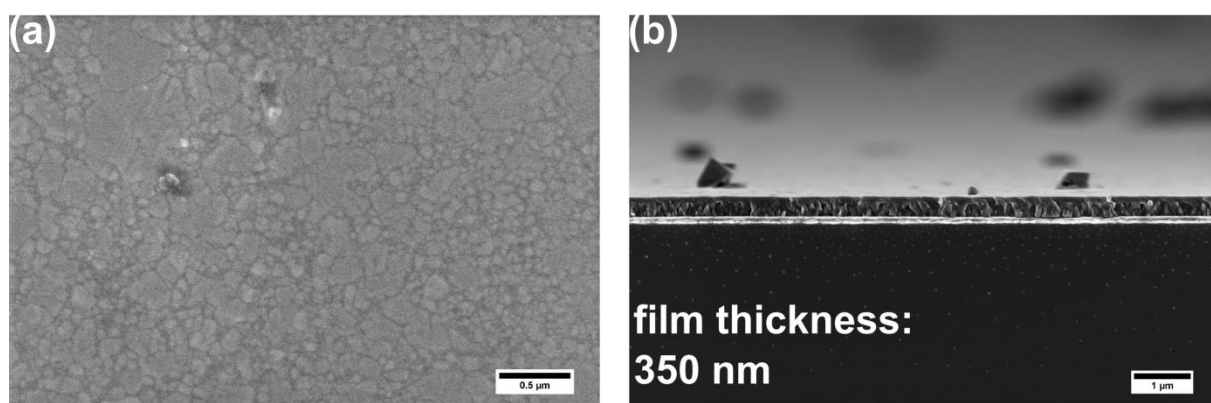
Figure S6.44: Top-view (a) and cross-section (b) SEM images of the UiO-66(NH$_2$) film obtained on a gold surface modified with HS-(CH$_2$)$_{15}$-CH$_3$ (Exp. 16). The images reveal an oriented film with a thickness of about 350 nm. The corresponding XRD is provided in Figure S6.41.

Figure S6.45: Top-view (a) and cross-section (b) SEM images of the UiO-66(NH$_2$) film obtained on a bare silicon surface (Exp. 17). The images reveal an oriented film with a thickness of about 140 nm and large (1.8 μm) crystals on top of this film. The corresponding XRD is provided in Figure S6.41.
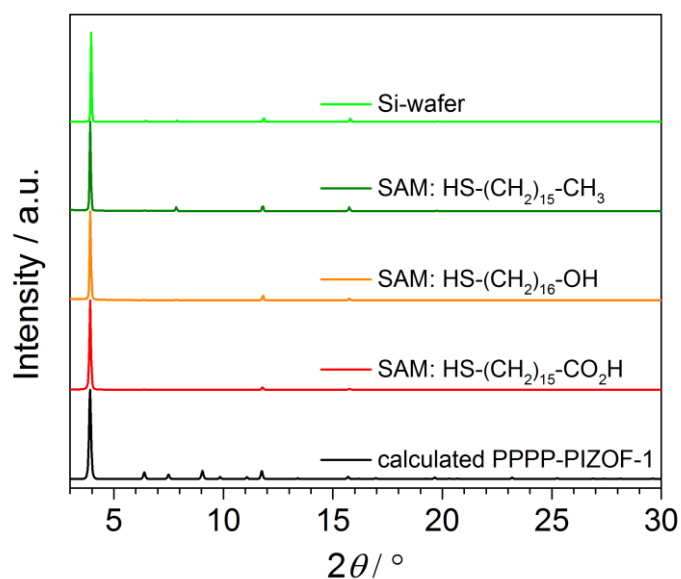
ii. PPPP–PIZOF-1

Figure S6.46: Calculated PXRD pattern of PPPP–PIZOF-1 and XRD patterns of PPPP–PIZOF-1 films obtained on SAM-modified gold surfaces (Exp. 41-43) and bare silicon surface (Exp. 44). The structural formulae of the thiols used for the formation of SAMs are shown in the Figure. The corresponding SEM images are shown in Figures S6.47-S6.50.
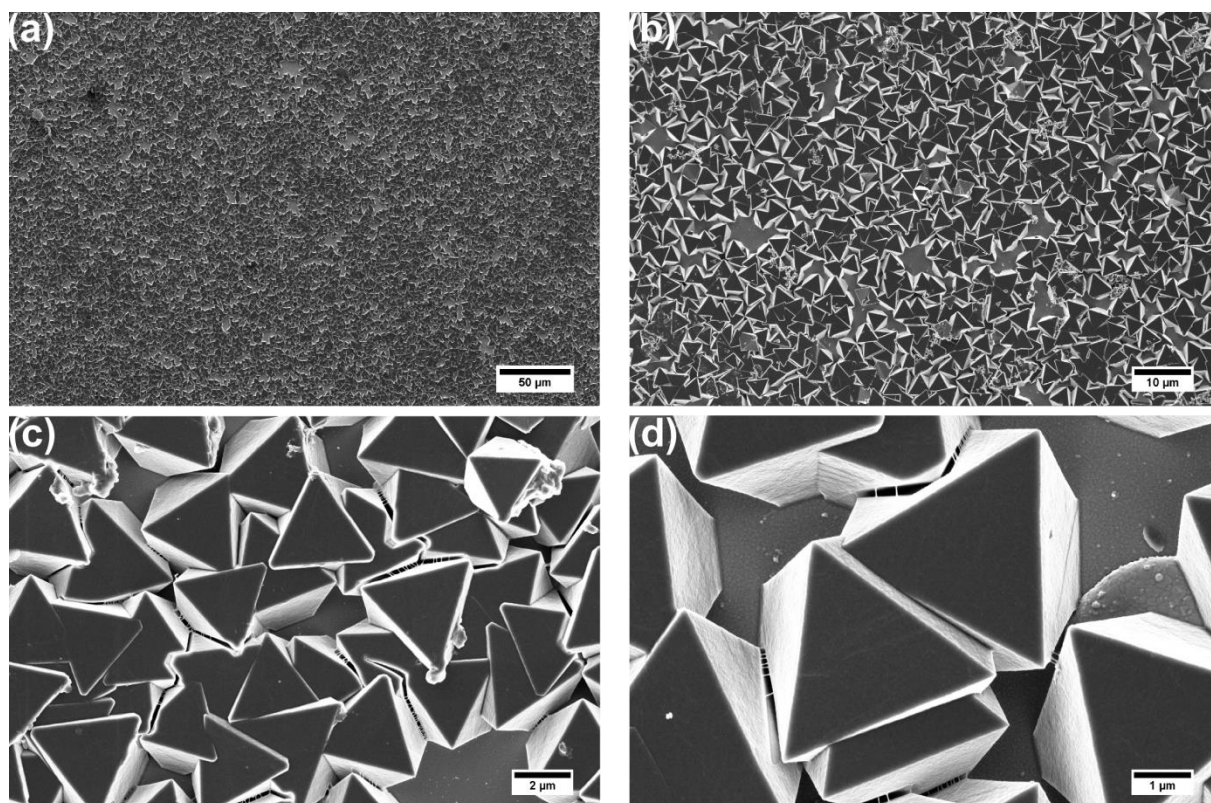
Figure S6.47: Top-view SEM images of the PPPP–PIZOF-1 film obtained on a gold surface modified with HS-$(CH_2)_{15}$-CO_2H (Exp. 41). The images reveal oriented crystals with an edge length of about 3.6 µm. The corresponding XRD is provided in Figure S6.46.
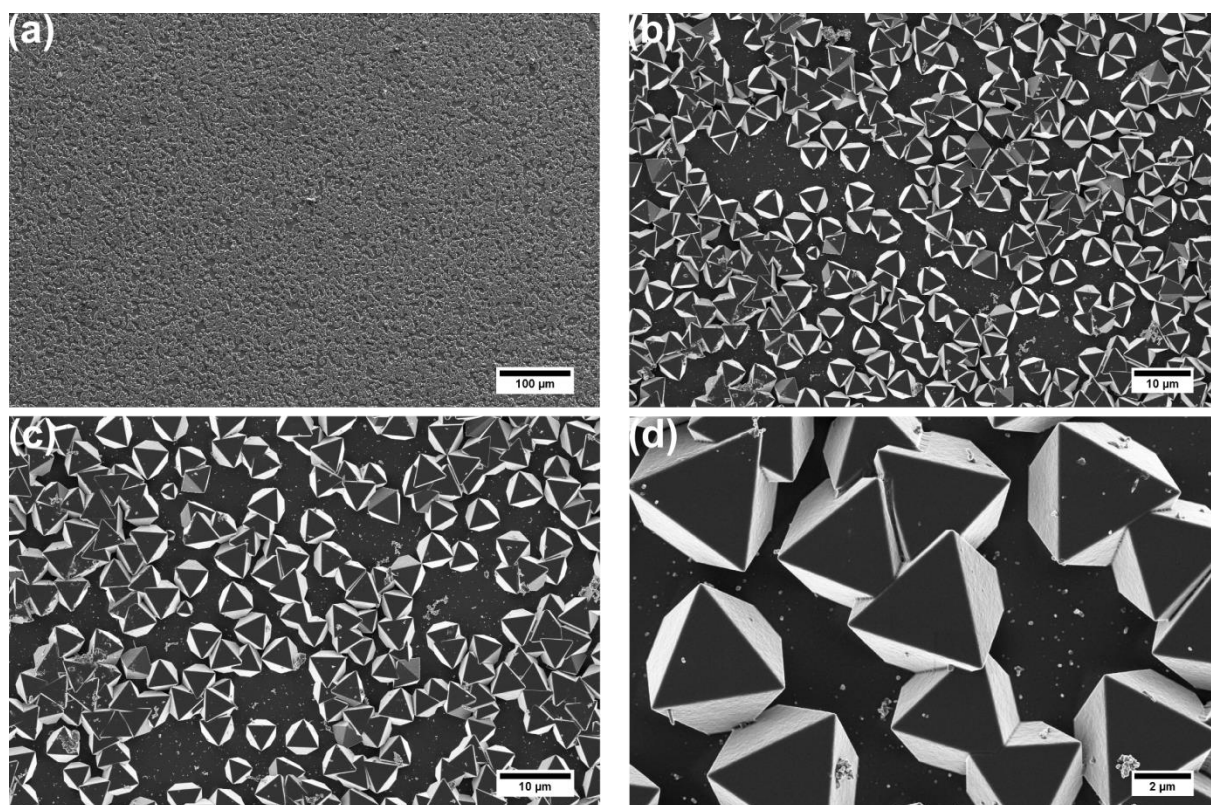
Figure S6.48: Top-view SEM images of the PPPP–PIZOF-1 film obtained on a gold surface modified with HS-$(CH_2)_{16}$-OH (Exp. 42). The images reveal oriented crystals with an edge length of about 4.9 μm. The corresponding XRD is provided in Figure S6.46.
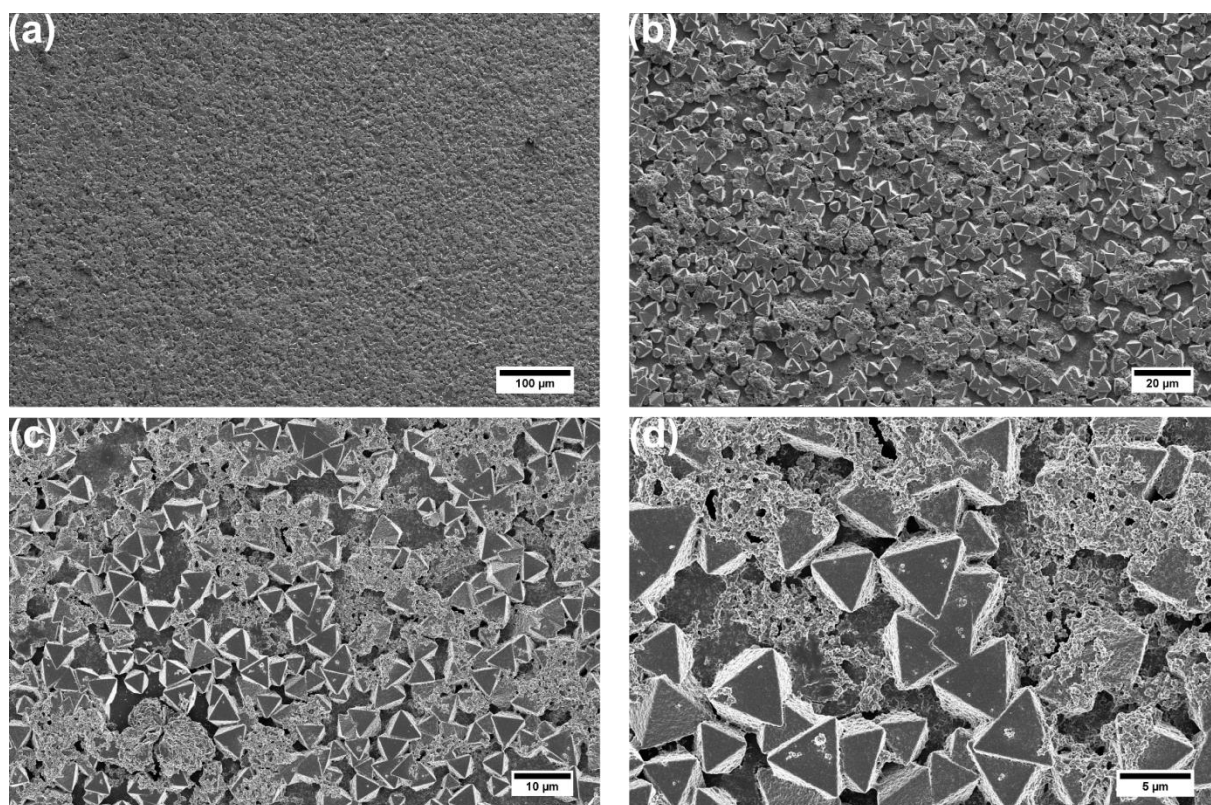
Figure S6.49: Top-view SEM images of the PPPP–PIZOF-1 film obtained on a gold surface modified with HS-$(CH_2)_{15}$-CH_3 (Exp. 43). The images reveal oriented crystals with an edge length of about 4.8 µm. The corresponding XRD is provided in Figure S6.46.
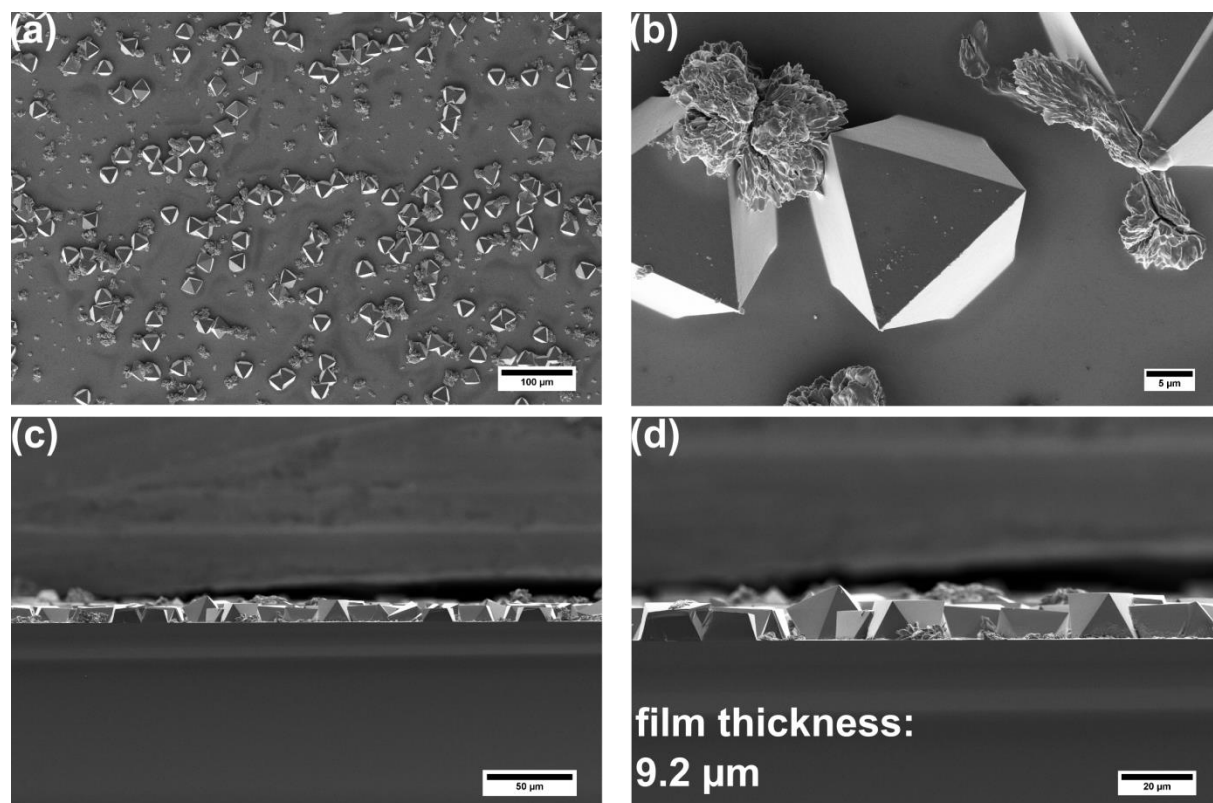
Figure S6.50: Top-view (a, b) and cross-section (c, d) SEM images of the PPPP–PIZOF-1 film obtained on a bare silicon surface (Exp. 44) showing oriented crystals with an edge length of about 22.5 μm on top of a film with a thickness of about 9.2 μm. The corresponding XRD is provided in Figure S6.46.

g. Accessible pores of MOF films
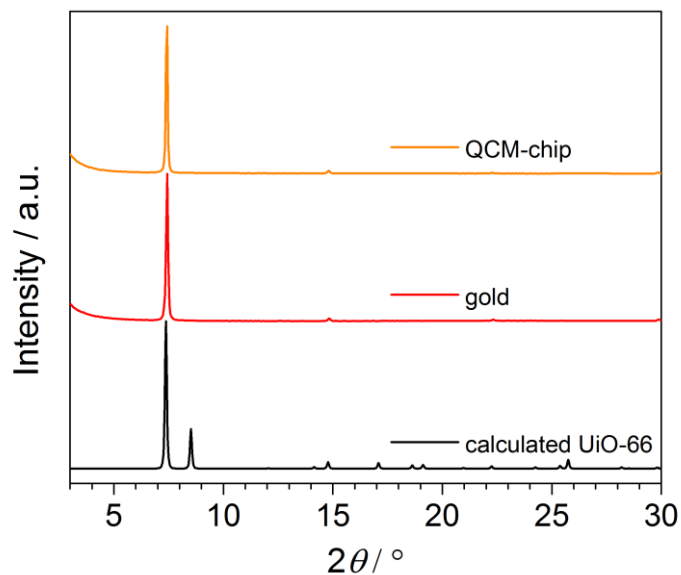
i. UiO-66(NH$_2$)

Figure S6.51: Calculated PXRD pattern of UiO-66 and XRD patterns of UiO-66(NH$_2$) films obtained on a QCM-chip (Exp. 18) and on a bare gold surface (Exp. 10).
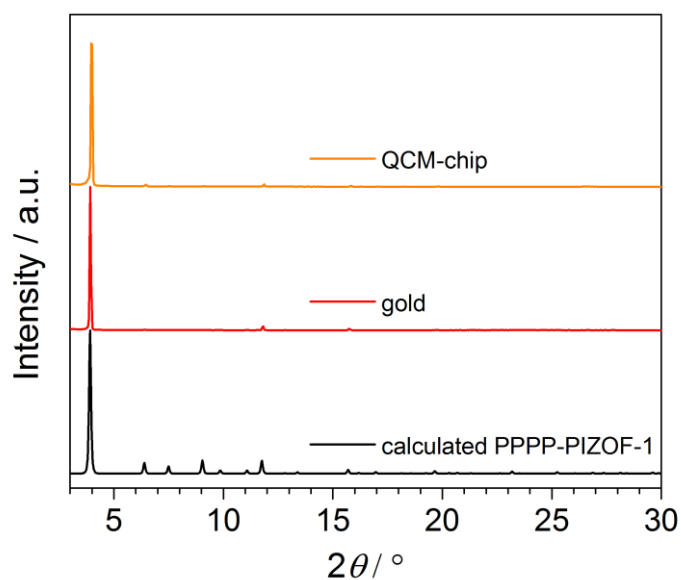
ii. PPPP–PIZOF-1

Figure S6.52: Calculated PXRD pattern of PPPP–PIZOF-1 and XRD patterns of PPPP–PIZOF-1 films obtained on a QCM-chip (Exp. 45) and on a bare gold surface (Exp. 28).

4. Homogeneity of UiO-66(NH₂) and the PPPP–PIZOF-1 films

a. Coverage

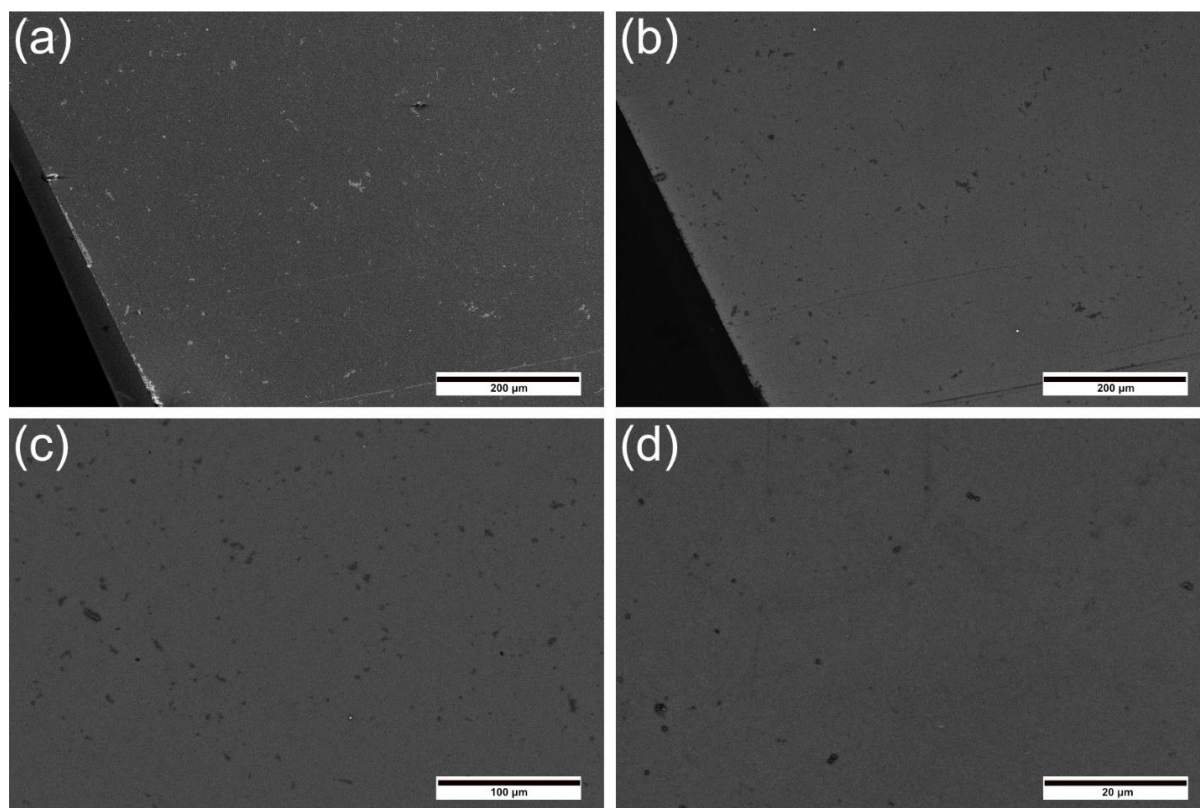Figure S6.53: SEM images of UiO-66(NH₂) films grown on 1.0 cm x 1.3 cm gold coated substrates (Exp.10). (a) Low magnification image taken at the edge of the substrate showing the film using secondary electron detection. (b) A corresponding Z-contrast image reveals a homogenous coverage of the gold layer to the very edge of the substrate. (c-d) An image of the middle part of the UiO-66(NH₂) film taken at higher magnification and with Z-contrast showing the complete coverage of the surface.

An often-observed phenomenon in film preparation through solution-based processes is a decrease in surface coverage at the edges of the substrate due to various effects such as drying. In the case of PPPP–PIZOF-1 we detect loosely packed MOF crystals in an area within 200 μm from the edges of the substrate as revealed by SEM micrographs using Z-contrast imaging (Figure S6.54), in addition to surface coverage throughout the remainder of the substrate. These results demonstrate a homogenous PPPP–PIZOF-1 film coverage of 93%.

Calculations with the image processing software revealed that within the area of the homogenous PPPP–PIZOF-1 film 1.3% of the gold surface is not covered by the film (Figure S6.55). Combining the two coverage factors, we calculate a total covered area of 91.7%.
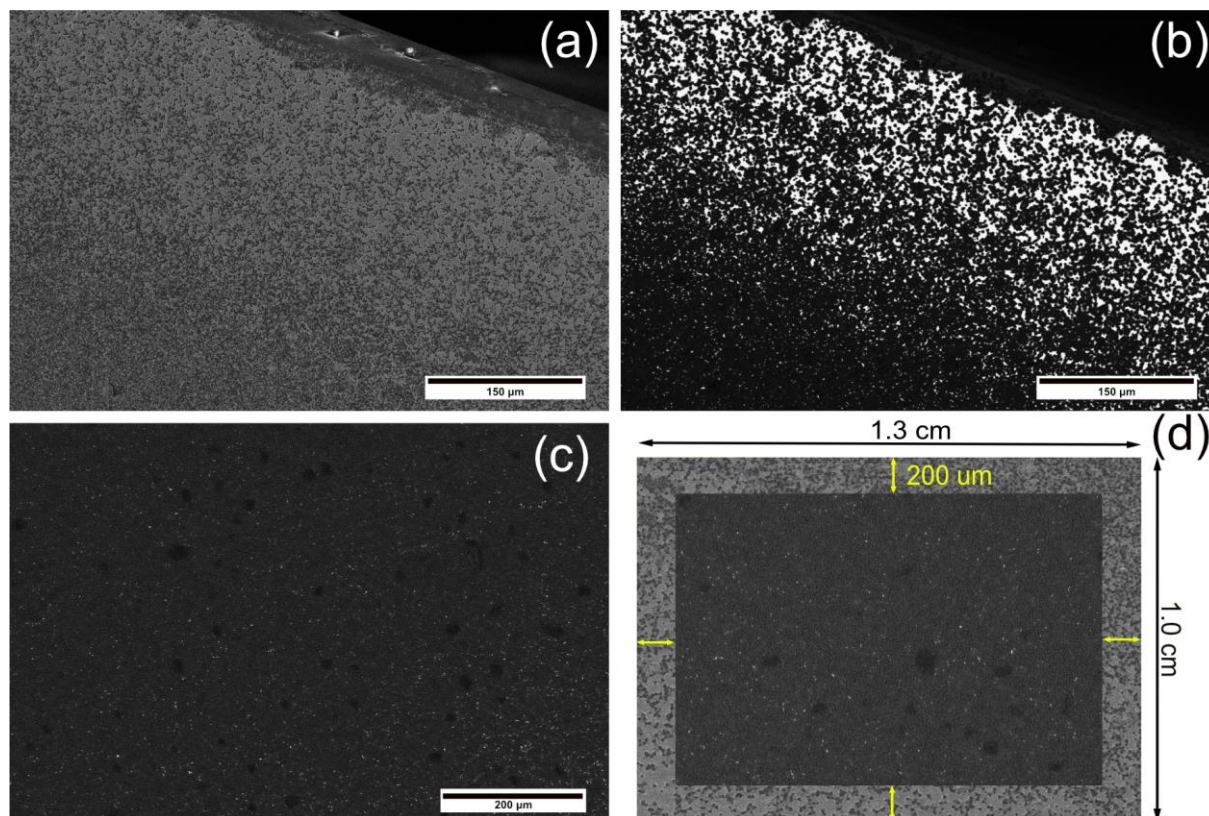

Figure S6.54: SEM images of PPPP–PIZOF-1 films grown on 1.0 cm x 1.3 cm gold substrates (Exp. 28). (a) Low magnification image taken at the edge of the substrate showing the film using secondary electron detection. (b) The corresponding Z-contrast image reveals a gradient in film coverage of the gold at the substrate edge. (c) An image taken at the middle part of the film at higher magnification and with Z-contrast, shows the homogenous coverage of the surface. (d) Schematic illustration of the coverage calculation.
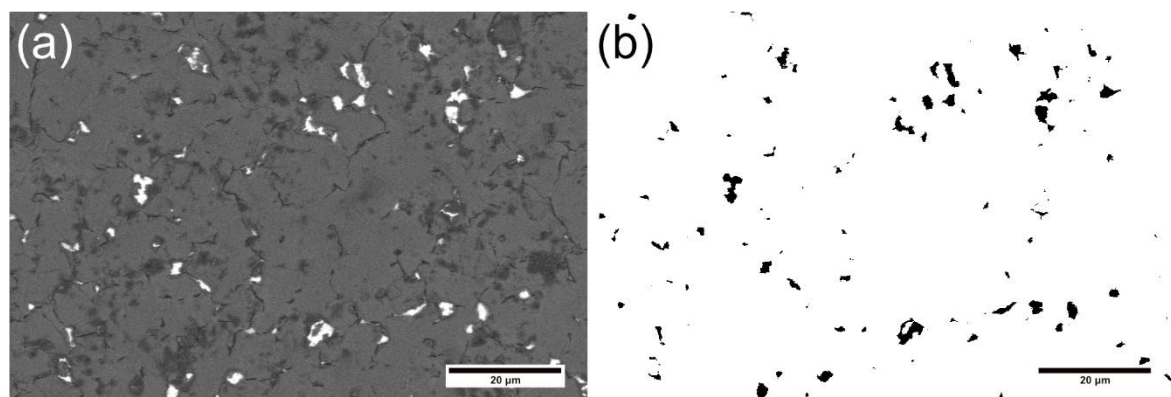
Figure S6.55: SEM image of PPPP-PIZOF-1 film with Z-contrast (a) showing the long-range coverage obtained with the PPPP–PIZOF-1 film, with the bright area representing the gold surface, and (b) showing the negative image of (a), with black areas representing the gold surface.
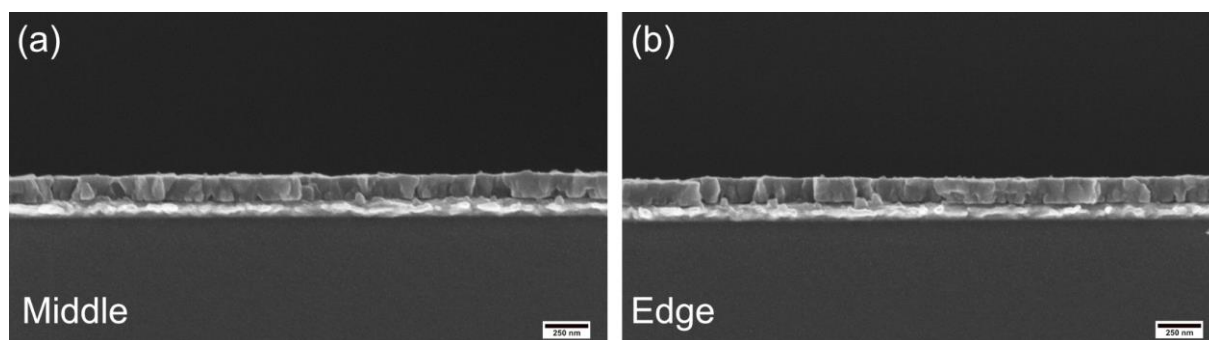
b. Thickness

Figure S6.56: SEM cross-section images of UiO-66(NH$_2$) taken at (a) the middle and (b) the edge of the film revealing a uniform film.

c. Crystallinity and Orientation

To assess the degree of crystallinity and the degree of orientation of the MOF films, 2.5 cm × 1.0 cm films were studied using 2D grazing-incidence wide-angle X-ray scattering (GIWAXS) measurements at five different sites of the film going from one edge of the substrate to the other, as indicated with red lines (Figure S6.57). Using a 50 µm wide X-ray beam which covered the whole substrate length of 1.0 cm at grazing incidence angle, allowed for high spatial resolution. The obtained 2D diffraction data for the five different sites reveal very high homogeneity in terms of coverage, crystallinity as well as degree of crystallite orientation within the films of both UiO-66(NH$_2$) and PPPP–PIZOF-1.
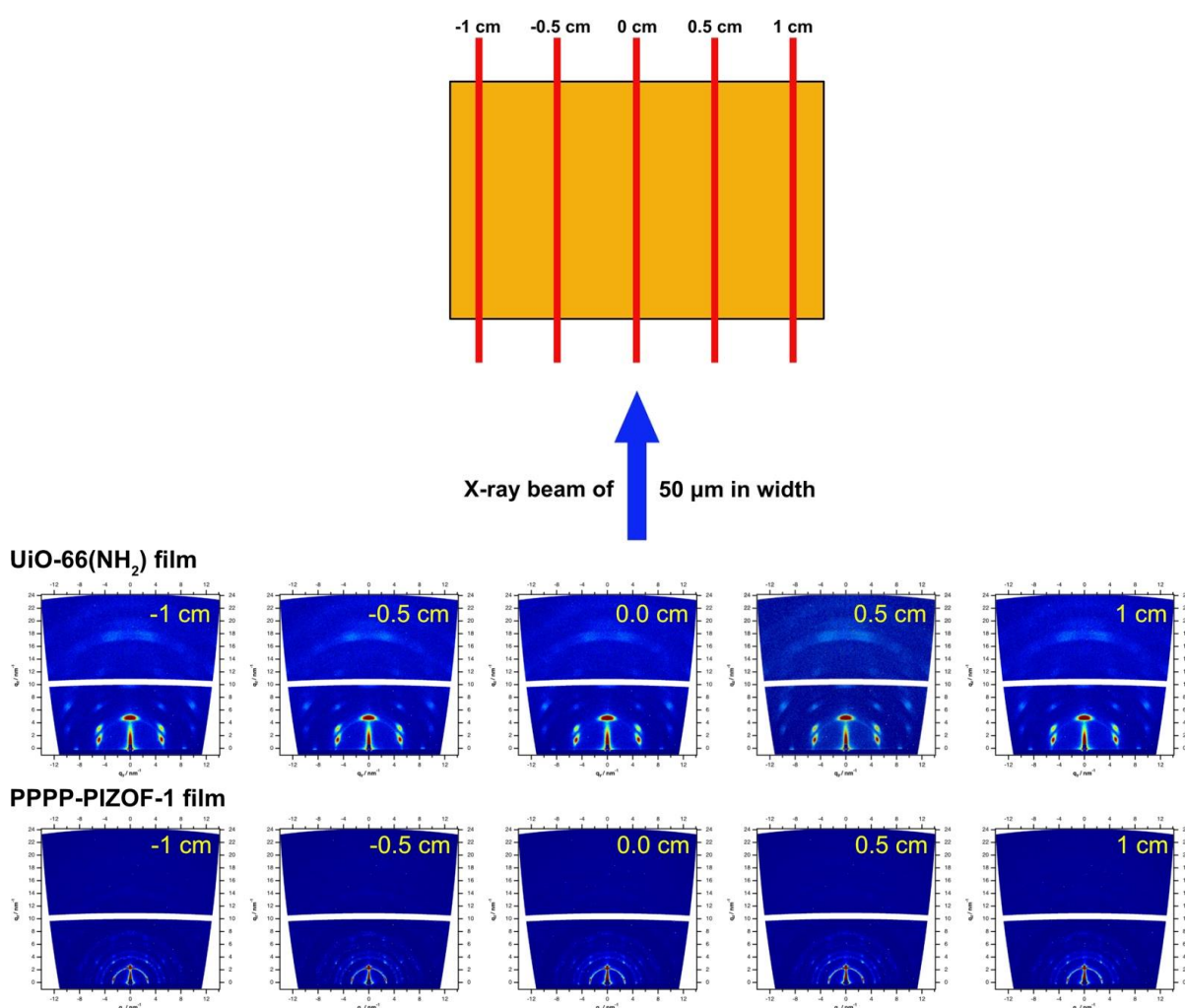

Figure S6.57: Top: illustration of the 2D GIWAXS line scan experiment. 2D GIWAXS patterns of UiO-66(NH$_2$) (upper line) and of PPPP–PIZOF-1 (lower line) reveal a high degree of orientation along the substrate.

d. Energy-dispersive X-ray (EDX) spectroscopy
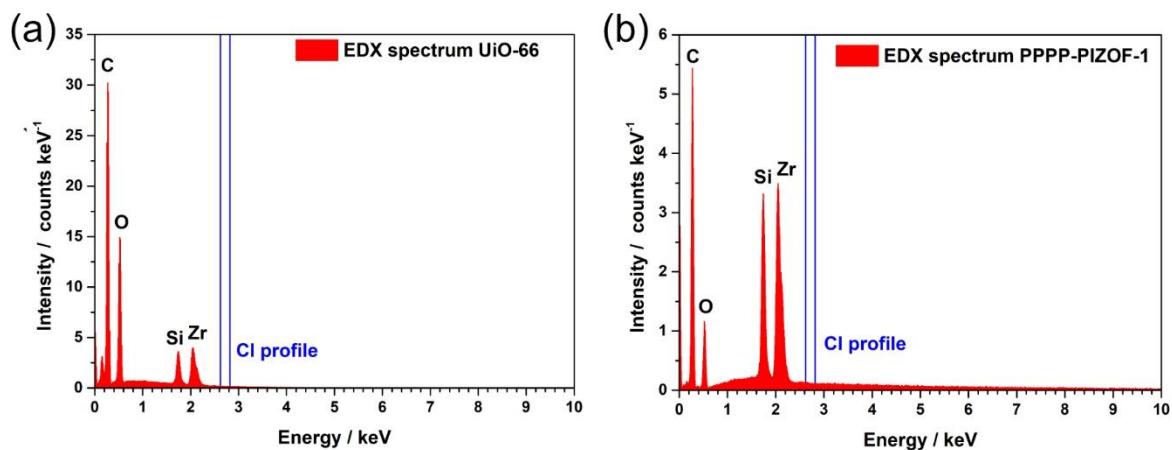

Figure S6.58: EDX spectra of oriented (a) UiO-66 and (b) PPPP–PIZOF-1 films grown on silicon substrates. Chlorine K_α and K_β lines are marked as blue insets. The absence of these lines indicates that the ZrOCl$_2$ precursor was consumed quantitatively. Note that the film were not washed, but solely dried under dynamic vacuum.
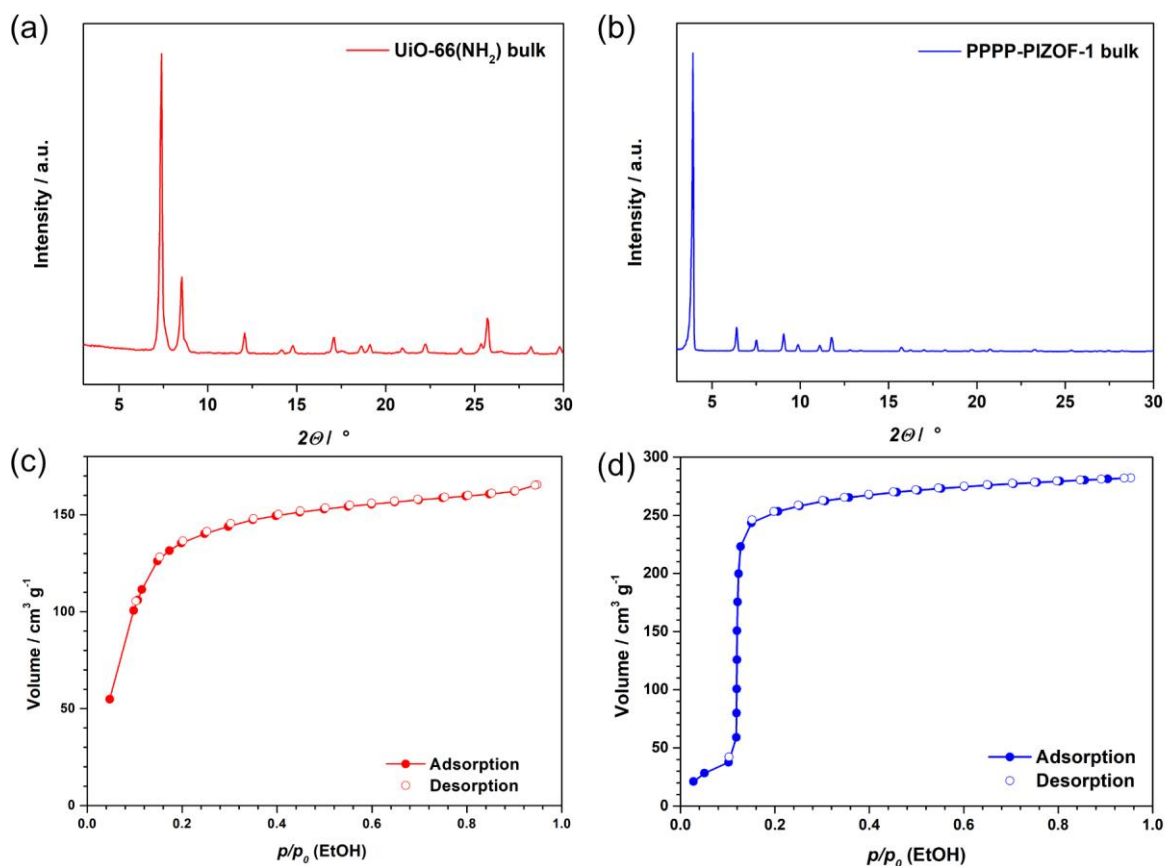
6. EtOH physisorption

Figure S6.59: XRD patterns of activated bulk (a) PPPP−PIZOF-1 and (b) UiO-66(NH$_2$) prior to the sorption experiments. (c) and (d) Ethanol sorption isotherms of the respective bulk materials at 293 K. Prior to the analysis the MOFs were activated at 120 °C for 6 h under high vacuum.

7. Macroscopic photographs of UiO-66(NH₂) and the PPPP–PIZOF-1 films
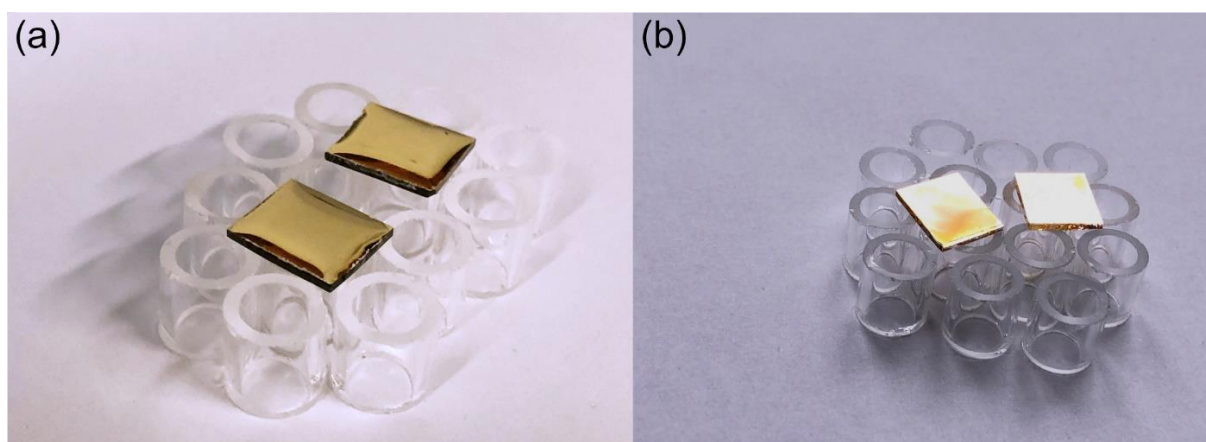
Figure S6.60: Macroscopic images of (a) gold substrate (1.3 cm x 1.0 cm) cast with the precursor solution prior to the synthesis. (b) Gold substrates retrieved from the reactor after synthesis without further drying under reduced pressure.
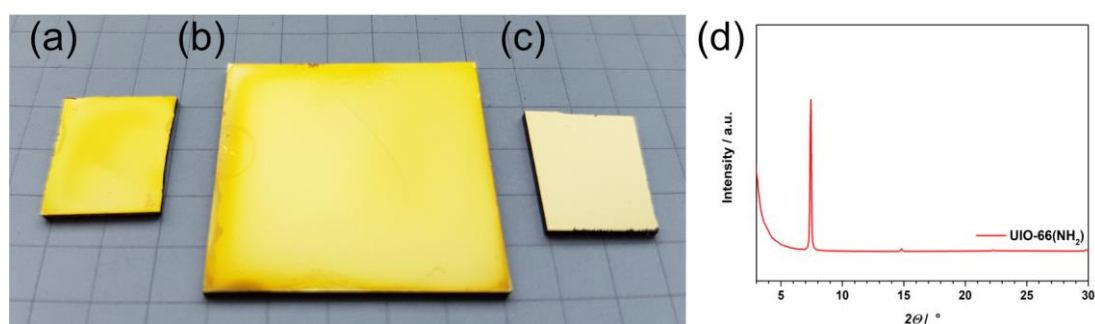
Figure S6.61: Macroscopic photographs of UiO-66(NH₂) films grown on a) 1.0 cm x 1.3 cm and b) 2.5 cm x 2.5 cm gold coated substrates. c) A bare gold coated substrate as a reference. d) XRD pattern of the film on the large substrate.
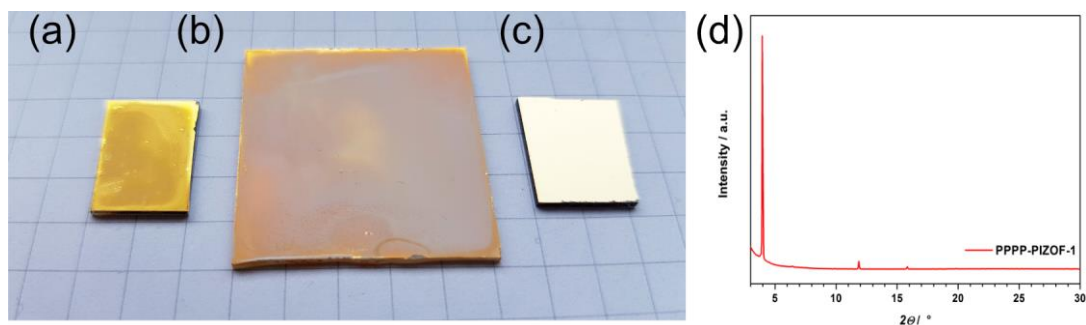
Figure S62. Macroscopic photographs of PPPP–PIZOF-1 films grown on a) 1.0 cm x 1.3 cm and b) 2.5 cm x 2.5 cm gold coated substrates. c) A bare gold surface as a reference. d) XRD pattern of the film on the large substrate.

8. References

1. Bronkhorst, *www.fluidat.com* **2017**.

2. Schaate, A.; Roy, P.; Godt, A.; Lippke, J.; Waltz, F.; Wiebcke, M.; Behrens, P., *Chem. - Eur. J.* **2011,** *17* (24), 6643-6651.

3. Lippke, J.; Brosent, B.; von Zons, T.; Virmani, E.; Lilienthal, S.; Preuße, T.; Hülsmann, M.; Schneider, A. M.; Wuttke, S.; Behrens, P.; Godt, A., *Inorg. Chem.* **2017,** *56* (2), 748-761.

4. Hinterholzinger, F. M.; Wuttke, S.; Roy, P.; Preuße, T.; Schaate, A.; Behrens, P.; Godt, A.; Bein, T., *Dalton Trans.* **2012,** *41* (14), 3899-3901.

7. Conclusion

This thesis is focussed on studying molecular frameworks, how the morphology of materials can be controlled and how it influences the properties of the materials, and how structural modifications change electronic properties.

In the third chapter, we discuss a novel ethoxy-functionalized benzodithiophene based COF, namely BDT-OEt COF, which was synthesized under solvothermal conditions. BDT-OEt COF features crystallinity, mesoporosity, and high surface area. A series of COFs consisting of both BDT and BDT-OEt building units in different ratios was synthesized. Highly crystalline, mesoporous frameworks were obtained for all BDT : BDT-OEt COFs. A nearly linear evolution from BDT to BDT-OEt COF was observed with regard to pore size and crystallite domain size upon the gradual incorporation of BDT-OEt building units into the COF backbone. Furthermore, we show that the final building unit ratios in the framework can be predetermined prior to the COF synthesis. Therefore, the COF backbones and chemical pore environment can be finely tuned towards desired properties while an eclipsed layer arrangement is retained. Molecular dynamics simulations and DFT calculations shed light on the preferred orientation of the ethoxy groups in the pores. Furthermore, the simulations illustrate that the incorporation of ethoxy chains causes a subtle lateral displacement of the BDT COF layers relative to each other.

In the following chapter, we demonstrate the preparation of COF films and coatings by depositing COF particles on conducting substrates in an electric field through electrophoretic deposition (EPD). Hereby, 2D and 3D imine and boronate ester-linked COFs of different particle sizes and morphologies were deposited on metal, transparent conducting metal oxides, or steel meshes. By adjusting the EPD parameters, such as deposition times, particle concentrations, and electrode potentials, film thicknesses could be tuned and predetermined. The obtained films feature an inherent textural porosity with interstitial voids between the deposited particles, thereby allowing for increased contact to active media for applications such as catalysis. In addition, we showed that through EPD, film composites consisting of mixed COFs can be straightforwardly prepared, enabling encoded functionalities such as multipore COF films. Finally, a BDT-ETTA COF film as well as a COF/Pt nanoparticle hybrid film were examined regarding their performance in photoelectrochemical (PEC) water splitting, where a 19- and 117-

fold improvement of the photocurrent, respectively, was found over our previously reported dense and oriented BDT-ETTA COF films. To put this work in perspective, it shows that film morphology plays a crucial role for different applications and should be considered in combination with the inherent properties of the COFs. This, as well as the simplicity and generality of the approach, underlines the importance of EPD as an addition to the toolbox of COF film preparation methods. Therefore, we believe that this work will assist in designing high-performance devices for specific applications.

In the fifth chapter, we report two novel, 2D imine-linked COFs based on the electron-rich Wurster-motif, named WTA and WBDT. The highly crystalline materials were analyzed by PXRD refinement and structure modeling. Nitrogen physisorption revealed the existence of dual-pore systems with high surface areas. Additionally, oriented thin films of the COFs were synthesized, which were subsequently used to study the optical properties and electronic energy levels. The macroscopic electrical conductivity of the COFs was studied by means of van-der-Pauw measurements on pressed pellets and oriented thin films grown on glass substrates. Depending on the linear linker in the COF, conductivities of the pristine materials as high as $1.64 \cdot 10^{-3}$ S m^{-1} were determined. Furthermore, different dopants, as well as different doping concentrations, were investigated to create the radical cation forms of the COFs, and their long-term effect on the electrical conductivity was assessed. The use of F$_4$TCNQ as a strong electron acceptor yielded conductivities as high as $3.67 \cdot 10^0$ S m^{-1}, the highest value for doped imine-linked COFs reported so far. Moreover, the impact of doping on the optical absorption and the formation of radicals in the COF could be correlated with the changes in conductivity. In contrast to previous work in the field of conductive COFs, it could be shown that the high conductivities resulting from doping are stable over time for the organic acceptor molecule F$_4$TCNQ. This stability is of central importance in order to be able to exploit high conductivities by doping permanently.

In the context of electrical conductivity, we discovered that the geometry of the linker can deviate from planarity and still show high conductivity values. In addition, non-planar COFs have the added value of high-crystallinity and robustness achieved through molecular docking sites. Encoding electrical conductivity in these non-planar systems requires the selection of suitable electroactive building blocks. Increasing the electrical conductivity in these systems through doping is highly dependent on the dopant, and we can attribute the long-term stability to a combination of factors, e.g., a robust framework

and a chemically innocent dopant. We believe that these results will contribute to the development of new strategies for the design of COFs for various applications, such as sensors or optoelectronics.

The sixth chapter is about the growth of highly oriented thin films of UiO-66, UiO-66(NH$_2$), UiO-67, UiO-68(NH$_2$), and even of an interpenetrated MOF, the PPPP–PIZOF-1, on a variety of surfaces—bare gold, gold surfaces modified with thiol SAMs, and bare silicon—by applying vapor-assisted conversion (VAC). The obtained MOF films exhibit a high degree of crystallinity and crystal orientation extending to large areas where the MOF crystallites are intergrown, forming almost flawless tile patterns. A detailed study regarding the parameters governing the MOF film formation, including modulator equivalents, precursor concentration, temperature, and reaction time reveals a link between the rate of the crystallization and the formation of the oriented MOF film. Tuning the crystallization process by including a modulator led to highly crystalline and oriented films. Remarkably, a reaction time of only 3 h and a temperature of 100 °C are required for the formation of oriented MOF films. Both UiO-66(NH$_2$) and PPPP–PIZOF-1 films show considerable ethanol uptake at room temperature, rendering these MOF films functional materials suitable for on-chip host–guest studies. On the basis of the above, we introduce the VAC process as a versatile, gentle, and efficient method for the synthesis of highly crystalline and oriented thin MOF films. We envision that VAC protocols will be generated for many additional MOF topologies, which so far were not deposited as homogeneous, porous thin films and macroscopic coatings. As such, VAC is an important addition to the toolbox of film deposition technologies for porous frameworks.

8. Curriculum Vitae

Name	Julian Markus Rotter
Date of birth	25. July 1988 in Munich
Nationality	German

PHD

since 06/2015	**Ludwig-Maximilians-Universität München (University of Munich)** Research group Prof. Bein, Physical Chemistry „*Molecular Frameworks - from morphological and structural control to electronic properties*"

EDUCATION

04/2013 – 03/2015	**Ludwig-Maximilians-Universität München** *Master of Science* in Chemistry Title of Master Thesis (Prof. Bein Research Group): *"Room Temperature Synthesis of Covalent Organic Framework Films through Vapor Assisted Conversion and the Synthesis of Pyromellitic Diimide Derivatives for Pore Functionalization"*
08/2013 – 12/2013	**Cornell University, Ithaca, New York, USA** *Visiting Researcher*, Prof. Dichtel Research Group
10/2009 – 02/2013	**Ludwig-Maximilians-Universität München** *Bachelor of Science* in Chemistry and Biochemistry
10/2008 – 09/2009	**Technische Universität München (Technical University of Munich)** Chemical Engineering
1999 – 2008	**Gymnasium Bad Aibling** *Abitur (A-levels)*

9. List of Publications

(1) Keller, N.; Sick, T.; Bach, N. N.; Koszalkowski, A.; Rotter, J. M.; Medina, D. D.; Bein, T. Dibenzochrysene enables tightly controlled docking and stabilizes photoexcited states in dual-pore covalent organic frameworks. *Nanoscale* **2019**, *11*, 23338–23345.

(2) Rotter, J. M.; Weinberger, S.; Kampmann, J.; Sick, T.; Shalom, M.; Bein, T.; Medina, D. D. Covalent Organic Framework Films through Electrophoretic Deposition—Creating Efficient Morphologies for Catalysis. *Chem. Mater.* **2019**, *31*, 10008–10016.

(3) Mähringer, A.; Jakowetz, A. C.; Rotter, J. M.; Bohn, B. J.; Stolarczyk, J. K.; Feldmann, J.; Bein, T.; Medina, D. D. Oriented Thin Films of Electroactive Triphenylene Catecholate-Based Two-Dimensional Metal-Organic Frameworks. *ACS Nano* **2019**, *13*, 6711–6719.

(4) Mähringer, A.; Rotter, J.; Medina, D. D. Nanostructured and Oriented Metal-Organic Framework Films enabling Extreme Surface Wetting Properties. *Beilstein J. Nanotechnol.* **2019,** *10,* 1994–2003.

(5) Sick, T.; Rotter, J. M.; Reuter, S.; Kandambeth, S.; Bach, N. N.; Döblinger, M.; Merz, J.; Clark, T.; Marder, T. B.; Bein, T.*; et al.* Switching On and Off Interlayer Correlations and Porosity in 2D Covalent Organic Frameworks. *JACS* [Online early access]. DOI: 10.1021/jacs.9b02800.

(6) Wuttke, S.; Medina, D. D.; Rotter, J. M.; Begum, S.; Stassin, T.; Ameloot, R.; Oschatz, M.; Tsotsalas, M. Bringing Porous Organic and Carbon-Based Materials toward Thin-Film Applications. *Adv. Funct. Mater.* **2018**, *28*, 1801545.

(7) Virmani, E.; Rotter, J. M.; Mähringer, A.; Zons, T. von; Godt, A.; Bein, T.; Wuttke, S.; Medina, D. D. On-Surface Synthesis of Highly Oriented Thin Metal-Organic Framework Films through Vapor-Assisted Conversion. *JACS* **2018**, *140*, 4812–4819.

(8) Sick, T.; Hufnagel, A. G.; Kampmann, J.; Kondofersky, I.; Calik, M.; Rotter, J. M.; Evans, A.; Döblinger, M.; Herbert, S.; Peters, K.*; et al.* Oriented Films of Conjugated 2D Covalent Organic Frameworks as Photocathodes for Water Splitting. *JACS* **2018**, *140*, 2085–2092.

(9) Medina, D. D.; Petrus, M. L.; Jumabekov, A. N.; Margraf, J. T.; Weinberger, S.; Rotter, J. M.; Clark, T.; Bein, T. Directional Charge-Carrier Transport in Oriented Benzodithiophene Covalent Organic Framework Thin Films. *ACS Nano* **2017**, *11*, 2706–2713.

(10) Lohse, M. S.; Rotter, J. M.; Margraf, J. T.; Werner, V.; Becker, M.; Herbert, S.; Knochel, P.; Clark, T.; Bein, T.; Medina, D. D. From benzodithiophene to diethoxy-benzodithiophene covalent organic frameworks – structural investigations. *CrystEngComm* **2016**, *18*, 4295–4302.

(11) Salonen, L. M.; Medina, D. D.; Carbó-Argibay, E.; Goesten, M. G.; Mafra, L.; Guldris, N.; Rotter, J. M.; Stroppa, D. G.; Rodríguez-Abreu, C. A supramolecular strategy based on molecular dipole moments for high-quality covalent organic frameworks. *Chem. Commun.* **2016**, *52*, 7986–7989.

(12) Medina, D. D.; Rotter, J. M.; Hu, Y.; Dogru, M.; Werner, V.; Auras, F.; Markiewicz, J. T.; Knochel, P.; Bein, T. Room temperature synthesis of covalent-organic framework films through vapor-assisted conversion. *JACS* **2015**, *137*, 1016–1019.

(13) DeBlase, C. R.; Hernández-Burgos, K.; Rotter, J. M.; Fortman, D. J.; dos S. Abreu, D.; Timm, R. A.; Diógenes, I. C. N.; Kubota, L. T.; Abruña, H. D.; Dichtel, W. R. Cation-Dependent Stabilization of Electrogenerated Naphthalene Diimide Dianions in Porous Polymer Thin Films and Their Application to Electrical Energy Storage. *Angew. Chem.* **2015**, *127*, 13423–13427.